**Quantum Monte Carlo Simulations of Ultracold Bosons in a Double Well**

by

Joel Christopher Corbo

A dissertation submitted in partial satisfaction of the
requirements for the degree of
Doctor of Philosophy

in

Physics

in the

Graduate Division

of the

University of California, Berkeley

Committee in charge:

Professor K. Birgitta Whaley, Co-chair
Professor Dmitry Budker, Co-chair
Professor Hartmut Häffner
Professor William A. Lester

Fall 2013

**Quantum Monte Carlo Simulations of Ultracold Bosons in a Double Well**

## Abstract

Quantum Monte Carlo Simulations of Ultracold Bosons in a Double Well

by

Joel Christopher Corbo

Doctor of Philosophy in Physics

University of California, Berkeley

Professor K. Birgitta Whaley, Co-chair

Professor Dmitry Budker, Co-chair

We present path integral ground state (PIGS) quantum Monte Carlo calculations for the ground state ($T = 0$) properties of repulsively interacting bosons in a three-dimensional external double well potential over a range of interaction strengths and potential parameters. We focus our calculations on ground state number statistics and the one-body density matrix in order to understand the level of squeezing and fragmentation that the system exhibits as a function of interaction strength, and we compare our PIGS results to both a standard and an improved two-mode model and a recently-proposed eight-mode model. In general, the various models agree with the PIGS simulations for weak interactions, but the full quantum Monte Carlo treatment is required to correctly predict the amount of squeezing and fragmentation exhibited for strong interactions. One novel and somewhat surprising result from our simulations involves the relationship between squeezing and interaction strength: rather than a monotonic relationship between these quantities, we find that for certain double well barrier heights the squeezing increases as a function of interaction strength until it reaches a maximum, after which it decreases again. We also see a similar relationship between fragmentation and interaction strength. We propose novel physical mechanisms to account for this behavior.

To all of my teachers,
for helping me discover the pleasure of finding things out,

and to all of my students,
for allowing me to relive that pleasure through them.

# Contents

# List of Figures

# List of Tables

## Acknowledgments

This dissertation marks the end of a journey at the University of California, Berkeley that I began over nine years ago. This period in my life has been a source of tremendous personal and intellectual growth and has seen the creation of many deep friendships and significant professional relationships that I hope to nurture throughout the rest of my life. Not unrelatedly, this period has also brought me through some of the most painful periods of self-doubt, anxiety, and depression that I have ever experienced. I wish to devote these acknowledgements to thanking the many people who have helped me to create the good times while guiding me, or just standing with me, through the bad.

First of all, I wish to thank my research group for being an oasis of remarkably intelligent, friendly, and functional people, which is due in no small part to the leadership of my advisor, Birgitta Whaley. Birgit has created an environment in which students can thrive while doing truly remarkable science. Working with her has been one of the most intellectually challenging experiences of my life, transforming me from a student into a scientist. I am grateful for the many fruitful conversations we've had about my research, her careful writing criticism, her consistent encouragement, and her genuine support of my interest in education, diversity, and outreach. Most of all, I am grateful that she took a chance on me when I asked to join her group in my sixth year of graduate school.

Jonathan DuBois has been an invaluable source of knowledge and guidance over the last four years. Despite no longer being a member of our group at Berkeley, he has spent countless hours teaching me about quantum Monte Carlo simulations and many-body quantum systems, despite having more than enough work to do on the projects that actually impacted his professional growth (and paid his salary). Not only did we have lots of great conversations about science, but he also shared with me many of his own struggles as a student, which helped me to normalize my own. I am grateful that he allowed me to see that side of him.

My research group has been a wonderful group of people to work with, share meals with, and talk with about topics as diverse as science, human nature, and whether one would prefer to be the wealthiest person alive hundreds of years ago or the average person alive today. I especially want to single out Brendan Abolins, for our many discussions about Monte Carlo simulations, the state of academia, and life as a grad student; Ty Volkoff, for being the best office-mate a guy could ask for; Jon Aytac, for our many impromptu conversations at Cafe Milano; and Stephan Hoyer, for telling me about the existence of the group and encouraging me to join it.

My work with the Compass Project has been equally as important to my time at Berkeley as my research has been. Through Compass, I have learned to be a teacher, a mentor, a leader, and most importantly, a creator. Compass and its beautiful community of people has been the fuel that has sustained me through the difficulties of grad school; I could very well have left Berkeley had Compass not come into my life when it did. By helping me to define my passion for education and to preview the kind of impact I can make on the world, Compass has changed my future for the better.

I can never sufficiently thank Badr Albanna, Hal Haggard, and Angie Little for being the spark that started the Compass blaze; for choosing me to teach for our first summer program; and for being the sort of people around whom I could drop my "everything is OK" facade, expose my vulnerabilities, and begin the process of coming out of my grad school low. It has truly been a pleasure and an honor to work with them and other amazing graduate students—Benji Alemán, Dimitri Dounas-Frazer, Punit Gandhi, John Haberstroh, Hilary Jacks, Jesse Livesey, Jacob Lynn, Nathan Roth, Josh Shiode, Josiah Schwab, Anna Zaniewski, and many more—to create something that has impacted so many lives and will continue to do so for years to come. And no one could ask for a better group of undergraduates than the ones that Compass has given me the privilege of teaching, mentoring, and working with side by side for the last six years, including Ana Aceves, Amber Archambo, Ankur Dhar, Charlie DePalmo, Drew Edelberg, Feli Hernandez, Geoff Iwata, Gloria Lee, Gina Quan, and T.J. Santos.

It's certainly impossible to thank everyone who has contributed to the achievement of completing my Ph.D., but I'd like to single out Dimitri Dounas-Frazer, for countless conversations about life, academia, relationships, The Future, and just about any other topic imaginable, and for being my consistent swimming/lifting/beach/work-sucks-let's-go-for-a-walk buddy; Jed Duersch and Val and Roger Morash, for being amazingly supportive friends and awesome brunch buddies; Chris Colon, for being my BFF since high school and always making time to hang out despite his crazy lawyering schedule; Norm Tubman, for adding a lot of fun and good conversations to my time at LLNL and after; Donna Sakima, Anne Takizawa, and Claudia Trujillo, for being the most helpful and invaluable members of the Berkeley physics department; Eric Brewe, for being my guide and advocate in the world of physics education research; Patrick Neer and Lawrence Cohen, for being excellent guides through the wilderness of mental health; Ivania Tausche, for dispensing wisdom and back-in-the-day Berkeley physics department stories with every haircut; Scott Hughes, for providing me with support long after my graduation from MIT; Wesley Capps, for being in a category of his own; and all of my other family, friends, and former teachers for always welcoming me with love, support, and open arms.

There is no way that I would be the person I am today without the constant love and support of my parents, Giuseppe and Aymara Corbo. From their own humble beginnings, they built a life together and created an environment that gave me a strong start in life. Through their example, they helped me develop many of the values—hard work, loyalty, dedication, altruism, honesty, friendship, and many more—that have shaped my personality. They instilled in me the value of education and provided me with many excellent educational experiences, so much so that I have now been a student for more years than the two of them put together. They nurtured my curiosity, guided me through lots of difficult decisions, and loved me unconditionally. I can never thank them enough for giving me what they have and being the wonderful people that they are.

Finally, I'd like to thank Allen Rabinovich, my partner and best friend for the last eleven years. There are countless ways, large and small, that Allen has contributed to making this dissertation possible, like helping me when I needed coding help, driving me places,

taking care of me when I was sick, and helping me stay calm when I felt really stressed out. More importantly, Allen has helped make my time at Berkeley so much richer that it otherwise might have been. We've seen great theater together. We've solved and written puzzles together. He's introduced me to music and art and movies and books that I may never have stumbled across on my own. Beyond all that, Allen's presence in my life, his love and support, have helped me to better know myself and to find the strength and conviction to make my time at Berkeley a success.

# Chapter 1

# Introduction

The history of Bose-Einstein condensation stretches back over a hundred years. By the end of the nineteenth century, physics had seemingly reached an apex. Newton's laws of motion and gravitation, Maxwell's laws of electromagnetism, and the laws of thermodynamics were all more or less complete, and they appeared to be sufficient to accomplish the main goal of physics: describing and predicting the behavior of the physical world. However, there were some loose ends—phenomena that could not be adequately explained with known physics—including the nature of the "luminiferous ether" through which light was thought to propagate and the nature of the "blackbody radiation" emitted by bodies in thermal equilibrium with their surroundings. Far from being minor issues, these two loose ends were the first hints of the two greatest revolutions in physics in the twentieth century: relativity and quantum mechanics.

In 1900, Max Planck developed a law that described blackbody radiation measurements extremely well [1]. However, the constants in the law had to be empirically determined because there was no satisfying way to derive them from the laws of classical physics. This remained the case until 1924, when Satyendra Nath Bose developed a theory of the statistical mechanics of photons that could be used to derive Planck's law [2]. Albert Einstein later extended Bose's work to massive particles [3, 4], thus developing the theory of a Bose gas governed by Bose-Einstein statistics. This extension led to the prediction of a *Bose-Einstein condensate* (BEC), a new state of matter in which a dilute gas of bosons is cooled to temperatures very close to absolute zero, causing a large fraction of the bosons to occupy the systems lowest quantum state and thereby allowing for quantum effects on a macroscopic scale.

Although Fritz London proposed Bose-Einstein condensation as an explanation for superfluidity in $^4$He in 1938 [5, 6], the strong interaction between helium atoms dramatically reduces the number of atoms in the condensed state; therefore this system is not considered to be a true BEC. In 1959, Charles Hecht proposed that one should try to observe BEC in a dilute, weakly-interacting atomic gas, arguing that spin-polarized hydrogen would be good candidate such an observation [7]. However, it wasn't until 1995 that true Bose-Einstein condensates were created in the laboratory in atomic gases of rubidium [8], sodium [9], and lithium [10, 11]. This amazing experimental triumph resulted in Eric Cornell, Wolfgang

Ketterle, and Carl E. Wieman receiving the 2001 Nobel Prize in Physics "for the achievement of Bose-Einstein condensation in dilute gases of alkali atoms, and for early fundamental studies of the properties of the condensates." Since that time, there has been an explosion of studies, both experimental and theoretical, into the preparation, properties, and practical uses of Bose-Einstein condensates.

One very fruitful area of BEC research involves studying a BEC trapped in an optical lattice, a trap consisting of a periodic series of potential maxima and minima created by using lasers to generate standing electromagnetic waves. Optical traps are nice to work with in the laboratory because the trap parameters, such as the number, depth, and separation of the minima, are easy to control. They also allow for the investigation of many-body, often macroscopic quantum phenomena, such as the coherence between the atoms in different lattice sites [12] and the transition between Mott insulator and superfluid regimes [13].

## 1.1 Applications of a BEC in a Double Well Potential

The special case of a trap with two minima is known as a double well potential, and a BEC in such a potential can be generated using the well-established technique of splitting a single BEC in a single well "lattice" by raising a barrier in the center of the well using laser beams of the appropriate wavelength and crossing angle [14–17]. The properties of a BEC in a double well potential are of great fundamental and practical interest, with broad implications for a variety of open questions in many-body condensed matter physics and applications in quantum computation. For instance, recent studies regarding quantum liquids subjected to confinement and disorder have shown that the transitions to superfluidity and to Bose-Einstein condensation can occur at different temperatures and that, even at zero temperature, the superfluid and condensate fractions can be different from one another [18, 19]. From a more practical perspective, schemes have been proposed for using condensed bosons in double wells as qubits for quantum computation, in analogy to Josephson charge qubits (in this context, the double well system is thought of as an "atomic Josephson junction") [20, 21].

One potentially powerful application of the double well system involves its use in atom interferometry. Conventional atom interferometers work on a similar principle to light interferometers: a hot beam of atoms is split and made to propagate along two different paths, and when recombined the relative phase shift between the beams results in a measurable interference pattern. Because atoms are composite objects that are sensitive to many environmental phenomena like gravitational, electric, and magnetic fields, atom interferometers can be used to accurately measure quantities as diverse as rotations [22], the gradient of the Earth's gravitational field [23], and fundamental constants like $\hbar/m_e$ [24].

However, to make atom interferometry practical for commercial use requires the interferometers to be small in size. This is possible by using atom chips, small silicon wafers with etched-on wires that can generate magnetic fields, to manipulate small clouds of BEC (see [25] for a thorough theoretical description). By splitting a BEC into a double well geometry and then recombining the two components, one can observe the interference patterns that

result from the differential phase shifts accumulated by the spatially separated BECs. Several groups have build functional atom chip-based, double well interferometers [26, 27].

Of course, there is uncertainty associated with making interferometric measurements. The lower bound on this uncertainty for an atomic BEC interferometer with no special correlations between the atoms is the standard quantum limit of $N^{-1/2}$, where $N$ is the total number of particles involved in the measurement. However, it is possible to induce correlations between the atoms that can reduce the uncertainty to the Heisenberg limit of $N^{-1}$ [28–30]. Initial proposals to reduce this uncertainty called for using superpositions of macroscopic quantum states known as Schrödinger cat states, in which the atoms are in an equal superposition of all being in one well and all being in the other. However, sensitivity to dissipation was found to limit the benefits of using these states [31].

This problem may be avoided by using *squeezed states*, which are entangled many-body states that have a distribution of particles with respect to some variable of interest that is narrower than a binomial distribution [32, 33]. In the context of the double well, the differential number distribution (the difference in the number of particles on the two sides of the barrier) is the relevant distribution and the amount of squeezing is proportional to $\mu/\delta$, where $\mu$ is the chemical potential of the particles and $\delta$ is the tunneling strength between the wells. Hence, one can increase squeezing either by increasing the interaction strength between the particles (and hence the chemical potential) or by decreasing the tunneling strength. The former can be achieved via a Feshbach resonance [34, 35], in which external magnetic fields are used to change the effective interparticle interaction strength over, in principle, many orders of magnitude [36], and the latter can be achieved by simply increasing the barrier height. Beginning in 2001, experimental efforts have succeeded in realizing squeezed states with cold atoms in the laboratory [12, 37–40].

## 1.2 Theoretical Studies of a BEC in a Double Well Potential

To date, the double well problem has been studied extensively using mean-field methods within a two-mode approximation, in which the many-body state of the system is computed in terms of the two lowest one-body states of the system [41–49]. In general, the mean-field approach is restricted to the limit of weak particle interactions, where squeezing is less significant. Indeed, of the studies listed here, only [48, 49] considered effects beyond the usual one-body tunneling ($J$) and onsite interaction ($U$) terms (i.e., they included two-body tunneling terms), and only [43, 44] explicitly considered squeezing. Recent theoretical work on understanding the double well in the context of an eight-mode approximation [50] has uncovered some deficiencies of the two-mode model: even in regimes where one would naively expect only the lowest two single particle modes to contribute based on energy arguments, the ground state can contain components of higher modes, and these modes have the potential to dramatically influence squeezing. This suggests that an analysis which takes into account

the exact many-body nature of the system is necessary to fully understand squeezing in the double well system [51, 52].

In addition to squeezing, the symmetry of the double well potential allows for *fragmentation* [53]. In a canonical BEC, we can express the system's many-body wavefunction in such a way that all of the particles are in the same one-body state. However, under the right conditions, the BEC can exhibit fragmentation, in which multiple one-body states are macroscopically occupied by the particles in the condensate. When population is further distributed over single-particle states with non-macroscopic occupation, the BEC is said to be *depleted*. Experimental studies have confirmed the presence of depletion in an atomic BEC in an optical lattice [54] as well fragmentation in a quasi-1D atomic BEC in a magnetic waveguide [55]. Much theoretical effort has also gone into understanding fragmentation [56, 57], including studies of fragmentation in a double well [45–47]. In particular, [45] predicted that the amount of fragmentation observed in a double well system would increase with the height of the barrier.

## 1.3 Dissertation Overview

In this dissertation, we present a systematic study of the phenomena of squeezing and fragmentation for a Bose-Einstein condensate in a three dimensional double well potential over a range of interaction strengths and barrier heights. We first analyze the properties of the condensate in the double well in the context of the two- and eight-mode models. One fundamental difference between this and previous two-mode work is that we explicitly examine well geometries that exhibit appreciable overlap in the one-body wavefunctions localized in the left and right wells rather than assuming that they are nearly isolated from each other. One particularly surprising observation that we have made in our study of these models is the existence of an optimal interaction strength that maximizes squeezing. This is in stark contrast to the predictions of the two-mode model with no overlap between the wells for which squeezing monotonically increases with interaction strength.

Unfortunately, the eight-mode model is only tractable for small numbers of particles, so we need a better method for computing condensate properties for stronger interaction strengths. To do so, we employ here the full many-body formalism of quantum Monte Carlo (QMC) by evaluating the ground state properties of the BEC using the path integral ground state (PIGS) method [58–60]. PIGS allows us to move beyond the range of validity of mean-field methods and into the regime of strongly interacting systems. We determine the amount of squeezing and fragmentation present in the BEC as a function of interaction strength and compare with the predictions of the two- and eight-mode models in order to understand when, how, and why these approximate models break down.

The dissertation is organized as follows. In Chapter 2, we review the theoretical background necessary for the rest of the dissertation, including squeezing and fragmentation. In Chapter 3, we analyze squeezing and fragmentation for the double well in the context of the two-mode model, and in Chapter 4 we do the same thing in the context of the eight-mode model. In

Chapter 5 we review the PIGS QMC method in the context of the system of interest: strongly interacting bosons in a double well potential. In Chapter 6, we review the squeezing and fragmentation results of QMC calculations for this system and compare them with the two- and eight-mode predictions in order to understand the new physics we observe. Finally, we comment on some ongoing work relating to entanglement entropy in Appendix A.

# Chapter 2

# Background: BEC, Squeezing, and Fragmentation

This chapter provides the theoretical background that underlies the rest of this dissertation. We begin with a brief review of Bose-Einstein condensation in a noninteracting gas. We then introduce the Hamiltonian for the interacting, double-well BEC system and discuss the approximations that go into modeling the particle interactions, and the general features of its ground state, and some standard methods for approximating and computing the ground state. Finally, we introduce and discuss squeezing and fragmentation and derive results that will be useful in later chapters.

## 2.1 Bose-Einstein Condensation

Recall from quantum mechanics that there are two basic types of particles in nature, bosons and fermions, which are distinguished by their spin: a boson has spin that is an integer multiple of $\hbar$ while a fermion has spin that is a half-integer multiple of $\hbar$. Additionally, the wavefunction of a system of $N$ bosons must be symmetric under the exchange of any two particles, while for fermions the wavefunction must be antisymmetric:

$$\psi_{B/F}(\ldots,\mathbf{r}_i,\ldots,\mathbf{r}_j,\ldots) = \pm\psi_{B/F}(\ldots,\mathbf{r}_j,\ldots,\mathbf{r}_i,\ldots). \tag{2.1}$$

In the case of non-interacting particles, this symmetry implies that multiple bosons can exist in the same single-particle state while multiple fermions cannot. To illustrate this, suppose we have a system of two noninteracting particles. Their wavefunction can be written as

$$\psi_{B/F}(\mathbf{r}_1,\mathbf{r}_2) = \frac{1}{\sqrt{2}}(\phi_a(\mathbf{r}_1)\phi_b(\mathbf{r}_2) \pm \phi_b(\mathbf{r}_1)\phi_a(\mathbf{r}_2)), \tag{2.2}$$

where the set of states $\phi_i(\mathbf{r})$ consists of the single-particle eigenstates for whatever potential the particles are experiencing. Notice that if $a = b$ (i.e., the particles are in the same state), this wavefuntion vanishes for fermions but not for bosons.

*Bose-Einstein condensation* (BEC) is a phenomenon that occurs when a gas of bosons is cooled to temperatures sufficiently low that a large fraction of the bosons occupy the system's lowest quantum state. In the case of noninteracting bosons, this state is the single-particle ground state of the system (we will defer discussion of interacting bosons until Section 2.2.2 and of how to characterize condensation in an interacting system until Section 2.4). The fraction of particles in the condensed state depends on the temperature of the system relative to the *condensation temperature* $T_c$ and the density of states for the system's external potential.

The Bose-Einstein distribution function gives the average occupation of a single-particle state $i$ for a system of $N$ non-interacting bosons with no internal degrees of freedom as

$$n_i = \frac{1}{e^{(\epsilon_i - \mu)/kT} - 1}, \tag{2.3}$$

where $\epsilon_i$ is the energy of the state $i$ and $\mu$ is the chemical potential. Notice that we must have that $\mu \leq \epsilon_i$ in order for the occupation of the state $i$ to be nonnegative. If we define the ground state to have zero energy (i.e., $\epsilon_0 = 0$), this means that $\mu \leq 0$. We can be more definitive about the behavior of $\mu$ by considering Eq. (2.3) for $i = 0$. In that case, some algebra gives

$$\mu = kT \ln\left(\frac{n_0}{1 + n_0}\right). \tag{2.4}$$

At high temperatures, the particles will be distributed over all of the states, so $n_0 \approx 0$ and $\mu \to -\infty$. For $T = 0$, all of the particles will condense to the ground state, so $n_0 = N$ and $\mu = 0$. Thus, the condensation temperature is defined as the highest temperature for which $\mu = 0$ or, alternatively, the lowest temperature for which $n_0 \approx 0$.

In order to compute the number of particles in the ground state as a function of temperature, we need to know the system's *density of states* $g(\epsilon)$, which is a measure of the number of states the system has between energies $\epsilon$ and $\epsilon + d\epsilon$ given an particular external potential. The density of states often has a power law form:

$$g(\epsilon) = C_\eta \epsilon^{\eta - 1}. \tag{2.5}$$

For a noninteracting system in a $d$-dimensional box, $\eta = d/2$, while for a noninteracting system in a $d$-dimensional harmonic oscillator, $\eta = d$. The coefficient $C_\eta$ can be computed in each of these cases, but the details are not important for our purposes. Given Eqs. (2.3) and (2.5), we can express the total number of particles in the system as

$$\begin{aligned} N &= N_0(T) + N_e(T) \\ &= N_0(T) + \int_0^\infty n(\epsilon, T) g(\epsilon)\, d\epsilon \\ &= N_0(T) + C_\eta \int_0^\infty \frac{\epsilon^{\eta - 1}}{e^{(\epsilon - \mu)/kT} - 1}\, d\epsilon \\ &= N_0(T) + C_\eta \Gamma(\eta)\, \mathrm{Li}_\eta(e^{\mu/kT})(kT)^\eta, \end{aligned} \tag{2.6}$$

where $\Gamma(x)$ is the gamma function and $\mathrm{Li}_n(x)$ is the polylogarithm [61], which is related to the Riemann zeta function by $\mathrm{Li}_n(1) = \zeta(n)$. Notice that the integral over $\epsilon$ does not contribute to the number of particles in the ground state $N_0$ because $g(\epsilon) \to 0$ as $\epsilon \to 0$. When $T = T_c$, then $\mu = 0$ and $N_0(T_c) = 0$, so we have

$$N = C_\eta \Gamma(\eta)\zeta(\eta)(kT_c)^\eta, \tag{2.7}$$

or

$$kT_c = \left(\frac{N}{C_\eta \Gamma(\eta)\zeta(\eta)}\right)^{1/\eta}. \tag{2.8}$$

With this result, we can rewrite Eq. (2.6) for $T < T_c$ to give us the occupation of the ground state as a function of $T$:

$$\frac{N_0}{N} = 1 - \left(\frac{T}{T_c}\right)^\eta. \tag{2.9}$$

We can also use Eq. (2.8) to help us estimate the temperature at which condensation should happen. As an example system, let's take the experiment described in [8], which used a 3-dimensional harmonic trap. Then, $\eta = 3$ and

$$C_3 = \frac{1}{2\hbar^3 \omega_x \omega_y \omega_z}. \tag{2.10}$$

For the experiment in question, $\omega_z = 120\,\mathrm{Hz}$, $\omega_x = \omega_y = 120/\sqrt{8}\,\mathrm{Hz}$, and $N \approx 4 \times 10^6$. Using these values, $T_c \approx 70\,\mathrm{nK}$.

For the rest of this dissertation, we shall ignore the effects of finite temperature and work at $T = 0$. At that temperature, the non-interacting ground state is given simply by $\psi_g(\mathbf{r}_1, \ldots, \mathbf{r}_N) = \phi_0(\mathbf{r}_1) \cdots \phi_0(\mathbf{r}_N)$, where $\phi_0(\mathbf{r})$ is the single-particle ground state of the appropriate potential. At any higher temperature, the non-interacting ground state would be more complicated because it would include particles in states of higher energy than the single-particle ground state due to the extra thermal energy in the system.

## 2.2 The Many-Body Double Well System

As discussed in Chapter 1, the system we are interested in studying is an interacting Bose gas in a three-dimensional double well trap. In order to understand the behavior of the system at $T = 0$, we need to be able to compute the many-body ground state of the system. We start with the Hamiltonian for $N$ bosons of mass $m$ interacting pairwise in an external potential:

$$\hat{H} = \sum_{j=1}^{N} \left(-\frac{\hbar^2}{2m}\nabla_j^2 + V_{ext}(\mathbf{r}_j)\right) + \sum_{j<k}^{N} V_{int}(\mathbf{r}_j, \mathbf{r}_k). \tag{2.11}$$

Notice that we have already made our first simplifying assumption: we assume that the interactions between the particles are only two-body, i.e., we ignore three- or higher-body

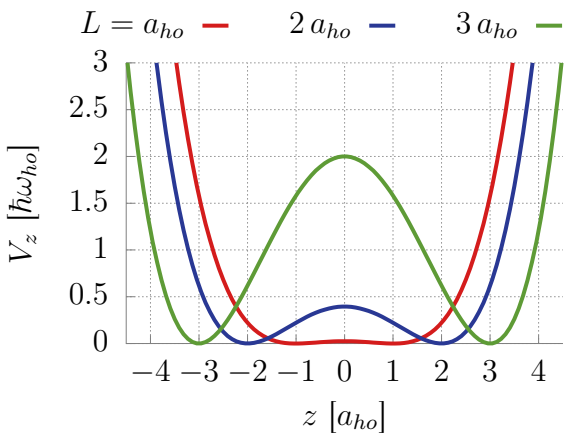


Figure 2.1: The $z$ component of the external potential for $\alpha = 4/81\, a_{ho}^{-2} \approx 0.05\, a_{ho}^{-22}$. The height of the barrier ($V_0 = m\omega_{ho}^2 \alpha L^4/2$) is $2/81\,\hbar\omega_{ho} \approx 0.025\,\hbar\omega_{ho}$, $32/81\,\hbar\omega_{ho} \approx 0.395\,\hbar\omega_{ho}$, and $2\,\hbar\omega_{ho}$ for $L = a_{ho}$, $2\,a_{ho}$, and $3\,a_{ho}$, respectively. The curvature parameter ($C_z = 4\alpha L^2$) is $16/81 \approx 0.2$, $64/81 \approx 0.8$, and $16/9 \approx 1.8$ for $L = a_{ho}$, $2\,a_{ho}$, and $3\,a_{ho}$, respectively.

interactions. This assumption is justified because the atomic gases used in experiments are sufficiently dilute that interactions between atoms are dominated by two-body effects. In the next two subsections, we discuss the details of the external and interaction potentials.

### 2.2.1 The External Potential

For the external potential, we use a three-dimensional double well potential of the form

$$V_{ext}(\mathbf{r}) = \frac{1}{2} m\omega_{ho}^2 \left( x^2 + y^2 + \alpha \left( z^2 - L^2 \right)^2 \right), \tag{2.12}$$

where $\omega_{ho}$ is the characteristic harmonic trap frequency in the $xy$ plane, $\alpha$ characterizes the height of the barrier between wells at $z = 0$, and $2L$ is the distance between the minima of the wells (see Figure 2.1). In terms of these parameters, the height of the barrier $V_0 = V_{ext}(0)$ is given by $m\omega_{ho}^2 \alpha L^4/2$; $V_0$ grows with increasing $\alpha$ or increasing $L$. Similarly, we can define a parameter $C_z$ that characterizes the curvature of the minima in the $z$-direction relative to the $x$- and $y$-directions by expanding the potential about $z = \pm L$:

$$V_{ext}(\mathbf{r})|_{z=\pm L} = \frac{1}{2} m\omega_{ho}^2 \left( x^2 + y^2 + 4\alpha L^2 (z \mp L)^2 + \mathcal{O}((z \mp L)^3) \right). \tag{2.13}$$

Then, $C_z = 4\alpha L^2$ and also grows with increasing $\alpha$ or increasing $L$. For reasons that we will discuss in Chapter 4, we restrict our attention in this dissertation to $\alpha = 4/81\, a_{ho}^2 \approx 0.05\, a_{ho}^2$ and $L = a_{ho}$, $2\,a_{ho}$, and $3\,a_{ho}$. Table 2.1 lists values of $V_0$ and $C_z$ for these values of $\alpha$ and $L$, as well as the energies of the first four states of the double well to give a sense of where they lie relative to the height of the barrier. These states will be relevant to the construction of models for the double well system in Chapters 3 and Chapter 4.

| | | Energy $[\hbar\omega_{ho}]$ | | | | |
|---|---|---|---|---|---|---|
| $L\ [a_{ho}]$ | $C_z$ | $\phi_0(z)$ | $\phi_1(z)$ | $\phi_2(z)$ | $\phi_3(z)$ | $V_0$ |
| 1 | 0.20 | 0.167 | 0.594 | 1.220 | 1.946 | 0.025 |
| 2 | 0.79 | 0.297 | 0.482 | 1.026 | 1.614 | 0.395 |
| 3 | 1.78 | 0.634 | 0.637 | 1.681 | 1.801 | 2 |

Table 2.1: Single-particle energies of the ground and first three excited states of the $z$ part of the double well potential, as well as the height of the double well barrier and curvature of the double well minima, for $\alpha = 4/81\, a_{ho}^{-2}$ and various $L$. Note that these energies do not include the contribution from motion in the $x$ and $y$ degrees of freedom of the state.

To give a realistic sense of the magnitude of the parameters of the external potential, we use the experiment described in [26]. The experiment used $^{23}$Na atoms and had a trap with $L = 6.5\,\mu$m, $\omega_{ho}/2\pi = 615\,$Hz, and $V_0 = h \times 4.7\,$kHz (equivalently, $\alpha = 6.1 \times 10^{-9}\,\text{nm}^{-2}$). In general, we will present our results in terms of the system's characteristic length $a_{ho} = (\hbar/m\omega_{ho})^{1/2}$ and energy $E_{ho} = \hbar\omega_{ho}$. For [26], $a_{ho} = 845\,$nm and $E_{ho} = 2.54\,$peV, so $L = 7.7\, a_{ho}$, $V_0 = 7.6\, E_{ho}$, and $\alpha = 0.26\, a_{ho}^{-2}$. These values are comparable to those that we use in this dissertation.

### 2.2.2 The Interaction Potential

As noted earlier, we will assume that the atomic gas that makes up our BEC is sufficiently dilute that we can ignore all but two-body particle interactions. Even with this simplification, the forces felt by two interacting neutral atoms are complicated. At short distances, one can approximate the strong Coulomb repulsion of the atoms' electrons by a hard sphere interaction, while at long distances, the interaction is dominated by the van der Waals force, which goes like $r^{-6}$. For notational convenience, let's define the separation between two atoms by $r_{ij} = |\mathbf{r}_{ij}| = |\mathbf{r}_i - \mathbf{r}_j|$. Then we can model the interparticle potential by

$$V_{int}(\mathbf{r}_i, \mathbf{r}_j) = \begin{cases} \infty & r_{ij} < r_c \\ -\frac{C}{r^6} & r_{ij} > r_c \end{cases}, \tag{2.14}$$

where $r_c$ is the characteristic distance at which the Coulomb repulsion dominates.

This potential is still relatively complicated, but it can be further simplified by taking into account the fact that the collisions between atoms are occurring at very low energy because the system is at ultracold temperatures. Recall from quantum scattering theory that the wavefunction for a system that consists of a plane wave scattering from a spherically symmetric potential is given at long distances by [62]

$$\psi = e^{ikz} + f(\theta)\frac{e^{ikr}}{r}, \tag{2.15}$$

where $f(\theta)$ is the scattering amplitude and the energy of the state is given by

$$E = \frac{\hbar^2 k^2}{2m}. \tag{2.16}$$

At low energy, then, $k \to 0$. One can show that $f(\theta)$ approaches a constant, $-a$, in the $k \to 0$ limit [62]. The constant $a$ is known as the *s-wave scattering length*. In this limit, the wavefunction (2.15) is only a function of the separation between the atoms, and reads

$$\psi(\mathbf{r}_i, \mathbf{r}_j) = 1 - \frac{a}{r_{ij}}. \tag{2.17}$$

This is the same result that one would find if one computed the wavefunction for two particles interacting via a hard sphere interaction:

$$V_{int}(\mathbf{r}_i, \mathbf{r}_j) = \begin{cases} \infty & r_{ij} < a \\ 0 & r_{ij} > a \end{cases}. \tag{2.18}$$

Hence, at very low energy we can use the hard sphere interaction potential in place of whatever complicated potential best models the interparticle interactions at high energy, as long as we choose the appropriate value of $a$. Conceptually, the scattering length encodes all of the low energy behavior in a two-body interaction.

It is instructive to study a particular potential in detail to get a sense of the order of magnitude of the length scales involved in this argument. For the potential (2.14), one can compute the scattering length exactly [63]:

$$a = r_{vdW} \frac{\Gamma(3/4)}{2\sqrt{2}\Gamma(5/4)} \left(1 - \tan\left(\frac{r_{vdW}^2}{2r_c^2} - \frac{3\pi}{8}\right)\right) \tag{2.19}$$

where $r_{vdW} = \left(\frac{2Cm}{\hbar^2}\right)^{1/4}$. For a typical dilute atomic gas, $r_c \approx 10\, a_\mathrm{B}$, $r_{vdW} \approx 100\, a_\mathrm{B}$, $a \approx 400\, a_\mathrm{B}$, and $n^{-1/3} \approx 4000\, a_\mathrm{B}$, where $a_\mathrm{B}$ is the Bohr radius. Hence, we see that the scattering length is larger than the short-range features of the potential while being much smaller than the average separation between the atoms.

There is a second useful way of expressing the hard sphere potential (2.18). The wavefunction of two scattering hard spheres satisfies

$$(\nabla^2 + k^2)\psi(\mathbf{r}_{ij}) = 0, \tag{2.20}$$

for $r_{ij} > a$, provided that we also set $\psi(\mathbf{r}_{ij}) = 0$ for $r_{ij} < a$. One can show that this is equivalent to [64]

$$(\nabla^2 + k^2)\psi(\mathbf{r}_{ij}) = 4\pi \frac{\tan(ka)}{k} \delta(\mathbf{r}_{ij}) \left(\psi(\mathbf{r}_{ij}) + r_{ij} \frac{\partial}{\partial r_{ij}} \psi(\mathbf{r}_{ij})\right). \tag{2.21}$$

In the $k \to 0$ limit and assuming that $\partial\psi(\mathbf{r}_{ij})/\partial r_{ij}$ does not diverge at the origin, this equation becomes

$$(\nabla^2 + k^2)\psi(\mathbf{r}_{ij}) = 4\pi a\, \delta(\mathbf{r}_{ij})\psi(\mathbf{r}_{ij}). \tag{2.22}$$

We can rewrite this as

$$-\frac{\hbar^2\nabla^2}{2m_r}\psi(\mathbf{r}_{ij}) + \frac{4\pi\hbar^2 a}{2m_r}\delta(\mathbf{r}_{ij})\psi(\mathbf{r}_{ij}) = \frac{\hbar^2 k^2}{2m_r}\psi(\mathbf{r}_{ij}), \tag{2.23}$$

where $m_r = m/2$ is the reduces mass of the system. This takes the form of Schrödinger's equation, with a contact potential [65, 66]

$$V_{int}(\mathbf{r}_i, \mathbf{r}_j) = \frac{4\pi\hbar^2 a}{m}\delta(\mathbf{r}_{jk}). \tag{2.24}$$

We use this contact potential instead of the hard sphere potential (2.18) in calculations of the BEC ground state in the context of the multimode models described in Chapters 3 and 4, although we use the true hard sphere potential in our quantum Monte Carlo simulations, as described in Chapter 5.

### Feshbach Resonance

In this dissertation, we focus on studying the ground state properties of atomic gas BECs as a function of the scattering length, which, as we have seen, provides a measure of the strength of the interactions between the atoms at ultra low energies. One of the motivations for looking at the system this way is that the scattering length is actually highly tunable in the laboratory due to the phenomenon of *Feshbach resonance*.

A Feshbach resonance [34, 35] is a resonance of a many-body system between a bound state and a scattering state of the system. Suppose that two atoms are interacting with each other via an interaction potential $V_o(r_{ij})$ such that they are in a scattering state $|s\rangle$ with energy $E_s$ with respect to this potential. Because $E_s \geq \lim_{r_{ij}\to\infty} V_o(r_{ij})$, we refer to this as an *open channel*. Let's denote the scattering length associated with the state $|s\rangle$ as $a_s$. Suppose further that the atoms could also interact via a second potential $V_c(r_{ij})$ of higher energy, and that this potential supports a bound state $|b\rangle$ of energy $E_b \approx E_s$. Because $E_b < \lim_{r_{ij}\to\infty} V_c(r_{ij})$, we refer to this as a *closed channel*. See Figure 2.2 for an energy diagram for these channels.

In general, degrees of freedom internal to the pair of atoms, e.g., their spin state, determine the (single) channel through which they interact and therefore their scattering properties. However, if there is a coupling between the open and closed channels, then the presence of the bound state $|b\rangle$ in the closed channel can modify the scattering length for the scattering state $|s\rangle$ in the open channel. This comes about because the atoms in the state $|s\rangle$ can temporarily scatter into $|b\rangle$ as an intermediate state before decaying back into the state $|s\rangle$; this alters $a_s$ to second order in the coupling strength. The closer $E_s$ and $E_b$ are to each other, the stronger the shift in $a_s$, so if one can control the energy of the bound state, one can in principle alter $a_s$ over a large range of values.

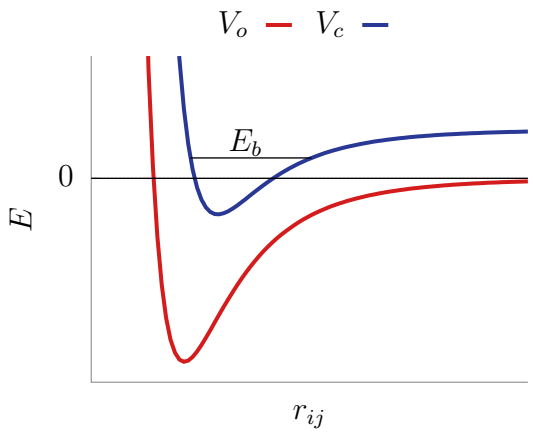


Figure 2.2: Energy diagram depicting the potential energy as a function of interatomic distance $r_{ij}$ for the open (red) and closed (blue) channels in a model Feshbach resonance. The total kinetic energy of the atoms is zero, which allows the system to be in a scattering state of the open channel but not of the closed channel. However, there is a bound state in the closed channel with energy $E_b$ close to zero.

We now make this qualitative description quantitative. The total Hilbert space of the system can be divided into two subspaces: the one that contains the scattering state $|s\rangle$ and the one that contains the bound state $|b\rangle$. If these are the only two states we consider, then of course these subspaces only have one element each (we can always generalize this to larger Hilbert spaces for more complicated situations). We can then explicitly write these states as basis vectors of the total Hilbert space by defining $|s\rangle = \binom{1}{0}$ and $|b\rangle = \binom{0}{1}$. Then we can write the atoms' interaction Hamiltonian in the total Hilbert space as

$$\begin{aligned}\hat{H}_{int} &= \hat{H}_o + \hat{H}_c + \hat{H}_{oc} \\ &= \begin{pmatrix} \gamma_o & 0 \\ 0 & 0 \end{pmatrix} + \begin{pmatrix} 0 & 0 \\ 0 & \gamma_c \end{pmatrix} + \begin{pmatrix} 0 & \gamma_{oc} \\ \gamma_{oc}^* & 0 \end{pmatrix},\end{aligned} \tag{2.25}$$

where $H_o$ is the Hamiltonian for the open channel, $H_c$ is the Hamiltonian for the closed channel, $H_{oc}$ is the Hamiltonian for the coupling between the open and closed channels; we have schematically illustrated the structure of these three Hamiltonians in basis spanned by $|s\rangle$ and $|b\rangle$.

Now, suppose we want to compute $\langle s|\hat{H}_{int}|s\rangle$ to second order in the perturbation $\hat{H}_{oc}$. We find

$$\begin{aligned}\langle s|\hat{H}_{int}|s\rangle &= \langle s|\hat{H}_o + \hat{H}_c|s\rangle + \langle s|\hat{H}_{oc}|s\rangle + \frac{|\langle b|\hat{H}_{oc}|s\rangle|^2}{E_s - E_b} \\ &= \langle s|\hat{H}_o|s\rangle + \frac{|\langle b|\hat{H}_{oc}|s\rangle|^2}{E_s - E_b}.\end{aligned} \tag{2.26}$$

To simplify this expression, we note that $\hat{H}_0$ is nothing more than the contact potential Eq. (2.24). Hence, we have that

$$\langle s|\hat{H}_o|s\rangle = 4\pi\hbar\omega_{ho}a_{ho}^2 a_s \langle s|\delta(\hat{\mathbf{r}}_{ij})|s\rangle . \tag{2.27}$$

Because this expression is only being perturbed by a small amount, we assume that we can write $\langle s|\hat{H}_{int}|s\rangle$ similarly:

$$\langle s|\hat{H}_{int}|s\rangle = 4\pi\hbar\omega_{ho}a_{ho}^2 a_{\text{eff}} \langle s|\delta(\hat{\mathbf{r}}_{ij})|s\rangle , \tag{2.28}$$

where $a_{\text{eff}}$ is some effective scattering length due to the effect of the bound state $|b\rangle$. We can substitute these expressions into Eq. (2.26), producing

$$a_{\text{eff}} = a_s - \frac{1}{E_b - E_s}\left(\frac{|\langle b|\hat{H}_{oc}|s\rangle|^2}{4\pi\hbar\omega_{ho}a_{ho}^2 \langle s|\delta(\hat{\mathbf{r}}_{ij})|s\rangle}\right). \tag{2.29}$$

So, as we described earlier, the effective scattering length of the scattering state is dependent on the difference in the energy between the bound and scattering states.

One particularly easy way of altering this energy difference for an atomic gas is via an external magnetic field. Because the atoms in the scattering and bound states have different magnetic moments ($\mu_s$ and $\mu_b$, respectively), they respond differently to an external magnetic field such that generally $E_s(B) \neq E_b(B)$. However, suppose that there is a magnetic field value $B_0$ for which $E_b = E_s = E_0$. Then, we can linearize the energies around $B_0$:

$$E_b(B) = E_0 - \mu_b(B - B_0) \tag{2.30a}$$
$$E_s(B) = E_0 - \mu_s(B - B_0). \tag{2.30b}$$

Substituting these into Eq. (2.29), we find [67]

$$a_{\text{eff}}(B) = a_s\left(1 - \frac{\Delta}{B - B_0}\right), \tag{2.31}$$

where

$$\Delta = \frac{1}{a_s(\mu_s - \mu_b)}\left(\frac{|\langle b|\hat{H}_{oc}|s\rangle|^2}{4\pi\hbar\omega_{ho}a_{ho}^2 \langle s|\delta(\hat{\mathbf{r}}_{ij})|s\rangle}\right). \tag{2.32}$$

Thus, we see that one can change the effective scattering length of the interaction by altering the external magnetic field experienced by the system.

Substantial tunability of both the magnitude and sign of $a$ has been demonstrated in the laboratory using magnetic Feshbach resonances [68–70]. A particularly impressive example is [36], in which $a$ for $^7$Li was tuned between 0.53 pm and 10.6 $\mu$m (corresponding to between $3.5 \times 10^{-7}\, a_{ho}$ and $7\, a_{ho}$, given the value of $\omega_{ho}$ referenced in the discussion of the external potential in Section 2.2.1). Our calculations go up to $0.5\, a_{ho}$ (about 420 nm), which is thus well within the range of experimental accessibility.

### 2.2.3 The Ground State

To recap, the Hamiltonian for the many-body, pairwise-interacting, double well system is given by

$$\hat{H} = \sum_{i=1}^{N} \left( \frac{\mathbf{p}_i^2}{2m} + V_{ext}(\mathbf{r}_i) \right) + \frac{4\pi\hbar^2 a}{m} \sum_{i<j} \delta(\mathbf{r}_{jk}), \tag{2.33}$$

with the external potential given by (2.12). We can also express this in second quantized form as

$$\hat{H} = \int \hat{\Psi}^\dagger(\mathbf{r}) \left( -\frac{\hbar^2}{2m}\nabla^2 + V_{ext}(\mathbf{r}) \right) \hat{\Psi}(\mathbf{r})\, d\mathbf{r} + \frac{2\pi\hbar^2 a}{m} \int \hat{\Psi}^\dagger(\mathbf{r})\hat{\Psi}^\dagger(\mathbf{r})\hat{\Psi}(\mathbf{r})\hat{\Psi}(\mathbf{r})\, d\mathbf{r}, \tag{2.34}$$

where the field operator $\hat{\Psi}(\mathbf{r})$ destroys a particle located at $\mathbf{r}$. In either form, our next goal is to compute the ground state of the system. This cannot be done analytically because of the presence of the interaction potential. Our options are either to compute an approximate analytical solution or to solve the exact problem as well as we can numerically. We will discuss analytical approximations in the rest of this section and the next two chapters and defer discussion of numerical solution methods until Chapter 5.

That said, there *is* one situation in which we do know the form of the many-body ground state: this is the noninteracting ($a = 0$) case. In that situation, each atom is simply in the single-body ground state of the Hamiltonian, which we will denote by $\phi_0(\mathbf{r})$. Hence,

$$\Psi_{gs}(\mathbf{r}_1, \ldots, \mathbf{r}_N) = \sum_{i=1}^{N} \phi_0(\mathbf{r}_i) \qquad (a = 0). \tag{2.35}$$

#### The Gross-Pitaevskii Equation

The simplest analytical approximation that one can make is to assume that the $N$-body ground state has the form of an $N$-term product of the same single-body wavefunction:

$$\Psi_{mf}(\mathbf{r}_1, \ldots, \mathbf{r}_N) = \prod_{i=1}^{N} \psi(\mathbf{r}_i). \tag{2.36}$$

In other words, one assumes that all of the atoms in the BEC are in the same state. In the $a \to 0$ limit, this approximation, known as the *mean-field approximation*, holds exactly at $T = 0$. One expects, then, that it is a reasonable approximation for small $a$.

Of course, we don't yet know which state $\psi(\mathbf{r})$ should be used in the mean-field approximation. To determine this, we first compute an expression for the energy of an arbitrary

state for the Hamiltonian (2.33):

$$\begin{aligned}
E[\psi,\psi^*] &= \int \Psi^*_{mf}(\mathbf{r}_1,\ldots,\mathbf{r}_N)\hat{H}\Psi_{mf}(\mathbf{r}_1,\ldots,\mathbf{r}_N)\,d\mathbf{r}_1\cdots d\mathbf{r}_N \\
&= \sum_{i=1}^{N}\int \Psi^*_{mf}(\mathbf{r}_1,\ldots,\mathbf{r}_N)\left(-\frac{\hbar^2\nabla_i^2}{2m}+V_{ext}(\mathbf{r}_i)\right)\Psi_{mf}(\mathbf{r}_1,\ldots,\mathbf{r}_N)\,d\mathbf{r}_1\cdots d\mathbf{r}_N \\
&\quad + \frac{4\pi\hbar^2 a}{m}\sum_{i<j}\int \Psi^*_{mf}(\mathbf{r}_1,\ldots,\mathbf{r}_N)\delta(\mathbf{r}_{jk})\Psi_{mf}(\mathbf{r}_1,\ldots,\mathbf{r}_N)\,d\mathbf{r}_1\cdots d\mathbf{r}_N \\
&= N\int \psi^*(\mathbf{r}_1)\left(-\frac{\hbar^2\nabla_1^2}{2m}+V_{ext}(\mathbf{r}_1)\right)\psi(\mathbf{r}_1)\,d\mathbf{r}_1 \\
&\quad + \frac{4\pi\hbar^2 a}{m}\frac{N(N-1)}{2}\int \psi^*(\mathbf{r}_1)|\psi(\mathbf{r}_1)|^2\psi(\mathbf{r}_1)\,d\mathbf{r}_1 \\
&= N\int \psi^*(\mathbf{r}_1)\left(-\frac{\hbar^2\nabla_1^2}{2m}+V_{ext}(\mathbf{r}_1)+\frac{4\pi\hbar^2 a}{m}\frac{N-1}{2}|\psi(\mathbf{r}_1)|^2\right)\psi(\mathbf{r}_1)\,d\mathbf{r}_1. \qquad (2.37)
\end{aligned}$$

We have expressed this energy as a functional of the wavefunction $\psi$ and its conjugate $\psi^*$. The correct wavefunction for the condensate is the one that minimizes this energy subject to the condition that $\psi$ is normalized. We can accomplish this minimization by introducing a Lagrange multiplier to form the new functional

$$\begin{aligned}
\Lambda[\psi,\psi^*] &= N\int \psi^*(\mathbf{r}_1)\left(-\frac{\hbar^2\nabla_1^2}{2m}+V_{ext}(\mathbf{r}_1)+\frac{4\pi\hbar^2 a}{m}\frac{N-1}{2}|\psi(\mathbf{r}_1)|^2\right)\psi(\mathbf{r}_1)\,d\mathbf{r}_1 \\
&\quad - N\mu\left(\int |\psi(\mathbf{r}_1)|^2 d\mathbf{r}_1 - 1\right), \qquad (2.38)
\end{aligned}$$

and setting equal to zero the derivative of that functional with respect to $\psi^*$:

$$\begin{aligned}
\frac{\delta}{\delta\psi^*(\mathbf{r})}\Lambda[\psi,\psi^*] &= N\left(-\frac{\hbar^2\nabla^2}{2m}+V_{ext}(\mathbf{r})+\frac{4\pi\hbar^2 a}{m}(N-1)|\psi(\mathbf{r})|^2-\mu\right)\psi(\mathbf{r}) \\
&= 0. \qquad (2.39)
\end{aligned}$$

This leads to the *Gross-Pitaevskii (GP) equation* [71, 72]:

$$\left(-\frac{\hbar^2}{2m}\nabla^2+V_{ext}(\mathbf{r})+\frac{4\pi\hbar^2}{m}(N-1)a|\psi(\mathbf{r})|^2\right)\psi(\mathbf{r})=\mu\psi(\mathbf{r}), \qquad (2.40)$$

which takes the form of a nonlinear Scrödinger equation for $\psi(\mathbf{r})$. The strength of the nonlinearity is controlled by $(N-1)a$ ($\approx Na$ for large $N$). For $Na$ large and positive (i.e., a dense and repulsive gas), the nonlinear term tends to spread the wavefunction out relative to the solution to the linear Scrödinger equation by imposing an energy cost on locally high particle densities, whereas for $Na$ large and negative (i.e., a dense and attractive gas), the opposite is true.

The GP equation is generally a valid description of the condensate as long as the number of atoms in the condensed state $N_0$ is approximately equal to $N$. However, we will discuss in more detail in Section 3.1, the Gross-Pitaevskii ground state is not capable of describing squeezing or fragmentation in a meaningful way; no matter the value of the scattering length $a$, the GP ground state exhibits no squeezing and no fragmentation. Hence, we must go beyond the simple mean-field approximation to have a chance at describing all of the physics that we see in our BEC simulations.

### Multimode Expansion

The other analytical method we will consider begins with the second-quantized form of the interacting double well Hamiltonian, Eq. (2.34). The field operator $\hat{\Psi}(\mathbf{r})$ in this expression can be written in terms of a complete basis of single-body states $\phi_i(\mathbf{r})$, which we will refer to as *modes*:

$$\hat{\Psi}(\mathbf{r}) = \sum_{i=1}^{\infty} \phi_i(\mathbf{r})\hat{a}_i. \tag{2.41}$$

The operator $\hat{a}_i$ destroys a particle in the mode $\phi_i(\mathbf{r})$ (while $\hat{a}_i^\dagger$ creates a particle in that mode), so intuitively one can interpret this sum as encompassing all of the different ways of destroying a particle at $\mathbf{r}$, which is what $\hat{\Psi}(\mathbf{r})$ does. The creation and annihilation operators for each mode obey the usual commutation relation $[\hat{a}, \hat{a}^\dagger] = 1$.

In principle, the modes can be any complete set of single-body states. In practice, one usually chooses to use the energy eigenstates of the external potential, or convenient linear combinations of those eigenstates. As we shall see in Chapters 3 and 4, we use linear combinations of the energy eigenstates of the double well that are localized in the left and right sides of the potential.

Upon substituting Eq. (2.41) into Eq. (2.34), we find

$$\hat{H} = \sum_{i,j=1}^{\infty} \hat{a}_i^\dagger \hat{a}_j \, \epsilon_{ij} + a \sum_{i,j,k,l=1}^{\infty} \hat{a}_i^\dagger \hat{a}_j^\dagger \hat{a}_k \hat{a}_l \, \kappa_{ijkl}, \tag{2.42}$$

where

$$\epsilon_{ij} = \int \phi_i^*(\mathbf{r}) \left( -\frac{\hbar^2}{2m}\nabla^2 + V_{ext}(\mathbf{r}) \right) \phi_j(\mathbf{r}) \, d\mathbf{r} \tag{2.43}$$

$$\kappa_{ijkl} = \frac{2\pi\hbar^2}{m} \int \phi_i^*(\mathbf{r})\phi_j^*(\mathbf{r})\phi_k(\mathbf{r})\phi_l(\mathbf{r}) \, d\mathbf{r}. \tag{2.44}$$

The Hamiltonian now has the form of a generalized Bose-Hubbard Hamiltonian [73] (the traditional Bose-Hubbard Hamiltonian has $i = j = k = l$ in the second term). We can interpret the parameters in the Hamiltonian as follows. The (single-particle) energy of a mode $\phi_i(\mathbf{r})$ is given by $\epsilon_{ii}$, while for $i \neq j$, the $\epsilon_{ij}$ parameters characterize the coupling between modes $\phi_i(\mathbf{r})$ and $\phi_j(\mathbf{r})$ that is independent of the two-body interactions. The $\kappa_{ijkl}$ parameters

characterize the strength of two-body interactions, which involve coupling among up to four different modes. Note that the value of these parameters are solely a function of the choice of modes $\phi_i(\mathbf{r})$.

In order to make computation of the ground state of the Hamiltonian (2.42) tractable, one can truncate the expansion of the field operator (2.41) by restricting it to only a finite number of modes. This makes the Hilbert space of the system finite, and, if the truncation is sufficiently severe, allows one to numerically diagonalize the Hamiltonian to find the ground state. For the double well system, the usual truncation is a two-mode model in which the field operator is expanded in terms of the two lowest single-particle energy states of the double well potential. Recently, an eight-mode model [50], which truncates the mode basis to the eight single-particle states of lowest energy, has also been considered. We discuss the computation and results of using the two- and eight-mode models in Chapters 3 and 4, respectively.

Before moving on to a discussion of squeezing, there are two more issues related to the multimode expansion worth discussing: the significance of the one-mode expansion and the construction of basis states that span the Hilbert space of the Hamiltonian.

**One-Mode Expansion** In the case of a one-mode expansion, the field operator can be expanded as $\hat{\Psi}(\mathbf{r}) = \phi(\mathbf{r})\hat{a}$. This leads to a Hamiltonian of the form

$$\hat{H} = \epsilon\,\hat{n} + a\kappa\,\hat{n}(\hat{n}-1), \tag{2.45}$$

where $\hat{n} = \hat{a}^\dagger\hat{a}$ is the number operator associated with the given mode, and we have used the commutation relation $[\hat{a}, \hat{a}^\dagger] = 1$ to simplify the second term. Because there is only one mode in this expansion, the ground state (indeed, the only possible state) consists of all of the particles in that mode:

$$\Psi_{gs}(\mathbf{r}_1, \ldots, \mathbf{r}_N) = \prod_{i=1}^{N} \phi(\mathbf{r}_i). \tag{2.46}$$

This is simply the ground state in the mean-field approximation (see Eq. (2.36)), and if we compute the energy of the one-mode Hamiltonian for this state, we get

$$\begin{aligned} E &= \langle \Psi_{gs}|\hat{H}|\Psi_{gs}\rangle \\ &= N\epsilon + aN(N-1)\kappa \\ &= N\int \phi^*(\mathbf{r})\left(-\frac{\hbar^2\nabla^2}{2m} + V_{ext}(\mathbf{r}) + \frac{4\pi\hbar^2 a}{m}\frac{N-1}{2}|\phi(\mathbf{r})|^2\right)\phi(\mathbf{r})\,d\mathbf{r}, \end{aligned} \tag{2.47}$$

which is the same energy functional that we used to derive the GP equation. Hence, the one-mode approximation in the multimode expansion is the same as the mean-field approximation that leads to the GP equation, so adding more modes will give us a better approximation to the actual behavior of the system than does the mean-field approximation.

**Basis States** It is useful to think through how to represent an arbitrary $N$-body state given the set of modes $\phi_i(\mathbf{r})$. First, choose a set of $N$ modes, with repetitions allowed, for the $N$ atoms to be in, and denote the set of indices of these modes as $I = \{i_1, \ldots, i_N\}$. Because these atoms are indistinguishable bosons, they must be in a completely symmetrized, normalized state. This state, known as a *Fock state*, is a sum over all of the different ways of assigning the $N$ atoms to the chosen $N$ modes:

$$\psi_I(\mathbf{r}_1, \ldots, \mathbf{r}_N) = \mathcal{A}_I \sum_{J \in P(I)} \phi_{j_1}(\mathbf{r}_1) \ldots \phi_{j_N}(\mathbf{r}_N), \tag{2.48}$$

where

$$\mathcal{A}_I = \sqrt{\frac{m(I,1)!m(I,2)!\ldots}{N!}}, \tag{2.49}$$

is the normalization constant. Here, $m(I, n)$ denotes the number of times $n$ appears in the set $I$ (i.e., the multiplicity of $n$ in $I$) and $P(I)$ denotes the set of distinguishable permutations of the elements of $I$.

The Fock states $\psi_I(\mathbf{r}_1, \ldots, \mathbf{r}_N)$ form a basis for the system's $N$-body Hilbert space, so it is possible to construct an arbitrary $N$-body state $\Psi(\mathbf{r}_1, \ldots, \mathbf{r}_N)$ as a sum over these states:

$$\Psi(\mathbf{r}_1, \ldots, \mathbf{r}_N) = \sum_{I \in \mathcal{S}} c_I \psi_I(\mathbf{r}_1, \ldots, \mathbf{r}_N), \tag{2.50}$$

where $\mathcal{S}$ is the set of all of the possible ways of choosing $N$ mode indices and $c_I$ assures normalization (i.e., $\sum |c_I|^2 = 1$).

We can also compute the size of the Hilbert space spanned by the states $\psi_I(\mathbf{r}_1, \ldots, \mathbf{r}_N)$ simply by counting how many of them there are, i.e., by counting the number of ways there are to distribute $N$ atoms among $M$ modes. (which is equivalent to determining how many ways there are of arranging $N$ identical objects and $M - 1$ identical partitions in a line). The answer is:

$$\dim(\hat{H}) = \frac{(N + M - 1)!}{N!(M - 1)!}. \tag{2.51}$$

In the limit of large $M$, this expression approaches $M^N$. Hence, if we would like to be able to numerically diagonalize the Hamiltonian, we need to restrict ourselves to a relatively small number of modes (or atoms) to make that computation tractable.

## 2.3 Number Squeezing

Number squeezing is a phenomenon that is related to the probability of finding different numbers of particle on one side or the other of a barrier; in the case of our system, the particles are atoms and the barrier is the one in the middle of the double well. Imagine that we measure the positions of all $N$ atoms; we will find some number of them in each half of the potential, with the probability of finding that particular partitioning of atoms determined

by the many-body wavefunction of the system. In an unsqueezed system, the distribution of partitioning is relatively broad and given by a binomial distribution, whereas the system is said to be squeezed when the probability of observing a half-and-half partitioning between the wells dominates over all other partitionings. In other words, fluctuations that lead to a large difference in the number of particles on the two sides of the potential are suppressed in squeezed systems.

The amount of squeezing a system exhibits depends on the strength of the interactions between the particles, because interactions can enhance or suppress number fluctuations. Naively, we expect that a system with stronger repulsive interaction will have smaller number fluctuations, and hence more squeezing, due to the energy cost of packing many strongly repulsive particles on the same side of the double well. Thus, squeezing should increase monotonically with (repulsive) interaction strength. This is indeed the prediction of the two-mode model when the two wells are well-separated [43]. However, as we shall see in Chapters 3, 4, and 6, this simple picture is not the whole story: squeezing is not monotonically related to interaction strength in all situations.

### 2.3.1 The Differential Number Distribution

To quantify the concept of squeezing, we will need the help of some new operators to define the differential number distribution, the distribution that encodes the partitioning probabilities described above. First, we define an operator $\hat{L}$, which measures the number of particles on the left side of the double well (i.e., for $z < 0$). For an $N$ atom system, it is given in the position representation by

$$\hat{L} = \sum_{i=1}^{N} \begin{cases} 1 & z_i < 0 \\ 0 & z_i > 0 \end{cases} . \tag{2.52}$$

We can then define $N_L = \langle\psi|\hat{L}|\psi\rangle$ as the average number of atoms in the left well for a given state $|\psi\rangle$. For a single-body wavefunction of the form $\psi(\mathbf{r}) = \psi(x)\psi(y)\psi(z)$, this definition gives

$$\begin{aligned} N_L &= \int_{-\infty}^{\infty}\int_{-\infty}^{\infty}\int_{-\infty}^{0} |\psi(x)\psi(y)\psi(z)|^2\, dxdydz \\ &= \int_{-\infty}^{0} |\psi(z)|^2\, dz, \end{aligned} \tag{2.53}$$

which is reasonable: a wavefunction localized completely on the left (right) gives $N_L = 1$ (0), and one that spans $z = 0$ gives $N_L$ between 1 and 0 depending on how much of the wavefunction is on each side. because $\hat{L}$ depends only on $z$, the $x$ and $y$ parts of the expectation value integrate to 1 (assuming proper normalization), so we can effectively ignore them. Also, if this wavefunction were the single-body ground state of the double well, then it would be even about $z = 0$ and we would have $N_L = 1/2$.

For the many-body case, let's first integrate the wavefunction $\Psi(\mathbf{r}_1, \ldots, \mathbf{r}_N)$ over all of the $x$ and $y$ coordinates, since we are only interested in knowing how the particles are distributed along the $a$ axis. This produces a density $\rho_z(z_1, \ldots, z_N)$ which depends only on the $z$ coordinates:

$$\rho_z(z_1, \ldots, z_N) = \int_{-\infty}^{\infty} \cdots \int_{-\infty}^{\infty} |\Psi(\mathbf{r}_1, \ldots, \mathbf{r}_N)|^2 \, dx_1 \ldots dx_N dy_1 \ldots dy_N \tag{2.54}$$

Then, we compute $N_L$ for this state:

$$\begin{aligned} N_L &= \int_{-\infty}^{0} \int_{-\infty}^{\infty} \cdots \int_{-\infty}^{\infty} \rho_z(z_1, \ldots, z_N) \, dz_1 \ldots dz_N \\ &\quad + \int_{-\infty}^{\infty} \int_{-\infty}^{0} \int_{-\infty}^{\infty} \cdots \int_{-\infty}^{\infty} \rho_z(z_1, \ldots, z_N) \, dz_1 \ldots dz_N \\ &\quad + \cdots + \int_{-\infty}^{\infty} \cdots \int_{-\infty}^{\infty} \int_{-\infty}^{0} \rho_z(z_1, \ldots, z_N) \, dz_1 \ldots dz_N \\ &= N \int_{-\infty}^{0} \int_{-\infty}^{\infty} \cdots \int_{-\infty}^{\infty} \rho_z(z_1, \ldots, z_N) \, dz_1 \ldots dz_N \\ &= N \int_{-\infty}^{0} \rho_1(z) \, dz. \end{aligned} \tag{2.55}$$

where we have taken advantage of the bosonic symmetry of the wavefunction to go from the first to the second line, and we defined the one-body density

$$\rho_1(z) = \int_{-\infty}^{\infty} \cdots \int_{-\infty}^{\infty} \rho_z(z_1, \ldots, z_N) \, dz_2 \ldots dz_N, \tag{2.56}$$

which is a function that correctly reproduces the probability of finding an atom at a given position $z$ at the expense of integrating out any information about two- or more-body correlations. For a wavefunction in the ground state, $\rho_1(z)$ would be even about $z = 0$ and, as in the single-body case, we would have $N_L = N/2$.

In analogy to $\hat{L}$, we can also write an expression for $\hat{R}$:

$$\hat{R} = \sum_{i=1}^{N} \begin{cases} 0 & z_i < 0 \\ 1 & z_i > 0 \end{cases}. \tag{2.57}$$

The differential number distribution is related to the operator $\hat{n} = \frac{1}{2}(\hat{L} - \hat{R})$, which is given by

$$\hat{n} = \frac{1}{2} \sum_{i=1}^{N} \begin{cases} 1 & z_i < 0 \\ -1 & z_i > 0 \end{cases}. \tag{2.58}$$

The distribution is simply the probability of measuring the system to have a particular value of $n$, given the particular state the system is in. As noted above, the ground state of the

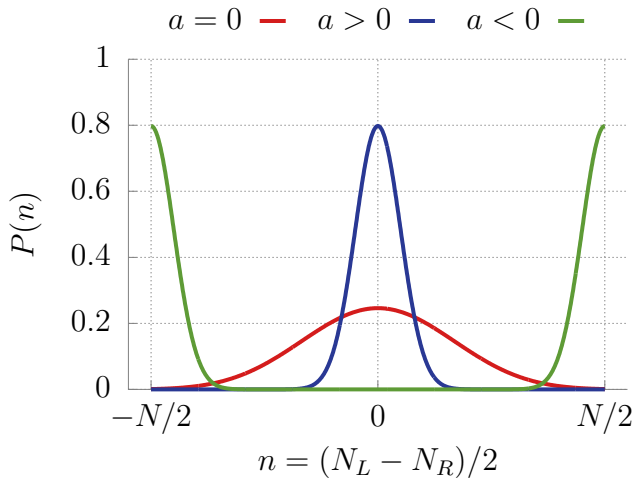


Figure 2.3: Sketch of the probability distribution function $P(n)$ related to the differential number operator $\hat{n}$ for positive (blue), negative (green), and zero (red) scattering length $a$. For $a = 0$, the PDF is the one given in Eq. (2.62). For $a > 0$, the interaction between the atoms is repulsive and the distribution is squeezed. For $a < 0$, the interaction is attractive and the distribution is approaching a Schrödinger cat state.

system has $\langle \hat{L} \rangle = \langle \hat{R} \rangle = N/2$, and hence $\langle \hat{n} \rangle = 0$ in this state. Because of the symmetry of the double well, the probability of measuring a particular value $n = (N_L - N_R)/2$ is equal to the probability of measuring $-n$. This implies that the differential number distribution is symmetric about $n = 0$, which is true independent of the strength of the interactions between the atoms. However, the *width* of the distribution does depend on the interaction strength. As we argued above, we expect that the number distribution will narrow (squeeze) for a repulsive interaction ($a > 0$) because configurations with many particles on one side of the double well and few on the other will be energetically disfavored relative to configurations that more evenly split the particles between the two sides (the opposite is true for attractive interactions). See Figure 2.3 for a sketch of the differential number distribution for different values of $a$.

Because we know that the many-body, noninteracting ground state is given by Eq. (2.35), we can compute the probability density for measuring a particular value of $n$. To do so, we have to write Eq. (2.35) in terms of eigenstates of $\hat{n}$. For a state $\phi(\mathbf{r})$ that is even about $z = 0$ (like $\phi_0(\mathbf{r})$), we can construct two normalized states that are eigenstates of $\hat{n}$:

$$\phi^l(\mathbf{r}) = \sqrt{2} \begin{cases} \phi(\mathbf{r}) & z_i < 0 \\ 0 & z_i > 0 \end{cases} \tag{2.59}$$

$$\phi^r(\mathbf{r}) = \sqrt{2} \begin{cases} 0 & z_i < 0 \\ \phi(\mathbf{r}) & z_i > 0 \end{cases}, \tag{2.60}$$

with eigenvalues $n = 1/2$ and $-1/2$, respectively. Because $\phi(\mathbf{r}) = (\phi^l(\mathbf{r}) + \phi^r(\mathbf{r}))/\sqrt{2}$, we can

write Eq. (2.35) as

$$\Psi_{gs}(\mathbf{r}_1,\ldots,\mathbf{r}_N) = \frac{1}{2^{N/2}}\sum_{i=1}^{N}(\phi_0^l(\mathbf{r}_i)+\phi_0^r(\mathbf{r}_i)) \qquad (a=0). \tag{2.61}$$

The number of terms in the sum with a given value of $n$ is given by $\binom{N}{N/2-n}$, and each term has a probability $2^{-N}$. Hence, the probability distribution function associated with $\hat{n}$ in the noninteracting ground state is

$$P(n) = \frac{1}{2^N}\frac{N!}{(\frac{N}{2}-n)!(\frac{N}{2}+n)!} \qquad -\frac{N}{2}\le n\le\frac{N}{2}, \tag{2.62}$$

which may be recognized as a binomial distribution centered at $n=0$.

### 2.3.2 The Squeezing Parameter

The width of the differential number distribution for a state $|\psi\rangle$ can be characterized by its standard deviation $\sigma_n^2 = \langle\psi|\hat{n}^2|\psi\rangle - \langle\psi|\hat{n}|\psi\rangle^2$. We would like to define a *squeezing parameter* that measures the amount of squeezing in the system relative to the noninteracting ($a=0$) case, in which the many-body ground state consists of a product of single-particle ground states. To do so, we need to know what $\sigma_n$ is when $a=0$.

We have already argued that $\langle\psi|\hat{n}|\psi\rangle = 0$ in the ground state of the double well regardless of the value of $a$; this is because the ground state is even about $z=0$, and therefore $|\hat{L}\rangle = |\hat{R}\rangle$. Before computing $\langle\psi|\hat{n}^2|\psi\rangle$, we will define some additional notation for convenience:

$$\hat{\theta}_i = \frac{1}{2}\begin{cases} 1 & z_i<0 \\ -1 & z_i>0 \end{cases}, \tag{2.63}$$

so that $\hat{n} = \sum_{i=1}^{N}\hat{\theta}_i$. Then, we have

$$\begin{aligned}\hat{n}^2 &= \sum_{i=1}^{N}\hat{\theta}_i\sum_{j=1}^{N}\hat{\theta}_j \\ &= \sum_{i=1}^{N}\hat{\theta}_i^2 + 2\sum_{i<j=1}^{N}\hat{\theta}_i\hat{\theta}_j \\ &= \frac{N}{4} + 2\sum_{i<j=1}^{N}\hat{\theta}_i\hat{\theta}_j. \end{aligned} \tag{2.64}$$

Also, we define

$$\mathcal{N}_{ij} = \int_{-\infty}^{\infty}\phi_i^*(\mathbf{r})\,\hat{\theta}\,\phi_j(\mathbf{r})\,d\mathbf{r}. \tag{2.65}$$

In the case of single-particle, noninteracting energy eigenstates of the three-dimensional double well, the wavefunction is separable into a product of the ground states of the two-dimensional harmonic oscillator and the one-dimensional double well. The 1D double well energy eigenstates are either an even or odd function of $z$, so we have

$$\begin{aligned}\int_{-\infty}^{\infty} \phi^*(z)\,\hat{\theta}\,\phi(z)\,dz &= \frac{1}{2}\left(\int_{-\infty}^{0} |\phi(z)|^2\,dz - \int_{0}^{\infty} |\phi(z)|^2\,dz\right) \\ &= \frac{1}{2}\left(\int_{-\infty}^{0} |\phi(z)|^2\,dz - \int_{-\infty}^{0} |\phi(z)|^2\,dz\right) \\ &= 0. \end{aligned} \tag{2.66}$$

Therefore, $\mathcal{N}_{ii} = 0$ for all single-particle energy eigenstates of the system.

If we denote the single-body ground state of the double well by $\phi_0(\mathbf{r})$, then we have

$$\begin{aligned}\langle\psi_g|\hat{n}^2|\psi_g\rangle &= \frac{N}{4} + 2\sum_{i<j=1}^{N} \int_{-\infty}^{\infty}\cdots\int_{-\infty}^{\infty} \phi_0^*(\mathbf{r}_1)\cdots\phi_0^*(\mathbf{r}_N)\,\hat{\theta}_i\hat{\theta}_j\,\phi_0(\mathbf{r}_1)\cdots\phi_0(\mathbf{r}_N)\,d\mathbf{r}_1\cdots d\mathbf{r}_N \\ &= \frac{N}{4} + 2\frac{N(N-1)}{2}\mathcal{N}_{00}^2 \\ &= \frac{N}{4}. \end{aligned} \tag{2.67}$$

Hence, we see that $\sigma_n = \sqrt{N}/2$ in the noninteracting ground state.

We define the squeezing parameter $S$ to be

$$S = 1 - \frac{\sigma_n^2}{N/4}. \tag{2.68}$$

With this definition, $S = 0$ in the noninteracting case, which corresponds to no squeezing. In the fully squeezed state, $\sigma_n = 0$ (the number distribution is as narrow as possible) and $S = 1$. Any value in between these two indicates an intermediate amount of squeezing.

### 2.3.3 Computing the Squeezing Parameter for Arbitrary States

In our study of the two- and eight-mode models, we will need to be able to compute the squeezing parameter, which depends on $\sigma_n$, for the predicted ground state. In general, the ground state $\Psi$ will be of the form of Eq. (2.50). The width $\sigma_n$ is a function of $\langle\psi_I|\hat{n}|\psi_J\rangle$ and $\langle\psi_I|\hat{n}^2|\psi_J\rangle$ for all of the possible $I$ and $J$:

$$\begin{aligned}\sigma_n^2 &= \langle\Psi|\hat{n}^2|\Psi\rangle - \langle\Psi|\hat{n}|\Psi\rangle^2 \\ &= \sum_{I,J\in\mathcal{S}} c_I^* c_J \langle\psi_I|\hat{n}^2|\psi_J\rangle - \left(\sum_{I,J\in\mathcal{S}} c_I^* c_J \langle\psi_I|\hat{n}|\psi_J\rangle\right)^2. \end{aligned} \tag{2.69}$$

We will spend the rest of this section computing general expressions for $\langle\psi_I|\hat{n}|\psi_J\rangle$ and $\langle\psi_I|\hat{n}^2|\psi_J\rangle$.

**Expectation value of $\hat{\mathbf{n}}$** Using the definition of the $N$-body basis state (2.48), we can begin to compute $\langle\psi_I|\hat{n}|\psi_J\rangle$:

$$\begin{aligned}\langle\psi_I|\hat{n}|\psi_J\rangle &= \mathcal{A}_I\mathcal{A}_J \sum_{\substack{K\in P(I)\\ L\in P(J)}} \sum_{n=1}^{N} \int_{-\infty}^{\infty} \psi_{k_1}^*(\mathbf{r}_1)\ldots\psi_{k_N}^*(\mathbf{r}_N)\,\hat{\theta}_n\,\psi_{l_1}(\mathbf{r}_1)\ldots\psi_{l_N}(\mathbf{r}_N)\,d\mathbf{r}_1\ldots d\mathbf{r}_N \\ &= \mathcal{A}_I\mathcal{A}_J\, N \sum_{\substack{K\in P(I)\\ L\in P(J)}} \mathcal{N}_{k_1 l_1} \prod_{n=2}^{N} \delta_{k_n l_n}. \end{aligned} \tag{2.70}$$

To go from the first to the second line, we take advantage of Bose symmetry to replace a sum of $N$ identical terms with $N$ times one of them. The structure of this expressions puts significant constraints on the allowable sets of states $I$ and $J$. Because $\delta_{ij} = 0$ for $i \neq j$, the two sets of states must differ from each other by at most one index; otherwise, $\langle\psi_I|\hat{n}|\psi_I\rangle = 0$. Let's look at the two nontrivial cases one at a time.

**All indices identical** For this case we have $\psi_I = \psi_J$ (i.e., $m(I,n) = m(J,n)$ for all $n$). Starting from Eq. (2.70), we have

$$\begin{aligned}\langle\psi_I|\hat{n}|\psi_J\rangle &= \mathcal{A}_I^2\, N \sum_{\substack{K\in P(I)\\ L\in P(I)}} \mathcal{N}_{k_1 l_1} \prod_{n=2}^{N} \delta_{k_n l_n} \\ &= \mathcal{A}_I^2\, N \sum_{k=1}^{\infty} \mathcal{N}_{kk} \frac{(N-1)!}{m(I,1)!\ldots(m(I,k)-1)!\ldots} \\ &= \sum_{k=1}^{\infty} m(I,k)\,\mathcal{N}_{kk}, \end{aligned} \tag{2.71}$$

where we went from the first line to the second by replacing the original sum by one in which we assigned each mode in turn to $\mathcal{N}_{ii}$ and used the number of ways of arranging the indices in $I$ (excluding the one reserved for $\mathcal{N}_{ii}$) as the multiplicity of each term. As noted previously, for single-particle energy eigenstates $\mathcal{N}_{ii} = 0$, so this expression agrees with the fact that $\langle\hat{n}\rangle = 0$ for such a state.

**One index different** The other nontrivial case is the one in which there is one difference between the set of states in $I$ and $J$. Suppose $I$ has an extra copy of a state (let's say state $p$) and a missing copy of a state (let's say state $q$) compared with $J$ (i.e., $m(I,p) = m(J,p) + 1$,

$m(I,q) = m(J,q) - 1$, and $m(I,n) = m(J,n)$ for all $n \neq p$ or $q$). Then,

$$\begin{aligned}\left(\frac{\mathcal{A}_J}{\mathcal{A}_I}\right)^2 &= \frac{m(J,1)!m(J,2)!\cdots}{m(I,1)!m(I,2)!\cdots} \\ &= \frac{(m(I,p)-1)!(m(I,q)+1)!}{m(I,p)!m(I,q)!} \\ &= \frac{m(I,q)+1}{m(I,p)}. \end{aligned} \tag{2.72}$$

Proceeding from Eq. (2.70) produces

$$\begin{aligned}\langle\psi_I|\hat{n}|\psi_J\rangle &= \mathcal{A}_I^2\sqrt{\frac{m(I,q)+1}{m(I,p)}}\,N\sum_{\substack{K\in P(I)\\L\in P(J)}}\mathcal{N}_{pq}\prod_{n=2}^{N}\delta_{k_n l_n} \\ &= \mathcal{A}_I^2\sqrt{\frac{m(I,q)+1}{m(I,p)}}\,N\mathcal{N}_{pq}\frac{(N-1)!}{m(I,1)!\ldots(m(I,p)-1)!\ldots} \\ &= \mathcal{A}_I^2\sqrt{\frac{m(I,q)+1}{m(I,p)}}\,m(I,p)\mathcal{N}_{pq}\frac{N!}{m(I,1)!m(I,2)!\ldots} \\ &= \sqrt{m(I,p)(m(I,q)+1)}\,\mathcal{N}_{pq}, \end{aligned} \tag{2.73}$$

where we went from the first line to the second by counting the number of terms in the sum, which is simply the number of ways of arranging the indices in $I$ excluding one copy of $p$.

**Expectation value of $\hat{\mathbf{n}}^2$** Again, using the definition of the $N$-body basis state (2.48), we can begin to compute $\langle\psi_I|\hat{n}^2|\psi_J\rangle$:

$$\begin{aligned}\langle\psi_I|\hat{n}^2|\psi_J\rangle &= \mathcal{A}_I\mathcal{A}_J\sum_{\substack{K\in P(I)\\L\in P(J)}}\int_{-\infty}^{\infty}\psi_{k_1}^*(\mathbf{r}_1)\ldots\psi_{k_N}^*(\mathbf{r}_N)\left(\frac{N}{4}+2\sum_{n<m=1}^{N}\hat{\theta}_n\hat{\theta}_m\right) \\ &\quad\times\psi_{l_1}(\mathbf{r}_1)\ldots\psi_{l_N}(\mathbf{r}_N)\,d\mathbf{r}_1\ldots d\mathbf{r}_N \\ &= \mathcal{A}_I\mathcal{A}_J\sum_{\substack{K\in P(I)\\L\in P(J)}}\left(\frac{N}{4}\prod_{n=1}^{N}\delta_{k_n l_n}+N(N-1)\mathcal{N}_{k_1 l_1}\mathcal{N}_{k_2 l_2}\prod_{n=3}^{N}\delta_{k_n l_n}\right), \end{aligned} \tag{2.74}$$

where, again, we used Bose symmetry to evaluate the sum over $n$ and $m$. As with $\langle\psi_I|\hat{n}|\psi_J\rangle$, there are constraints on the possible sets of states $I$ and $J$ due to the Kronecker deltas: the first term in parentheses must have $I = J$, while the second term must have $I$ and $J$ differ by at most two indices. We evaluate each case individually.

**All indices identical** For this case we have $\psi_I = \psi_J$ (i.e., $m(I,n) = m(J,n)$ for all $n$). Starting from Eq. (2.74), we can simplify the sums again by counting terms:

$$\begin{aligned}
\langle\psi_I|\hat{n}^2|\psi_J\rangle &= \mathcal{A}_I^2 \sum_{\substack{K\in P(I)\\ L\in P(I)}} \left( \frac{N}{4} \prod_{n=1}^{N} \delta_{k_n l_n} + N(N-1)\mathcal{N}_{k_1 l_1}\mathcal{N}_{k_2 l_2} \prod_{n=3}^{N} \delta_{k_n l_n} \right) \\
&= \mathcal{A}_I^2 \left( \frac{N}{4} \frac{N!}{m(I,1)!\cdots} + N(N-1) \left( \sum_{k=1}^{\infty} \mathcal{N}_{kk}^2 \frac{(N-2)!}{m(I,1)!\cdots(m(I,k)-2)!\cdots} \right.\right. \\
&\quad + \sum_{k<l=1}^{\infty} (\mathcal{N}_{kl}\mathcal{N}_{lk} + \mathcal{N}_{lk}\mathcal{N}_{kl} + \mathcal{N}_{kk}\mathcal{N}_{ll} + \mathcal{N}_{ll}\mathcal{N}_{kk}) \\
&\quad \left.\left. \times \frac{(N-2)!}{m(I,1)!\cdots(m(I,k)-1)!\cdots(m(I,l)-1)!\cdots} \right) \right) \\
&= \frac{N}{4} + \sum_{k=1}^{\infty} m(I,k)(m(I,k)-1)\mathcal{N}_{kk}^2 + 2\sum_{k<l=1}^{\infty} m(I,k)m(I,l)(\mathcal{N}_{kl}^2 + \mathcal{N}_{kk}\mathcal{N}_{ll}).
\end{aligned} \tag{2.75}$$

In the noninteracting ground state, all atoms are in the same mode for which $\mathcal{N}_{ii} = 0$, so this reduces to $N/4$, as we concluded previously.

**One index different** As before, we assume that $I$ has an extra copy of state $p$ and a missing copy of state $q$ compared with $J$ (i.e., $m(I,p) = m(J,p) + 1$, $m(I,q) = m(J,q) - 1$, and $m(I,n) = m(J,n)$ for all $n \neq p$ or $q$), so that result (2.72) still holds. The first term in Eq. (2.74) goes to zero, and the rest becomes

$$\begin{aligned}
\langle\psi_I|\hat{n}^2|\psi_J\rangle &= \mathcal{A}_I^2 \sqrt{\frac{m(I,q)+1}{m(I,p)}}\, N(N-1) \left( (\mathcal{N}_{pq}\mathcal{N}_{pp} + \mathcal{N}_{pp}\mathcal{N}_{pq}) \frac{(N-2)!}{m(I,1)!\ldots(m(I,p)-2)!\ldots} \right. \\
&\quad + (\mathcal{N}_{pq}\mathcal{N}_{qq} + \mathcal{N}_{qq}\mathcal{N}_{pq}) \frac{(N-2)!}{m(I,1)!\ldots(m(I,p)-1)!\ldots(m(I,q)-1)!\ldots} \\
&\quad + \sum_{\substack{k=1\\ k\neq p,q}}^{\infty} (\mathcal{N}_{pq}\mathcal{N}_{kk} + \mathcal{N}_{kk}\mathcal{N}_{pq} + \mathcal{N}_{pk}\mathcal{N}_{kq} + \mathcal{N}_{kq}\mathcal{N}_{pk}) \\
&\quad \left. \times \frac{(N-2)!}{m(I,1)!\ldots(m(I,k)-1)!\ldots(m(I,p)-1)!\ldots} \right).
\end{aligned} \tag{2.76}$$

We can continue to simplify:

$$\begin{aligned}\langle\psi_I|\hat{n}^2|\psi_J\rangle &= 2\sqrt{\frac{m(I,q)+1}{m(I,p)}}\Bigg(m(I,p)(m(I,p)-1)\mathcal{N}_{pq}\mathcal{N}_{pp}+m(I,p)m(I,q)\mathcal{N}_{pq}\mathcal{N}_{qq}\\ &\quad+\sum_{\substack{k=1\\k\neq p,q}}^{\infty}m(I,p)m(I,k)\,\mathcal{N}_{pk}\mathcal{N}_{kq}\Bigg)\\ &= 2\sqrt{m(I,p)(m(I,q)+1)}\Bigg(\sum_{k=1}^{\infty}m(I,k)(\mathcal{N}_{pq}\mathcal{N}_{kk}+\mathcal{N}_{pk}\mathcal{N}_{kq})\\ &\quad-\mathcal{N}_{pq}((m(I,p)+1)\mathcal{N}_{pp}+m(I,q)\mathcal{N}_{qq})\Bigg).\end{aligned} \tag{2.77}$$

**Two indices different** There are four distinct ways for two indices to be different between the sets $I$ and $J$, each of which results in a slightly different form for $\langle\psi_I|\hat{n}^2|\psi_J\rangle$. Because the computations proceed similarly to what we've seen above, we will skip the derivations and go right to the results:

1. If $I$ has 2 extra copies of $p$ and two missing copies of $q$ compared to $J$ (i.e., $m(I,p)=m(J,p)+2$, $m(I,q)=m(J,q)-2$, and $m(I,n)=m(J,n)$ for all $n\neq p$ or $q$), we find
$$\langle\psi_I|\hat{n}^2|\psi_J\rangle=\sqrt{(m(I,q)+2)(m(I,q)+1)m(I,p)(m(I,p)-1)}\,\mathcal{N}_{pq}^2. \tag{2.78}$$
2. If $I$ has 2 extra copies of $p$, a missing copy of $q$, and a missing copy of $s$ compared to $J$ (i.e., $m(I,p)=m(J,p)+2$, $m(I,q)=m(J,q)-1$, $m(I,s)=m(J,s)-1$, and $m(I,n)=m(J,n)$ for all $n\neq p$, $q$, or $s$), we find
$$\langle\psi_I|\hat{n}^2|\psi_J\rangle=2\sqrt{(m(I,q)+1)(m(I,s)+1)m(I,p)(m(I,p)-1)}\,\mathcal{N}_{pq}\mathcal{N}_{ps}. \tag{2.79}$$
3. If $I$ has one extra copy $p$, one extra copy of $r$, and two missing copies of $q$ compared to $J$ (i.e., $m(I,p)=m(J,p)+1$, $m(I,r)=m(J,r)+1$, $m(I,q)=m(J,q)-2$, and $m(I,n)=m(J,n)$ for all $n\neq p$, $q$, or $r$), we find
$$\langle\psi_I|\hat{n}^2|\psi_J\rangle=2\sqrt{(m(I,q)+2)(m(I,q)+1)m(I,p)m(I,r)}\,\mathcal{N}_{pq}\mathcal{N}_{rq}. \tag{2.80}$$
4. If $I$ has one extra copy $p$, one extra copy of $r$, a missing copy of $q$, and a missing copy of $s$ compared to $J$ (i.e., $m(I,p)=m(J,p)+1$, $m(I,r)=m(J,r)+1$, $m(I,q)=m(J,q)-1$, $m(I,s)=m(J,s)-1$, and $m(I,n)=m(J,n)$ for all $n\neq p$, $q$, $r$, or $s$), we find
$$\langle\psi_I|\hat{n}^2|\psi_J\rangle=2\sqrt{(m(I,q)+1)(m(I,s)+1)m(I,p)m(I,r)}\,(\mathcal{N}_{pq}\mathcal{N}_{rs}+\mathcal{N}_{ps}\mathcal{N}_{rq}). \tag{2.81}$$

To summarize, we can use all of the expressions for $\langle\psi_I|\hat{n}|\psi_J\rangle$ and $\langle\psi_I|\hat{n}^2|\psi_J\rangle$ derived in this section to exactly evaluate the squeezing parameter for any state of the form Eq. (2.50). We will apply this computational machinery when computing the squeezing parameter in the two- and eight-mode models in the coming chapters.

## 2.4 Fragmentation and Depletion

As we have stated previously, Bose-Einstein condensation is characterized by the ground state of a many-body system exhibiting macroscopic occupation of one single-body state. However, we have thus far avoided giving a technical definition of condensation for a system with interacting constituents. In particular, *which* single-particle state is occupied when there are interactions? We will address this question in this section, and in the process introduce *fragmentation*, which is the phenomenon in which a system exhibits macroscopic occupation of more than one single-body state. Fragmentation is particularly relevant for systems that contain symmetry, like the spatial symmetry in the double well. We will also introduce *depletion*, in which an (often small) fraction of the atoms in the system distribute themselves among all of the single-body states that are not macroscopically occupied. The distinction between these two phenomena is often a subtle one in practice.

### 2.4.1 The One-Body Density Matrix

As we have seen, Bose-Einstein condensation in a non-interacting system is defined by the macroscopic occupation of the system's single-body ground state wavefunction. In other words, the condensate fraction, which is the ratio of the number of particles occupying the ground state to the total number of particles, becomes of order 1. When interactions are introduced, the single-body energy eigenstates of the system are no longer relevant to the construction of the many-body state, so this simple definition of condensation no longer applies. For a uniform system, momentum is a good quantum number regardless of the presence of interactions, and so the condensate may always be associated with the macroscopic occupation of the zero momentum state [74].

In a finite, non-uniform, interacting system like ours, neither of these prescriptions apply. However, a general criterion for identifying condensation that does apply in such systems was proposed by Penrose and elaborated on during the 1950's based on an analysis of the *one-body reduced density matrix* (OBDM or 1-RDM) of the system [75–80]. The OBDM for a pure many-body quantum state $\Psi(\mathbf{r}_1, \ldots, \mathbf{r}_N)$, defined in terms of the field operator $\hat{\Psi}(\mathbf{r})$ and its adjoint, is given by

$$\rho(\mathbf{r}, \mathbf{r}') = \langle \Psi | \hat{\Psi}^\dagger(\mathbf{r}) \hat{\Psi}(\mathbf{r}') | \Psi \rangle \,. \tag{2.82}$$

Intuitively, the OBDM characterizes the correlations between the particle density at points $\mathbf{r}$ and $\mathbf{r}'$ by measuring the probability of destroying a particle at $\mathbf{r}'$ and recreating it at $\mathbf{r}$.

We can write the OBDM in terms an integral over position-space wavefunctions. To do so, we define a $3N$-dimensional vector $R = \{\mathbf{r}_1, \ldots, \mathbf{r}_N\}$ that encodes the coordinates of all of the atoms in the system, and we associate with it a position ket $|R\rangle$ such that

$$\langle R | S \rangle = \prod_{i=1}^{N} \delta(\mathbf{r}_i - \mathbf{s}_i). \tag{2.83}$$

Then, we can write the $\hat{\Psi}^\dagger(\mathbf{r})\hat{\Psi}(\mathbf{r}')$ operator in the position basis:

$$\langle R|\hat{\Psi}^\dagger(\mathbf{r})\hat{\Psi}(\mathbf{r}')|S\rangle = \sum_{i=1}^{N} \delta(\mathbf{r}-\mathbf{r}_i)\delta(\mathbf{r}'-\mathbf{s}_i)\prod_{\substack{j=1\\j\neq i}}^{N}\delta(\mathbf{r}_j-\mathbf{s}_j). \tag{2.84}$$

The result is a sum over the $N$ different ways of removing a particle at $\mathbf{r}'$ and replacing it at $\mathbf{r}$ while leaving the other $N-1$ particles alone.

With this definition, we find

$$\begin{aligned}
\rho(\mathbf{r},\mathbf{r}') &= \langle\Psi|\hat{\Psi}^\dagger(\mathbf{r})\hat{\Psi}(\mathbf{r}')|\Psi\rangle \\
&= \int_{-\infty}^{\infty}\cdots\int_{-\infty}^{\infty}\langle\Psi|R\rangle\,\langle R|\hat{\Psi}^\dagger(\mathbf{r})\hat{\Psi}(\mathbf{r}')|S\rangle\,\langle S|\Psi\rangle\; dRdS \\
&= \int_{-\infty}^{\infty}\cdots\int_{-\infty}^{\infty}\Psi^*(\mathbf{r}_1,\ldots,\mathbf{r}_N)\sum_{i=1}^{N}\delta(\mathbf{r}-\mathbf{r}_i)\delta(\mathbf{r}'-\mathbf{s}_i)\prod_{\substack{j=1\\j\neq i}}^{N}\delta(\mathbf{r}_j-\mathbf{s}_j)\Psi(\mathbf{s}_1,\ldots,\mathbf{s}_N)\,dR\,dS \\
&= N\int_{-\infty}^{\infty}\cdots\int_{-\infty}^{\infty}\Psi^*(\mathbf{r}_1,\ldots,\mathbf{r}_N)\delta(\mathbf{r}-\mathbf{r}_1)\delta(\mathbf{r}'-\mathbf{s}_1)\prod_{j=2}^{N}\delta(\mathbf{r}_j-\mathbf{s}_j)\Psi(\mathbf{s}_1,\ldots,\mathbf{s}_N)\,dR\,dS \\
&= N\int_{-\infty}^{\infty}\cdots\int_{-\infty}^{\infty}\Psi^*(\mathbf{r},\mathbf{r}_2\ldots,\mathbf{r}_N)\Psi(\mathbf{r}',\mathbf{r}_2\ldots,\mathbf{r}_N)\,d\mathbf{r}_2\ldots d\mathbf{r}_N
\end{aligned} \tag{2.85}$$

Notice that when $\mathbf{r}=\mathbf{r}'$, the OBDM reproduces the particle density, so that

$$\int_{-\infty}^{\infty}\rho(\mathbf{r},\mathbf{r})\,d\mathbf{r} = N. \tag{2.86}$$

Because the OBDM is Hermitian and positive definite, it is possible to diagonalize it in terms of a set of eigenfunctions $\chi_i(\mathbf{r})$ and (real, positive) eigenvalues $N_i$ that satisfy

$$\int_{-\infty}^{\infty}\rho(\mathbf{r},\mathbf{r}')\chi_i(\mathbf{r}') = N_i\chi_i(\mathbf{r}), \tag{2.87}$$

so that

$$\rho(\mathbf{r},\mathbf{r}') = \sum_{i=1}^{\infty}N_i\chi_i^*(\mathbf{r})\chi_i(\mathbf{r}'). \tag{2.88}$$

In this context, the eigenfunctions are known as *natural orbitals* and the eigenvalues as *occupation numbers*. As a matter of notation, the natural orbital with highest occupation is given an index of 0, the next highest an index of 1, and so on, and we denote the fraction of particles occupying a given natural orbital by $n_i = N_i/N$. Condensation is related to the OBDM because a natural orbital that is occupied in the thermodynamic limit (i.e., that has nonzero $n_i$ as $N$ approaches infinity) is interpreted as a condensate. This definition also

allows for analysis of condensation in finite systems ($N < \infty$); if one diagonalizes an OBDM and finds an eigenvalue of order $N$, then condensation is present in the system.

What is the meaning of the natural orbitals? Suppose that we expand the field operator in a basis of the natural orbitals (which we can do because, as eigenfunctions of a Hermitian operator, the natural orbitals form a good basis):

$$\hat{\Psi}(\mathbf{r}) = \sum_{i=1}^{\infty} \chi_i(\mathbf{r})\hat{c}_i. \tag{2.89}$$

Then the OBDM can be written as

$$\begin{aligned}\rho(\mathbf{r},\mathbf{r}') &= \langle\Psi|\hat{\Psi}^\dagger(\mathbf{r})\hat{\Psi}(\mathbf{r}')|\Psi\rangle \\ &= \sum_{i,j=1}^{\infty} \langle\Psi|\hat{c}_i^\dagger\hat{c}_j|\Psi\rangle\, \chi_i^*(\mathbf{r})\chi_j(\mathbf{r}').\end{aligned} \tag{2.90}$$

Because this must have the form of Eq. (2.88), the state $|\Psi\rangle$ must have a form such that

$$\langle\Psi|\hat{c}_i^\dagger\hat{c}_j|\Psi\rangle = N_i\delta_{ij}. \tag{2.91}$$

Now, suppose $|\Psi\rangle$ is expressed in the generic form of Eq. (2.50) but with the modes *also* chosen to be the natural orbitals. Then one possible state $|\Psi\rangle$ that satisfies (2.91) (assuming the $N_i$ are integers) is the state which is a symmetrized product of $N_i$ bosons in each of the single-body states $\chi_i(\mathbf{r})$. In that sense, one can think of the natural orbitals as the equivalent single-body states that are being occupied by the bosons in the system.

However, there are in principle many other states that satisfy condition (2.91), which consist of linear combinations with various numbers of particles in the various natural orbitals. This ambiguity arises because the OBDM contains no information about the two- or more-body correlations between the atoms in the system; all of that information is integrated out. Therefore, there is no way in general to reconstruct the exact many-body wavefunction of the system with only the OBDM as input (which would be equivalent to inverting the integration in Eq. (2.85)), although it can be done in with some assumptions in certain regimes with a system of electrons [81, 82]. Therefore, the interpretation of the natural orbitals described above is useful for gaining intuition about the behavior of the system, but cannot be taken as the true nature of the many-body state.

### Depletion

As we stated, condensation is related to the OBDM because its signature is an occupation number $N_i$ of order $N$; when we encounter such a situation, we interpret the system as having $N_i$ atoms in the condensate. The remaining small population distributed among the other natural orbitals is known as the *depletion* [83]. It is possible to compute the depletion for a homogeneous Bose gas (i.e., one not trapped in an external potential) by following the

method of Bogoliubov [83]. One starts with the Hamiltonian (2.34) and approximates the field operator by assuming that it exhibits small fluctuations about a dominant condensate wavefunction:

$$\hat{\psi}(\mathbf{r}) = \psi(\mathbf{r}) + \delta\hat{\psi}(\mathbf{r}). \tag{2.92}$$

After some work, one finds that

$$n_0 = 1 - \frac{8}{3}\sqrt{\frac{na^3}{\pi}} + \cdots, \tag{2.93}$$

where $n_0$ is the occupation of the zero momentum single-body state and $n$ is the atom density. We interpret the quantity $1 - n_0$, the occupation of all of the states besides the one with zero momentum, as the depletion. The depletion is negligible in the dilute limit, $na^3 \ll 1$.

To get a sense of this condition in physical terms, recall that the typical spacing between atoms in a BEC is $n^{-1/3} \approx 4000\, a_{\mathrm{B}}$. Writing this in terms of the $a_{ho}$ from [26], one finds that $n^{-1/3} \approx 0.25\, a_{ho}$, and therefore the dilute limit is given by $a \ll 0.25\, a_{ho}$. Our calculations go up to a scattering length of $a = 0.5\, a_{ho}$ where the diluteness condition is violated and depletion should be present.

### 2.4.2 Fragmented Condensates in the Double Well

In a typical BEC, only one natural orbital has significant occupation (i.e., only one $n_i$ is of order $N$). However, it is possible to have a situation in which more than one natural orbital has significant occupation; in that situation, we say that we have a *fragmented* condensate [53]. We note that fragmentation and depletion can be distinguished in the thermodynamic limit because the occupation of individual depleted orbitals goes to zero as $N$ goes to infinity, but the fragmented states maintain a finite occupation in that limit.

In general, fragmentation occurs in systems with symmetries that lead to degeneracies in the ground state [46]. In practice, such degeneracies alone are typically not enough to induce fragmentation because exact degeneracies are very sensitive to small perturbations. However, if the particles in the system have interactions that dominate over the energy splittings generated by perturbations, then fragmentation can be achieved [46]. We will now discuss some simple examples of these ideas in the case of the double well.

To start, let's take our atoms to be noninteracting for simplicity, and let's put them in a double well with $L = 0$ (according to Eq. (2.12), this is not actually a double well at all, but a pure quartic potential). The ground state is a product of $N$ copies of the single-body ground state $\phi_0(\mathbf{r})$ and is not degenerate. The OBDM is

$$\begin{aligned}\rho_{L=0}(\mathbf{r}, \mathbf{r}') &= N \int_{-\infty}^{\infty} \cdots \int_{-\infty}^{\infty} \phi_0^*(\mathbf{r})\phi_0(\mathbf{r}') \prod_{i=2}^{N} |\phi_0(\mathbf{r}_i)|^2 \, d\mathbf{r}_2 \ldots d\mathbf{r}_N \\ &= N\phi_0(\mathbf{r})\phi_0(\mathbf{r}'),\end{aligned} \tag{2.94}$$

which has only one nonzero $N_i$ and is thus clearly not fragmented.

Now, let's put our noninteracting atoms into a double well with $L \to \infty$, in other words, one with a very high barrier and with very large separation between the well minima. In that limit, we can think of the two wells as being isolated from each other. Therefore, there are two degenerate ground states: the ground state of the left well in isolation, and the ground state of the right well in isolation. Let's denote these by $\phi_L(\mathbf{r})$ and $\phi_R(\mathbf{r})$. Suppose further that there are $N_L$ atoms in the left well and $N_R$ atoms in the right well; because the wells are isolated, these quantities cannot change. Hence, the ground state of the whole system is a Fock state (2.48) with $N_L$ atoms in the $\phi_L(\mathbf{r})$ mode and $N_R$ atoms in the $\phi_R(\mathbf{r})$ mode. The OBDM for this state is given by

$$\begin{aligned}
\rho_{L\to\infty}(\mathbf{r},\mathbf{r}') &= N\frac{N_L!N_R!}{N!}\int_{-\infty}^{\infty}\cdots\int_{-\infty}^{\infty}\sum_{\substack{J\in P(I)\\K\in P(I)}}\phi^*_{j_1}(\mathbf{r})\ldots\phi^*_{j_N}(\mathbf{r}_N)\phi_{k_1}(\mathbf{r}')\ldots\phi_{k_N}(\mathbf{r}_N)\,d\mathbf{r}_2\ldots d\mathbf{r}_N \\
&= \frac{N_L!N_R!}{(N-1)!}\sum_{\substack{J\in P(I)\\K\in P(I)}}\phi^*_{j_1}(\mathbf{r})\phi_{k_1}(\mathbf{r}')\prod_{n=2}^{N}\delta_{j_nk_n} \\
&= \frac{N_L!N_R!}{(N-1)!}\left(\phi^*_L(\mathbf{r})\phi_L(\mathbf{r}')\frac{(N-1)!}{(N_L-1)!N_R!}+\phi^*_R(\mathbf{r})\phi_R(\mathbf{r}')\frac{(N-1)!}{N_L!(N_R-1)!}\right) \\
&= N_L\phi^*_L(\mathbf{r})\phi_L(\mathbf{r}')+N_R\phi^*_R(\mathbf{r})\phi_R(\mathbf{r}'). \qquad (2.95)
\end{aligned}$$

This state has two eigenvalues of order $N$, so this represents a fragmented state. Evidently, the more isolated the wells of the double well (and hence the more degenerate the ground state), the more fragmented the BEC becomes.

In the case of repulsively interacting atoms, we can further make an intuitive argument that fragmentation should increase with interaction strength (similar to the argument we made relating squeezing and interaction strength). The crux of the argument is that strong repulsive interactions decrease number fluctuations, which localizes a fixed number of atoms on each side of the well. Hence, the ground state will look increasingly like the isolated-well Fock state, which is fragmented, the stronger the repulsive interactions. This result is discussed in detail for the two-mode model in Reference [45], and we will return to it in Chapter 3.

Finally, we would like to illustrate the distinction between a fragmented and a non-fragmented double well OBDM graphically. First of all, let's integrate out the $x$ and $y$ parts of the OBDM, to produce $\rho_z(z,z')$:

$$\rho_z(z,z') = \int_{-\infty}^{\infty}\int_{-\infty}^{\infty}\rho(x,y,z;x,y,z')\,dx\,dy. \qquad (2.96)$$

Because of reflection symmetry about $z=0$, the $z$-OBDM satisfies $\rho_z(z,z') = \rho_z(-z,-z')$, and because of Bose symmetry it satisfies $\rho_z(z,z') = \rho_z(z',z)$. This means that if we were to plot $\rho_z(z,z')$, it would be symmetric about the lines $z=z'$ and $z=-z'$.

For a fragmented state like (2.95), most of the nonzero part of the $z$-OBDM lies along the diagonal $z=z'$ (in the example here, this is because $\phi_L(\mathbf{r})$ is only nonzero for negative

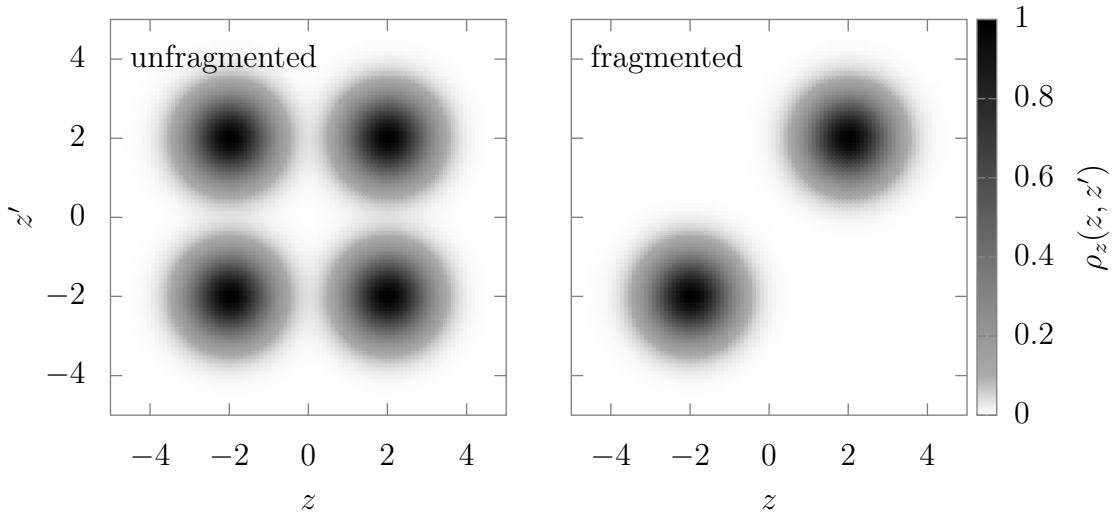


Figure 2.4: A comparison of an unfragmented (left) and fragmented (right) $z$-OBDM for a double well with well minima at $\pm 2$. Notice that both plots have symmetry about the lines $z = z'$ and $z = -z'$. The missing features in the fragmented plot compared with the unfragmented plot represent the probabilities for destroying a particle with positive (negative) $z$ and creating one with negative (positive) $z$ (i.e., tunneling). The diagonal density $\rho_z(z, z)$ is the total density of the system.

$z$, while the opposite is true for $\phi_R(\mathbf{r})$). We can interpret this as meaning that there is low probability of moving an atom from a region with $z > 0$ to one with $z < 0$, i.e., number fluctuations are suppressed. On the other hand, for a non-fragmented state like (2.94), there is nonzero $z$-OBDM along both diagonals $z = z'$ and $z = -z'$ (because $\phi_0(\mathbf{r})$ is nonzero for both positive and negative $z$). Hence, there is a high probability of moving atoms from one side of the double well to the other. Interestingly, the density $n(z) = \rho(z, z')$ can be identical in both cases, so it does not contain any information about the degree of fragmentation. See Figure 2.4 for a graphical example of these $z$-OBDMs.

### 2.4.3 The Fragmentation and Depletion Parameters

For convenience, we define fragmentation and depletion parameters, $F$ and $D$ respectively, that range from 0 to 1 depending on the degree of fragmentation and depletion, in analogy to the squeezing parameter $S$. Reference [46] demonstrates that a condensate with $G$-fold degeneracy in its ground state can fragment into $G$ parts, assuming low degeneracy ($G \approx 1$). From the energies listed in Table 2.1, we see that the single-particle ground state has near-degeneracy (i.e., $G \to 2$) when $L$ becomes large. Hence, it is reasonable to assume that, for the double well, at most two natural orbitals participate in fragmentation, and the rest, if occupied, constitute a small amount of depletion. Mathematically, this implies that

$n_0 + n_1 \approx 1$. This motivates us to define the following parameters:

$$F = 1 - |n_0 - n_1| \tag{2.97a}$$
$$D = 1 - (n_0 + n_1). \tag{2.97b}$$

With these definitions, a single condensate is represented by $F \approx D \approx 0$ and a doubly fragmented condensate is represented by $F \approx 1$ and $D \approx 0$.

We would like to note, however, the unfortunate but unavoidable arbitrariness inherent in these definitions, due to the fact that it is not clear cut how to distinguish fragmentation from depletion in practice. As we shall see in our discussion of the two- and eight-mode models in the next two chapters, the OBDM for an $m$-mode model can be written in terms of exactly $m$ natural orbitals. This means that, by construction, the two-mode model cannot have depletion as we have defined it. In the case of the eight-mode model, for large values of $a$ we find situations in which the $\chi_2(\mathbf{r})$ through $\chi_7(\mathbf{r})$ natural orbitals are populated with a few percent of the density each, and rather than vanishing in the thermodynamic limit, these populations increase with increasing $N$ (see Figure 4.9). Should this count as depletion or fragmentation? The PIGS simulations have a different built-in limitation: the OBDM is sampled on a discretized grid that has 51 entries on a side, so it can be diagonalized into 51 natural orbitals. Even in this case, there are situations in which a few percent of the system's density populates $\chi_2(\mathbf{r})$. Is this really depletion, or is it a sign of three-way fragmentation? Ultimately, we will stick with the definitions of $F$ and $D$ in Eq. (2.97) while warning the reader of the ambiguity we just described.

## 2.5 Summary

In this chapter, we introduced the basic ideas necessary to understanding the rest of this dissertation, including a description of Bose-Einstein condensation and the nature of the external potential and interactions that characterize the Hamiltonian of our system. We then discussed several methods for computing approximate ground states of the Hamiltonian, including the mean-field approximation and multimode expansions. Finally, we defined squeezing and fragmentation in terms of the width $\sigma_n$ of the differential number distribution $\hat{n}$ and the eigenvalues $n_i$ of the one-body density matrix $\rho(\mathbf{r}, \mathbf{r}')$, and defined parameters to characterize the amount of squeezing, fragmentation, and depletion exhibited by the system:

$$S = 1 - \frac{\sigma_n^2}{N/4} \tag{2.98a}$$
$$F = 1 - |n_0 - n_1| \tag{2.98b}$$
$$D = 1 - (n_0 + n_1). \tag{2.98c}$$

# Chapter 3

# Two-Mode Model and Predictions

In this chapter, we discuss the two-mode model for a Bose-Einstein condensate in a double well potential. After motivating the need for the model, we will introduce the two modes that we will use to construct the model, and we will explore the structure of the Hamiltonian that results from expanding in those modes, including implications for squeezing and fragmentation. Finally, we will derive squeezing and fragmentation predictions as a function of interaction strength for a variety of particle numbers and double well geometries. Some of these predictions conflict with naive expectations about the relationships between these quantities, and we will explore the physical explanations for these conflicts. These predictions will be revisited as comparisons to our quantum Monte Carlo results in Chapter 6.

## 3.1 Motivation for the Multimode Expansion

In Section 2.2.3, we discussed two approximations that one can make to the many-body double well Hamiltonian in order to compute the ground state: the mean-field approximation (which leads to the Gross-Pitaevskii equation) and the multimode expansion. However, the Gross-Pitaevskii formalism is inadequate for our purposes in this study because it is not capable of exhibiting squeezing or fragmentation.

In the GP ground state, all atoms are in the state that is the solution of the GP equation (2.40):

$$\Psi(\mathbf{r}_1, \ldots, \mathbf{r}_N) = \prod_{i=1}^{N} \psi_{GP}(\mathbf{r}_i). \tag{3.1}$$

Because the GP equation takes the form of a nonlinear Schrödinger equation with a symmetric external potential, the state $\psi_{GP}(\mathbf{r})$ must be an even function of $z$. By the arguments of Section 2.3.2 (see the discussion after Eq. (2.65)), this means that the squeezing parameter $S = 0$ for the GP ground state regardless of the value of $a$. Hence, we cannot use GP states if we are interested in studying the effect of interactions on squeezing. Similarly, the GP formalism fails in the analysis of fragmentation. No matter the value of $a$, the GP ground

state results in a OBDM of the form of Eq. (2.94), for which there is no fragmentation. In order to study either squeezing or fragmentation, we must go beyond GP to (at least) a two-mode model.

## 3.2 The Two-Mode Model

In this section, we will discuss the states that make up the modes of the two-mode model and the Hamiltonian that describes it.

### 3.2.1 The Modes

Recall that in multimode models we expand the field operator $\hat{\Psi}(\mathbf{r})$ in terms of a finite number of single-body modes $\phi_i(\mathbf{r})$ to generate the Hamiltonian (2.42). For the two-mode model, we choose modes that are linear combinations of the ground and first excited states ($\psi_g(\mathbf{r})$ and $\psi_e(\mathbf{r})$) of the double well potential. Because the terms in this potential depend on only one coordinate each, the 3D double well energy eigenstate have the form of products of the eigenstates of the 1D harmonic oscillator and 1D double well:

$$\psi_{g/e}(\mathbf{r}) = \chi_0(x)\chi_0(y)\phi_{0/1}(z), \tag{3.2}$$

where $\phi_0(z)$ and $\phi_1(z)$ are the (numerically generated) ground and first excited states, respectively, of the 1D double well and

$$\chi_0(x) = \left(\frac{m\omega}{\pi\hbar}\right)^{1/4} e^{-\frac{m\omega}{2\hbar}x^2} = \frac{1}{\pi^{1/4}\sqrt{a_{ho}}} e^{-\frac{x^2}{2a_{ho}^2}}, \tag{3.3}$$

is the ground state of the 1D harmonic oscillator. The states conventionally used in the two-mode model are linear combinations of the single-particle eigenstates (3.2) that are localized in the left and right wells of the potential. These are

$$\psi_{l/r}(\mathbf{r}) = \chi_0(x)\chi_0(y)\phi_{l/r}(z), \tag{3.4}$$

where

$$\phi_{l/r}(z) = \frac{1}{\sqrt{2}}(\phi_0(z) \pm \phi_1(z)). \tag{3.5}$$

See Figure 3.1 for examples of $\phi_{0/1}(z)$ and $\phi_{l/r}(z)$ for various potentials. The shape of the potential influences the qualitative features of these functions in important ways. In particular, the higher and wider the barrier (i.e., the larger $L$), the more separated the wells and therefore the more that $\phi_{l/r}(z)$ are confined to having nonzero values on only one side of the potential. From Eq. (3.5), this is equivalent to the fact that the higher and wider the barrier, the more equal $|\phi_0(z)|^2$ and $|\phi_1(z)|^2$ become. These observations will be very important when we discuss the ways in which the shape of the potential influences the system's ground state and hence squeezing and fragmentation.

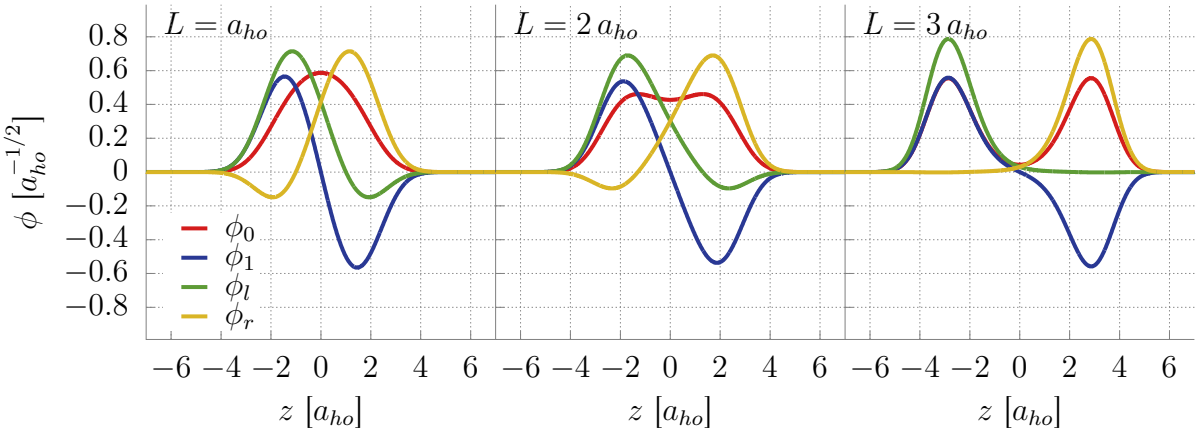


Figure 3.1: The ground and first excited states of the $z$ part of the double well potential ($\phi_0$ and $\phi_1$), and the left/right localized linear combinations of those states ($\phi_l$ and $\phi_r$) for $\alpha = 4/81\, a_{ho}^{-2}$ and $L = a_{ho}$, $2\,a_{ho}$, and $3\,a_{ho}$.

**Fock state representation** Generic states in the two-mode model can be expressed as Fock states with a definite number of atoms in each mode. Since the total number of atoms $N$ is held fixed, the different Fock states can be indexed by a single integer $n$, which we will take to be the number of atoms in the $\psi_l(\mathbf{r})$ mode. It is convenient to express these Fock states in terms of creation and annihilation operators for the modes:

$$|n\rangle = \frac{1}{\sqrt{n!(N-n)!}} (\hat{a}_l^\dagger)^n (\hat{a}_r^\dagger)^{N-n} |0\rangle\,, \tag{3.6}$$

where $|0\rangle$ is the vacuum. This expression includes implicit symmetrization of the modes via the use of a permanent:

$$(\hat{a}_l^\dagger)^n (\hat{a}_r^\dagger)^{N-n} |0\rangle = \frac{1}{\sqrt{N!}} \operatorname{perm} \begin{pmatrix} \phi_l(\mathbf{r}_1) & \phi_l(\mathbf{r}_2) & \cdots & \phi_l(\mathbf{r}_N) \\ \vdots & \vdots & \vdots & \vdots \\ \phi_l(\mathbf{r}_1) & \phi_l(\mathbf{r}_2) & \cdots & \phi_l(\mathbf{r}_N) \\ \phi_r(\mathbf{r}_1) & \phi_r(\mathbf{r}_2) & \cdots & \phi_r(\mathbf{r}_N) \\ \vdots & \vdots & \vdots & \vdots \\ \phi_r(\mathbf{r}_1) & \phi_r(\mathbf{r}_2) & \cdots & \phi_r(\mathbf{r}_N) \end{pmatrix}. \tag{3.7}$$

Notice that the first $n$ rows of the matrix are identical, as are the last $N-n$ rows. This expression for the two-mode Fock states is equivalent to the expression in terms of wavefunctions from Eq. (2.48).

Given this Fock state, a generic two-mode state can be written as

$$|\psi\rangle = \sum_{i=0}^{N} c_n |n\rangle\,, \tag{3.8}$$

where $\sum_{i=0}^{N} |c_n|^2 = 1$.

### 3.2.2 The Hamiltonian

Now that we've chosen modes (see Eq. (3.4))), we can expand $\hat{\Psi}(\mathbf{r}$ in terms of these modes:

$$\hat{\Psi}(\mathbf{r}) = \psi_l(\mathbf{r})\hat{a}_l + \psi_r(\mathbf{r})\hat{a}_r. \tag{3.9}$$

Then the Hamiltonian (2.42) becomes

$$\begin{aligned}\hat{H} = {} & \epsilon_{ll}\hat{n}_l + \epsilon_{rr}\hat{n}_r + \epsilon_{lr}(\hat{a}_l^\dagger\hat{a}_r + \hat{a}_r^\dagger\hat{a}_l) \\ & + a\kappa_{llll}\hat{a}_l^\dagger\hat{a}_l^\dagger\hat{a}_l\hat{a}_l + a\kappa_{rrrr}\hat{a}_r^\dagger\hat{a}_r^\dagger\hat{a}_r\hat{a}_r + a\kappa_{llrr}(\hat{a}_l^\dagger\hat{a}_l^\dagger\hat{a}_r\hat{a}_r + \hat{a}_r^\dagger\hat{a}_r^\dagger\hat{a}_l\hat{a}_l + 4\hat{a}_l^\dagger\hat{a}_r^\dagger\hat{a}_l\hat{a}_r) \\ & + 2a\kappa_{lllr}(\hat{a}_l^\dagger\hat{a}_l^\dagger\hat{a}_l\hat{a}_r + \hat{a}_r^\dagger\hat{a}_l^\dagger\hat{a}_l\hat{a}_l) + 2a\kappa_{lrrr}(\hat{a}_l^\dagger\hat{a}_r^\dagger\hat{a}_r\hat{a}_r + \hat{a}_r^\dagger\hat{a}_r^\dagger\hat{a}_r\hat{a}_l).\end{aligned} \tag{3.10}$$

Because $\phi_l(z) = \phi_r(-z)$, we know that two different $\epsilon_{ij}$ parameters are actually equal if one of them is given by the other with all $l$ indices turned into $r$'s, and vice versa (i.e., $\epsilon_{ll} = \epsilon_{rr}$ and $\epsilon_{lr} = \epsilon_{rl}$, the latter of which we already assumed in the above expression for $\hat{H}$). A similar situation holds for the $\kappa_{ijkl}$ parameters. Hence, we will simplify notation by defining

$$\Delta = \epsilon_{ll} = \epsilon_{rr} \tag{3.11a}$$
$$\delta = -2\epsilon_{lr} \tag{3.11b}$$
$$\kappa_0 = \kappa_{llll} = \kappa_{rrrr} \tag{3.11c}$$
$$\kappa_1 = \kappa_{lllr} = \kappa_{lrrr} \tag{3.11d}$$
$$\kappa_2 = \kappa_{llrr}. \tag{3.11e}$$

Additionally, we can use the commutation relations for the creation and annihilation operators and the fact that $\hat{n}_l + \hat{n}_r = N\hat{I}$ (where $\hat{I}$ is the identity operator) to simplify the Hamiltonian further:

$$\begin{aligned}\hat{H} = {} & \Delta(\hat{n}_l + \hat{n}_r) - \delta/2(\hat{a}_l^\dagger\hat{a}_r + \hat{a}_r^\dagger\hat{a}_l) \\ & + a\kappa_0(\hat{a}_l^\dagger(\hat{a}_l\hat{a}_l^\dagger - 1)\hat{a}_l + \hat{a}_r^\dagger(\hat{a}_r\hat{a}_r^\dagger - 1)\hat{a}_r) + a\kappa_2(\hat{a}_l^\dagger\hat{a}_l^\dagger\hat{a}_r\hat{a}_r + \hat{a}_r^\dagger\hat{a}_r^\dagger\hat{a}_l\hat{a}_l + 4\hat{n}_l\hat{n}_r) \\ & + 2a\kappa_1(\hat{a}_l^\dagger\hat{a}_r\hat{n}_l + \hat{a}_r^\dagger(\hat{a}_l\hat{a}_l^\dagger - 1)\hat{a}_l + \hat{a}_l^\dagger(\hat{a}_r\hat{a}_r^\dagger - 1)\hat{a}_r + \hat{a}_r^\dagger\hat{a}_l\hat{n}_r) \\ = {} & \Delta N\hat{I} - \delta/2(\hat{a}_l^\dagger\hat{a}_r + \hat{a}_r^\dagger\hat{a}_l) \\ & + a\kappa_0(\hat{n}_l^2 + \hat{n}_r^2 - \hat{n}_l - \hat{n}_r) + a\kappa_2(\hat{a}_l^\dagger\hat{a}_l^\dagger\hat{a}_r\hat{a}_r + \hat{a}_r^\dagger\hat{a}_r^\dagger\hat{a}_l\hat{a}_l + 4\hat{n}_l\hat{n}_r) \\ & + 2a\kappa_1(\hat{a}_l^\dagger\hat{a}_r\hat{n}_l + \hat{a}_r^\dagger\hat{a}_l\hat{n}_l + \hat{a}_l^\dagger\hat{a}_r\hat{n}_r + \hat{a}_r^\dagger\hat{a}_l\hat{n}_r - \hat{a}_r^\dagger\hat{a}_l - \hat{a}_l^\dagger\hat{a}_r) \\ = {} & \Delta N\hat{I} - \delta/2(\hat{a}_l^\dagger\hat{a}_r + \hat{a}_r^\dagger\hat{a}_l) \\ & + a\kappa_0(N^2\hat{I} - 2\hat{n}_l\hat{n}_r - N\hat{I}) + a\kappa_2(\hat{a}_l^\dagger\hat{a}_l^\dagger\hat{a}_r\hat{a}_r + \hat{a}_r^\dagger\hat{a}_r^\dagger\hat{a}_l\hat{a}_l + 4\hat{n}_l\hat{n}_r) \\ & + 2a\kappa_1(N-1)(\hat{a}_r^\dagger\hat{a}_l + \hat{a}_l^\dagger\hat{a}_r).\end{aligned} \tag{3.12}$$

Grouping terms with like operators produces the final form of the two-mode Hamiltonian:

$$\begin{aligned}\hat{H} = & N(\Delta + a(N-1)\kappa_0)\hat{I} \\ & - 2a(\kappa_0 - 2\kappa_2)\hat{n}_l\hat{n}_r \\ & - (\delta/2 - 2a(N-1)\kappa_1)(\hat{a}_l^\dagger\hat{a}_r + \hat{a}_r^\dagger\hat{a}_l) \\ & + a\kappa_2(\hat{a}_l^\dagger\hat{a}_l^\dagger\hat{a}_r\hat{a}_r + \hat{a}_r^\dagger\hat{a}_r^\dagger\hat{a}_l\hat{a}_l). \end{aligned} \tag{3.13}$$

In the Fock basis, this Hamiltonian has non-zero matrix elements only along its main five diagonals (i.e., it is "pentadiagonal"). Because it is real and Hermitian, and therefore symmetric, only three of the five diagonals have unique values. The formulas for the relevant matrix elements are

$$\langle n|\hat{n}_l\hat{n}_r|n\rangle = n(N-n) \tag{3.14a}$$

$$\langle n+1|\hat{a}_l^\dagger\hat{a}_r|n\rangle = \sqrt{(n+1)(N-n)} \tag{3.14b}$$

$$\langle n+2|\hat{a}_l^\dagger\hat{a}_l^\dagger\hat{a}_r\hat{a}_r|n\rangle = \sqrt{(n+1)(n+2)(N-n)(N-n-1)}. \tag{3.14c}$$

**Interpretation of the two-mode parameters** There are two natural bases in which we can interpret the parameters (3.11): the "ground/excited" basis and the "left/right" basis. Let's first consider the energy parameters $\Delta$ and $\delta$, which are related to $\epsilon_{ij}$, in these bases.

In the left/right basis, we can interpret $\Delta$ as the energy of the $\psi_l(\mathbf{r})$ and $\psi_r(\mathbf{r})$ modes, which are equal by symmetry, and $-\delta/2$ as the tunneling strength between these two modes. These are related to the energies of the ground and excited states, $E_g$ and $E_e$. To extract this relation, we compute

$$\begin{aligned}\epsilon_{ll/lr} &= \int \psi_l^*(\mathbf{r}) \left(-\frac{\hbar^2}{2m}\nabla^2 + V_{ext}(\mathbf{r})\right) \psi_{l/r}(\mathbf{r})\, d\mathbf{r} \\ &= \frac{1}{2}\int \left(\psi_g^*(\mathbf{r}) + \psi_e^*(\mathbf{r})\right) \left(-\frac{\hbar^2}{2m}\nabla^2 + V_{ext}(\mathbf{r})\right) \left(\psi_g(\mathbf{r}) \pm \psi_e(\mathbf{r})\right)\, d\mathbf{r} \\ &= \frac{1}{2}\int \left(\psi_g^*(\mathbf{r}) + \psi_e^*(\mathbf{r})\right) \left(E_g\psi_g(\mathbf{r}) \pm E_e\psi_e(\mathbf{r})\right)\, d\mathbf{r} \\ &= \frac{1}{2}(E_g \pm E_e). \end{aligned} \tag{3.15}$$

So $\Delta$ is the average of the energies $E_g$ and $E_e$, and $\delta$ is the energy difference $E_e - E_g$. In general, $\Delta$ is not very sensitive to the size and strength of the double well barrier (i.e., the value of $L$) because the 2D harmonic oscillator part of the potential always contributes an energy $\hbar\omega_{ho}$ and the 1D double well part will contribute a comparable value. On the other hand, $\delta$ is quite sensitive to the value of $L$. As $L$ grows, $\psi_g(\mathbf{r})$ and $\psi_e(\mathbf{r})$ become more degenerate (i.e., $E_g$ and $E_e$ become closer in value), and hence $\delta$ approaches zero. See Table 3.1 for representative numerical values.

Now, we move on to the interpretation of $\kappa_0$, $\kappa_1$, and $\kappa_2$. These parameters (multiplied by $a$) give the strength of three different kinds of two-body interaction: respectively, these

| $L$ $[a_{ho}]$ | $\Delta$ $[\hbar\omega_{ho}]$ | $\delta$ $[\hbar\omega_{ho}]$ | $\kappa$ $[\hbar\omega_{ho}/a_{ho}]$ | | |
|---|---|---|---|---|---|
| | | | $\kappa_0$ | $\kappa_1$ | $\kappa_2$ |
| 1 | 1.38 | $4.28 \times 10^{-1}$ | $5.74 \times 10^{-2}$ | $9.09 \times 10^{-4}$ | $6.79 \times 10^{-3}$ |
| 2 | 1.39 | $1.85 \times 10^{-1}$ | $5.31 \times 10^{-2}$ | $-1.22 \times 10^{-3}$ | $2.85 \times 10^{-3}$ |
| 3 | 1.64 | $3.02 \times 10^{-3}$ | $6.93 \times 10^{-2}$ | $-1.25 \times 10^{-4}$ | $1.35 \times 10^{-6}$ |

Table 3.1: Values of the energies $\Delta$ and $\delta$ and two-body interaction parameters $\kappa_0$, $\kappa_1$, and $\kappa_2$ for three trap geometries ($L = a_{ho}$, $2, a_{ho}$, and $3, a_{ho}$, with $\alpha = 4/81\, a_{ho}^{-2}$). Notice that values of $\delta$, $\kappa_1$, and $\kappa_2$ are very sensitive to the value of $L$.

are two atoms interacting in the same well, two atoms interacting such that one stays in its original well and the other tunnels through the barrier to the other well, and two atoms interacting such that both tunnel through the barrier. As with $\Delta$ and $\delta$, we can express the $\kappa$ parameters both in the left/right basis and the ground/excited basis:

$$\begin{aligned}
\kappa_0 &= \kappa_{llll} = \kappa_{rrrr} \\
&= (\kappa_{gggg} + \kappa_{eeee} + 6\kappa_{ggee})/4 && \text{(3.16a)} \\
\kappa_1 &= \kappa_{lllr} = \kappa_{lrrr} \\
&= (\kappa_{gggg} - \kappa_{eeee})/4 && \text{(3.16b)} \\
\kappa_2 &= \kappa_{llrr} \\
&= (\kappa_{gggg} + \kappa_{eeee} - 2\kappa_{ggee})/4. && \text{(3.16c)}
\end{aligned}$$

The details of these computations are left as an exercise for the reader, except that we comment that $\kappa_{ggge} = \kappa_{geee} = 0$ because $\psi_e(\mathbf{r})$ is an odd function of $z$. Because $\kappa_0$ and $\kappa_2$ are both the integral of a positive function ($|\psi_l(\mathbf{r})|^4$ and $|\psi_l(\mathbf{r})|^2|\psi_r(\mathbf{r})|^2$, respectively), they are both positive. Additionally, because $\kappa_0 - |\kappa_1| = (\min(\kappa_{gggg}, \kappa_{eeee}) + 3\kappa_{ggee})/2 > 0$ and $\kappa_0 - \kappa_2 = 2\kappa_{ggee} > 0$, we know that $\kappa_0 > |\kappa_1|$ and $\kappa_0 > \kappa_2$. We cannot say anything in general about the sign of $\kappa_1$ or the relative size of $|\kappa_1|$ and $\kappa_2$.

However, we can say something about how the presence of the double well barrier (i.e., the size of $L$) affects the relative size of these three parameters. We defining a function $f(\mathbf{r})$ as the difference between the excited and ground state densities of the 1D double well:

$$f(\mathbf{r}) = |\psi_e(\mathbf{r})|^2 - |\psi_g(\mathbf{r})|^2, \tag{3.17}$$

and then use it to reexpress $\kappa_0$, $\kappa_1$, and $\kappa_2$:

$$\begin{aligned}\kappa_0 &= \frac{1}{4}\int |\psi_g(\mathbf{r})|^4 + |\psi_e(\mathbf{r})|^4 + 6|\psi_g(\mathbf{r})|^2|\psi_e(\mathbf{r})|^2\, d\mathbf{r} \\ &= \int 2|\psi_g(\mathbf{r})|^4 + 2|\psi_g(\mathbf{r})|^2 f(\mathbf{r}) + \frac{1}{4}f^2(\mathbf{r})\, d\mathbf{r} \qquad (3.18a)\\ \kappa_1 &= \frac{1}{4}\int |\psi_g(\mathbf{r})|^4 - |\psi_e(\mathbf{r})|^4\, d\mathbf{r} \\ &= \int -\frac{1}{2}|\psi_g(\mathbf{r})|^2 f(\mathbf{r}) - \frac{1}{4}f^2(\mathbf{r})\, d\mathbf{r} \qquad (3.18b)\\ \kappa_2 &= \frac{1}{4}\int |\psi_g(\mathbf{r})|^4 + |\psi_e(\mathbf{r})|^4 - 2|\psi_g(\mathbf{r})|^2|\psi_e(\mathbf{r})|^2\, d\mathbf{r} \\ &= \int \frac{1}{4}f^2(\mathbf{r})\, d\mathbf{r}. \qquad (3.18c)\end{aligned}$$

Because the ground and first excited states of the system become degenerate for high barriers, $f(\mathbf{r})$ vanishes in the $L \to \infty$ limit. Hence, $\kappa_0 \gg |\kappa_1| \gg \kappa_2$ for large $L$. Otherwise, $\kappa_0 > |\kappa_1| \approx \kappa_2$. See Table 3.1 for representative numerical values.

**Interpretation of the two-mode operators** We can interpret the terms of the two-mode Hamiltonian (3.13) in the context of the Fock states (3.6) as follows.

**Common energy, $N(\Delta + a(N-1)\kappa_0)\hat{I}$** The coefficient of $\hat{I}$ is the energy that each Fock state $|n\rangle$ has in common, which is a sum over all $N$ atoms of the single-body energy $\Delta$ of each atom and an interaction energy $a\kappa_0$ associated with each pair of atoms. Because the ground state of a Hamiltonian is unaffected by shifting the values on the diagonal of the Hamiltonian by the same amount, we will ignore this term when analyzing squeezing and fragmentation analytically.

**State-dependent energy, $-2a(\kappa_0 - 2\kappa_2)\hat{n}_l\hat{n}_r$** The term proportional to the operator $-\hat{n}_l\hat{n}_r$ represents the state-dependent energy of each Fock state, which is due to interparticle interaction (notice that its coefficient is proportional to $a$). This operator is diagonal in the Fock basis:

$$-\hat{n}_l\hat{n}_r\,|n\rangle = -n(N-n)\,|n\rangle\,. \qquad (3.19)$$

The eigenvalue $n(N-n)$ is minimized for $n = N/2$, so the ground state of this operator is $|N/2\rangle$, the Fock state which divides the atoms equally between the two wells.

**One-body transition energy, $-(\delta/2 - 2a(N-1)\kappa_1)(\hat{a}_l^\dagger\hat{a}_r + \hat{a}_r^\dagger\hat{a}_l)$** The term proportional to the operator $-(\hat{a}_l^\dagger\hat{a}_r + \hat{a}_r^\dagger\hat{a}_l)$ represents the energy due to transitions between Fock states that involve a single atom switching from the $\psi_l(\mathbf{r})$ mode to the $\psi_r(\mathbf{r})$ mode, or vice versa. One can think of this transition as one-body tunneling across the barrier. The

strength of this term is related to $\delta$, the "traditional" tunneling strength across the barrier, but also to the scattering length $a$. In other words, the strength of the two-body interactions has an effect on the amount of one-body tunneling across the barrier exhibited by a Fock state. Depending on the sign of $\kappa_1$ and the relative sizes of $\delta$ and $a$, the overall tunneling coefficient can be positive, negative, or zero.

In the left/right Fock basis, the one-body tunneling operator is non-zero only along the diagonals above and below the main diagonal. To compute the ground state for this operator, it is simplest to convert it to the ground/excited basis:

$$\begin{aligned}
-(\hat{a}_l^\dagger \hat{a}_r + \hat{a}_r^\dagger \hat{a}_l) &= -\frac{1}{2}\left((\hat{a}_g^\dagger + \hat{a}_e^\dagger)(\hat{a}_g - \hat{a}_e) + (\hat{a}_g^\dagger - \hat{a}_e^\dagger)(\hat{a}_g + \hat{a}_e)\right) \\
&= -\frac{1}{2}(\hat{n}_g - \hat{n}_e - \hat{a}_g^\dagger \hat{a}_e + \hat{a}_e^\dagger \hat{a}_g + \hat{n}_g - \hat{n}_e + \hat{a}_g^\dagger \hat{a}_e - \hat{a}_e^\dagger \hat{a}_g) \\
&= \hat{n}_e - \hat{n}_g. \qquad (3.20)
\end{aligned}$$

In this form, it is clear that the ground state for this operator alone is the one in which all of the atoms are in the $\psi_g(\mathbf{r})$ state. We can convert this state back into the left/right Fock basis with the help of Eq. (3.6):

$$\begin{aligned}
|\psi_{gs}\rangle &= \frac{1}{\sqrt{N!}}(\hat{a}_g^\dagger)^N |0\rangle \\
&= \frac{1}{\sqrt{N!}2^{N/2}}(\hat{a}_l^\dagger + \hat{a}_r^\dagger)^N |0\rangle \\
&= \frac{1}{\sqrt{N!}2^{N/2}} \sum_{n=0}^{N} \binom{N}{n} (\hat{a}_l^\dagger)^n (\hat{a}_r^\dagger)^{N-n} |0\rangle \\
&= \frac{1}{2^{N/2}} \sum_{n=0}^{N} \sqrt{\frac{n!(N-n)!}{N!}} \binom{N}{n} |n\rangle \\
&= \frac{1}{2^{N/2}} \sum_{n=0}^{N} \sqrt{\binom{N}{n}} |n\rangle . \qquad (3.21)
\end{aligned}$$

Hence, the ground state of the one-body tunneling operator is a binomially-distributed linear combination of all of the Fock states $|n\rangle$. If the sign of the coefficient on this operator were to be switched, then the ground state would have all of the atoms in the $\psi_e(\mathbf{r})$ state, and a similar computation would yield a ground state of

$$|\psi_{gs}\rangle = \frac{1}{2^{N/2}} \sum_{n=0}^{N} (-1)^{N-n} \sqrt{\binom{N}{n}} |n\rangle . \qquad (3.22)$$

In other words, the magnitude of the coefficients would be the same, but their signs would now alternate.

**Two-body transition energy, $a\kappa_2(\hat{a}_l^\dagger\hat{a}_l^\dagger\hat{a}_r\hat{a}_r + \hat{a}_r^\dagger\hat{a}_r^\dagger\hat{a}_l\hat{a}_l)$** The term proportional to the operator $\hat{a}_l^\dagger\hat{a}_l^\dagger\hat{a}_r\hat{a}_r + \hat{a}_r^\dagger\hat{a}_r^\dagger\hat{a}_l\hat{a}_l$ represents the energy due to transitions between Fock states that involve two atoms switching from the $\psi_l(\mathbf{r})$ mode to the $\psi_r(\mathbf{r})$ mode, or vice versa. Thus, one can think of it as tunneling involving two atoms simultaneously. Because its coefficient is proportional to $a$, this tunneling mediated entirely by the two-body interparticle interaction.

In the left/right Fock basis, this operator has non-zero values on the diagonals two above and two below the main diagonal. One interesting consequence of this is that one can put the operator into block diagonal form. For example, for $N = 6$, this transformation looks like

$$\begin{pmatrix} 0 & 0 & A_1 & 0 & 0 & 0 & 0 \\ 0 & 0 & 0 & A_2 & 0 & 0 & 0 \\ B_1 & 0 & 0 & 0 & A_3 & 0 & 0 \\ 0 & B_2 & 0 & 0 & 0 & A_4 & 0 \\ 0 & 0 & B_3 & 0 & 0 & 0 & A_5 \\ 0 & 0 & 0 & B_4 & 0 & 0 & 0 \\ 0 & 0 & 0 & 0 & B_5 & 0 & 0 \end{pmatrix} \rightarrow \left(\begin{array}{cccc|ccc} 0 & A_1 & 0 & 0 & 0 & 0 & 0 \\ B_1 & 0 & A_3 & 0 & 0 & 0 & 0 \\ 0 & B_3 & 0 & A_5 & 0 & 0 & 0 \\ 0 & 0 & B_5 & 0 & 0 & 0 & 0 \\ \hline 0 & 0 & 0 & 0 & 0 & A_2 & 0 \\ 0 & 0 & 0 & 0 & B_2 & 0 & A_4 \\ 0 & 0 & 0 & 0 & 0 & B_4 & 0 \end{array}\right). \tag{3.23}$$

This implies that the ground state for this operator should contain only the even or only the odd Fock states. We can compute the ground state exactly by using the same trick of first converting it to the ground/excited basis. We start by squaring Eq. (3.20):

$$(\hat{a}_l^\dagger\hat{a}_r)^2 + (\hat{a}_r^\dagger\hat{a}_l)^2 + \hat{a}_l^\dagger\hat{a}_r\hat{a}_r^\dagger\hat{a}_l + \hat{a}_r^\dagger\hat{a}_l\hat{a}_l^\dagger\hat{a}_r = (\hat{n}_e - \hat{n}_g)^2. \tag{3.24}$$

We can rearrange this to produce

$$\begin{aligned}(\hat{a}_l^\dagger\hat{a}_r)^2 + (\hat{a}_r^\dagger\hat{a}_l)^2 &= (\hat{n}_e - \hat{n}_g)^2 - (\hat{n}_r + 1)\hat{n}_l - (\hat{n}_l + 1)\hat{n}_r \\ &= \hat{n}_g^2 + \hat{n}_e^2 - 4\hat{n}_g\hat{n}_e - N \\ &= 6\hat{n}_g^2 - 6N\hat{n}_g + N(N-1). \end{aligned} \tag{3.25}$$

This operator is diagonal in the ground/excited basis, and it's ground state is the Fock state with $n = N/2$ in that basis (this is independent of the sign of the coefficient of this operator).

As before, we can convert this back to the left/right basis:

$$\begin{aligned}
|\psi_{gs}\rangle &= \frac{1}{(N/2)!}(\hat{a}_g^\dagger \hat{a}_e^\dagger)^{N/2}\,|0\rangle \\
&= \frac{1}{(N/2)!2^{N/2}}((\hat{a}_l^\dagger)^2 + (\hat{a}_r^\dagger)^2)^{N/2}\,|0\rangle \\
&= \frac{1}{(N/2)!2^{N/2}}\sum_{p=0}^{N/2}\binom{N/2}{p}(\hat{a}_l^\dagger)^{2p}(\hat{a}_r^\dagger)^{N-2p}\,|0\rangle \\
&= \frac{1}{(N/2)!2^{N/2}}\sum_{\substack{n=0\\ n\in\text{evens}}}^{N}\binom{N/2}{n/2}(\hat{a}_l^\dagger)^{n}(\hat{a}_r^\dagger)^{N-n}\,|0\rangle \\
&= \frac{1}{2^{N/2}}\sum_{\substack{n=0\\ n\in\text{evens}}}^{N}\frac{\sqrt{n!(N-n)!}}{(n/2)!((N-n)/2)!}\,|n\rangle\,. \qquad (3.26)
\end{aligned}$$

As expected, the ground state consists of a linear combination of every other Fock state.

**Angular momentum representation** Many sources in the literature express the two-mode Hamiltonian in terms of angular-momentum-like operators in addition to the form just described. Although we will not use this representation explicitly, we include a description of it here to facilitate the interpretation of our results in the context of work that does use it.

To begin, we define

$$\hat{J}_x = \frac{1}{2}(\hat{a}_l^\dagger \hat{a}_r + \hat{a}_r^\dagger \hat{a}_l) \qquad (3.27a)$$

$$\hat{J}_y = \frac{1}{2i}(\hat{a}_l^\dagger \hat{a}_r - \hat{a}_r^\dagger \hat{a}_l) \qquad (3.27b)$$

$$\hat{J}_z = \frac{1}{2}(\hat{n}_l - \hat{n}_r), \qquad (3.27c)$$

from which one can compute

$$\hat{J}^2 = \frac{N}{2}\left(\frac{N}{2}+1\right). \qquad (3.28)$$

We can also compute the commutation relations among these operators:

$$[\hat{J}_i, \hat{J}_j] = i\epsilon_{ijk}\hat{J}_k. \qquad (3.29)$$

These are the SU(2) commutation relations, which the operators defined in (3.27) must obey if we are to interpret them as angular momentum operators.

The operators in the two-mode Hamiltonian (3.13) can be rewritten in terms of the $\hat{J}_i$ operators:

$$\begin{aligned}
\hat{n}_l\hat{n}_r &= (\hat{J}_z + \frac{N}{2})(\hat{J}_z - \frac{N}{2}) \\
&= \hat{J}_z^2 - \frac{N^2}{4} && \text{(3.30a)} \\
\hat{a}_l^\dagger\hat{a}_r + \hat{a}_l^\dagger\hat{a}_r &= 2\hat{J}_x && \text{(3.30b)} \\
\hat{a}_l^\dagger\hat{a}_l^\dagger\hat{a}_r\hat{a}_r + \hat{a}_l^\dagger\hat{a}_l^\dagger\hat{a}_r\hat{a}_r &= (\hat{J}_x + i\hat{J}_y)^2 + (\hat{J}_x - i\hat{J}_y)^2 \\
&= 2(\hat{J}_x^2 - \hat{J}_y^2) \\
&= 2\left(2\hat{J}_x^2 + \hat{J}_z^2 - \frac{N}{2}\left(\frac{N}{2}+1\right)\right). && \text{(3.30c)}
\end{aligned}$$

By substituting these into Eq. (3.13), we produce the two-mode Hamiltonian in the angular momentum representation:

$$\begin{aligned}
\hat{H} = N(\Delta + a(3N+2)(\kappa_0 - \kappa_2)/2)\hat{I} \\
- 2a(\kappa_0 - 3\kappa_2)\hat{J}_z^2 \\
- (\delta - 4a(N-1)\kappa_1)\hat{J}_x \\
+ 4a\kappa_2\hat{J}_x^2. && \text{(3.31)}
\end{aligned}$$

The Fock basis $|n\rangle$ is still a good basis in which to express this Hamiltonian. Indeed, these states are eigenstates of $\hat{J}^2$ and $\hat{J}_z$:

$$\hat{J}^2|n\rangle = \frac{N}{2}\left(\frac{N}{2}+1\right)|n\rangle \quad \text{(3.32a)}$$

$$\hat{J}_z|n\rangle = \left(n - \frac{N}{2}\right)|n\rangle, \quad \text{(3.32b)}$$

Therefore, we can think of an $N$ particle two-mode system as being equivalent to a spin-$N/2$ system, with the Fock states as the states of definite angular momentum projection in the $z$ direction.

## 3.3 Ground State Properties in the Two-Mode Model

Now that we have derived and interpreted the two-mode Hamiltonian, we can proceed with considering the ground state properties of interest to us, namely squeezing and fragmentation. In order to compute the ground state for a given potential, we numerically construct and diagonalize the Hamiltonian; the state with the smallest eigenvalue is the ground state. The Hilbert space for the system in the two-mode model has dimension $N+1$, so this diagonalization is feasible for $N$ up to several thousand.

In the Fock basis, the ground state looks like

$$|\psi_{gs}\rangle = \sum_{n=0}^{N} c_n |n\rangle , \tag{3.33}$$

where, by normalization,

$$\sum_{n=0}^{N} |c_n|^2 = 1. \tag{3.34}$$

Because the Hamiltonian has all real entries, it follows that all of the $c_n$ are real. Additionally, because of the symmetry of the double well, the $c_n$ obey $|c_n| = |c_{N-n}|$. For the rest of this section, we will assume that we have computed the ground state and therefore know the weights $c_n$.

### 3.3.1 Two-Mode Squeezing

Recall that $S = 1 - 4\sigma_n^2/N$, where $\sigma_n^2 = \langle \hat{n}^2 \rangle - \langle \hat{n} \rangle^2$. To compute a formula for the squeezing parameter as a function of the two-mode ground state, we can make use of the expressions for the expectation values of $\hat{n}$ and $\hat{n}^2$ computed in Section 2.3.3. Because $\phi_l(z) = \phi_r(-z)$, it is straightforward to show that $\mathcal{N}_{ll} = -\mathcal{N}_{rr}$ and $\mathcal{N}_{lr} = \mathcal{N}_{rl} = 0$. The latter implies that $\langle m|\hat{n}|n\rangle = \langle m|\hat{n}^2|n\rangle = 0$ for $n \neq m$, because the expressions for these expectation values (Eqs. (2.73)), (2.77, (2.78), (2.79), (2.80), and (2.81)) are all proportional to $\mathcal{N}_{lr}$.

Given these observations, Eq. (2.71) implies that

$$\begin{aligned}
\langle \psi_{gs}|\hat{n}|\psi_{gs}\rangle &= \sum_{n=0}^{N} |c_n|^2 \langle n|\hat{n}|n\rangle \\
&= \sum_{n=0}^{N} |c_n|^2 (n\mathcal{N}_{ll} + (N-n)\mathcal{N}_{rr}) \\
&= -\mathcal{N}_{ll} \sum_{n=0}^{N} |c_n|^2 (N - 2n) \\
&= -\mathcal{N}_{ll} \left( N - 2\sum_{n=0}^{N} n|c_n|^2 \right).
\end{aligned} \tag{3.35}$$

We can evaluate the sum:

$$\begin{aligned}\sum_{n=0}^{N} n|c_n|^2 &= \frac{N}{2}|c_{N/2}|^2 + \sum_{n=0}^{N/2-1}\left(n|c_n|^2 + (N-n)|c_{N-n}|^2\right)\\ &= \frac{N}{2}|c_{N/2}|^2 + N\sum_{n=0}^{N/2-1}|c_n|^2\\ &= \frac{N}{2}\left(|c_{N/2}|^2 + 2\sum_{n=0}^{N/2-1}|c_n|^2\right)\\ &= \frac{N}{2},\end{aligned} \tag{3.36}$$

where we made use of $|c_n| = |c_{N-n}|$ and $\sum_{n=0}^{N}|c_n|^2 = 1$. Hence, $\langle\psi_{gs}|\hat{n}|\psi_{gs}\rangle = 0$.

Similarly, starting with Eq. (2.75) we find

$$\begin{aligned}\langle\psi_{gs}|\hat{n}^2|\psi_{gs}\rangle &= \sum_{n=0}^{N}|c_n|^2\langle n|\hat{n}^2|n\rangle\\ &= \sum_{n=0}^{N}|c_n|^2\Big(\frac{N}{4} + n(n-1)\mathcal{N}_{ll}^2 + (N-n)(N-n-1)\mathcal{N}_{rr}^2\\ &\quad + 2n(N-n)(\mathcal{N}_{lr}^2 + \mathcal{N}_{ll}\mathcal{N}_{rr})\Big)\\ &= \frac{N}{4} + \mathcal{N}_{ll}^2\sum_{n=0}^{N}|c_n|^2((N-2n)^2 - N)\\ &= \frac{N}{4} - \mathcal{N}_{ll}^2\left(N - \sum_{n=0}^{N}|c_n|^2(N-2n)^2\right).\end{aligned} \tag{3.37}$$

Hence, the squeezing parameter in the two-mode model is

$$\begin{aligned}S^{(2)} &= 1 - \frac{\langle\hat{n}^2\rangle - \langle\hat{n}\rangle^2}{N/4}\\ &= 1 - \left(1 - 4\mathcal{N}_{ll}^2\left(1 - \frac{1}{N}\sum_{n=0}^{N}|c_n|^2(N-2n)^2\right)\right)\\ &= 4\mathcal{N}_{ll}^2\left(1 - \frac{1}{N}\sum_{n=0}^{N}|c_n|^2(N-2n)^2\right),\end{aligned} \tag{3.38}$$

Depending on the values of the coefficients $c_n$, the sum in this expression can range from 0 (for the state $|N/2\rangle$) to $N^2$ (for the state $\frac{1}{\sqrt{2}}(|0\rangle \pm |N\rangle)$). These correspond to $S^{(2)} = 4\mathcal{N}_{ll}^2$ and $-4(N-1)\mathcal{N}_{ll}^2$, respectively, which are the largest and smallest values possible for this squeezing

| $L$ $[a_{ho}]$ | $\mathcal{N}_{ll}$ | $S^{(2)}_{max}$ |
|---|---|---|
| 1 | 0.420 | 0.704 |
| 2 | 0.453 | 0.820 |
| 3 | 0.500 | 0.999 |

Table 3.2: Values of $\mathcal{N}_{ll}$ and $S^{(2)}_{max}$ for $L = a_{ho}$, $2\,a_{ho}$, and $3\,a_{ho}$. Notice that the stronger the barrier, the more capacity the system has to squeeze.

parameter. Therefore, $|N/2\rangle$ corresponds to a maximally-squeezed state in this model, which makes intuitive sense because it is a state with no number fluctuations whatsoever. Based on the intuitive argument from Section 2.3 relating squeezing and interaction strength, we expect this state to be the ground state in the $a \to \infty$ limit. To emphasize that no state can have $S^{(2)}$ greater than this, we define

$$S^{(2)}_{max} = 4\mathcal{N}^2_{ll}. \tag{3.39}$$

Similarly, $\frac{1}{\sqrt{2}}(|0\rangle \pm |N\rangle)$ corresponds to a Schrödinger cat state, which is a state with maximal number fluctuations; we expect it to be the ground state in the $a \to -\infty$ limit. Finally, we have seen previously that $c_n^2 = \frac{1}{2^N}\binom{N}{n}$ when $a = 0$. For this state, the sum in $S^{(2)}$ equals $N$, and therefore $S^{(2)} = 0$. This makes sense, since we designed the squeezing parameter such that it equals 0 in the noninteracting case.

$S^{(2)}_{max}$ is a function of the geometry of the double well trap. In particular, it is sensitive to the amount of the mode $\phi_l(\mathbf{r})$ that is contained in the left half of the potential: if $\phi_l(\mathbf{r})$ is nonzero only when $z < 0$, then $\mathcal{N}_{ll} = 1/2$ and $S^{(2)}_{max} = 1$. However, if part of this mode "leaks" into the right half of the potential (and vice versa for $\phi_r(\mathbf{r})$), then maximal squeezing is not possible because there is nonzero probability of measuring an uneven splitting of the particles between the two wells even in the pure $|N/2\rangle$ state. By looking at Figure 3.1, we see that this leakage is minimized when the barrier is stronger (i.e., for larger $L$), so larger $L$ leads to a higher possibility for squeezing. See Table 3.2 for representative values of $S^{(2)}_{max}$.

In addition to this direct influence of double well geometry on the maximum squeezing possible for a given system, we will also see in Section 3.4 that the inclusion of two-body interaction terms in the two-mode Hamiltonian influences the system such that $|N/2\rangle$ is not the ground state in the $a \to \infty$ limit. Instead, a state with nonzero number fluctuations is the true ground state in that limit, and therefore the system can never achieve a squeezing of $S^{(2)}_{max}$.

Finally, we comment on the relationship between the two-mode number operators $\hat{n}_l$ and $\hat{n}_r$ and the operators $\hat{L}$ and $\hat{R}$ that come into the definition of the differential number distribution. Recall that $\hat{n} = (\hat{L} - \hat{R})/2$, and notice that an equivalent way of writing $S^{(2)}$ is

$$S^{(2)} = S^{(2)}_{max}\left(1 - \frac{4}{N}\,\langle\psi_{gs}|(\frac{\hat{n}_l - \hat{n}_r}{2})^2|\psi_{gs}\rangle\right). \tag{3.40}$$

In the infinitely strong barrier limit (in which $S^{(2)}_{max} = 1$), comparison of this expression with the definition of $S$ (Eq. (2.68)) implies that $\hat{n}_l = \hat{L}$ and $\hat{n}_r = \hat{R}$. However, these equalities do not hold if $S^{(2)}_{max} \neq 1$. One can thus interpret $S^{(2)}_{max}$ as compensating for the fact that, in general, the operators in the two-mode Hamiltonian ($\hat{n}_l$ and $\hat{n}_r$) are not the same as the operators in the definition of squeezing ($\hat{L}$ and $\hat{R}$).

### 3.3.2 Two-Mode Fragmentation

We can study fragmentation in the two-mode model by expanding the OBDM (2.82) in terms of the modes (3.4) and diagonalizing it to find the occupation of the natural orbitals. We begin by simplifying the OBDM:

$$\begin{aligned}
\rho(\mathbf{r},\mathbf{r}') &= \sum_{n,m=1}^{N} c_m c_n \langle m|(\psi_l(\mathbf{r})\hat{a}_l^\dagger + \psi_r(\mathbf{r})\hat{a}_r^\dagger)(\psi_l(\mathbf{r}')\hat{a}_l + \psi_r(\mathbf{r}')\hat{a}_r)|n\rangle \\
&= \sum_{n,m=1}^{N} c_m c_n \big(\psi_l(\mathbf{r})\psi_l(\mathbf{r}')n\delta_{nm} + \psi_r(\mathbf{r})\psi_r(\mathbf{r}')(N-n)\delta_{nm} \\
&\quad + \psi_r(\mathbf{r})\psi_l(\mathbf{r}')\sqrt{(n+1)(N-n)}\delta_{m,n+1} + \psi_l(\mathbf{r})\psi_r(\mathbf{r}')\sqrt{n(N-n+1)}\delta_{m,n-1}\Big) \\
&= \frac{N}{2}(\psi_l(\mathbf{r})\psi_l(\mathbf{r}') + \psi_r(\mathbf{r})\psi_r(\mathbf{r}')) + A(\psi_l(\mathbf{r})\psi_r(\mathbf{r}') + \psi_r(\mathbf{r})\psi_l(\mathbf{r}')),
\end{aligned} \tag{3.41}$$

where

$$A = \sum_{n=0}^{N-1} c_n c_{n+1}\sqrt{(n+1)(N-n)}. \tag{3.42}$$

We can write this expression as a product of matrices, to make the diagonalization process explicit:

$$\begin{aligned}
\rho(\mathbf{r},\mathbf{r}') &= \begin{pmatrix}\psi_l(\mathbf{r}) & \psi_r(\mathbf{r})\end{pmatrix}\begin{pmatrix}N/2 & A \\ A & N/2\end{pmatrix}\begin{pmatrix}\psi_l(\mathbf{r}') \\ \psi_r(\mathbf{r}')\end{pmatrix} \\
&= \begin{pmatrix}\psi_g(\mathbf{r}) & \psi_e(\mathbf{r})\end{pmatrix}\begin{pmatrix}N/2+A & 0 \\ 0 & N/2-A\end{pmatrix}\begin{pmatrix}\psi_g(\mathbf{r}') \\ \psi_e(\mathbf{r}')\end{pmatrix} \\
&= n_0^{(2)}\psi_g(\mathbf{r})\psi_g(\mathbf{r}') + n_1^{(2)}\psi_e(\mathbf{r})\psi_e(\mathbf{r}'),
\end{aligned} \tag{3.43}$$

where the occupation numbers are given by

$$n_{0/1}^{(2)} = \frac{1}{2} \pm \frac{1}{N}\sum_{n=0}^{N-1}\sqrt{(N-n)(n+1)}\, c_n c_{n+1}. \tag{3.44}$$

We see that the natural orbitals are the single-particle ground and first excited states of the double well, and their occupations depend on the form of the ground state of the system.

Using this result, we can express the fragmentation and depletion parameters (2.97) as

$$F^{(2)} = 1 - \frac{2}{N}\left|\sum_{n=0}^{N-1}\sqrt{(N-n)(n+1)}\,c_n c_{n+1}\right| \tag{3.45a}$$

$$D^{(2)} = 0. \tag{3.45b}$$

Because this model only has two modes, $D$ must equal 0. For both the maximally-squeezed state $|N/2\rangle$ and the Schrödinger cat state $\frac{1}{\sqrt{2}}(|0\rangle \pm |N\rangle)$, we have $F^{(2)} = 1$ and the system is maximally fragmented. On the other hand, for the noninteracting ground state, we can show that the sum in this expression evaluates to $N/2$:

$$\begin{aligned}\sum_{n=0}^{N-1}\sqrt{(N-n)(n+1)}\,c_n c_{n+1} &= \frac{N!}{2^N}\sum_{n=0}^{N-1}\sqrt{\frac{(N-n)(n+1)}{n!(N-n)!(n+1)!(N-n-1)!}} \\ &= \frac{N}{2^N}\sum_{n=0}^{N-1}\binom{N-1}{n} \\ &= \frac{N}{2}.\end{aligned} \tag{3.46}$$

This implies that $F^{(2)} = 0$. Hence, all of the particles are in the single-particle ground state and there is no fragmentation, as one would expect for the noninteracting ground state.

## 3.4 Two-Mode Model Predictions

There have been many studies of the double well BEC system that have used the two-mode model; these include [41–49]. The vast majority of these studies analyze a version of the two-mode model in which $\kappa_1 = \kappa_2 = 0$ (we call this the nearly-degenerate two-mode model and describe it below). Only [45, 48] studied the full two-mode Hamiltonian, and [49] studied the two-mode Hamiltonian with only $\kappa_2 = 0$. Additionally, only [43, 44, 47] addressed squeezing in their work, and only [45–47] addressed fragmentation.

By explicitly constructing and diagonalizing the Hamiltonian (3.13) and inserting the resulting ground state into the expressions for $S^{(2)}$ and $F^{(2)}$ (Eqs. (3.38)) and (3.45a), we can analyze squeezing and fragmentation from within the full two-mode model. We will discuss the predictions of this model here and use them to revise our conceptual understanding of these phenomena. Before doing so, we will briefly discuss the nearly-degenerate two-mode model to put our new results into context.

### 3.4.1 The Nearly-Degenerate Two-Mode Model

In the nearly-degenerate two-mode model, we assume that the two modes (3.4) are nearly degenerate, that is, that $\phi_0^2(z) \approx \phi_1^2(z)$. Physically, this can be achieved by imposing a high

and/or wide barrier (i.e., a large value of $L$). Mathematically, this amounts to assuming that $\kappa_{gggg} = \kappa_{ggee} = \kappa_{eeee}$, so that $\kappa_1 = \kappa_2 = 0$. This assumption reduces the two-mode Hamiltonian to

$$\hat{H} = -\frac{\delta}{2}(\hat{a}_l^\dagger \hat{a}_r + \hat{a}_r^\dagger \hat{a}_l) - 2a\kappa_0 \hat{n}_l \hat{n}_r \tag{3.47}$$

$$\hat{H} = -\delta \hat{J}_x - 2a\kappa_0 \hat{J}_z^2. \tag{3.48}$$

This Hamiltonian has two natural limits. In the case where tunneling dominates ($a = 0$), the ground state is the usual noninteracting ground state, $\frac{1}{2^{N/2}} \sum_{n=0}^{N} \sqrt{\binom{N}{n}} |n\rangle$, for which $S = 0$ and $n_0 = 1$ (i.e., there is no squeezing or fragmentation). In the case where interactions dominate ($\delta = 0$), the ground state is $|N/2\rangle$, for which $S = 1$ and $n_0 = 1/2$ (i.e., there is maximal squeezing and fragmentation). This behavior matches the arguments made in Sections 2.3 and 2.4.

We can be more complete than just describing two limiting cases. The authors of [43] used the nearly degenerate two-mode model to compute an approximate analytical expression for the squeezing parameter $S$. In our notation, this is given by

$$S_{nd2} = 1 - 2^{1/3} \begin{cases} \left(\frac{1}{2^{2/3} + Na/\tilde{a}}\right)^{1/2} & a \leq \tilde{a}N \\ N\left(\frac{\tilde{a}}{a}\right)^2 & a > \tilde{a}N \end{cases}, \tag{3.49}$$

where $\tilde{a} = \delta/(2^{10/3}\pi\kappa)$ is purely a function of the geometry of the double well. As $a$ ranges between zero and infinity, Eq. (3.49) predicts that $S_{nd2}$ will vary monotonically between 0 and 1 (apart from a discontinuity at $a = \tilde{a}N$ that is an artifact of the approximations that went into the derivation of $S_{nd2}$ and that vanishes with $N$ like $N^{-3}$).

Additionally, the authors of [45] studied fragmentation. Although they used the full two-mode Hamiltonian, their results connect with the nearly degenerate two-mode model. They derived two parameters, $\mathcal{C}^{(1)}$ and $\mathcal{C}^{(2)}$, to use as measures of the degree of fragmentation exhibited by the system. They referred to these parameters as the degree of first- and second-order coherence across the barrier, respectively. In our notation, they are given by

$$\mathcal{C}^{(1)} = 1 - F^{(2)} \tag{3.50a}$$

$$\begin{aligned} \mathcal{C}^{(2)} &= \frac{N^2 - 4\sigma_n^2}{N^2 - 2N + 4\sigma_n^2} \\ &= \frac{N - 1 + S}{N - 1 - S}. \end{aligned} \tag{3.50b}$$

We see that $\mathcal{C}^{(1)}$ is a proxy for the fragmentation parameter and $\mathcal{C}^{(2)}$ is a proxy for the squeezing parameter. For a nonzero interaction strength, [45] showed that $\mathcal{C}^{(1)}$ monotonically decrease from a maximum of 1 at low barrier heights to a minimum of 0 at high barrier heights. This represents a monotonic increase in fragmentation. Similarly, they showed that $\sigma_n$ monotonically decrease from a maximum of $\sqrt{N/4}$ at low barrier heights to a minimum

of 0 at high barrier heights, which represents a monotonic increase in squeezing. All of this is consistent with our understanding that a high barrier generates degeneracy between the modes of the two-mode model.

### 3.4.2 Squeezing Analysis

We're now ready to consider our new two-mode model results. In Figure 3.2 we show the behavior of $S$ as a function of $a$ for a variety of particle numbers and in three different double well geometries for both the nearly degenerate two-mode model and the exact two-mode model. In general, the models agree well only for small values of $a$, and the deviations between them tend to grow with $N$. There are several features of the results in Figure 3.2 that we will discuss in detail: the lack of monotonicity of $S$ (especially for low barriers), the tendency of $S$ to increase as the mode degeneracy increases (i.e., for higher barriers), and the tendency of $S$ to decrease as a function of $N$ for large $a$. Ideally, one could simply use the expression for $S$ in Eq. (3.38) to explain these trends. For example, the form of $S^{(2)}_{max}$ implies that, in general, one should expect more squeezing for potentials with higher degeneracy; this is supported by the data. However, the difficulty with this approach is that there is no explicit analytical expression for the $c_n$'s for the exact two-mode Hamiltonian. Hence, we will return to describing the physics behind the features in the $S$ vs. $a$ plot after discussing the qualitative nature of the ground state.

The degree of squeezing is of course a reflection of the composition of the ground state. In Figure 3.3, we visualize this composition by plotting the squared magnitude of the coefficients $c_n = \langle n|\psi_{ground}\rangle$ as a function of $a$ for 8 and 64 particles and for $L = a_{ho}$, $2\,a_{ho}$, and $3\,a_{ho}$. The squeezing argument in Section 2.3 would suggest that these plots should smoothly transition from a binomial distribution centered at $n = N/2$ to the sole occupancy of the $n = N/2$ state as $a$ increases from 0. This is clearly not what happens for 64 particles: for $L = a_{ho}$ the ground state settles into a very wide "striped" pattern, with occupancy of every other Fock state, for $L = 2\,a_{ho}$ it settles into a different striped pattern, and for $L = 3\,a_{ho}$ it settles into a narrow but wider-than-one-state distribution. Even for 8 particles, the distribution narrows to $|4\rangle$ only for the highest barrier ($L = 3\,a_{ho}$). Based on definition (3.38) for $S^{(2)}$, the width or "spread" of these patterns gives a sense of the degree of squeezing: narrower means more squeezing and vice versa because the quantity $(N - 2n)^2$ is larger for states near $n = N/2$. Given this understanding, we see that the progression of these patterns is consistent with the squeezing plots in Figure 3.2.

In order to understand why the ground state looks the way it does, we will study it in different parameter regimes. Typically, the nearly-degenerate two-mode Hamiltonian (3.47) has been described in terms of three regimes: Rabi, Josephson, and Fock (see, e.g., [84]). These regimes are defined by the value of the dimensionless parameter $\chi = 4a\kappa_0/\delta$. We can rewrite the nearly-degenerate two-mode Hamiltonian in terms of $\chi$ by dividing (3.47) by $\delta/2$:

$$\hat{H} = -(\hat{a}_l^\dagger \hat{a}_r + \hat{a}_r^\dagger \hat{a}_l) - \chi \hat{n}_l \hat{n}_r. \tag{3.51}$$

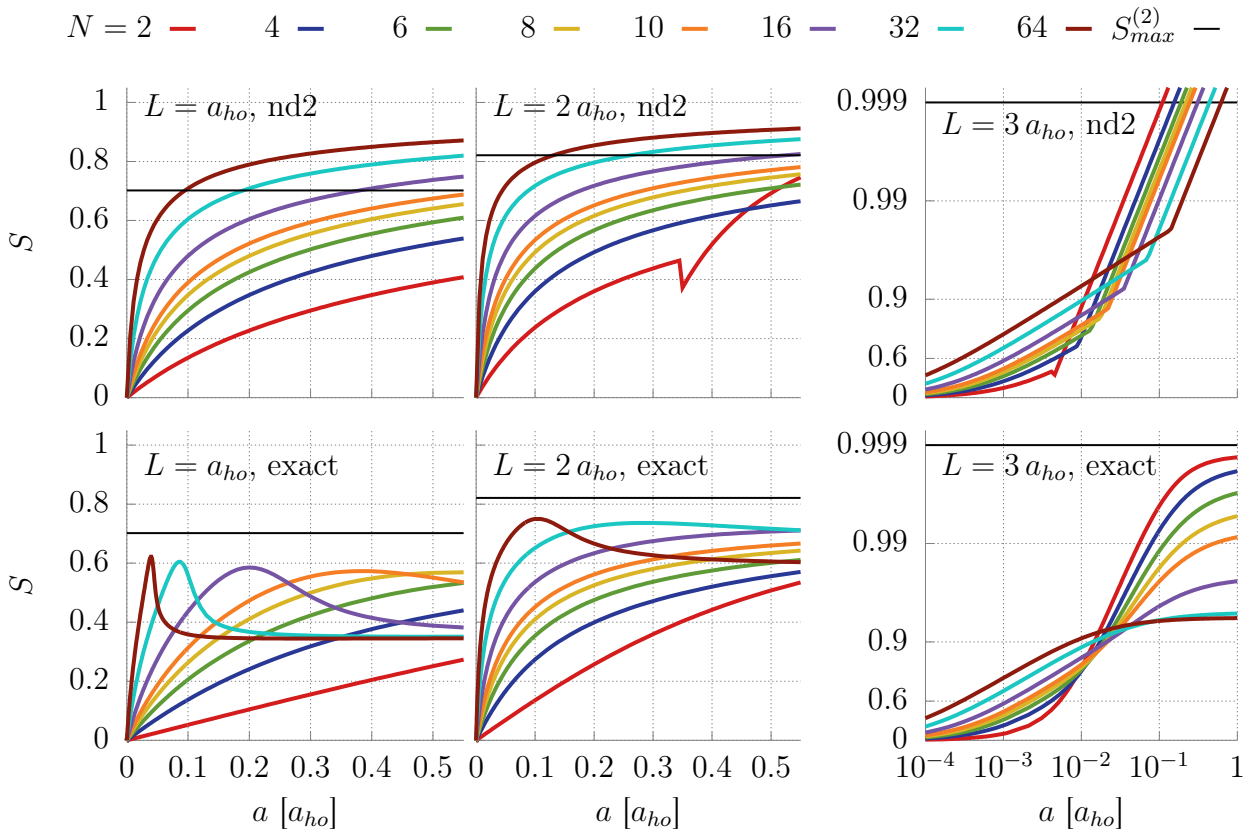


Figure 3.2: Squeezing $S$ vs. scattering length $a$ for various particle number $N$ between 2 and 64 for three different potentials ($L = a_{ho}$, $2\,a_{ho}$, and $3\,a_{ho}$ from left to right). The upper and lower plots are of $S$ as computed in the nearly degenerate two-mode model (i.e., using Eq. (3.49)) and the exact two-mode model, respectively. Notice that the rightmost ($L = 3\,a_{ho}$) plots have a logarithmic scale for $S$. All plots also indicate the value of $S^{(2)}_{max}$ from Eq. (3.39).

Then, the Rabi regime has $\chi \ll N^{-1}$, the Josephson regime has $N^{-1} \ll \chi \ll N$, and the Fock regime has $N \ll \chi$. Physically, the Rabi regime is the one in which the two-body interactions are negligible compared with the effects of single-particle tunneling, whereas in the other two regimes the two-body interactions dominate. The Josephson and Fock regimes are further distinguished in that the interactions are so strong in the Fock regime that number fluctuations are suppressed (i.e., the ground state is $|N/2\rangle$) while in the Josephson regime there are still some fluctuations due to one-particle tunneling.

To make contact between these regimes and the exact two-mode model, we rewrite the two-mode Hamiltonian as

$$\hat{H} = -(\hat{a}_l^\dagger \hat{a}_r + \hat{a}_r^\dagger \hat{a}_l) + \chi_1(a, N)\hat{H}', \tag{3.52}$$

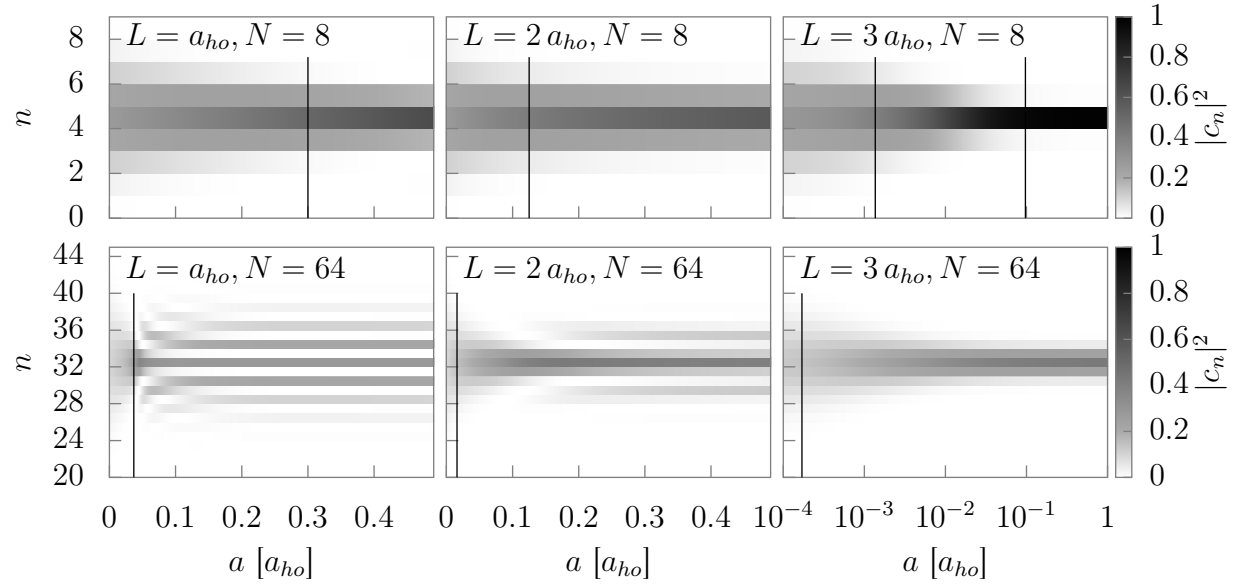


Figure 3.3: The components of the ground state ($c_n = \langle n|\psi_{ground}\rangle$) for the double well potential as a function of scattering length $a$ as computed in the exact two-mode model for $N = 8$ (top row) and 64 (bottom row) for $L = a_{ho}$, $2\,a_{ho}$, and $3\,a_{ho}$ (left to right). The vertical lines indicate the boundaries between the Rabi-, Josephson-, and Fock-like regions, from left to right in each plot (although only the $L = 3\,a_{ho}$, $N = 8$ plot has a Fock-like regime visible in the plot). In addition to the indicated regimes, the $L = a_{ho}$, $N = 8$ plot has a Fock-like regime between $a = 9.03$ and 121 (and a Josephson-like regime thereafter) and the $L = a_{ho}$, $N = 64$ plot has a Fock-like regime between $a = 1.85$ and 1.98 (and a Josephson-like regime thereafter).

where

$$\hat{H}' = -\hat{n}_l\hat{n}_r + \chi_2(\hat{a}_l^\dagger\hat{a}_l^\dagger\hat{a}_r\hat{a}_r + \hat{a}_r^\dagger\hat{a}_r^\dagger\hat{a}_l\hat{a}_l), \tag{3.53}$$

$$\chi_1(a, N) = \frac{a\chi_1^*}{a(N-1) - a^*}, \tag{3.54}$$

$$\chi_2 = \frac{\kappa_2}{2(\kappa_0 - 2\kappa_2)}, \tag{3.55}$$

and we have defined $a^* = \delta/4\kappa_1$ and $\chi_1^* = -(\kappa_0 - 2\kappa_2)/\kappa_1$ for convenience. Note that we have divided out the coefficient of the one-body tunneling terms in this transformation in order to put all of the $a$ and $N$ dependence into $\chi_1$. Note also that $\chi_1 = \chi$ and $\chi_2 = 0$ when $\kappa_1 = \kappa_2 = 0$, so this Hamiltonian reduces to the nearly-degenerate two-mode Hamiltonian (3.51), as it should. This motivates us to generalize the definitions of the three two-mode regimes: there is a Rabi-like regime for $|\chi_1| \ll N^{-1}$ a Josephson-like regime for $N^{-1} \ll |\chi_1| \ll N$, and a Fock-like regime for $N \ll |\chi_1|$. In Figure 3.4 we plot $|\chi_1|$ as a function of $a$ for both positive

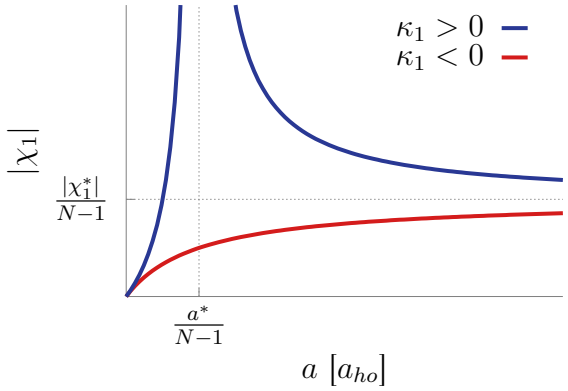


Figure 3.4: Schematic plot of $|\chi_1|$ as a function of $a$ for both positive (red) and negative (blue) $\kappa_1$. For positive $\kappa_1$, $|\chi_1|$ asymptotes to $|\chi_1^*|/(N-1)$ from below, and there may or may not be Josephson- or Fock-like regimes depending on the size of $|\chi_1^*|/(N-1)$ compared with $N$ and $N^{-1}$. For negative $\kappa_1$, $|\chi_1|$ diverges at $a^*/(N-1)$ and then asymptotes to $|\chi_1^*|/(N-1)$ from above; all three regimes are present for some range of $a$.

| $L\ [a_{ho}]$ | $a^*\ [a_{ho}]$ | $\chi_1^*$ | $\chi_2$ |
|---|---|---|---|
| 1 | 117.6 | −48.2 | $7.74 \times 10^{-2}$ |
| 2 | −37.9 | 38.8 | $3.01 \times 10^{-2}$ |
| 3 | −6.0 | 553.2 | $9.73 \times 10^{-6}$ |

Table 3.3: Values of $a^*$, $\chi_1^*$, and $\chi_2$, the parameters of the transformed two-mode Hamiltonian (3.52), for $L = a_{ho}$, $2\,a_{ho}$, and $3\,a_{ho}$.

and negative $\kappa_1$. Depending on the values of the various parameters, there may or may not be a Josephson- or Fock-like regime exhibited by the system, although there will always be a Rabi-like regime. See Table 3.3 for representative numerical values for these parameters.

How close these are to the "true" Rabi, Josephson, and Fock regimes (i.e., the regimes as defined in the nearly degenerate case) depends on the value of $\chi_2$, and hence the structure of $\hat{H}'$. In Figure 3.5, we plot the ground state of $\hat{H}'$ as a function of $\chi_2$ for $N = 8$ and 64. The ground state progresses from $|N/2\rangle$ to a striped pattern as $\chi_2$ increases. Recall from the discussion around Eq. (3.23) that $\hat{H}'$ can be rewritten in a block-diagonal form with two tridiagonal blocks, where each block involves either the even-numbered or the odd-numbered Fock states. This accounts for the striped pattern. This also invites an analogy between $\hat{H}'$ and (3.51) that allows us to identify $\chi_2 \ll N^{-1}$ as the regime in which $-\hat{n}_l\hat{n}_r$ dominates (and hence the ground state has true Rabi, Josephson, and Fock regimes) and $N \ll \chi_2$ as the regime in which two-body tunneling dominates.

We also note that there is an additional subtlety when $\chi_2 > 1$. In order for $\chi_1$ to truly be determining the relative contribution of $\hat{a}_l^\dagger\hat{a}_r + \hat{a}_r^\dagger\hat{a}_l$ and $\hat{H}'$ in Hamiltonian (3.52), the two

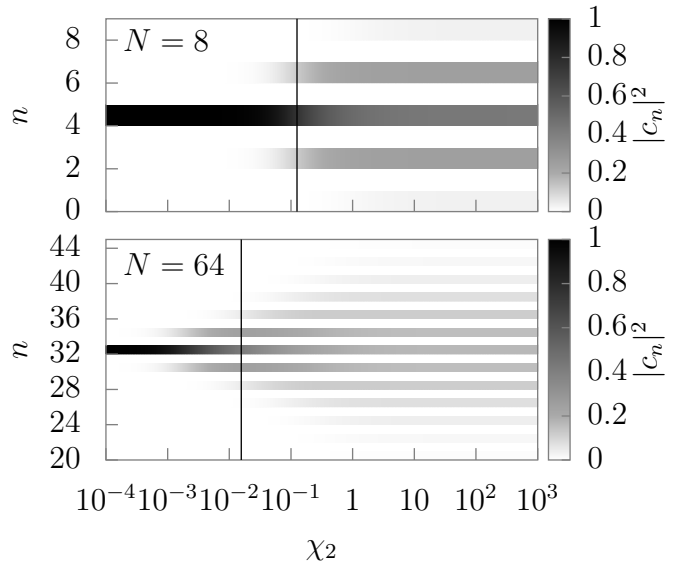


Figure 3.5: The components of the ground state of $\hat{H}'$ as a function of $\chi_2$ for $N = 8$ and 64. The vertical line indicates the location of $\chi_2 = N^{-1}$, which forms the boundary between the values of $\chi_2$ for which true Rabi, Josephson, and Fock regimes are found (to the left) and not found (to the right).

terms in $\hat{H}'$ must have both have coefficients that do not exceed 1 in magnitude. This does not hold for large $\chi_2$. In that situation, one should pull the factor of $\chi_2$ out of $\hat{H}'$, and then the Rabi-, Josephson-, and Fock-like regimes are defined instead by the size of the product $\chi_1\chi_2$.

Given this interpretation of $\chi_1$ and $\chi_2$, we can understand the patterns in Figure 3.6, in which is plotted the ground state of Eq. (3.52) as a function of $\chi_1$ for various $\chi_2$ for $N = 8$ and 64. In the Rabi-like regime (small $\chi_1$), the ground state is close to the binomial distribution of the one-body tunneling terms no matter the size of $\chi_2$. In the Fock-like regime, (large $\chi_1$), the ground state varies from $|N/2\rangle$ to a wide striped pattern as $\chi_2$ increases. The Josephson-like regime interpolates between the other two, with a narrow "neck" where the binomial and striped patters touch. Recall that $S$ varies like the width of these distributions, so the neck corresponds to a peak in $S$.

With this understanding, we can now interpret the trends in two-mode data as seen in Figs. 3.2 and 3.3. The closer we are to the degenerate two-mode system (i.e., larger $L$, smaller $\kappa_2$, and smaller $\chi_2$), the closer the ground state will be to $|N/2\rangle$ (as opposed to a striped state) for large a. This implies that there will generally be more squeezing with increased degeneracy. Likewise, $S$ is more likely to vary monotonically with $a$ the closer the system is to the degenerate limit: because the large $a$ state is narrower, the neck in the Josephson-like regime (and hence the peak in $S$) will be less pronounced or non-existent. Finally, for large $a$, $\chi_1 = \chi_1^*/(N-1)$. As $N$ increases, this quantity decreases, and therefore the Hamiltonian becomes increasingly dominated by the one-body tunneling terms, which have a wide ground

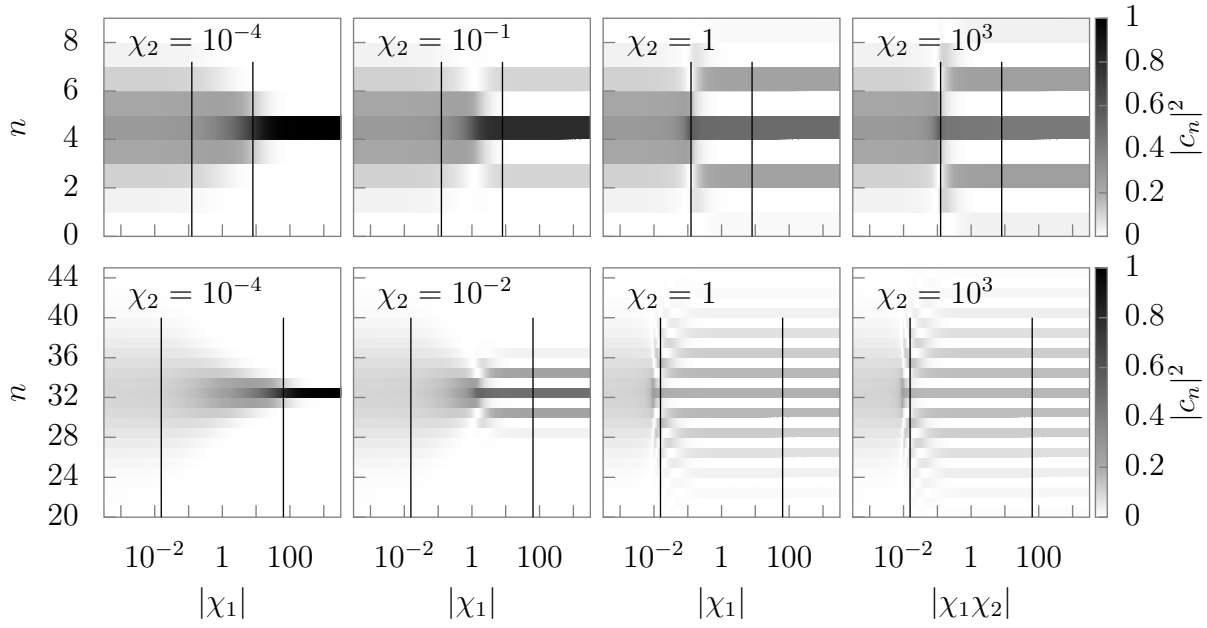


Figure 3.6: The components of the ground state of Eq. (3.52) as a function of $\chi_1$ (or $|\chi_1\chi_2|$) for $N = 8$ and 64 (top and bottom plots, respectively) and for a variety of $\chi_2$ (increasing from left to right). Increasing $\chi_2$ corresponds to a weakening of the double well barrier. The vertical lines indicate the boundaries between the Rabi-, Josephson-, and Fock-like regimes, from left to right in each plot.

state. Hence, we expect $S$ to decrease with increasing $N$ for large $a$.

### 3.4.3 Fragmentation Analysis

To investigate fragmentation in the exact two-mode model, we plot the fragmentation parameter $F$ as a function of $a$ for three geometries in Figure 3.7. Recall that the larger $F$ is, the more fragmentation there is in the system. In general, we see that fragmentation increases with $a$. The exception occurs for low $L$ and large $a$, for which $n_1$ becomes greater than $n_0$, and therefore the amount of squeezing drops from a maximum of 1. However, the most notable feature of this plot is that for low barriers ($L = a_{ho}$), systems with larger $N$ experience much more fragmentation than systems with smaller $N$, whereas the opposite is true for systems with high barriers ($L = 3\,a_{ho}$). Equivalently, we could describe this trend by noting that for small $N$ increasing the barrier height increases the amount of fragmentation, while for large $N$ increasing the barrier height decreases the amount of fragmentation.

We can understand these trends via the structure of the ground state, as illustrated in Figure 3.3. First, consider the high barrier limit ($L = 3\,a_{ho}$). Based on the arguments above, we expect the ground state to be narrower (closer to $|N/2\rangle$) for smaller $N$. From the analytic

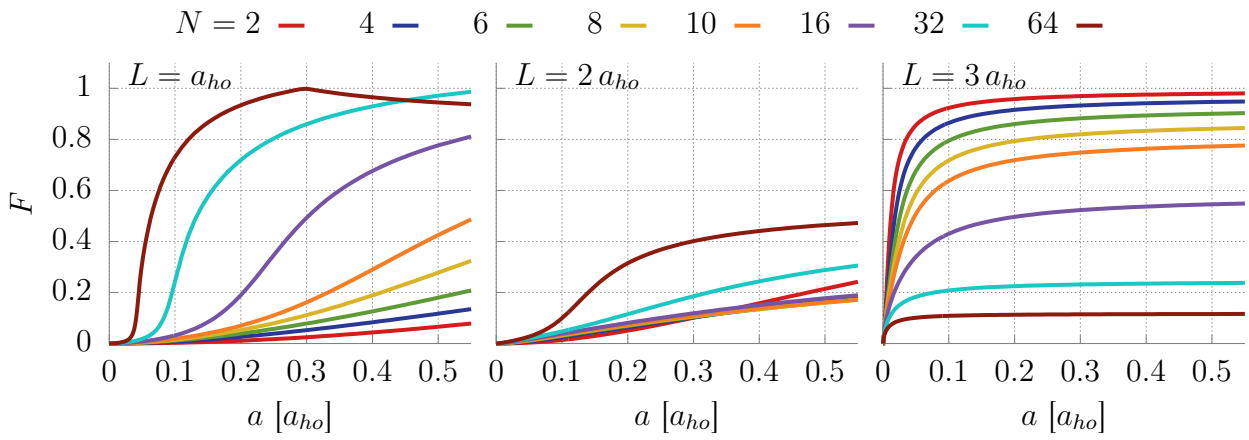


Figure 3.7: The fragmentation $F$ vs. scattering length $a$ for various particle number $N$ between 2 and 64 for three different potentials ($L = a_{ho}$, $2\,a_{ho}$, and $3\,a_{ho}$, from left to right) in the exact two-mode model. Because there are only two modes in this model, the depletion parameter $D$ equals 0.

form of $F^{(2)}$ given in Eq. (3.45a), we see that the terms in the sum depend on $c_i c_{i+1}$, i.e. the product of two adjacent $c_i$'s; the smaller the products, the more fragmentation there is. In general, then, we expect a narrower ground state to have more fragmentation, because it will have smaller $c_i c_{i+1}$ products than a wider ground state (indeed, if the ground state is $|N/2\rangle$, all of the $c_i c_{i+1}$ products are zero). Hence, fragmentation decreases with $N$ at large $a$ for $L = 3\,a_{ho}$.

For low barriers ($L = a_{ho}$), the situation is different. As $N$ increases, the ground state widens (as with $L = 3\,a_{ho}$), but it does so by developing a striped pattern. Despite the fact that the pattern is wide for large $N$, the striping will cause the $c_i c_{i+1}$ products to be small because for each pair of adjacent $c_i$'s, one of them will be close to zero. Hence, there will be more fragmentation for large $N$ than for small $N$ at large $a$ for $L = 3\,a_{ho}$.

The fragmentation pattern in the intermediate barrier regime ($L = 2\,a_{ho}$) is clearly a crossover between the low and high barrier situations.

## 3.5 Summary

In this chapter, we analyzed the interacting double well BEC system from the perspective of a two-mode model. We defined the relevant modes and constructed the Hamiltonian, which can be diagonalized for a for a given interacting strength $a$ and double well geometry to generate the ground state of the system. We then used this ground state to compute the amount of expected squeezing and fragmentation.

Previous studies, often conducted with a restricted two-mode model only relevant when the barrier is strong, predicted that squeezing should monotonically increase with $a$ and that

fragmentation should monotonically increase with barrier strength. Instead, by including all possible contributions to the two-mode Hamiltonian, we find much more rich behavior:

1. Squeezing is not necessarily monotonic with $a$, especially for weak barriers.
2. For a given $N$, squeezing tends to increase with barrier strength.
3. For a given barrier strength, squeezing tends to decrease with $N$ for large $a$.
4. For weak barriers and fixed $a$, fragmentation tends to increase with $N$, whereas for strong barriers fragmentation tends to decrease with $N$.

These trends can be explained by understanding how $a$, $N$, and the double well geometry parameters influence the relative importance of the terms in the exact two-mode Hamiltonian, and therefore change the nature of the ground state. For example:

1. A strong barrier ($\chi_2 \ll N^{-1}$) with strong interactions ($|\chi_1| \gg N$) corresponds to a ground state close to $|N/2\rangle$, for which both squeezing and fragmentation are large.
2. Weak interactions ($|\chi_1| \ll N^{-1}$) corresponds to a ground state close to the binomially-distributed non-interacting ground state, for which both squeezing and fragmentation are small. This is true regardless of the shape of the barrier.
3. A weak barrier ($\chi_2 \gg N$) with strong interactions ($|\chi_1| \gg N$) corresponds to a striped ground state, for which both squeezing is large but fragmentation is small.
4. Increasing $N$ tends to increase the relative "width" of the ground state, i.e., the number of Fock states around $|N/2\rangle$ with significant contribution to the ground state.

# Chapter 4

# Eight-Mode Model and Predictions

In the last chapter, we investigated the BEC double well system in the context of the two-mode model. In this chapter, we make use of a recently proposed eight-mode model to investigate the effects on squeezing and fragmentation of adding more modes to the multimode expansion. This understanding will help us bridge the conceptual gap between the predictions of the two-mode model and the results of the exact ("infinite-mode") quantum Monte Carlo results of Chapter 6.

## 4.1 The Eight-Mode Model

As an attempt to improve on the two-mode model, several authors [50, 85] have proposed an eight-mode model in which the field operator $\hat{\Psi}(\mathbf{r})$ is expanded in terms of linear combinations of the eight lowest energy eigenstates of the 3D double well potential. In this section, we will discuss the states and Hamiltonian of this model.

### 4.1.1 The Modes

Recall from Section 3.2 that the modes of the two-mode model are products of states of the 2D harmonic oscillator and the 1D double well. This also holds for the eight-mode model; in fact, two of the modes included in the eight-mode model are the modes from the two-mode model, Eq. (3.4). However, there are subtleties associated with the choice of which modes to include in the eight-mode model. We will explore these subtleties by first looking at the harmonic oscillator and double well states individually, and then seeing how the choice of double well geometry impacts the energies of the states when we combine them into modes.

### 2D Harmonic Oscillator States

Let's begin with the harmonic oscillator. The first three eigenstates of the 1D harmonic oscillator are

$$\chi_0(x) = \left(\frac{1}{\sqrt{\pi}a_{ho}}\right)^{1/2} e^{-\frac{x^2}{2a_{ho}^2}} \tag{4.1a}$$

$$\chi_1(x) = \left(\frac{1}{\sqrt{\pi}a_{ho}}\right)^{1/2} \sqrt{2}\frac{x}{a_{ho}} e^{-\frac{x^2}{2a_{ho}^2}} \tag{4.1b}$$

$$\chi_2(x) = \left(\frac{1}{\sqrt{\pi}a_{ho}}\right)^{1/2} \frac{1}{\sqrt{2}}\left(\frac{2x^2}{a_{ho}^2} - 1\right) e^{-\frac{x^2}{2a_{ho}^2}}, \tag{4.1c}$$

and of course, there are infinitely more of these. One can construct an eigenstate of the 2D harmonic oscillator by taking a product of two of the 1D states:

$$\chi_{i,j}(x,y) = \chi_i(x)\chi_j(y). \tag{4.2}$$

This state has energy $(i+j+1)\hbar\omega_{ho}$. Hence, the 2D harmonic oscillator ground state has $\{i,j\} = \{0,0\}$; the first excited states have $\{i,j\} = \{1,0\}$ and $\{0,1\}$; the second excited states have $\{i,j\} = \{2,0\}$, $\{1,1\}$, and $\{0,2\}$; and so on. In general, the $p$th 2D harmonic oscillator energy level has energy $E_p^{\text{2D}} = (p+1)\hbar\omega_{ho}$ and degeneracy $p+1$, for $p = 0, 1, \ldots$.

Because the 2D harmonic oscillator potential is circularly symmetric, it is possible to write its eigenstates in terms of linear combinations of the $\chi_i(x)$ states that have definite angular momentum in the $z$-direction. We can label these states with the usual azimuthal angular momentum quantum number $m$. For a given level $p$, $|m|$ can take values $\{p, p-2, p-4, \ldots, 0\}$ [86], which gives the same $p+1$ degeneracy as above. Using the notation $\chi_{p,m}(s,\theta)$ (where $s$ and $\theta$ are polar coordinates in the $xy$-plane), we have

$$\chi_{0,0}(s,\theta) = \chi_0(x)\chi_0(y) = \frac{1}{\sqrt{\pi}a_{ho}} e^{-\frac{s^2}{2a_{ho}^2}} \tag{4.3a}$$

$$\chi_{1,\pm1}(s,\theta) = \frac{1}{\sqrt{2}}\left(\chi_0(x)\chi_1(y) \pm i\,\chi_1(x)\chi_0(y)\right) = \chi_{0,0}(s,\theta)\frac{s}{a_{ho}} e^{\pm i\phi} \tag{4.3b}$$

$$\chi_{2,0}(s,\theta) = \frac{1}{\sqrt{2}}\left(\chi_0(x)\chi_2(y) + \chi_2(x)\chi_0(y)\right) = \chi_{0,0}(s,\theta)\left(\frac{s^2}{a_{ho}^2} - 1\right) \tag{4.3c}$$

$$\chi_{2,\pm2}(s,\theta) = \frac{1}{2}\left(\chi_0(x)\chi_2(y) - \chi_2(x)\chi_0(y)\right) \pm \frac{i}{\sqrt{2}}\chi_1(x)\chi_1(y) = \chi_{0,0}(s,\theta)\frac{s^2}{a_{ho}^2} e^{\pm 2i\phi}, \tag{4.3d}$$

and so on.

### 1D Double Well States

The eigenstates $\phi_i(z)$ of the 1D double well are not analytically calculable, although we can compute them numerically. We will denote a state's energy by $\epsilon_i$. Because these states are

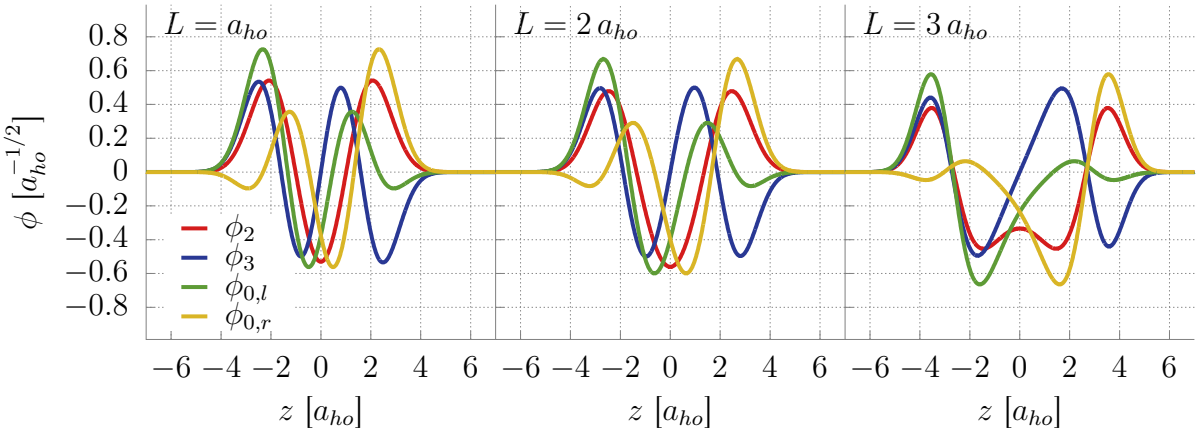


Figure 4.1: The second and third excited states of the $z$ part of the double well potential ($\phi_2$ and $\phi_3$), and the left/right localized linear combinations of those states ($\phi_{0,l}$ and $\psi_{0,r}$) for $\alpha = 4/81\, a_{ho}^{-2}$ and $L = a_{ho}$, $2\,a_{ho}$, and $3\,a_{ho}$.

even about $z$ for even $i$ and odd about $z$ for odd $i$, linear combinations of two consecutive states are (roughly) localized in the left or right side of $z = 0$. Hence, we define

$$\phi_{q,l/r}(z) = \frac{1}{\sqrt{2}}(\phi_{2q}(z) \pm \phi_{2q+1}(z)). \tag{4.4}$$

The $q$th double well energy level has degeneracy 2 and, following the notation of Section 3.2.2, energy $\Delta_q = (\epsilon_{2p} + \epsilon_{2p+1})/2$, for $q = 0, 1, \ldots$. The first pair of states $\phi_{0,l/r}(z)$ is the same as that from the two-mode model, and is plotted in Figure 3.1. For comparison (and because these will be relevant to the eight-mode model) the second pair $\phi_{1,l/r}(z)$ is plotted in Figure 4.1. Notice that there is generally more "spillover" of these left- and right-localized states into the "wrong" side of the double well for these states compared to the two-mode states. This is related to the fact that higher barriers are required to achieve the same amount of degeneracy between $\phi_{2q}(z)$ and $\phi_{2q+1}(z)$ for higher values of $q$; we can get a sense of this by comparing the relevant energies in Table 2.1. This comparison will be helpful when we discuss the differences in predicted squeezing between the two- and eight-mode states.

### Constructing Modes

In our multimode models, each mode is chosen to be a product of a state $\chi_{p,m}(s, \theta)$ and a state $\phi_{q,l/r}(z)$. The modes with a given $p$ and $q$ have an energy $E_{pq} = (p+1)\hbar\omega_{ho} + \Delta_q$ and a degeneracy $2(p+1)$. The ground state clearly has $p = q = 0$, but it is impossible to determine the order of the rest of the modes without knowing the relative size of $\hbar\omega_{ho}$ and $\Delta_q$. This is the subtlety to which we alluded to earlier: an $n$-mode approximation only makes sense if one uses the $n$ modes of lowest energy, which requires making additional assumptions about the external potential.

For the eight-mode model described in [50, 85], the additional assumption made is that the shape of the double well part of the potential is such that we can treat the $\phi_{q,l/r}(z)$ states as quasi-harmonic oscillator states for each well (i.e., $\phi_{q,l/r}(z) \approx \chi_q(z \pm L)$) with energy $\Delta_q \approx (q + 1/2)\hbar\omega_{ho}$. In essence, we are assuming that the minima of the double well are well-approximated by quadratic functions with the same curvature as the harmonic part of the potential. With this assumption, the energy of a mode is given by $E_{pq} \approx (p + q + 3/2)\hbar\omega_{ho}$.

We can now re-express the modes by taking advantage of the result in [86] that the states of a 3D harmonic oscillator potential can be expressed in terms of three quantum numbers, $n$, $l$, and $m$, that mimic the quantum numbers of the hydrogen atom. The principle quantum number $n$, which we define by $n = p + q + 1$, determines a mode's energy $E_n = (n + 1/2)\hbar\omega_{ho}$ and takes on integer values starting with 1. The orbital quantum number $l$ determines a mode's total angular momentum $|\mathbf{L}| = \sqrt{l(l+1)}\hbar$ and is restricted to take on values $\{n - 1, n - 3, \ldots, 0\}$ rather than all integer values between 0 and $n - 1$ as it would in the hydrogen atom. The magnetic quantum number $m$ determines the $z$-component of a mode's angular momentum $L_z = m\hbar$ and takes on integer values from $-l$ to $l$

With these definitions, the ground level ($n = 1$) has $l = 0$ and corresponds to the modes with $p = q = 0$:

$$\psi^{l/r}_{100}(\mathbf{r}) = \chi_{0,0}(s, \theta)\phi_{0,l/r}(z). \tag{4.5}$$

The first excited level ($n = 2$) has $l = 1$ and corresponds to the modes with $\{p, q\} = \{1, 0\}$ and $\{0, 1\}$:

$$\psi^{l/r}_{210}(\mathbf{r}) = \chi_{0,0}(s, \theta)\phi_{1,l/r}(z) \tag{4.6a}$$

$$\psi^{l/r}_{21\pm1}(\mathbf{r}) = \chi_{1,\pm1}(s, \theta)\phi_{0,l/r}(z). \tag{4.6b}$$

The second excited level ($n = 3$) has $l = 2$ and 0 and corresponds to the modes with $\{p, q\} = \{2, 0\}$, $\{1, 1\}$, and $\{0, 2\}$:

$$\psi^{l/r}_{300}(\mathbf{r}) = \chi_{0,0}(s, \theta)\phi_{2,l/r}(z) \tag{4.7a}$$

$$\psi^{l/r}_{320}(\mathbf{r}) = \chi_{2,0}(s, \theta)\phi_{0,l/r}(z) \tag{4.7b}$$

$$\psi^{l/r}_{32\pm1}(\mathbf{r}) = \chi_{1,\pm1}(s, \theta)\phi_{1,l/r}(z) \tag{4.7c}$$

$$\psi^{l/r}_{32\pm2}(\mathbf{r}) = \chi_{2,\pm2}(s, \theta)\phi_{0,l/r}(z). \tag{4.7d}$$

In general, we have

$$\psi^{l/r}_{nlm}(\mathbf{r}) = \chi_{p,m}(s, \theta)\phi_{q,l/r}(z), \tag{4.8}$$

with $n = p + q + 1$ and $l = p + q \bmod 2$. Each level $n$ has degeneracy $2\sum_{i=1}^{n} i$. The two-mode model truncates the set of included modes to the $n = 1$ level. The eight-mode model includes both levels $n = 1$ and 2:

$$\psi^{l/r}_{100}(\mathbf{r}) = \chi_{0,0}(s, \theta)\phi_{0,l/r}(z) \tag{4.9a}$$

$$\psi^{l/r}_{210}(\mathbf{r}) = \chi_{0,0}(s, \theta)\phi_{1,l/r}(z) \tag{4.9b}$$

$$\psi^{l/r}_{21\pm1}(\mathbf{r}) = \chi_{1,\pm1}(s, \theta)\phi_{0,l/r}(z). \tag{4.9c}$$

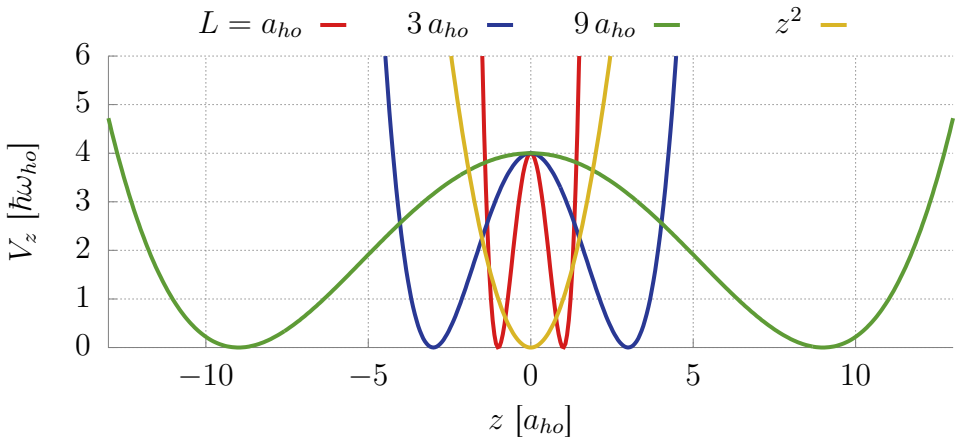


Figure 4.2: Plot of the $z$ part of the double well potential for $V_0 = 4$ and $L = a_{ho}$, $3\,a_{ho}$, and $9\,a_{ho}$, which are examples of potentials with a pancake, spherical, and cigar geometry, respectively. We also include a plot of $z^2$ to give a visual comparison between the curvature of the potential in the $z$ direction to what it would be in $x$ and $y$. Notice that at the double well minima, the spherical geometry has a similar curvature to $z^2$, while the pancake and cigar geometries have a much larger and smaller curvature, respectively, than $z^2$.

The next sensible truncation would result in a twenty-mode model, and so on.

As we stated above, the modes (4.9) define a sensible eight-mode model only to the extent that these are the modes of lowest energy, which is the case in the approximation in which the curvature of the double well minima are similar in all three Cartesian directions. We will refer to this case as the *spherical geometry*. However, there are two other cases to consider. If the curvature in $z$ is much higher than in $x$ and $y$ ("$\omega_z$" $\gg \omega_{ho}$, which we refer to as the *pancake geometry*), then the energy of the modes will be dominated by $\Delta_q$. Alternatively, if the curvature in $z$ is much lower than in $x$ and $y$ ("$\omega_z$" $\ll \omega_{ho}$, which we refer to as the *cigar geometry*), then the energy of the modes will be dominated by $(p+1)\hbar\omega_{ho}$. In either case, modes with the same $n$ will have different energies, and therefore we can no longer think of $n$ as indexing distinct energy levels.

To illustrate these ideas, we compare three geometries with the same barrier height but with different locations of the double well minima; see Figure 4.2 for a plot of the potentials. In Figure 4.3, we compare the energies of the $n = 1$, 2, and 3 levels of each of these geometries. Notice that the spherical geometry is the only one for which all of the states in each level have (almost) the same energy. For both the pancake and cigar geometries, this is not the case, as we anticipated.

This, finally, allows us to explain why we chose the three double well geometries illustrated in Figure 2.1. In order to apply the eight-mode model, we needed to choose geometries that are in the spherical potential regime. As the plots in Figure 4.4 illustrate, this is true of our geometries to good approximation. The salient difference among our chosen geometries is the widely varying barrier strength. Hence, this choice allows us to study the effect of barrier

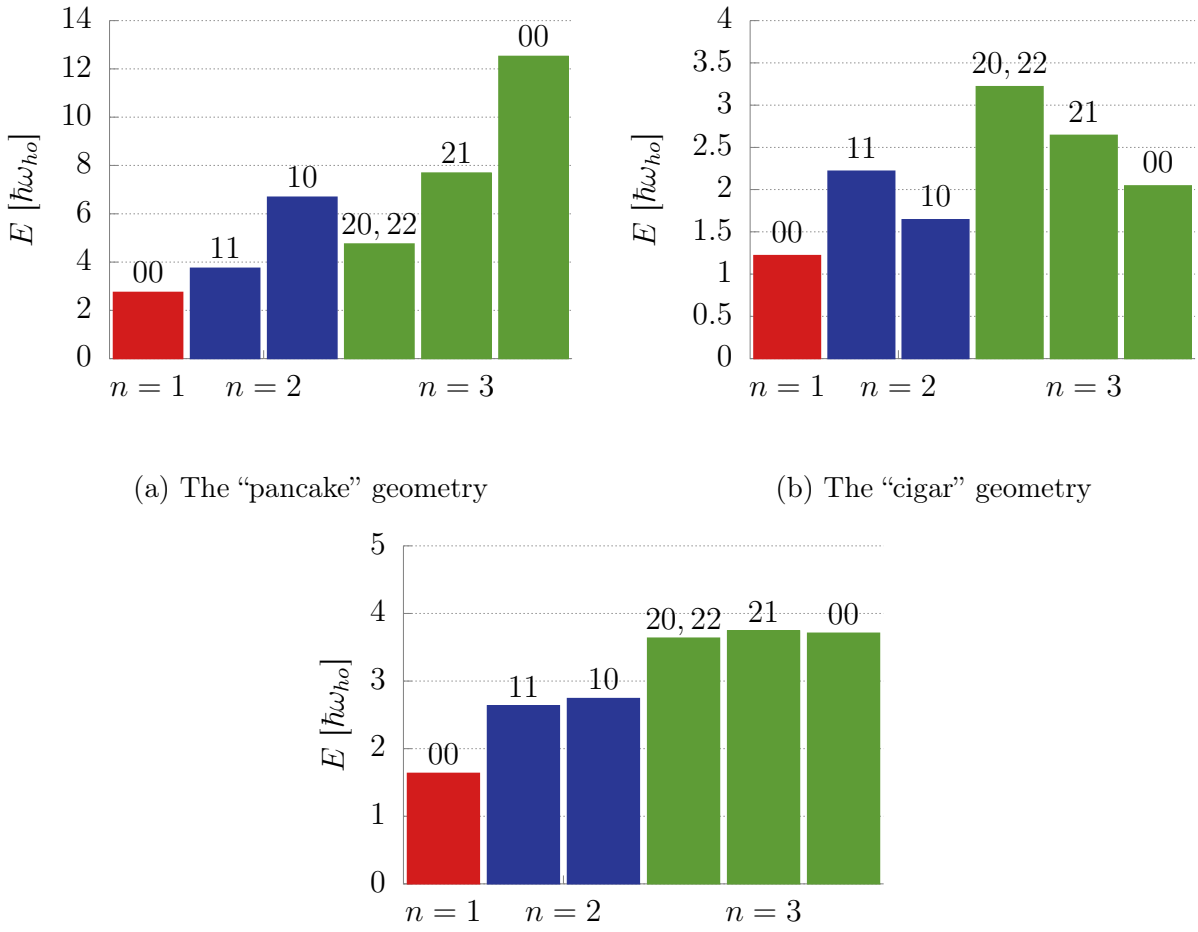


(a) The "pancake" geometry

(b) The "cigar" geometry

(c) The "spherical" geometry

Figure 4.3: Plots of the energies of the $n = 1$, $n = 2$, and $n = 3$ single-particle modes of the double well system for a "pancake" geometry ($V_0 = 4\,\hbar\omega_{ho}$, $L = a_{ho}$), a "cigar" geometry ($V_0 = 4\,\hbar\omega_{ho}$, $L = 9\,a_{ho}$), and a "spherical" geometry ($V_0 = 4\,\hbar\omega_{ho}$, $L = 3\,a_{ho}$). The integers above the bars indicate the angular momentum of the modes, in the form $l|m|$. The $n = 1$ states correspond to the states of the 2-mode model, the $n = 1$ and $n = 2$ states combined correspond to the modes of the 8-mode model, and including all three would correspond to a 20-mode model. The spherical geometry is the only one for which the energies of the modes increase with $n$, so it is the only one for which the eight-mode model is appropriate.

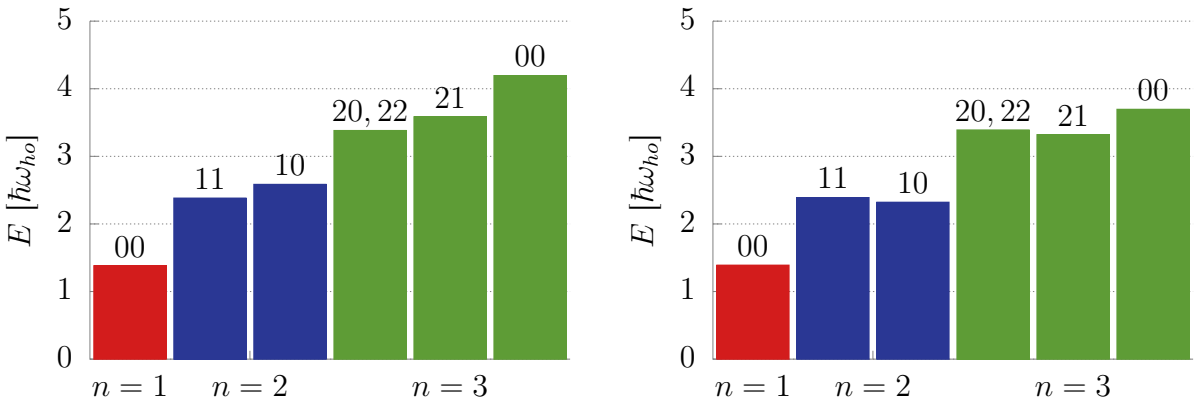


(a) $L = a_{ho}$




(b) $L = 2\,a_{ho}$

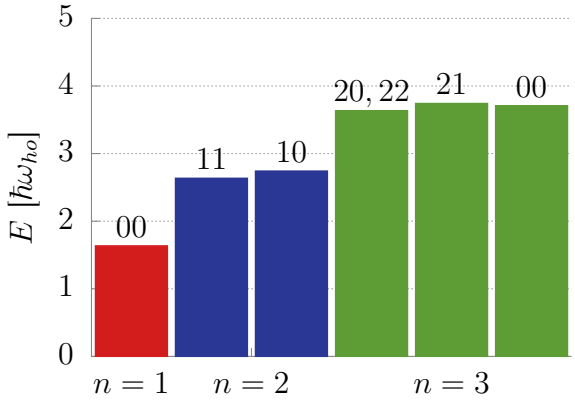


(c) $L = 3\,a_{ho}$

Figure 4.4: Plots of the energies of the modes in the eight-mode model ($n = 1$ and 2) as well as in the $n = 3$ level, for $\alpha = 4/81\,a_{ho}^{-2}$ and various $L$. The integers above the bars indicate the angular momentum of the modes, in the form $l|m|$. Notice that for each $L$, the energies of the modes in each level are comparable, and the energies of modes from different levels are relatively distinct. Thus, the eight-mode model is appropriate to use for these three geometries.

strength on the relationships among squeezing, fragmentation, and interaction strength while being able to use intuition gained from the eight-mode model.

The notation (4.8) that we chose for the modes is informative, but cumbersome. To simplify the notation, we simply number the modes according to the following system:

$$\begin{aligned}
\psi_1(\mathbf{r}) &= \psi^r_{100}(\mathbf{r}) & \psi_2(\mathbf{r}) &= \psi^l_{100}(\mathbf{r}) \\
\psi_3(\mathbf{r}) &= \psi^r_{210}(\mathbf{r}) & \psi_4(\mathbf{r}) &= \psi^l_{210}(\mathbf{r}) \\
\psi_5(\mathbf{r}) &= \psi^r_{211}(\mathbf{r}) & \psi_6(\mathbf{r}) &= \psi^l_{211}(\mathbf{r}) \\
\psi_7(\mathbf{r}) &= \psi^r_{21-1}(\mathbf{r}) & \psi_8(\mathbf{r}) &= \psi^l_{21-1}(\mathbf{r}).
\end{aligned} \tag{4.10}$$

**Fock State Representation**

As in the two-mode model, states in the eight mode-model can be expressed in terms of a basis of Fock states, each with a fixed number of particles in each mode:

$$|n_1, n_2, \ldots, n_8\rangle = \frac{1}{\sqrt{n_1! n_2! \cdots n_8!}} (\hat{a}_1^\dagger)^{n_1} (\hat{a}_2^\dagger)^{n_2} (\hat{a}_3^\dagger)^{n_3} (\hat{a}_4^\dagger)^{n_4} (\hat{a}_5^\dagger)^{n_5} (\hat{a}_6^\dagger)^{n_6} (\hat{a}_7^\dagger)^{n_7} (\hat{a}_8^\dagger)^{n_8} |0\rangle , \tag{4.11}$$

For the purpose of constructing an explicit matrix representation of the Hamiltonian of the system, we would like to number these Fock states with a single integer, such that the first $N+1$ states match the two-mode Fock states. The choice of how to accomplish this is arbitrary, but we present here one possible numbering scheme.

First, it is useful to know the size of the Hilbert space of the system given $N$ atoms in $M$ modes, which is equivalent to the number of ways of arranging $N$ identical balls in $M$ bins. Imagine that all of the balls were laid out in a line. To divide them into $M$ bins, one can insert $M-1$ partitions in various places along the line of balls. This is equivalent to starting with $N+M-1$ identical objects, and choosing $M-1$ of them to be partitions. The number of ways of doing this, and hence the dimension of the Hilbert space, is

$$D(N, M) = \binom{N+M-1}{M-1} = \frac{(N+M-1)!}{N!(M-1)!}. \tag{4.12}$$

Next, we describe a scheme for ordering the Fock states. Suppose that we have a Fock state $|n_1, n_2, \ldots, n_M\rangle$ with a particular occupation of each mode, and this Fock state has index $i$. To find the next Fock state $(i+1)$, we follow this algorithm:

1. Starting with $n_1$, find the first nonzero occupation number. Let's call this $n_p$.
2. Increment $n_{p+1}$ by 1.
3. Set $n_1$ equal to $n_p - 1$.
4. If $p \neq 1$, set $n_p$ equal to 0.

| | Fock index | | | | | | | | | | | | | | | | | | | |
|---|---|---|---|---|---|---|---|---|---|---|---|---|---|---|---|---|---|---|---|---|
| Mode | 0 | 1 | 2 | 3 | 4 | 5 | 6 | 7 | 8 | 9 | 10 | 11 | 12 | 13 | 14 | 15 | 16 | 17 | 18 | 19 |
| 1 | 3 | 2 | 1 | 0 | 2 | 1 | 0 | 1 | 0 | 0 | 2 | 1 | 0 | 1 | 0 | 0 | 1 | 0 | 0 | 0 |
| 2 | 0 | 1 | 2 | 3 | 0 | 1 | 2 | 0 | 1 | 0 | 0 | 1 | 2 | 0 | 1 | 0 | 0 | 1 | 0 | 0 |
| 3 | 0 | 0 | 0 | 0 | 1 | 1 | 1 | 2 | 2 | 3 | 0 | 0 | 0 | 1 | 1 | 2 | 0 | 0 | 1 | 0 |
| 4 | 0 | 0 | 0 | 0 | 0 | 0 | 0 | 0 | 0 | 0 | 1 | 1 | 1 | 1 | 1 | 1 | 2 | 2 | 2 | 3 |

Table 4.1: A table of the occupation numbers for the Fock states in a system with 3 atoms and 4 modes, ordered by Fock index.

If we give the Fock state with $n_1 = N$ the index 0, then this algorithm assigns a unique integer to each possible Fock state given a particular $N$ and $M$. See Table 4.1 for an example of this scheme for $N = 3$ and $M = 4$.

Given a particular Fock state with a set of occupation numbers $n_p$, it is possible to determine its index $i$ without resorting to starting from the $i = 0$ state and following this algorithm. Because of the way that the states are ordered, we know that a state with a given values of $n_M$ must come after all of the states with smaller $n_M$; by counting all such states, we get an integer $i_M$ which is less than or equal to the index of the state. Likewise, a state with a given value of $n_M$ and $n_{M-1}$ must come after all states with the same $n_M$ and smaller $n_{M-1}$; we can again count all such states to get an integer $i_{M-1}$. In general,

$$i_q = \sum_{p=0}^{n_q-1} D(\sum_{j=1}^{q} n_j - p, q-1). \tag{4.13}$$

The index of the state is then simply a sum of the $i_q$'s:

$$\begin{aligned} i &= \sum_{q=2}^{M} i_q \\ &= \sum_{q=2}^{M} \sum_{p=0}^{n_q-1} D(\sum_{j=1}^{q} n_j - p, q-1). \end{aligned} \tag{4.14}$$

### 4.1.2 The Hamiltonian

As with the two-mode model, we expand the field operators in terms of the eight modes (4.10):

$$\hat{\Psi}(\mathbf{r}) = \sum_{i=1}^{8} \psi_i(\mathbf{r}) \hat{a}_i, . \tag{4.15}$$

and similarly for $\hat{\Psi}^\dagger(\mathbf{r})$. Expanding the Hamiltonian (2.42) in terms of so many modes is a rather messy process, so we will proceed by breaking the Hamiltonian into two parts:

$$\hat{H}_1 = \sum_{i,j=1}^{8} \hat{a}_i^\dagger \hat{a}_j \, \epsilon_{ij} \tag{4.16a}$$

$$\hat{H}_2 = \sum_{i,j,k,l=1}^{8} \hat{a}_i^\dagger \hat{a}_j^\dagger \hat{a}_k \hat{a}_l \, \kappa_{ijkl}. \tag{4.16b}$$

Then $\hat{H} = \hat{H}_1 + a\hat{H}_2$.

To compute $\hat{H}_1$, it is useful to first compute $\epsilon_{ij}$. Using the notation

$$E_0 = 1 + \frac{1}{2}(\epsilon_0 + \epsilon_1) \tag{4.17a}$$

$$E_1 = 1 + \frac{1}{2}(\epsilon_2 + \epsilon_3) \tag{4.17b}$$

$$E_2 = 2 + \frac{1}{2}(\epsilon_0 + \epsilon_1) \tag{4.17c}$$

$$\delta_0 = \epsilon_1 - \epsilon_0 \tag{4.17d}$$

$$\delta_1 = \epsilon_3 - \epsilon_2, \tag{4.17e}$$

it is straightforward to show that

$$\epsilon_{ij} = \begin{pmatrix} E_0 & \delta_0/2 & 0 & 0 & 0 & 0 & 0 & 0 \\ \delta_0/2 & E_0 & 0 & 0 & 0 & 0 & 0 & 0 \\ 0 & 0 & E_1 & \delta_1/2 & 0 & 0 & 0 & 0 \\ 0 & 0 & \delta_1/2 & E_1 & 0 & 0 & 0 & 0 \\ 0 & 0 & 0 & 0 & E_2 & \delta_0/2 & 0 & 0 \\ 0 & 0 & 0 & 0 & \delta_0/2 & E_2 & 0 & 0 \\ 0 & 0 & 0 & 0 & 0 & 0 & E_2 & \delta_0/2 \\ 0 & 0 & 0 & 0 & 0 & 0 & \delta_0/2 & E_2 \end{pmatrix}. \tag{4.18}$$

Thus, we have

$$\begin{aligned} \hat{H}_1 = {} & E_0(\hat{n}_1 + \hat{n}_2) + E_1(\hat{n}_3 + \hat{n}_4) + E_2(\hat{n}_5 + \hat{n}_6 + \hat{n}_7 + \hat{n}_8) \\ & + \frac{\delta_0}{2}(\hat{a}_1^\dagger \hat{a}_2 + \hat{a}_5^\dagger \hat{a}_6 + \hat{a}_7^\dagger \hat{a}_8 + \text{h.c.}) + \frac{\delta_1}{2}(\hat{a}_3^\dagger \hat{a}_4 + \text{h.c.}). \end{aligned} \tag{4.19}$$

We see that tunneling is only allowed between modes with the same set of $n$, $l$, and $m$ quantum numbers. Since the component of a Fock state's angular momentum in the $z$ direction consists of $\hbar$ times the sum of the $m$ values for the Fock state's occupied modes, one-body tunneling between two Fock states must conserve $L_z$.

Next we study $\hat{H}_2$, starting with a computation of $\kappa_{ijkl}$:

$$\begin{aligned}
\kappa_{ijkl} &= \frac{2\pi\hbar^2}{m}\int \phi_i^*(\mathbf{r})\phi_j^*(\mathbf{r})\phi_k(\mathbf{r})\phi_l(\mathbf{r})\,d\mathbf{r} \\
&= 2\pi\hbar\omega_{ho}a_{ho}^2\int_0^{2\pi}\int_0^{\infty}\chi_{p_i,-m_i}(s,\theta)\chi_{p_j,-m_j}(s,\theta)\chi_{p_k,m_k}(s,\theta)\chi_{p_l,m_l}(s,\theta)\,s\,ds\,d\theta \\
&\quad\times\int_{-\infty}^{\infty}\phi_{q_i,l/r}(z)\phi_{q_j,l/r}(z)\phi_{q_k,l/r}(z)\phi_{q_l,l/r}(z)\,dz \\
&= \frac{2}{\pi}\hbar\omega_{ho}\int_0^{\infty}e^{-2s^2}s^{1+p_i+p_j+p_k+p_l}ds\int_0^{2\pi}e^{i(m_k+m_l-m_i-m_j)\phi}d\phi \\
&\quad\times\int_{-\infty}^{\infty}\phi_{q_i,l/r}(z)\phi_{q_j,l/r}(z)\phi_{q_k,l/r}(z)\phi_{q_l,l/r}(z)\,dz \\
&= 4\hbar\omega_{ho}2^{-\frac{1}{2}(4+|m_i|+|m_j|+|m_k|+|m_l|)}\Gamma\left(\frac{1}{2}(2+|m_i|+|m_j|+|m_k|+|m_l|)\right)\delta_{0,m_k+m_l-m_i-m_j} \\
&\quad\times\int_{-\infty}^{\infty}\phi_{q_i,l/r}(z)\phi_{q_j,l/r}(z)\phi_{q_k,l/r}(z)\phi_{q_l,l/r}(z)\,dz
\end{aligned} \tag{4.20}$$

Because of the $\phi$ integral, this quantity equals zero unless $m_k + m_l - m_i - m_j = 0$, which is a condition that can only be satisfied if the two-body tunneling from modes $k$ and $l$ to modes $i$ and $j$ conserves $L_z$. If $m_i = m_j = m_k = m_l = 0$ (i.e., the tunneling involves any four of the modes $\psi_1(\mathbf{r})$, $\psi_2(\mathbf{r})$, $\psi_3(\mathbf{r})$, and $\psi_4(\mathbf{r})$), then

$$\kappa_{ijkl} = \hbar\omega_{ho}\int_{-\infty}^{\infty}\phi_{q_i,l/r}(z)\phi_{q_j,l/r}(z)\phi_{q_k,l/r}(z)\phi_{q_l,l/r}(z)\,dz. \tag{4.21}$$

For all other $L_z$-conserving two-body tunneling (e.g., from two modes with $m = 0$ to one with $m = 1$ and one with $m = -1$), we have

$$\kappa_{ijkl} = \frac{1}{2}\hbar\omega_{ho}\int_{-\infty}^{\infty}\phi_{q_i,l/r}(z)\phi_{q_j,l/r}(z)\phi_{q_k,l/r}(z)\phi_{q_l,l/r}(z)\,dz. \tag{4.22}$$

Remember that the 1D double well states are only known numerically, so it is therefore not possible to analytically compute the value of the $z$ integral in these expressions. However, one can determine that the integral can take on one of nineteen possible distinct values depending on the particular set of modes being integrated. Because of this complexity, we forgo writing out an explicit expression for $\hat{H}_2$; the sheer number of terms would make this expression both overwhelming and uninformative, and one can generate the Hamiltonian matrix computationally without explicitly writing out all these terms.

The critical take-away from the analysis of the eight-mode Hamiltonian is that there are no tunneling processes that can change the value of $L_z$ of the system. This observation will be very useful when computing the ground state of the system.

### 4.1.3 Ground State Properties

As in the two-mode case, we can express the eight-mode Hamiltonian in a Fock basis and diagonalize the resulting matrix to find the ground state. Based on Eq. (4.12), the size of this matrix is

$$D(N,8) = \frac{(N+7)!}{5040N!}, \tag{4.23}$$

which grows very rapidly with $N$. This restricts the practical usefulness of the eight-mode model to small $N$ because of the computational cost of diagonalizing large matrices. However, recall that none of the terms in the Hamiltonian can change $L_z$, the projection of the total angular momentum of the system along the $z$ direction. This implies that the Hamiltonian has a block-diagonal form, with each block corresponding to a different value of $m \in \{-N, -N+2, \ldots, N-2, N\}$. By symmetry, the ground state has $m = 0$, so one can make the diagonalization process easier by only diagonalizing the $m = 0$ block of the Hamiltonian. This block has dimension

$$\begin{aligned} D_{m=0}(N,8) &= D(N,4)D^2(0,2) + D(N-2,4)D^2(1,2) + \cdots + D(0,4)D^2(N/2,2) \\ &= \sum_{i=0}^{N/2} D(N-2i,4)D^2(i,2) \\ &= \frac{7(N+4)}{4(N+7)(N+1)} D(N,8), \end{aligned} \tag{4.24}$$

where the first term in the sum corresponds to the part of the Hilbert space with all of the atoms in $m = 0$ modes; the second corresponds to $N-2$ atoms in $m = 0$ modes, one atom in an $m = 1$ mode, and one atom in an $m = -1$ mode; and so on. For large $N$, the size of this restricted Hamiltonian is a factor of $N$ smaller than the full Hamiltonian. By diagonalizing only this restricted matrix, we were able to compute eight-mode model results for up to $N = 10$. See Figure 4.5 for a plot that compares the rate of growth of $D(N,8)$ and $D_{m=0}(N,8)$.

#### Squeezing and Fragmentation

One can in principle compute analytical expression for the squeezing, fragmentation, and depletion parameters in the eight-mode model ($S^{(8)}$, $F^{(8)}$, and $D^{(8)}$) that are analogous to those in the two-mode model (Eqs. (3.38), (3.45a), and (3.45b)). However, these expressions are sufficiently complicated in form that they are not very illuminating, so we will not compute them analytically here.

However, there is one aspect of squeezing that we can consider analytically. Recall that in the two-mode model, the maximum possible amount of squeezing was restricted to be less than or equal to $S^{(2)}_{max}$ (Eq. (3.39)). Using eight-mode model notation, we can write this quantity as

$$S^{(2)}_{max} = 4\mathcal{N}^2_{11}. \tag{4.25}$$

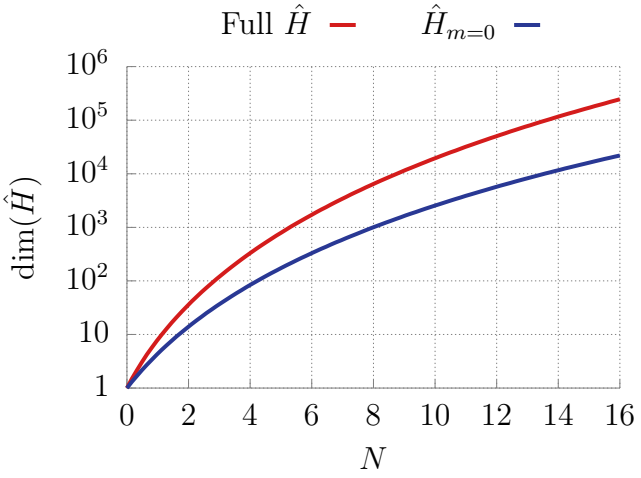


Figure 4.5: The growth of the Hilbert space of the eight-mode model Hamiltonian as a function of $N$. The extremely rapid growth of the size of the Hamiltonian matrix makes it impractical to diagonalize for $N$ greater than about 10.

| $L$ $[a_{ho}]$ | $\mathcal{N}_{11}$ | $\mathcal{N}_{33}$ | $S^{(2)}_{max}$ | $S^{(8)}_{max}$ |
|---|---|---|---|---|
| 1 | 0.420 | 0.358 | 0.704 | 0.512 |
| 2 | 0.453 | 0.380 | 0.820 | 0.577 |
| 3 | 0.500 | 0.473 | 0.999 | 0.895 |

Table 4.2: Values of $\mathcal{N}_{11}$, $\mathcal{N}_{33}$, $S^{(2)}_{max}$, and $S^{(8)}_{max}$ for $L = a_{ho}$, $2\,a_{ho}$, and $3\,a_{ho}$. Notice that the stronger the barrier, the more capacity the system has to squeeze. Also notice that the amount of squeezing possible in the modes with $z$ part $\phi_{1,l/r}(z)$ is consistently smaller than in the modes with $\phi_{0,l/r}(z)$.

We could equally well have written it in terms of modes 2, 5, 6, 7, or 8 instead of 1, because all of these modes have the same form of the $z$ part of their wavefunctions ($\phi_{0,l/r}(z)$). However, modes 3 and 4 have a different $z$ part ($\phi_{1,l/r}(z)$), which suggests that we define an analogous expression

$$S^{(8)}_{max} = 4\mathcal{N}^2_{33}. \tag{4.26}$$

Recall that $\mathcal{N}_{ii}$ effectively measures the fraction of a mode $i$ on the "wrong" side of $z = 0$; the more "spillover," the smaller $\mathcal{N}_{ii}$. In general, the modes with $\phi_{1,l/r}(z)$ will have more spillover for a given double well geometry than states with $\phi_{0,l/r}(z)$ (one can see this by comparing the wavefunctions illustrated in Figs. 3.1 and 4.1). This means that $S^{(8)}_{max} < S^{(2)}_{max}$; see Table 4.2 for representative values of $S^{(2)}_{max}$ and $S^{(8)}_{max}$.). Hence, we expect that a ground state will have less squeezing if it is dominated by modes 3 and 4 (i.e., $\psi^{l/r}_{210}(\mathbf{r})$) than if it is dominated by the other six modes, even if in both cases it has the same value of $n_l - n_r$.

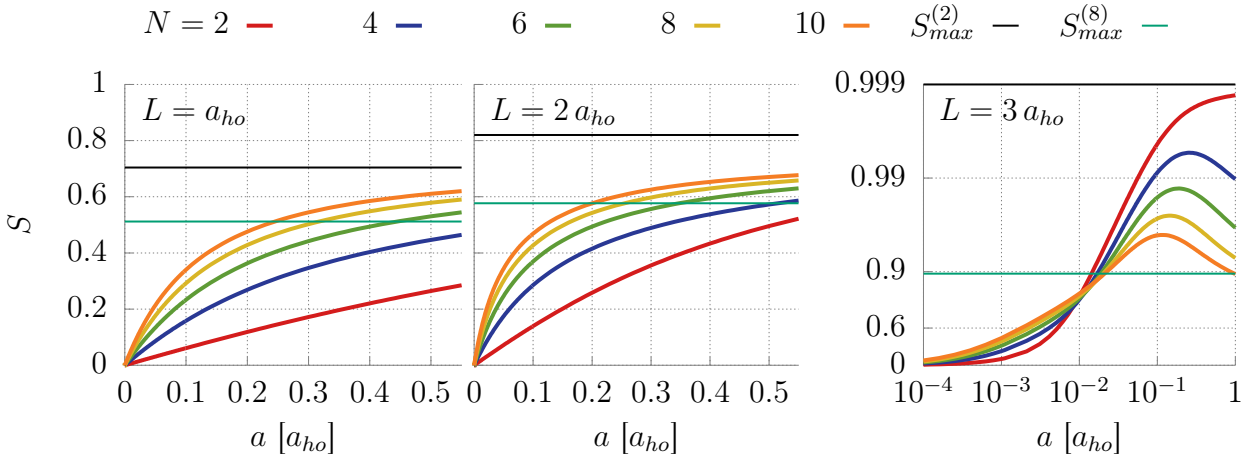


Figure 4.6: Squeezing $S$ vs. scattering length $a$ for various particle number $N$ between 2 and 10 for three different potentials ($L = a_{ho}$, $2\,a_{ho}$, and $3\,a_{ho}$, from left to right) in the eight-mode model. Notice that the rightmost ($L = 3\,a_{ho}$) plot has a logarithmic scale for $S$. The horizontal lines indicate the values of $S^{(2)}_{max}$ and $S^{(8)}_{max}$, defined in Eqs. (4.25) and (4.26), respectively.

## 4.2 Eight-Mode Model Predictions

To the best of our knowledge, no studies have been done of squeezing or fragmentation from within the eight-mode model. In this section we rectify this gap while building more intuition that will help us interpret the results of our quantum Monte Carlo simulations in Chapter 6.

### 4.2.1 Squeezing Analysis

In Figure 4.6 we show the behavior of the squeezing parameter $S$ (Eq. (2.68)) as a function of the scattering length $a$ for a variety of particle numbers and in three different double well geometries for the eight-mode model. We do not go beyond 10 particles because of the computational cost of diagonalizing the resulting Hamiltonian, discussed above. We see that the squeezing behavior for the low barriers ($L = a_{ho}$ and $2\,a_{ho}$) looks qualitatively similar to the equivalent cases in the nearly degenerate and exact two-mode models (see Figure 3.2). However, for $L = 3\,a_{ho}$ we see qualitatively different behavior: the squeezing has a maximum, and it is in general smaller than for the two-mode case. We would like to account for this behavior, despite the fact that we cannot analyze the eight-mode Hamiltonian as easily as we did the two-mode Hamiltonian because of its complexity.

One way to do this is to look at the composition of the ground state via plots analogous to Figure 3.3. However, because the Hilbert space is so large, it is not useful to plot the contribution to the ground state of each individual Fock state. Instead, we sum the contributions of all Fock states for which the difference in $N_l$ and $N_r$ is the same, regardless

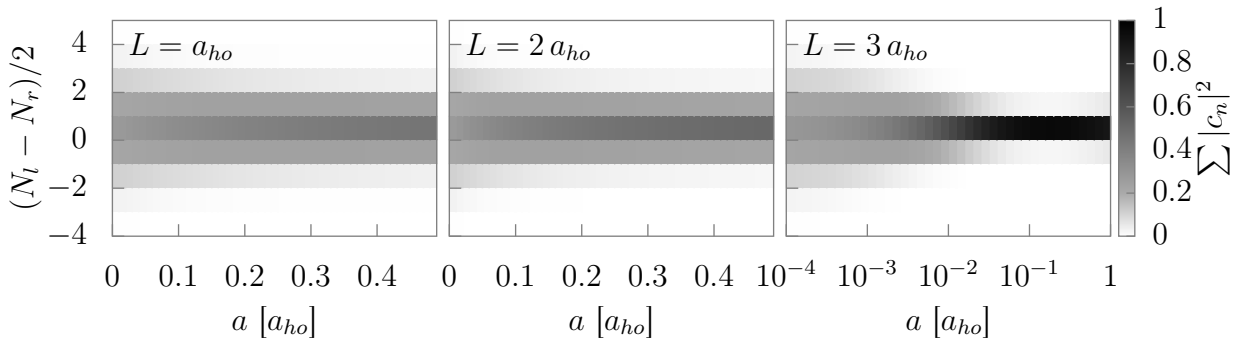


Figure 4.7: A representation of the ground state for the double well potential as a function of scattering length $a$ as computed in the eight-mode model for $N = 8$ and various $L$ (1, 2, and 3, from left to right). The quantity plotted is the sum of $|c_n|^2$ for the components of the ground state that have a given value for the difference between the number of particles in left and right modes.

of which exact modes are occupied; see Figure 4.7 for the resulting plot. By comparing Figure 4.6 and Figure 4.7, we see that a narrower distribution corresponds to more squeezing (as in the two-mode model), and that, therefore, the maximum in the $L = 3\,a_{ho}$ squeezing data corresponds to a narrow neck in the state distribution. Hence, the distribution of Fock states in the ground state accounts for the maxima that differentiates the two- and eight-mode squeezing predictions for $L = 3\,a_{ho}$.

Another way to think about the cause of the maximum in the $L = 3\,a_{ho}$ squeezing data is in terms of the quantities $S^{(2)}_{max}$ and $S^{(8)}_{max}$, which are also plotted in Figure 4.6. Recall that we argued earlier that states with more contributions from atoms in 210 modes would exhibit less squeezing than states with more contributions from 100 and $21 \pm 1$ modes. In Figure 4.8, we plot the fraction of particles in the eight-mode model ground state that are in the 210 modes. For the largest $a$ plotted, that fraction reaches as high as 8 percent, with larger fractions for larger $N$. This is reasonable: in general, the repulsive interaction between the atoms drives them away from each other, and in an eight-mode model, one way that the atoms can avoid each other is by occupying modes with different values of $m$. Hence, we expect that, for a given $a$, increasing the number of particles in the system will result in a larger fraction of them occupying the 210 modes. The occupation of these modes can then reduce the amount of squeezing via the spillover mechanism proposed above.

### 4.2.2 Fragmentation Analysis

In Figure 4.9, we plot the fragmentation parameter $F$ and depletion parameter $D$ (Eqs. (2.97a) and (2.97b), respectively) as a function of scattering length $a$ in the eight-mode model for a variety of particle numbers and double well geometries. The main qualitative differences between these prediction and those of the two-mode model in Figure 3.7 are that the eight-mode states exhibit less fragmentation and more depletion.

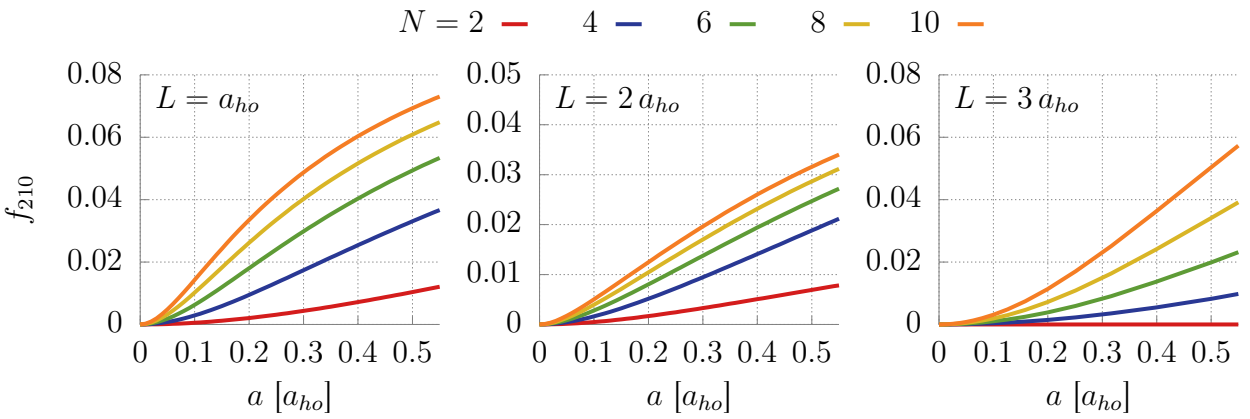


Figure 4.8: Fraction $f_{210}$ of particles in the 210 modes of the eight-mode model as a function of the scattering length $a$ for various particle number $N$ between 2 and 10 and for three different potentials ($L = a_{ho}$, $2\,a_{ho}$, and $3\,a_{ho}$, from left to right). The total fraction of particles in the 100 and $21 \pm 1$ modes (not shown) is given by $1 - f$.

Recall that $F$ and $D$ are defined in terms of $n_0$ and $n_1$, the occupation numbers of the first two natural orbitals. In the two-mode model, these are the only two occupation numbers, so there is no depletion. In the eight-mode model, there are eight natural orbitals to occupy. The fact that there is less fragmentation and simultaneously more depletion in the eight-mode case implies that the occupation of the orbitals is spread out among more than just the first two, but that $n_0$ is larger relative to $n_1$ in the eight-mode case than in the two-mode case. This is not particularly surprising. In the two-mode case, the only way to reduce $n_0$ is to increase $n_1$. However, because the eight-mode states can occupy the other six natural orbitals, a reduction in $n_0$ can be compensated by an increase in any of $n_1$ through $n_7$. Hence, conditions that would have led to pure fragmentation in the two-mode case leads to less fragmentation with some depletion in the eight-mode case.

## 4.3 Summary

In this chapter, we analyzed the interacting double well BEC system from the perspective of an eight-mode model. The modes for this model are more complicated than those for the two-mode model; among other differences, they exhibit nonzero angular momentum. We noted that the projection of this angular momentum along the $z$-axis for a Fock state is conserved under the action of the eight-mode Hamiltonian. We also noted that the shape of the double well influences the energies of the modes, and therefore determines whether or not an eight-mode description of the system is appropriate.

The eight-mode Hamiltonian is quite complicated and has a Hilbert space that grows rapidly with $N$; the larger the Hilbert space, the more difficult numerical diagonalization of the Hamiltonian. Although we did not write out the Hamiltonian in detail, we did give

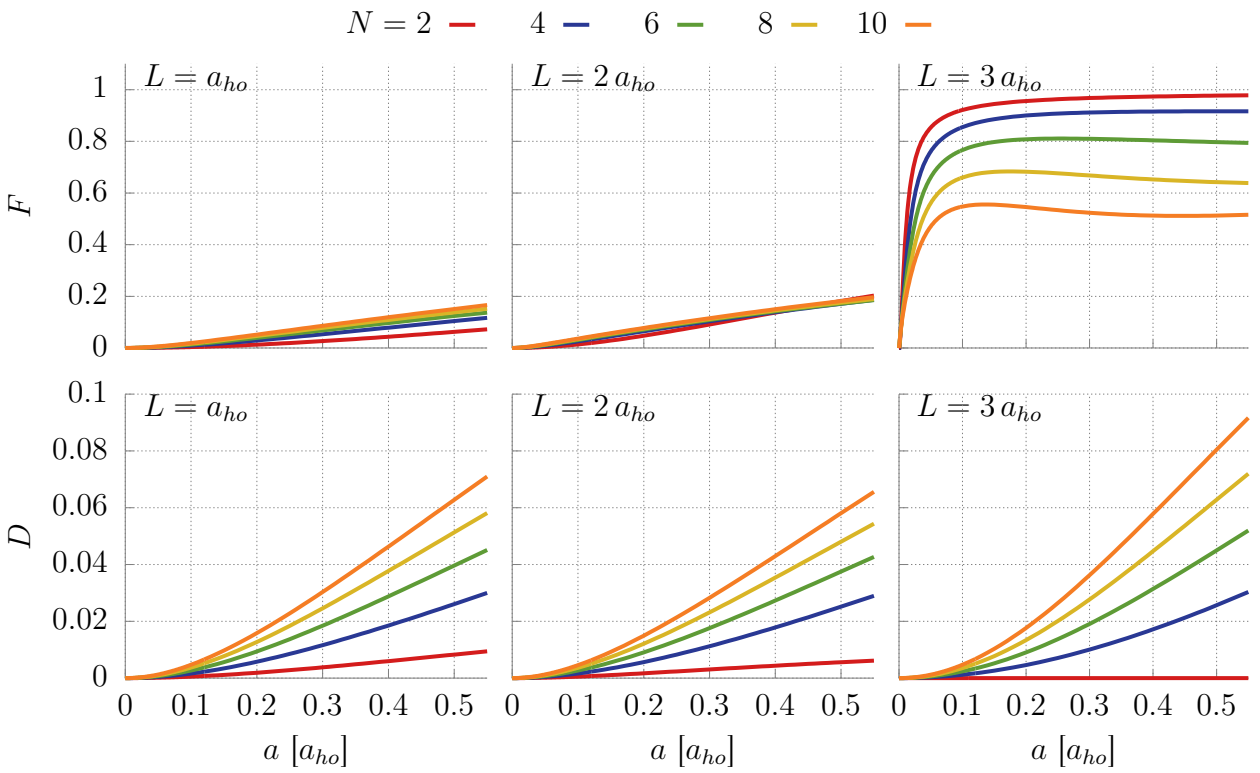


Figure 4.9: The fragmentation $F$ (top) and depletion $D$ (bottom) vs. scattering length $a$ for various particle number $N$ between 2 and 10 for three different potentials ($L = a_{ho}$, $2\,a_{ho}$, and $3\,a_{ho}$, from left to right) in the eight-mode model.

arguments to show that it has a block diagonal form, with each block containing states with a specific value of $L_z$. By ignoring all blocks but the one with $L_z = 0$, we can make the problem of diagonalizing the Hamiltonian to find the ground state somewhat more tractable. The largest value of $N$ for which we could diagonalize the Hamiltonian is 10, for which $\hat{H}$ has a dimension of 2548.

Finally, we investigated squeezing, fragmentation, and depletion in the eight-mode ground state. Compared with the two-mode ground state, we found that the eight mode ground state

- exhibits less squeezing, especially for $L = 3\,a_{ho}$,
- exhibits a maximum in $S$ for $L = 3\,a_{ho}$, and
- exhibits less fragmentation and more depletion.

Physically, these effects can be understood as a consequence of the occupation of modes in the $n = 2$ energy level in addition to the two-mode model's $n = 1$ modes. Because the $n = 2$ modes spread into the "wrong" well more so than the $n = 1$ modes, they lead to more

particle fluctuations across the barrier for the same value of $N_l - N_r$. Hence, $n = 2$ modes will tend to suppress both squeezing and fragmentation in eight-mode ground states relative to two-mode ground states, to the extent that they are occupied. The presence of a maximum in the squeezing parameter comes about because of a competition between this effect and the usual suppression of particle fluctuations that comes about because of increasing the scattering length. Finally, the presence of more than two natural orbitals in the eight-mode model allows for non-zero depletion when the "extra" modes are occupied, as opposed to the two-mode model in which depletion as we have defined it is not possible.

# Chapter 5

# Quantum Monte Carlo: The Path Integral Ground State Method

In last two chapters, we explored the ground state properties of the double well BEC system by approximating its Hamiltonian via multimode expansions. We found that the results that one obtains, especially for moderate to large scattering lengths, are quite sensitive both to the number of modes in the expansion and the number of "negligible" terms kept in the Hamiltonian. Assuming that this pattern continues, it would be desirable to have an "infinite-mode" expansion, i.e., to solve for the ground state exactly. In order to do so, we use the path integral ground state quantum Monte Carlo method, which is a member of a family of computational methods that are used to simulate quantum many-body systems. In this chapter, we describe our implementation of PIGS in detail in anticipation of the simulated results we will present in Chapter 6.

## 5.1 Overview

Quantum Monte Carlo (QMC) is a class of computer algorithms that simulates quantum many-body systems. In QMC, the quantum problem to be solved is expressed in terms of Richard Feynman's path integral formulation of quantum mechanics [87], and then these quantum paths are mapped onto a classical system of interacting polymer chains. At their core, all QMC algorithms work by using the Monte Carlo method to evaluate the high-dimensional integrals that result from this mapping. Because Monte Carlo integration is inherently stochastic, there is statistical uncertainty in the results produced by QMC; this is the price one pays for being able to solve the exact quantum problem. Fortunately, this uncertainty can be reduced with increased simulation time as well as by clever choices of various computational details, as discussed in detail in Section 5.3.

QMC methods can be classified based on a wide variety of criteria, such as whether the particles in the system live on a lattice or in the continuum, whether the method is computing the system's ground state or a (mixed) state at finite temperature, or whether the method

uses the variational principle or projection operators to compute the desired state. In our work, we use the path integral ground state (PIGS) method [58], which is an exact ground state ($T = 0$) QMC method (where "exact" means that, in principle, all systematic errors can be reduced below the level of statistical errors). PIGS uses imaginary time propagation to project out the ground state of the system from a trial wave function, which is chosen to be as good an approximation to the true ground state as possible. The imaginary time propagator is discretized into a number of *time slices*, so that the path of each particle through imaginary time can be thought of as a classical chain of *beads* (one per slice) connected by *links*, with the chains interacting with each other. The links represent the kinetic energy part of the imaginary time propagator while the interactions between the chains represents the potential energy part of the propagator. Through this discretization, the problem of calculating the ground state properties of the system (like the squeezing parameter $S$) are reduced to that of evaluating integrals of very high dimension ($3NM$ for a three-dimensional system of $N$ particles with $M$ time slices). These integrals are solved using Monte Carlo techniques.

PIGS provides several key advantages over other ground state methods, the most significant of which is the ability to evaluate unbiased estimators for any observable [58, 60]; this means that the choice of trial wave function only impacts the efficiency of the computation, rather than biasing the result. PIGS may also be tailored to evaluate off-diagonal observables such as the one-body (or $N$-body) reduced density matrix directly and without bias, as demonstrated by an unprecedented degree of accuracy and agreement with experiment in the evaluation of the condensate fraction for bulk liquid helium [59].

Computationally, PIGS is very well suited to trivial parallelization due to the statistical nature of the technique, requiring neither communication between parallel processes nor shared memory. In addition, the memory requirements for PIGS are modest, with even the largest system sizes requiring only on the order of 1 GB of memory. Each parallel run can, however, require a long run time in order to sufficiently de-correlate from the initial, randomly-chosen state of the system.

In our PIGS implementation for the double well system, we use a fourth-order approximation to the imaginary time propagator [88, 89], modified to incorporate hard sphere interactions between the bosons [90] where the hard sphere diameter is the $s$-wave scattering length $a$. For a trial wave function, we use a form that is the product of $N$ copies of the ground state of a single particle in a double well (which would be the true ground state in the absence of interactions) and a pair correlation (Jastrow) term that is the exact zero-energy $s$-wave scattering solution for two hard spheres. A good trial function is essential here because the energy level structure of the system, i.e. the very small energy gap between the ground and first excited states, would require a very long path in imaginary time to achieve convergence with a poor approximation to the ground state wavefunction.

In the next sections, we discuss the general structure of the PIGS method and particular details of our implementation of it.

## 5.2 Path Integral Ground State

As we stated above, PIGS allows us to calculate the ground state properties of a many-body quantum system. This does not mean that PIGS allows us to compute the ground state wavefunction itself; instead, one can only calculate the ground state expectation value of whatever operators may be of interest. In this section, we discuss how to do this using imaginary time propagation, Monte Carlo integration, and Metropolis sampling to implicitly determine the ground state probability density distribution.

### 5.2.1 Imaginary Time Propagation

The first key idea behind PIGS is imaginary time propagation. Given a many-body system described by a Hamiltonian $\hat{H}$, one can guess a trial many-body ground state wavefunction $|\psi_T\rangle$. The trial wavefunction can be expanded as a sum of the energy eigenstates $|\psi_n\rangle$ of $\hat{H}$:

$$|\psi_T\rangle = \sum_{n=0}^{\infty} c_n |\psi_n\rangle . \tag{5.1}$$

We would like to be able to eliminate all of the components of this trial function apart from the true ground state $|\psi_0\rangle$. To do so, we can apply the operator $e^{-\tau\hat{H}/\hbar}$, which we can interpret as an *imaginary time translation operator* or *imaginary time propagator* (by analogy to the (real) time translation operator $e^{-it\hat{H}/\hbar}$). Upon normalization, this produces a new state $|\chi\rangle$:

$$\begin{aligned}
|\chi\rangle &= \frac{e^{-\tau\hat{H}/\hbar}|\psi_T\rangle}{\sqrt{\langle\psi_T|e^{-2\tau\hat{H}/\hbar}|\psi_T\rangle}} \\
&= \frac{e^{-\tau\hat{H}/\hbar}\sum_{n=0}^{\infty} c_n|\psi_n\rangle}{\sqrt{\sum_{m=0}^{\infty}\sum_{n=0}^{\infty} c_m^* c_n \langle\psi_m|e^{-2\tau\hat{H}/\hbar}|\psi_n\rangle}} \\
&= \frac{\sum_{n=0}^{\infty} c_n e^{-\tau E_n/\hbar}|\psi_n\rangle}{\sqrt{\sum_{m=0}^{\infty}\sum_{n=0}^{\infty} c_m^* c_n e^{-2\tau E_n/\hbar}\langle\psi_m|\psi_n\rangle}} \\
&= \frac{\sum_{n=0}^{\infty} c_n e^{-\tau E_n/\hbar}|\psi_n\rangle}{\sqrt{\sum_{n=0}^{\infty}|c_n|^2 e^{-2\tau E_n/\hbar}}} \\
&= \frac{c_0|\psi_0\rangle + \sum_{i=1}^{\infty} e^{-\tau(E_n-E_0)/\hbar}c_n|\phi_n\rangle}{\sqrt{|c_0|^2 + \sum_{i=1}^{\infty} e^{-2\tau(E_n-E_0)/\hbar}|c_n|^2}}.
\end{aligned} \tag{5.2}$$

If we assume a non-degenerate ground state, then $E_0$ is (by definition) the smallest energy and therefore

$$\lim_{\tau\to\infty}|\chi\rangle = \frac{c_0}{\sqrt{|c_0|^2}}|\psi_0\rangle = e^{i\phi_0}|\psi_0\rangle . \tag{5.3}$$

In other words, in the limit of long imaginary time $\tau$, we can use the imaginary time propagator to project the ground state out of the trial wavefunction (up to an irrelevant global phase factor which we can eliminate by choosing $c_0$ to be real). Also, notice that the normalization factor here is not equal to 1 as it would be if we had applied the real time translation operator; this is because the imaginary time translation operator is not unitary. Regardless, the normalization factor is irrelevant in the PIGS algorithm, for reasons that we will come back to shortly, so we will ignore it from now on.

### Expectation Values

In order to estimate the ground state expectation value of an operator of interest $\hat{O}$, one can compute the expectation value of that observable with respect to the state $|\chi\rangle$:

$$\langle\chi|\hat{O}|\chi\rangle = \langle\psi_T|e^{-\tau\hat{H}/\hbar}\hat{O}e^{-\tau\hat{H}/\hbar}|\psi_T\rangle\,. \tag{5.4}$$

Because this quantity approaches the actual ground state expectation value in the $\tau\to\infty$ limit, it can be used as unbiased estimator of that expectation value. Of course, in an actual simulation $\tau$ cannot really be set to infinity, but it can in principle be made sufficiently large such that any error that arises from its finiteness is smaller than the statistical error associated with the simulation.

To compute this estimator for $\langle\hat{O}\rangle$ in a simulation, it must be written in a particular basis. We choose a position basis, written in terms of a $3N$-dimensional position vector $|R\rangle = |\mathbf{r}_1, \mathbf{r}_2, \cdots, \mathbf{r}_N\rangle$ that encodes the position of all $N$ particles. Unfortunately, it is in general not possible to express $\langle R|e^{-\tau\hat{H}/\hbar}|R'\rangle$ in this basis analytically; it is only possible to approximate it in the $\tau\to 0$ limit. This seems to be a problem: we need large $\tau$ to decay to the ground state but small $\tau$ to properly express the imaginary time propagator. To remedy this problem, we replace $\tau$ by $\beta M$:

$$\langle\chi|O|\chi\rangle = \left\langle\psi_T\left|\left(e^{-\beta\hat{H}/\hbar}\right)^M\hat{O}\left(e^{-\beta\hat{H}/\hbar}\right)^M\right|\psi_T\right\rangle, \tag{5.5}$$

where $\beta$ is small enough to well-approximate the propagator while $M$ is large enough to decay the trial function to the ground state. We then insert $2M+1$ copies of the identity in the position basis

$$\hat{I} = \int |R\rangle\langle R|\,dR, \tag{5.6}$$

into this expression to convert it into an integral:

$$\begin{aligned}\langle\chi|\hat{O}|\chi\rangle &= \int \langle\psi_T|R_0\rangle\langle R_0|e^{-\beta\hat{H}/\hbar}|R_1\rangle\ldots\langle R_{M-1}|e^{-\beta\hat{H}/\hbar}|R_M\rangle\,O(R_M)\\ &\quad\times\langle R_M|e^{-\beta\hat{H}/\hbar}|R_{M+1}\rangle\ldots\langle R_{2M-1}|e^{-\beta\hat{H}/\hbar}|R_{2M}\rangle\langle R_{2M}|\psi_T\rangle\,dR_0\ldots dR_{2M}\\ &= \int \psi_T^*(R_0)\psi_T(R_{2M})\prod_{i=0}^{2M-1}G(R_i,R_{i+1},\beta)O(R_M)\,dR_0\ldots dR_{2M}.\end{aligned} \tag{5.7}$$

For notational convenience, we define $G(R_i, R_{i+1}, \beta) = \langle R_i | e^{-\beta \hat{H}/\hbar} | R_{i+1} \rangle$ as the imaginary time propagator in the position basis.

### Off-Diagonal Observables

The discussion thus far implicitly assumes that $\hat{O}$ is diagonal in the position basis, so that $\langle R_i | \hat{O} | R_j \rangle = \langle R_i | R_j \rangle \, O(R_j) = \delta(R_i - R_j) O(R_j)$. Suppose instead that we were interested in computing on off-diagonal observable, $\hat{P}$, for which $\langle R_i | \hat{P} | R_j \rangle = P(R_i, R_j)$. Then we would modify Eq. (5.7):

$$\langle \chi | \hat{P} | \chi \rangle = \int \psi_T^*(R_0) \psi_T(R_{2M+1}) \prod_{\substack{i=0 \\ i \neq M}}^{2M} G(R_i, R_{i+1}, \beta) \, P(R_M, R_{M+1}) \, dR_0 \ldots dR_{2M+1}. \quad (5.8)$$

Because there is no propagator connecting the configurations $M$ and $M+1$, the path is said to be "broken." Apart from that, the paths are sampled in the same way as for diagonal observables, and the value of $\langle \hat{P} \rangle$ is estimated by averaging over $P(R_M, R_{M+1})$ for the accepted paths.

The OBDM is an off-diagonal observable. To compute it, the path of only one of the $N$ particles is broken while $\mathbf{r}_M = \mathbf{r}_{M+1}$ for the others [59]. One then uses the set of accepted paths to make a histogram of the occurrences of particular pairs of $z_M^{broken}$ and $z_{M+1}^{broken}$; this histogram is $\rho(z, z')$. In order to normalize the OBDM, we multiply it by a factor such that the sum of its eigenvalues (i.e., the total occupation of the natural orbitals) is 1. Because the histogram has to have a finite bin size, this method can generate non-physical negative eigenvalues, but these vanish given long enough simulations.

### The Local Energy

The calculation of the energy, i.e., the expectation value of the Hamiltonian, is a special case that is worth discussing. While $\hat{H}$ is an off-diagonal operator in the position representation because the kinetic energy contains derivatives, it obviously commutes with the imaginary

time propagator. This allows us to define the so-called *local energy* $E_L$:

$$\begin{aligned}
\langle\chi|\hat{H}|\chi\rangle &= \left\langle \psi_T \left| \left(e^{-\beta\hat{H}/\hbar}\right)^M \hat{H} \left(e^{-\beta\hat{H}/\hbar}\right)^M \right| \psi_T \right\rangle \\
&= \left\langle \psi_T \left| \left(e^{-\beta\hat{H}/\hbar}\right)^{2M} \hat{H} \right| \psi_T \right\rangle \\
&= \int \psi_T^*(R_0) \prod_{i=0}^{2M-1} G(R_i, R_{i+1}, \beta) \langle R_{2M}|\hat{H}|\psi_T\rangle \, dR_0 \ldots dR_{2M} \\
&= \int \psi_T^*(R_0)\psi_T(R_{2M}) \prod_{i=0}^{2M-1} G(R_i, R_{i+1}, \beta) \frac{\langle R_{2M}|\hat{H}|\psi_T\rangle}{\langle R_{2M}|\psi_T\rangle} \, dR_0 \ldots dR_{2M} \\
&= \int \psi_T^*(R_0)\psi_T(R_{2M}) \prod_{i=0}^{2M-1} G(R_i, R_{i+1}, \beta) E_L(R_{2M}) \, dR_0 \ldots dR_{2M}, \qquad (5.9)
\end{aligned}$$

where

$$E_L(R) = \left. \frac{\hat{H}\psi_T}{\psi_T} \right|_R . \qquad (5.10)$$

Hence, the local energy can be computed like a diagonal observable despite the fact that $\hat{H}$ is not diagonal. Since $\psi_T$ and $\hat{H}$ are both known, it is straightforward to calculate this function and to estimate its value with the PIGS method. One can equivalently estimate the energy using $E_L(R_0)$, and in fact the best option is to do both and average the results.

### 5.2.2 Monte Carlo Integration

Given an analytical form for $G(R_i, R_{i+1}, \beta)$, the problem of computing the ground state expectation value of an observable has been transformed into that of solving an integral of very high $(3MN)$ dimension, Eq. (5.7). For one-dimensional numerical integration, one typically uses some form of quadrature to numerically compute the value of the integral; this requires $k$ evaluations of the integrand, where $k$ is the number of quadrature points. For a $D$-dimensional integral, this method requires $k^D$ function evaluations. The integrals we need to be able to solve have $D = 3NM \approx 10^4$. Even if we only had 2 quadrature points per dimension, evaluation of an integral with this number of dimensions would require about $2^{10^4}$ function evaluations. Assuming a typical processor speed of $10^9$ evaluations per second, this computation would take about $10^{2984}$ times the age of the universe to complete. This is clearly a problem.

Monte Carlo integration was designed to solve exactly this problem. Instead of using a deterministic method, like quadrature, Monte Carlo integration uses statistical sampling of the integrand to calculate the value of a definite integral of the form $\int \pi(X) f(X) dX$. Here $\pi(X)$ is interpreted as a probability distribution over which the integral of $f(X)$ is computed, and $X$ is known as the *configuration* of the system. The configurations are

generated randomly based on some update method that proposes a new configuration $X_j$ given an old configuration $X_i$ (with probability $\mathcal{P}(X_i \to X_j)$) and an algorithm which decides whether or not the new configuration is accepted (with probability $\mathcal{A}(X_i \to X_j)$). This process can take whatever form we like, as long as it results in the accepted configurations being distributed according to $\pi(X)$. After $k$ accepted configurations have been generated, the value of the integral may be estimated by taking an average:

$$\int \pi(X) f(X) dX \approx \frac{1}{k} \sum_{\text{accepted} X} f(X_i). \tag{5.11}$$

How do we ensure that the accepted configurations are distributed according to $\pi(X)$? First, let's define a *transition probability* $p(X_i \to X_j)$, which is the probability of transitioning from a configuration $X_i$ to a configuration $X_j$. It is given by

$$p(X_i \to X_j) = \mathcal{P}(X_i \to X_j)\mathcal{A}(X_i \to X_j). \tag{5.12}$$

In other words, the probability of transitioning from $X_i$ to $X_j$ is the probability of proposing a transition from $X_i$ to $X_j$ (which is determined by our update methods, discussed in Section 5.3.3) times the probability of accepting the proposed transition (which we will describe shortly). These transition probabilities must satisfy

$$\sum_j p(X_i \to X_j) = 1, \tag{5.13}$$

because the probability of transitioning from $X_i$ to any other configuration is 1. Additionally, it must be the case that the probability of being in a configuration $X_i$ is the sum of the probability of being in any configuration times the probability of transitioning from that configuration to $X_i$:

$$\pi(X_i) = \sum_j \pi(X_j) p(X_j \to X_i). \tag{5.14}$$

These expression can be rewritten as

$$(1 - p(X_i \to X_i)) = \sum_{j \neq i} p(X_i \to X_j) \tag{5.15a}$$

$$\pi(X_i)(1 - p(X_i \to X_i)) = \sum_{j \neq i} \pi(X_j) p(X_j \to X_i). \tag{5.15b}$$

Making the obvious substitution results in the constraint that the transition probabilities must satisfy:

$$\sum_{j \neq i} \pi(X_i) p(X_i \to X_j) - \pi(X_j) p(X_j \to X_i) = 0. \tag{5.16}$$

In principle, this constraint can be satisfied by many choices of transition probabilities. In practice, the usual choice that is made is to enforce *detailed balance*:

$$\pi(X_i) p(X_i \to X_j) = \pi(X_j) p(X_j \to X_i) \quad \forall\, i, j, \tag{5.17}$$

which is equivalent to

$$\pi(X_i)\mathcal{P}(X_i \to X_j)\mathcal{A}(X_i \to X_j) = \pi(X_j)\mathcal{P}(X_j \to X_i)\mathcal{A}(X_j \to X_i) \quad \forall\, i, j. \tag{5.18}$$

In order to satisfy detailed balance, the acceptance probabilities $\mathcal{A}(X_i \to X_j)$ are determined using the Metropolis algorithm [91]:

1. Randomly generate a configuration $X_1$, and write it to the list of accepted configurations.
2. Generate a new configuration $X_2$ by some update method, with probability $\mathcal{P}(X_1 \to X_2)$.
3. Accept the configuration $X_2$ with probability
$$\mathcal{A}(X_1 \to X_2) = \min\left(1, \frac{\pi(X_2)}{\pi(X_1)}\frac{\mathcal{P}(X_2 \to X_1)}{\mathcal{P}(X_1 \to X_2)}\right). \tag{5.19}$$
4. If $X_2$ is accepted, write it to the list of accepted configurations and go to step 2, using it as the "old" configuration. If $X_2$ is rejected, write $X_1$ to the list of accepted configurations and go to step 2, using $X_1$ as the "old" configuration.

This algorithm is run until a predetermined number of accepted configurations is generated, and then they are averaged to give an estimate of the integral as in Eq. (5.11). The error associated with this estimate may be estimated by the standard error of the distribution of values $A(X_i)$.

In addition to ensuring detailed balance by choosing acceptance probabilities according to the Metropolis algorithm, we must also ensure that our simulation is *ergodic*, which means that it must be able to eventually generate any allowed configuration of the system starting with any allowed configuration. If this is not the case, then there will be some configurations with nonzero $\pi(X)$ that cannot be sampled by the simulation even in principle, and therefore there is no way for the simulation to reproduce $\pi(X)$ correctly. Ergodicity is determined by our choice of update methods: we require that whatever method we choose proposes transitions between allowed configurations with nonzero probability.

To connect this back to the calculation of $\langle\chi|\hat{O}|\chi\rangle$, we can directly map the integral (5.7) to the Monte Carlo integration method by defining $X = \{R_0, R_1, \cdots, R_{2M}\}$, $f(X) = O(R_M)$, and

$$\pi(X) = \psi_T^*(R_0)\psi_T(R_{2M}) \prod_{i=0}^{2M-1} G(R_i, R_{i+1}, \beta). \tag{5.20}$$

Had we included normalization, $\pi(X)$ would have the properties of a probability distribution: $\pi(X) < 1$ for all $X$, and $\int \pi(X)dX = 1$. However, because it is the ratio of probabilities $\pi(X_1)$ and $\pi(X_2)$ that comes into the Metropolis acceptance probability (5.19), we can ignore the normalization without any consequences. Hence, the Monte Carlo algorithm generates configurations of atom coordinates that are distributed according to a probability distribution which is the square of the ground state wavefunction (in the limit of large $M$), and this method thereby allows us to evaluate the integral that we need in order to compute the ground state properties of the system.

## 5.3 Computational Details

When implementing a PIGS method, one needs to make choices about three main parts of the implementation: the trial function, the propagator, and the update method(s). The double well system presents challenges that make these choices particularly important:

1. The symmetry of the double well creates a relatively small energy gap between the ground state and the first excited state, which means that it takes a long amount of imaginary time to decay the trial function to the ground state. More imaginary time means more slices and therefore longer simulation times to get useful results, which quickly becomes prohibitive. A higher-order propagator and better trial function can help to mitigate this challenge.

2. A strong double well barrier makes it difficult to move particles from one side to the other, which can spoil ergodicity by making if difficult to transition from configurations with a certain number of particles on one side of the barrier to configurations with a different number. This problem is serious when calculating the squeezing parameter and the OBDM, both of which require good sampling of different number configurations. Therefore, we must choose path update methods that address this issue.

Below we describe computational details regarding the trial function, the propagator, and the update methods, with explicit consideration of mitigating these challenges.

**Floating point errors** Additionally, we comment here on a general technique that we use to avoid floating point errors in our computations. Double precision floating point numbers in Fortran 90 can store values between $10^{-308}$ and $10^{308}$. Notice that the form of the probability distribution (5.20) is a product of about $M$ numbers that are all less than one. Even if they were each as large as 0.1, the computation of $\pi(X)$ can easily overwhelm the precision of Fortran's floats because the number of slices $M$ can be as high as several thousand.

To solve this problem, $\pi(X)$ is computed in terms of the sum of the natural logarithm of these small numbers:

$$\ln \pi(X) = \ln \psi_T^*(R_0) + \ln \psi_T(R_{2M}) + \sum_{i=0}^{2M-1} \ln G(R_i, R_{i+1}, \beta). \tag{5.21}$$

In fact, all similar quantities in the PIGS algorithm are computed in this way. This is helpful because the natural logarithm of a number of size $10^b$ has size $b$:

$$\ln(a10^b) = \ln a + b \ln 10, \tag{5.22}$$

so therefore floats in Fortran can easily support the addition and subtraction of the logarithms of many very small numbers without incurring floating point errors. The logarithm can always be exponentiated if needed. For example, in the Metropolis acceptance probability (5.19), we use

$$\frac{\pi(X_2)}{\pi(X_1)} = e^{\ln \pi(X_2) - \ln \pi(X_1)}. \tag{5.23}$$

### 5.3.1 Trial Function

Any trial function used in the PIGS algorithm will eventually converge to the ground state as long as it has nonzero overlap with the ground state. Of course, the closer it is to the ground state to begin with, the fewer imaginary time slices are necessary for this convergence to happen. In the noninteracting case, the exact ground state is simply a product of the single particle ground states for each particle:

$$\Psi_{gs}(R) = \prod_{i=1}^{N} \psi_g(\mathbf{r}_i) \qquad (a = 0), \tag{5.24}$$

where $\psi_g(\mathbf{r}_i) = \chi_0(x_i)\chi_0(y_i)\phi_0(z_i)$, a product of the analytical harmonic oscillator ground state wavefunction in the $x$ and $y$ directions and a numerically calculated one-dimensional double well ground state wave function in the $z$ direction. To take into account interactions, we include pair correlation (Jastrow) terms of the form $1 - a/r_{ij}$ in our trial function:

$$\psi_T(R) = \prod_{i=1}^{N} \psi_g(\mathbf{r}_i) \prod_{j<k}^{N} \left(1 - \frac{a}{r_{jk}}\right), \tag{5.25}$$

where $r_{ij} = |\mathbf{r}_i - \mathbf{r}_j|$. This pair correlation function is the exact zero-energy $s$-wave scattering solution for two hard spheres of diameter $a$ [79].

As we stated, the ground state wavefunction of the 1D double well potential must be computed numerically. We do this using a shooting method [92, Section 18.1] in Mathematica, which computes the wavefunction for $|z| \leq z_c$, where $z_c$ is a cutoff chosen so that the wavefunction is close to zero there. This method proceeds by numerically solving the Shrödinger equation over the interval $|z| \leq z_c$ as an initial value problem with $\psi(-z_c) = 0$ and $\psi'(-z_c) = 1$. Of course, we do not know the correct eigenenergies in advance. Instead, we think of the energy $\epsilon$ in the Shrödinger equation as a parameter that can be varied, so that the wavefunction is a function of both $z$ and $\epsilon$. The eigenenergies and eigenstates are then the ones for which $\psi(z_c, \epsilon) = 0$. For $|z| > z_c$, we set the wavefunction equal to $e^{A+Bz+Cz^2+Dz^3}$, with the coefficients of the cubic polynomial chosen so that the wavefunction is continuous at $z_c$ and has continuous first, second, and third derivatives there. This ensures that the Laplacian of the trial function, which must be computed to evaluate the local energy, is smooth at $z_c$.

#### Computing the Local Energy

Recall that the local energy (5.10) depends on the trial function and on the Hamiltonian, which we can write as

$$\hat{H} = -\lambda \nabla_R^2 + V(R), \tag{5.26}$$

where $\lambda = \hbar^2/2m$, $\nabla_R = \sum_{i=1}^{N} \boldsymbol{\nabla}_i = \sum_{i=1}^{N} (\partial_{x_i}\mathbf{x}_i + \partial_{y_i}\mathbf{y}_i + \partial_{z_i}\mathbf{z}_i)$, and $V(R)$ contains all of the external and interaction potential terms. In order to avoid floating point errors, our

PIGS code does its computations using the natural logarithm of quantities like $\psi_T(R)$ and its derivatives:

$$\begin{aligned}
\ln\psi_T(R) &= \sum_{i=1}^{N}\ln\psi_g(\mathbf{r}_i) + \sum_{j<k}^{N}\ln\left(1-\frac{a}{r_{jk}}\right) \\
&= \sum_{i=1}^{N}\left(-\ln(\sqrt{\pi}a_{ho}) - \frac{1}{2a_{ho}^2}(x_i^2+y_i^2) + \ln\phi_0(z_i)\right) + \sum_{j<k}^{N}\ln\left(1-\frac{a}{r_{jk}}\right) \quad (5.27a)\\
\nabla_R\ln\psi_T(R) &= \sum_{i=1}^{N}\left(-\frac{1}{a_{ho}^2}(x_i\,\mathbf{x}_i + y_i\,\mathbf{y}_i) + \frac{d}{dz_i}\ln\phi_0(z_i)\,\mathbf{z}_i\right) + \sum_{j<k}^{N}(\boldsymbol{\nabla}_j+\boldsymbol{\nabla}_k)\ln\left(1-\frac{a}{r_{jk}}\right) \\
&= \sum_{i=1}^{N}\left(-\frac{1}{a_{ho}^2}(x_i\,\mathbf{x}_i + y_i\,\mathbf{y}_i) + \frac{d}{dz_i}\ln\phi_0(z_i)\,\mathbf{z}_i\right) \quad (5.27b)\\
\nabla_R^2\ln\psi_T(R) &= \sum_{i=1}^{N}\left(-\frac{2}{a_{ho}^2} + \frac{d^2}{dz_i^2}\ln\phi_0(z_i)\right) + \sum_{j<k}^{N}(\nabla_j^2+\nabla_k^2)\ln\left(1-\frac{a}{r_{jk}}\right) \\
&= -\frac{2N}{a_{ho}^2} + \sum_{i=1}^{N}\frac{d^2}{dz_i^2}\ln\phi_0(z_i) - 2a^2\sum_{j<k}^{N}\frac{1}{(r_{jk}-a)^2 r_{jk}^2}. \quad (5.27c)
\end{aligned}$$

These quantities and the helpful vector calculus relations

$$\nabla_R\ln f = \frac{\nabla_R f}{f} \quad (5.28a)$$

$$\nabla_R^2\ln f = \frac{\nabla_R^2 f}{f} - \frac{|\nabla_R f|^2}{f^2}, \quad (5.28b)$$

allow for the explicit calculation of an expression for the local energy:

$$\begin{aligned}
E_L(R) &= -\lambda\frac{\nabla_R^2\psi_T(R)}{\psi_T(R)} + V(R) \\
&= -\lambda\left(\nabla_R^2\ln\psi_T(R) + |\nabla_R\ln\psi_T(R)|^2\right) + V(R) \\
&= -\lambda\left(-\frac{2N}{a_{ho}^2} + \sum_{i=1}^{N}\left(-\frac{x_i^2+y_i^2}{a_{ho}^4} + \frac{\phi_0''(z_i)}{\phi_0(z_i)}\right) - 2a^2\sum_{j<k}^{N}\frac{1}{(r_{jk}-a)^2 r_{jk}^2}\right) + V(R). \quad (5.29)
\end{aligned}$$

### 5.3.2 Propagator Decomposition

As noted earlier, it is in general not possible to write the imaginary time propagator $G(R_i, R_{i+1}, \beta) = \langle R_i|e^{-\beta\hat{H}/\hbar}|R_{i+1}\rangle$ analytically, with the exception of a few cases for which the exact solution is known. In the absence of an exact solution, one can approximately evaluate the propagator by using operator algebra to express the exponential of the Hamiltonian in

terms of exponentials of the kinetic and potential parts of the Hamiltonian. Because these generally do not commute with each other, this method does not usually allow for an analytic form for the propagator. However, if $\beta \ll 1$ then we may write the propagator in a form that can indeed be evaluated analytically when terms proportional to higher powers of $\beta$ are ignored. For our short-time propagator, we use a fourth-order propagator decomposition for the external potential and modify the free particle part of the propagator to incorporate the hard sphere interaction.

### External Potential

First, we would like to take care of the external potential part of the propagator. In general, we want to use a propagator expansion that gives accurate results for as large a value of $\beta$ as possible, because for a fixed amount of imaginary time, larger $\beta$ means fewer time slices and therefore less computational time needed to get results.

The simplest propagator expansion that one can make to split off the external potential is the *Trotter approximation* [93], which is accurate to first order in $\beta$:

$$e^{-\beta(\hat{T}+\hat{V})} = e^{-\beta\hat{T}}e^{-\beta\hat{V}} + \mathcal{O}(\beta^2). \tag{5.30}$$

Here $\hat{T}$ and $\hat{V}$ can be any operators, but we will think of them for now as the usual kinetic and potential energy operators of the system. There is a simple modification of the Trotter approximation that produces an expression accurate to second order in $\beta$:

$$e^{-\beta(\hat{T}+\hat{V})} = e^{-\frac{\beta}{2}\hat{V}}e^{-\beta\hat{T}}e^{-\frac{\beta}{2}\hat{V}} + \mathcal{O}(\beta^3). \tag{5.31}$$

A more complex expansion due to Chin [88, 89] is accurate to fourth order in $\beta$:

$$e^{-\beta(\hat{T}+\hat{V})} = e^{-\frac{\beta}{6}\hat{V}}e^{-\frac{\beta}{2}\hat{T}}e^{-\frac{2\beta}{3}\hat{V}_C}e^{-\frac{\beta}{2}\hat{T}}e^{-\frac{\beta}{6}\hat{V}} + \mathcal{O}(\beta^5), \tag{5.32}$$

where

$$\hat{V}_C = \hat{V} + \frac{\beta^2}{48}[\hat{V},[\hat{T},\hat{V}]]. \tag{5.33}$$

We can evaluate this expression by making use of a test function $f(R)$:

$$\begin{aligned}
[\hat{T},\hat{V}] &= \hat{T}\hat{V}f - \hat{V}\hat{T}f \\
&= -\lambda(\nabla^2(Vf) - V\nabla^2 f) \\
&= -\lambda(\nabla\cdot(V\nabla f + f\nabla]V) - V\nabla^2 f) \\
&= -\lambda(2\nabla V\cdot\nabla f + f\nabla^2 V) \\
&= -\lambda(2\nabla V\cdot\nabla + \nabla^2 V)f,
\end{aligned} \tag{5.34}$$

and hence

$$\begin{aligned}
[\hat{V},[\hat{T},\hat{V}]]f &= \hat{V}[\hat{T},\hat{V}]f - [\hat{T},\hat{V}]\hat{V}f \\
&= -\lambda(2V\nabla V\cdot\nabla f + Vf\nabla^2 V - 2\nabla V\cdot\nabla(Vf) - Vf\nabla^2 V) \\
&= -\lambda(-2f|\nabla V|^2) \\
&= 2\lambda|\nabla V|^2 f.
\end{aligned} \tag{5.35}$$

Therefore, we have

$$V_C(R) = V(R) + \frac{\lambda}{24}\beta^2|\nabla_R V(R)|^2. \tag{5.36}$$

We use the Chin propagator in our simulations because it is accurate enough for our purposes without introducing too much complexity.

One important subtlety to consider in implementing the Chin propagator is how to implement the hard sphere interaction potential $\hat{V}_{hs}$. Naively, one might choose to include it in $\hat{V}$ together with $\hat{V}_{ext}$, but this would require taking the gradient of the hard sphere potential (2.18), which produces a singularity. Instead, we choose to group it with the kinetic part of the Hamiltonian by replacing $\hat{T}$ with $\hat{T} + \hat{V}_{hs}$ and treating $\hat{V}$ as strictly the external potential in the above expressions. This allows us to trivially evaluate the commutator term in $\hat{V}_C$ (Eq. (5.33)), because $\hat{V}_{hs}$ and $\hat{V}_{ext}$, as functions of position only, commute with each other:

$$\begin{aligned}
\hat{V}_C &= \hat{V}_{ext} + \frac{\beta^2}{48}[\hat{V_{ext}}, [\hat{T} + \hat{V}_{hs}, \hat{V}_{ext}]] \\
&= \hat{V}_{ext} + \frac{\beta^2}{48}[\hat{V}_{ext}, [\hat{T}, \hat{V}_{ext}] + [\hat{V}_{hs}, \hat{V}_{ext}]] \\
&= \hat{V}_{ext} + \frac{\beta^2}{48}[\hat{V}_{ext}, [\hat{T}, \hat{V}_{ext}]].
\end{aligned} \tag{5.37}$$

With that, we can use the Chin decomposition to rewrite the propagator:

$$\begin{aligned}
G(R_i, R_{i+1}, \beta) &\approx \langle R_i|e^{-\frac{\beta}{6\hbar}\hat{V}}e^{-\frac{\beta}{2\hbar}(\hat{T}+\hat{V}_{hs})}e^{-\frac{2\beta}{3\hbar}\hat{V}_C}e^{-\frac{\beta}{2\hbar}(\hat{T}+\hat{V}_{hs})}e^{-\frac{\beta}{6\hbar}\hat{V}}|R_{i+1}\rangle \\
&= e^{-\frac{\beta}{6\hbar}V(R_i)}\,\langle R_i|e^{-\frac{\beta}{2\hbar}(\hat{T}+\hat{V}_{hs})}e^{-\frac{2\beta}{3\hbar}\hat{V}_C}e^{-\frac{\beta}{2\hbar}(\hat{T}+\hat{V}_{hs})}|R_{i+1}\rangle\, e^{-\frac{\beta}{6\hbar}V(R_{i+1})} \\
&= e^{-\frac{\beta}{6\hbar}(V(R_i)+4V_C(R_j)+V(R_{i+1}))}\int \langle R_i|e^{-\frac{\beta}{2\hbar}(\hat{T}+\hat{V}_{hs})}|R_j\rangle\,\langle R_j|e^{-\frac{\beta}{2\hbar}(\hat{T}+\hat{V}_{hs})}|R_{i+1}\rangle\, dR_j \\
&= e^{-\frac{\beta}{6\hbar}(V(R_i)+4V_C(R_j)+V(R_{i+1}))}\int G_{hs}(R_i, R_j, \beta/2)G_{hs}(R_j, R_{i+1}, \beta/2)\, dR_j,
\end{aligned} \tag{5.38}$$

where $G_{hs}(R_i, R_{i+1}, \beta)$ is propagator for $N$ hard spheres without an external potential. By using this factorization, we have introduced a new configuration $R_j$ between each pair of original configurations $R_i$ and $R_{i+1}$, so that there are now $4M + 1$ configurations instead of $2M+1$. Treating all of these on equal footing, we can rewrite the probability distribution (5.20) as

$$\pi(X) = \psi_T^*(R_0)\psi_T(R_{4M})e^{\frac{1}{6\hbar}\beta(V(R_0)-V(R_{4M}))}\prod_{i=0}^{4M-1} f(R_i)\, G_{hs}(R_i, R_{i+1}, \beta/2), \tag{5.39}$$

where

$$f(R_i) = \begin{cases} e^{-\frac{1}{3\hbar}\beta V(R_i)} & i = 0, 2, 4, \ldots \\ e^{-\frac{2}{3\hbar}\beta V(R_i) - \frac{1}{36\hbar^3}\lambda\beta^3|\nabla V(R_i)|^2} & i = 1, 3, 5, \ldots \end{cases}. \tag{5.40}$$

We can simplify notation by redefining $M$ as the total number of slices (keeping in mind that this must equal an integer of the form $4n+1$) and making the replacement $\beta/2 \to \beta$. Then we have

$$\pi(X) = \psi_T^*(R_0)\psi_T(R_M)e^{\frac{1}{3\hbar}\beta(V_{dw}(R_0)-V_{dw}(R_M))}\prod_{i=0}^{M-1} f(R_i)G_{hs}(R_i, R_{i+1}, \beta), \tag{5.41}$$

where

$$f(R_i) = \begin{cases} e^{-\frac{2}{3\hbar}\beta V(R_i)} & i = 0, 2, 4, \ldots \\ e^{-\frac{4}{3\hbar}\beta V(R_i) - \frac{2}{9\hbar^3}\lambda\beta^3|\nabla V(R_i)|^2} & i = 1, 3, 5, \ldots \end{cases}. \tag{5.42}$$

**Hard sphere propagator**

The final step in decomposing the propagator is to find an expression for $G_{hs}(R_i, R_{i+1}, \beta)$. Several methods have been proposed in the literature for approximating the two-body hard sphere propagator, including the image approximation [94, 95]

$$G_{image}(R, R', \beta) = G_{free}(R, R', \beta)\left(1 - e^{-\frac{\hbar(r-a)(r'-a)}{2\beta\lambda}}\right), \tag{5.43}$$

and the propagator of Cao and Berne [90]

$$G_{CB}(R, R', \beta) = G_{free}(R, R', \beta)\left(1 - \left(1 - \frac{(r-a)(r'-a)}{rr'}\right)e^{-\frac{\hbar(r-a)(r'-a)(1+\cos\gamma)}{2\beta\lambda}}\right), \tag{5.44}$$

where $r = |\mathbf{r}_1 - \mathbf{r}_2|$ is the separation between the atoms and $\gamma$ is the angle between $\mathbf{r}_1$ and $\mathbf{r}_2$. One important feature of a good hard sphere propagator is that it should equal the propagator for free particles in the $a \to 0$ limit. The image approximation does not have this behavior, so we will not consider it further.

It is also possible to express the hard sphere propagator exactly [96], although we had to invent and implement a trick to make it practical for our system, as we will discuss below. One critical consideration for choosing a propagator is that we want to be able to use an imaginary time step that is as large as possible without spoiling the accuracy of the propagator. We ultimately chose to implement the exact hard sphere propagator because it allows for larger time steps than the Cao and Berne propagator (e.g., $10^{-2}\,\omega_{ho}^{-1}$ compared to $10^{-4}\,\omega_{ho}^{-1}$ for equivalent results).

We will build up to the final result of the hard sphere propagator for $N$ atoms by describing the propagators for two free particles and two hard spheres in particle and center-of-mass coordinates, which are necessary for constructing the $N$-body hard sphere propagator.

**Two free particles** First, we consider the case of two free particles, where $\hat{H} = \hat{T}$, $R = \{\mathbf{r}_1, \mathbf{r}_2\}$, and $P = \{\mathbf{p}_1, \mathbf{p}_2\}$. Recall that a momentum eigenstate in the position basis is given by

$$\langle \mathbf{r}|\mathbf{p}\rangle = \frac{1}{(2\pi\hbar)^{3/2}}e^{\frac{i}{\hbar}\mathbf{p}\cdot\mathbf{r}}. \tag{5.45}$$

With that result, we can calculate $G_{free}(\mathbf{r}_i, \mathbf{r}_{i+1}, \beta)$ by inserting two complete sets of momentum eigenstates:

$$\begin{aligned} G_{free}(R_i, R_{i+1}, \beta) &= \langle R_i | e^{-\beta \hat{T}/\hbar} | R_{i+1} \rangle \\ &= \int \langle R_i | P_1 \rangle \langle P_1 | e^{-\beta \hat{T}/\hbar} | P_2 \rangle \langle P_2 | R_{i+1} \rangle \, dP_1 dP_2 \\ &= \int \left( \frac{1}{(2\pi\hbar)^3} e^{\frac{i}{\hbar} P_1 \cdot R_i} \right) \left( \delta(P_1 - P_2) e^{-\frac{P_2^2}{2m\hbar}\beta} \right) \left( \frac{1}{(2\pi\hbar)^3} e^{-\frac{i}{\hbar} P_2 \cdot R_{i+1}} \right) dP_1 dP_2 \\ &= \frac{1}{(2\pi\hbar)^6} \int e^{-\frac{P_2^2}{2m\hbar}\beta - \frac{i}{\hbar} P_2 \cdot (R_{i+1} - R_i)} \, dP_2 \\ &= \left( \frac{\hbar}{4\pi\beta\lambda} \right)^3 e^{-\frac{\hbar (R_i - R_{i+1})^2}{4\beta\lambda}}, \end{aligned} \tag{5.46}$$

where, again, $\lambda = \hbar^2/2m$.

**Two interacting particles in center of mass coordinates** Now we consider the case of two particles interacting with a potential $V_{int}(\mathbf{r}_1 - \mathbf{r}_2)$. In order to write the propagator for this case, it is helpful to define position and momentum operators in center of mass coordinates:

$$\hat{r}_{cm} = \frac{1}{2}(\hat{r}_1 + \hat{r}_2) \tag{5.47a}$$
$$\hat{r}_{rel} = \hat{r}_1 - \hat{r}_2 \tag{5.47b}$$
$$\hat{p}_{cm} = \hat{p}_1 + \hat{p}_2 \tag{5.47c}$$
$$\hat{p}_{rel} = \frac{1}{2}(\hat{p}_1 - \hat{p}_2). \tag{5.47d}$$

One can readily confirm that this choice of operators leads to the following properties:

$$[\hat{r}_{cm}, \hat{p}_{cm}] = i\hbar \tag{5.48a}$$
$$[\hat{r}_{rel}, \hat{p}_{rel}] = i\hbar \tag{5.48b}$$
$$[\hat{r}_{rel}, \hat{p}_{cm}] = 0 \tag{5.48c}$$
$$[\hat{r}_{cm}, \hat{p}_{rel}] = 0, \tag{5.48d}$$

and

$$\hat{p}_{cm} = \hat{p}_1 + \hat{p}_2 = -i\hbar \left( \frac{\partial}{\partial r_1} + \frac{\partial}{\partial r_2} \right) = -i\hbar \frac{\partial}{\partial r_{cm}} \tag{5.49a}$$
$$\hat{p}_{rel} = \frac{1}{2}(\hat{p}_1 - \hat{p}_2) = -i\hbar \frac{1}{2} \left( \frac{\partial}{\partial r_1} - \frac{\partial}{\partial r_2} \right) = -i\hbar \frac{\partial}{\partial r_{rel}}. \tag{5.49b}$$

Hence, the new operators (5.47) behave in the same way as the usual position and momentum operators for individual particles. We are therefore justified in treating them as we would individual particle operators in calculations, and we can use them to define new coordinates:

$$\hat{r}_{cm}\,|\mathbf{r}_1,\mathbf{r}_2\rangle = \frac{1}{2}(\mathbf{r}_1+\mathbf{r}_2)\,|\mathbf{r}_1,\mathbf{r}_2\rangle = \mathbf{r}_{cm}\,|\mathbf{r}_1,\mathbf{r}_2\rangle \tag{5.50a}$$

$$\hat{r}_{rel}\,|\mathbf{r}_1,\mathbf{r}_2\rangle = (\mathbf{r}_1-\mathbf{r}_2)\,|\mathbf{r}_1,\mathbf{r}_2\rangle = \mathbf{r}_{rel}\,|\mathbf{r}_1,\mathbf{r}_2\rangle \tag{5.50b}$$

$$\hat{p}_{cm}\,|\mathbf{p}_1,\mathbf{p}_2\rangle = (\mathbf{p}_1+\mathbf{p}_2)\,|\mathbf{p}_1,\mathbf{p}_2\rangle = \mathbf{p}_{cm}\,|\mathbf{p}_1,\mathbf{p}_2\rangle \tag{5.50c}$$

$$\hat{p}_{rel}\,|\mathbf{p}_1,\mathbf{p}_2\rangle = \frac{1}{2}(\mathbf{p}_1-\mathbf{p}_2)\,|\mathbf{p}_1,\mathbf{p}_2\rangle = \mathbf{p}_{rel}\,|\mathbf{p}_1,\mathbf{p}_2\rangle \tag{5.50d}$$

With this coordinate transformation, we can rewrite the 2-body interacting Hamiltonian in terms of a free particle of mass $2m$ with position $\mathbf{r}_{cm}$ and momentum $\mathbf{p}_{cm}$ and a (non-free) particle of mass $m/2$ with position $\mathbf{r}_{rel}$ and momentum $\mathbf{p}_{rel}$:

$$\begin{aligned}\hat{H} &= \frac{1}{2m}\left(\hat{p}_1^2+\hat{p}_2^2\right)+V_{int}(\hat{r}_1-\hat{r}_2)\\ &= \frac{1}{4m}\hat{p}_{cm}^2+\left(\frac{1}{m}\hat{p}_{rel}^2+V_{int}(\hat{r}_{rel})\right)\\ &= \hat{H}_{cm}+\hat{H}_{rel}.\end{aligned} \tag{5.51}$$

Because of the commutation relations (5.48), we know that

$$e^{\hat{H}} = e^{\hat{H}_{cm}+\hat{H}_{rel}} = e^{\hat{H}_{cm}}e^{\hat{H}_{rel}}. \tag{5.52}$$

This allows us to express the propagator in a nice form:

$$\begin{aligned}G_{int}(R,R',\beta) &= \langle R|e^{-\beta\hat{H}/\hbar}|R'\rangle\\ &= \langle \mathbf{r}_{cm},\mathbf{r}_{rel}|e^{-\beta\hat{H}_{cm}/\hbar}e^{-\beta\hat{H}_{rel}/\hbar}|\mathbf{r}'_{cm},\mathbf{r}'_{rel}\rangle\\ &= \langle \mathbf{r}_{cm}|e^{-\beta\hat{H}_{cm}/\hbar}|\mathbf{r}'_{cm}\rangle\,\langle \mathbf{r}_{rel}|e^{-\beta\hat{H}_{rel}/\hbar}|\mathbf{r}'_{rel}\rangle\\ &= G_{free}^{2m}(\mathbf{r}_{cm},\mathbf{r}'_{cm},\beta)\,G_{int}^{m/2}(\mathbf{r}_{rel},\mathbf{r}'_{rel},\beta)\\ &= \left(\frac{\hbar}{2\pi\beta\lambda}\right)^{\frac{3}{2}}e^{-\frac{\hbar(\mathbf{r}_{cm}-\mathbf{r}'_{cm})^2}{2\beta\lambda}}G_{int}^{m/2}(\mathbf{r}_{rel},\mathbf{r}'_{rel},\beta),\end{aligned} \tag{5.53}$$

where the superscript on $G$ indicates the effective mass for the propagator. Because the center-of-mass part of the propagator is known, all we need to finish this computation is the relative-motion part of the propagator.

**Two free particles in center of mass coordinates** We will return briefly to the free particle case to compute it in center of mass coordinates. One method of doing this is obvious:

$$\begin{aligned} G_{free}(R,R',\beta) &= \left(\frac{\hbar}{2\pi\beta\lambda}\right)^{\frac{3}{2}} e^{-\frac{\hbar(\mathbf{r}_{cm}-\mathbf{r}'_{cm})^2}{2\beta\lambda}} G^{m/2}_{free}(\mathbf{r}_{rel},\mathbf{r}'_{rel},\beta) \\ &= \left(\frac{\hbar}{2\pi\beta\lambda}\right)^{\frac{3}{2}} e^{-\frac{\hbar(\mathbf{r}_{cm}-\mathbf{r}'_{cm})^2}{2\beta\lambda}} \left(\frac{\hbar}{8\pi\beta\lambda}\right)^{\frac{3}{2}} e^{-\frac{\hbar(\mathbf{r}_{rel}-\mathbf{r}'_{rel})^2}{8\beta\lambda}} \\ &= \left(\frac{\hbar}{4\pi\beta\lambda}\right)^{3} e^{-\frac{\hbar}{4\beta\lambda}\left(2(\mathbf{r}_{cm}-\mathbf{r}'_{cm})^2+\frac{1}{2}(\mathbf{r}_{rel}-\mathbf{r}'_{rel})^2\right)} \\ &= \left(\frac{\hbar}{4\pi\beta\lambda}\right)^{3} e^{-\frac{\hbar((\mathbf{r}_1-\mathbf{r}'_1)^2+(\mathbf{r}_2-\mathbf{r}'_2)^2)}{4\beta\lambda}}, \end{aligned} \tag{5.54}$$

which agrees with Eq. (5.46).

It is also possible, and useful, to evaluate the relative-motion part of the free propagator in spherical coordinates. To do so, we define $\mathbf{k} = \mathbf{p}_{rel}/\hbar$ so that the integration measure $d\mathbf{p}_{rel}$ becomes $\hbar^3 k^2 \sin\theta dk\, d\theta\, d\phi$. We also make use of the identity

$$e^{-i\mathbf{k}\cdot\mathbf{r}} = \sum_{l=0}^{\infty} (-i)^l (2l+1) j_l(kr) P_l(\cos\alpha), \tag{5.55}$$

where $P_l(x)$ is a Legendre polynomial, $j_l(x)$ is the spherical Bessel function of the first kind, and $\alpha$ is the angle between $\mathbf{k}$ and $\mathbf{r}$. We find

$$\begin{aligned} G^{m/2}_{free}(\mathbf{r}_{rel},\mathbf{r}'_{rel},\beta) &= \frac{1}{(2\pi\hbar)^3}\int e^{-\beta\frac{\mathbf{p}^2_{rel}}{m\hbar}} e^{-i\frac{\mathbf{p}_{rel}}{\hbar}\cdot(\mathbf{r}_{rel}-\mathbf{r}'_{rel})}\, d\mathbf{p}_{rel} \\ &= \frac{1}{(2\pi)^3}\int e^{-\beta\frac{\hbar k^2}{m}} e^{-i\mathbf{k}\cdot(\mathbf{r}_{rel}-\mathbf{r}'_{rel})}\, k^2 \sin\theta\, dk\, d\theta\, d\phi \\ &= \frac{1}{(2\pi)^3}\int e^{-\beta\frac{\hbar k^2}{m}} \sum_{l=0}^{\infty}(-i)^l(2l+1) j_l(kr_{rel}) P_l(\cos\alpha) \\ &\quad \times \sum_{n=0}^{\infty} i^n (2n+1) j_n(kr'_{rel}) P_n(\cos\alpha')\, k^2 \sin\theta\, dk\, d\theta\, d\phi \\ &= \frac{1}{(2\pi)^3}\sum_{l=0}^{\infty}\sum_{n=0}^{\infty}(-1)^l (i)^{l+n}(2l+1)(2n+1) \\ &\quad \times \int_0^{\infty} k^2 e^{-\beta\frac{\hbar^2k^2}{m}} j_l(kr_{rel}) j_n(kr'_{rel})\, dk \\ &\quad \times \int_0^{\pi}\int_0^{2\pi} \sin\theta P_l(\cos\alpha) P_n(\cos\alpha')\, d\phi\, d\theta. \end{aligned} \tag{5.56}$$

The angular integral may be evaluated by rotating the coordinate system such that $\mathbf{r}_{rel}$ lies in the positive $z$-direction and $\mathbf{r}'_{rel}$ lies in the $xz$-plane with an angle $\gamma$ between them. In that

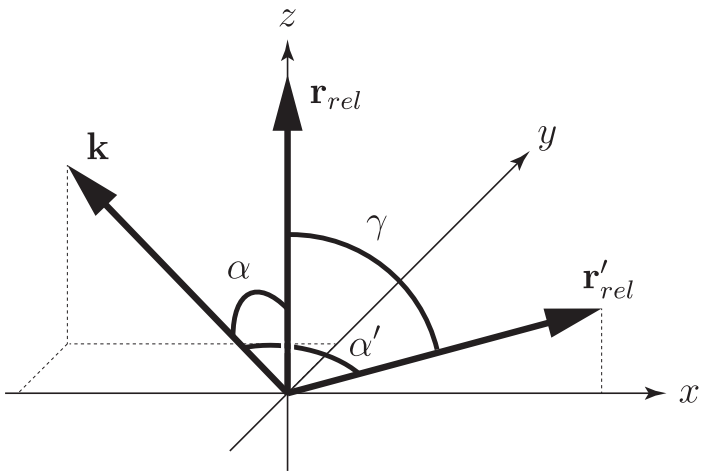


Figure 5.1: The geometry of the vectors necessary to compute the angular integral in the expression for $G^{m/2}_{free}(\mathbf{r}_{rel}, \mathbf{r}'_{rel}, \beta)$. For convenience, we choose $\mathbf{r}_{rel}$ to lie along the $z$-axis and $\mathbf{r}'_{rel}$ to lie in the $xz$-plane.

case, $\mathbf{r}_{rel} = r_{rel}\hat{z}$, $\mathbf{r}'_{rel} = r'_{rel}(\sin\gamma\,\hat{x} + \cos\gamma\,\hat{z})$, and $\mathbf{k} = k(\sin\theta\cos\phi\,\hat{x} + \sin\theta\sin\phi\,\hat{y} + \cos\theta\,\hat{z})$; see Figure 5.1. We can then compute

$$\cos\alpha = \frac{\mathbf{r}_{rel}\cdot\mathbf{k}}{r_{rel}\,k} = \cos\theta \tag{5.57a}$$

$$\cos\alpha' = \frac{\mathbf{r}'_{rel}\cdot\mathbf{k}}{r'_{rel}\,k} = \sin\gamma\sin\theta\cos\phi + \cos\gamma\cos\theta, \tag{5.57b}$$

and the angular integral becomes

$$\int_0^{\pi}\int_0^{2\pi} \sin\theta P_l(\cos\theta)P_n(\sin\gamma\sin\theta\cos\phi + \cos\gamma\cos\theta)\,d\phi\,d\theta = \frac{4\pi}{2l+1}P_l(\cos\gamma)\delta_{ln}. \tag{5.58}$$

Upon substituting this result into $G^{m/2}_{free}$, we find

$$G^{m/2}_{free}(\mathbf{r}_{rel}, \mathbf{r}'_{rel}, \beta) = \frac{1}{2\pi^2}\sum_{l=0}^{\infty} P_l(\cos\gamma)(2l+1)\left(\int_0^{\infty} k^2 e^{-\beta\frac{\hbar k^2}{m}} j_l(kr_{rel})j_l(kr'_{rel})\,dk\right). \tag{5.59}$$

This expression will become useful when we treat the case of two hard spheres.

**Two hard spheres in center of mass coordinates** We now move on to the case of two hard spheres. The exact propagator for two hard spheres can be written in spherical coordinates in form very similar to $G^{m/2}_{free}(\mathbf{r}_{rel}, \mathbf{r}'_{rel}, \beta)$ [96]:

$$G^{m/2}_{hs}(\mathbf{r}_{rel}, \mathbf{r}'_{rel}, \beta) = \frac{1}{2\pi^2}\sum_{l=0}^{\infty} P_l(\cos\gamma)(2l+1)\left(\int_0^{\infty} k^2 e^{-\beta\frac{\hbar k^2}{m}} \frac{R_l(r_{rel},k)R_l(r'_{rel},k)}{D_l(k)}\,dk\right), \tag{5.60}$$

where

$$R_l(r,k) = j_l(kr)y_l(ka) - y_l(kr)j_l(ka) \tag{5.61a}$$
$$D_l(k) = j_l^2(ka) + y_l^2(ka), \tag{5.61b}$$

$a$ is the hard sphere diameter, and $y_l(x)$ is the spherical Bessel function of the second kind. Unfortunately, this expression cannot be rewritten in a convenient analytical form. To use it, we must terminate the sum at some appropriate $l_{max}$ and tabulate it as a function of $r_{rel}^i$, $r_{rel}^{i+1}$, and $\gamma$. We'd like for $l_{max}$ to be as small as possible.

One interesting observation about $G_{hs}^{m/2}(\mathbf{r}_{rel}, \mathbf{r}'_{rel}, \beta)$ is that it has the same form as $G_{free}^{m/2}(\mathbf{r}_{rel}, \mathbf{r}'_{rel}, \beta)$, apart from the form of the argument of the integral; in fact, they become equal in the $a \to 0$ limit. This observation is useful because the *difference* between $G_{hs}^{m/2}$ and $G_{free}^{m/2}$ converges with respect to $l_{max}$ much faster than $G_{hs}^{m/2}$ alone. To see that, we make the following transformation:

$$\begin{aligned}
G_{hs}^{m}(R,R',\beta) &= G_{free}^{m}(R,R',\beta)\frac{G_{hs}^{m}(R,R',\beta)}{G_{free}^{m}(R,R',\beta)} \\
&= G_{free}^{m}(R,R',\beta)\frac{G_{free}^{2m}(\mathbf{r}_{cm},\mathbf{r}'_{cm},\beta)G_{hs}^{m/2}(\mathbf{r}_{rel},\mathbf{r}'_{rel},\beta)}{G_{free}^{2m}(\mathbf{r}_{cm},\mathbf{r}'_{cm},\beta)G_{free}^{m/2}(\mathbf{r}_{rel},\mathbf{r}'_{rel},\beta)} \\
&= G_{free}^{m}(R,R',\beta)\frac{G_{hs}^{m/2}(\mathbf{r}_{rel},\mathbf{r}'_{rel},\beta)}{G_{free}^{m/2}(\mathbf{r}_{rel},\mathbf{r}'_{rel},\beta)} \\
&= G_{free}^{m}(R,R',\beta)\frac{G_{free}^{m/2}(\mathbf{r}_{rel},\mathbf{r}'_{rel},\beta) - G_{free}^{m/2}(\mathbf{r}_{rel},\mathbf{r}'_{rel},\beta) + G_{hs}^{m/2}(\mathbf{r}_{rel},\mathbf{r}'_{rel},\beta)}{G_{free}^{m/2}(\mathbf{r}_{rel},\mathbf{r}'_{rel},\beta)} \\
&= G_{free}^{m}(R,R',\beta)\left(1 - \frac{G_{free}^{m/2}(\mathbf{r}_{rel},\mathbf{r}'_{rel},\beta) - G_{hs}^{m/2}(\mathbf{r}_{rel},\mathbf{r}'_{rel},\beta)}{G_{free}^{m/2}(\mathbf{r}_{rel},\mathbf{r}'_{rel},\beta)}\right) \\
&= G_{free}^{m}(R,R',\beta)\,\tilde{G}_{hs}^{m/2}(\mathbf{r}_{rel},\mathbf{r}'_{rel},\beta).
\end{aligned} \tag{5.62}$$

The new form of the hard sphere propagator, $\tilde{G}_{hs}^{m/2}$, can be written as

$$\begin{aligned}
\tilde{G}_{hs}^{m/2}(\mathbf{r}_{rel},\mathbf{r}'_{rel},\beta) &= 1 - \frac{G_{free}^{m/2}(\mathbf{r}_{rel},\mathbf{r}'_{rel},\beta) - G_{hs}^{m/2}(\mathbf{r}_{rel},\mathbf{r}'_{rel},\beta)}{G_{free}^{m/2}(\mathbf{r}_{rel},\mathbf{r}'_{rel},\beta)} \\
&= 1 - \frac{4}{\pi^{1/2}}\left(\frac{2\beta\lambda}{\hbar}\right)^{3/2} e^{\frac{\hbar(\mathbf{r}_{rel}-\mathbf{r}'_{rel})^2}{8\beta\lambda}} \sum_{l=0}^{\infty} P_l(\cos\gamma)(2l+1) \\
&\quad \times \int_0^\infty k^2 e^{-\frac{2\beta\lambda k^2}{\hbar}} A_l(k, r_{rel}, r'_{rel})\, dk,
\end{aligned} \tag{5.63}$$

where

$$A_l(k, r_{rel}, r'_{rel}) = j_l(kr_{rel})j_l(kr'_{rel}) - \frac{R_l(r_{rel},k)R_l(r'_{rel},k)}{D_l(k)}. \tag{5.64}$$

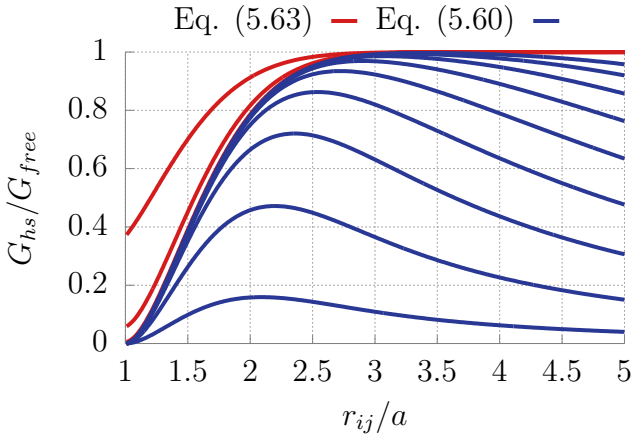


Figure 5.2: The ratio of the hard sphere propagator to the free propagator for $r_{jk}^i = r_{jk}^{i+1}$, $\gamma = 0$, and $a^2 = 2\beta\lambda/\hbar$. The blue curves are plots of $G_{hs}^{m/2}/G_{free}^{m/2}$ computed as in Eq. (5.60) for various $l_{max}$; the lowest blue curve has $l_{max} = 0$ and the highest $l_{max} = 8$. The red curves are plots of $\tilde{G}_{hs}^{m/2}$ computed as in Eq. (5.63) for various $l_{max}$; the highest red curve has $l_{max} = 0$ and the lowest $l_{max} = 8$ (although the curves from $l_{max} = 2$ through $l_{max} = 8$ are visually indistinguishable). The rapid convergence of $\tilde{G}_{hs}^{m/2}$ compared with $G_{hs}^{m/2}/G_{free}^{m/2}$ is a general feature of these functions.

Figure 5.2 compares $\tilde{G}_{hs}^{m/2}$ with $G_{hs}^{m/2}/G_{free}^{m/2}$. As we stated, $\tilde{G}_{hs}^{m/2}$ converges significantly faster. In fact, by using this form we can terminate the sum at an $l_{max}$ that is about 2 to 10 times smaller (depending on the value of $a$) than would be necessary to achieve the same precision using Eq. (5.60).

**$N$ Hard Spheres** We saw that for two hard spheres, we can write the propagator as

$$G_{hs}^m(R, R', \beta) = G_{free}^m(R, R', \beta)\, \tilde{G}_{hs}^{m/2}(\mathbf{r}_{rel}, \mathbf{r}'_{rel}, \beta). \tag{5.65}$$

In order to generalize this to $N$ hard spheres, we use the pair product approximation [94]:

$$G_{hs}^m(R_i, R_{i+1}, \beta) = G_{free}^m(R_i, R_{i+1}, \beta) \prod_{j<k}^{N} \tilde{G}_{hs}^{m/2}(r_{jk}^i, r_{jk}^{i+1}, \gamma, \beta). \tag{5.66}$$

Conceptually, in this approximation the propagator for $N$ hard spheres is given by the propagator for $N$ free particles modified by pairwise hard sphere interactions between each pair of atoms. Hence, by using this approximation we are assuming that three- and more-body interactions are negligible, which is consistent with assumption we made when defining the interactions in Section 2.2.

By combining Eqs. (5.41) and (5.66), we have completely defined the propagator, and therefore the probability distribution $\pi(X)$, for the system.

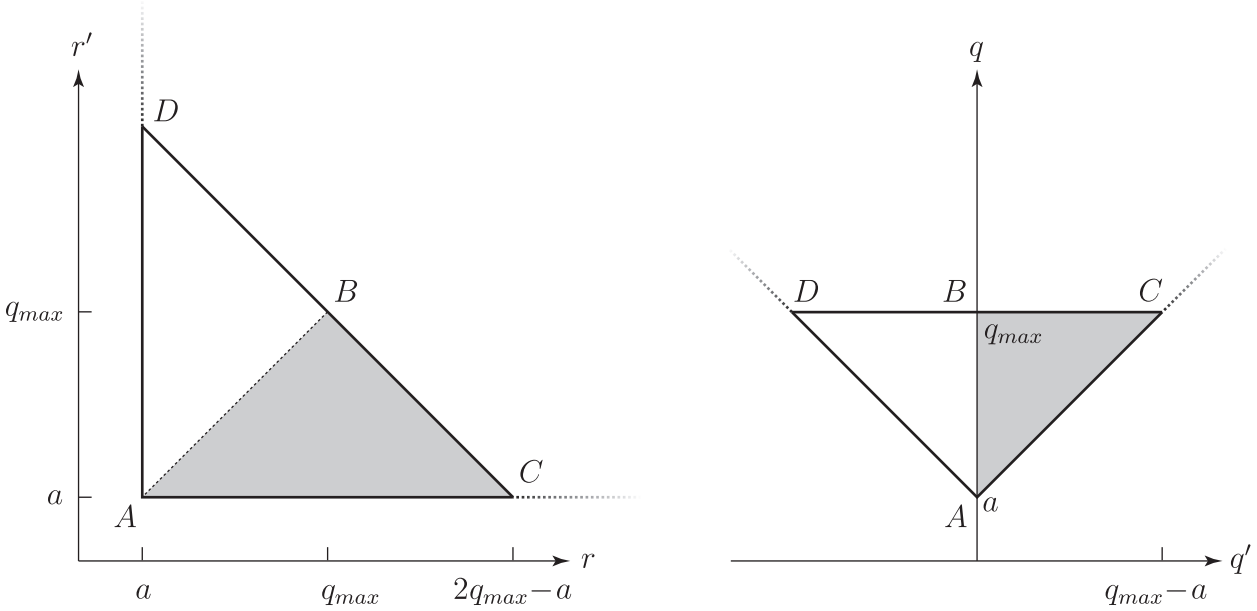


Figure 5.3: The region, in gray, for which $\tilde{G}_{hs}^{m/2}(r, r', \gamma, \beta)$ is tabulated, as a function of $q_{max}$, in both the plane defined by $r$ and $r'$ and the plane defined by $q = (r + r')/2$ and $q' = (r - r')/2$.

**Tabulating the propagator** Because the hard sphere propagator cannot be solved analytically, in order to use it we need to tabulate it as a function of $r$, $r'$, and $\gamma$. In practice, we tabulated it as a function of $q = (r + r')/2$, $q' = (r - r')/2$, and $\gamma$. We let $\gamma$ range from 0 to $\pi$ in increments of $\pi/24$, $q'$ range between 0 and $q - 1$ in increments of $0.05\,a$, and $q$ range between $a$ and $q_{max}$ in increments of $0.05\,a$. The choice of $q_{max}$ varied significantly based on the value of the dimensionless parameter $\alpha = 2\beta\lambda/\hbar a^2$, which controlled the stability of the integrals we were calculating. For the smallest $\alpha$ we used ($\alpha = 0.25$), we had $q_{max} = 3\,a$, while for the largest $\alpha$ ($\alpha = 6.25 \times 10^8$), we had $q_{max} = 15\,a$. See Figure 5.3 for a visual representation of these coordinates.

### 5.3.3 Update methods

There are a few general details related to the implementation of update methods that we will address before describing each method and its effectiveness in detail.

First, it is often useful to use update methods such that the probability of proposing a move from $X_i$ to $X_j$ is equal to the probability of proposing the reverse move: $\mathcal{P}(X_i \to X_j) = \mathcal{P}(X_j \to X_i)$. For example, for a single-particle update, $\mathcal{P}(X_i \to X_j) = e^{-(\mathbf{r}_i - \mathbf{r}_j)^2}$ satisfies this condition. By choosing an update method such that this condition is satisfied, we simplify the expression for the acceptance probability (5.19). This will be the case for the update methods we use.

**Ergodicity** As we discussed previously, any update method we choose must be ergodic, i.e., it must be able to generate any allowed configuration of the system. If this is not the case, then there is no way for the Metropolis algorithm to reproduce $\pi(X)$ correctly for any inaccessible configurations. However, an update method can be ergodic in principle but still cause problems with reproducing $\pi(X)$ if the probabilities of proposing transitions to certain configurations are very small (but nonzero!) relative to the probabilities of proposing transitions to other configurations. In that situation, the simulation will sample certain configurations very infrequently, necessitating long simulation times to correctly reproduce $\pi(X)$. Thus, for all practical purposes, such a simulation is not ergodic.

For simulations with a double well trapping potential, the key difficulty with achieving ergodicity has to do with the motion of particles between the two wells, which we can intuitively understand as follows. In general, paths which are entirely located in one well are more probable than paths that cross the barrier because of the extra potential energy associated with the parts of the crossing paths that are in the barrier region. The larger this difference in probability, the less likely it will be that paths that start in one well will move to the other over the course of the simulation; instead, they get stuck on one side. This problem becomes worse the larger the barrier, so we have a much easier time simulating the system for $L = a_{ho}$ and $2\,a_{ho}$ than for $L = 3\,a_{ho}$.

Surprisingly, this problem is also exacerbated for small $N$ and small $a$, which one can understand as follows. In the context of the simulation, $N$ is the number of paths and $a$ is the closest distance that different paths at the same time slice can approach each other. When both of these are small, paths can "settle down" into the bottoms of the wells where the potential energy is low. However, when $N$ and $a$ are large, the paths are forced to spread out into regions where the potential is larger. This makes it easier for them to transition through the barrier because the "probability penalty" incurred to do so is not as great. This leads to the counterintuitive result that it is easier to achieve convergence for high barrier simulations with strong interactions and more particles

This ergodicity problem impacts the computation of $S$ more severely than other diagonal observables, such as the energy or density. Since $S$ is a function of $(n_l - n_r)^2$, which only changes value when the center of a path crosses the barrier at $z = 0$, reduced ergodicity with respect to particle motion across the barrier leads to long autocorrelation times for $S$. Hence, one must wait a long time before the simulation generates enough independent values of $(n_l - n_r)^2$ to properly compute $S$.

Sampling issues also arise when computing the OBDM. In that case, these are mostly due to the fact that we sampled the OBDM on a grid. If the mesh is too coarse (too few grid points), then the basis is too small to get produce accurate natural orbitals and occupation numbers, but if it is too fine (too many grid points), then it will take the simulation too long to get good enough statistics on each point. Hence, one needs to strike a balance between these two extremes. We chose to generate an OBDM that is $51 \times 51$ entries.

**Sampling efficiency** One way that an update process could work is by producing new configurations that are completely independent of the proceeding configurations; this is known as *direct sampling*. It is possible to use direct sampling with the double well BEC system by randomly generating $3NM$ real numbers for each new configuration. This would have to be done in a finite box, but since the wavefunction is effectively zero far enough away from the double well, there is always going to be some box that one can define such that the probability of accepting a move outside of that box is as close to zero as one likes. Since those moves would have been rejected anyway, there is no need to allow the possibility of explicitly generating them. However, this is often a bad choice in practice. If the system is such that a large fraction of parameter space has $\pi(X) \approx 0$ inside the box, the Metropolis algorithm would spend most of its time rejecting moves generated by direct sampling, which is inefficient.

Instead, one can use Markov chain sampling [97], in which a new configuration is generated based on the old configuration. For example, one simple way to do this is to shift the position of a randomly selected atom in a random direction by an amount distributed according to a Gaussian random variable. There are of course many other ways to generate new configurations. Later in this section, we will discuss the update methods we use, which all employ Markov chain sampling.

Generally, there are parameters in the Markov chain algorithm that one can adjust to alter the efficiency of the simulation; for the proceeding example, the width of the Gaussian distribution is one such parameter. The efficiency of an update method is related to the rate at which the simulation decorrelates from the random initial configuration in which it starts. The quicker this decorrelation happens (i.e., the quicker the simulation "forgets" its arbitrary starting configuration), the more efficient the algorithm. In practice, this is not a useful way of deciding whether an update method is efficient because it requires one to actually run the simulation multiple times with different update method parameters to decide which set of parameters is the best.

Instead, a useful rule of thumb is to shift the parameters so that the acceptance rate of the Metropolis algorithm is about 50%. This ensures that the proposed updates are not too close to the original configurations, in which case the simulation would sweep out parameter space too slowly, or too far from the original configuration, in which case we would run the risk of reproducing the problem associated with direct sampling. The signature of the former situation is an acceptance rate close to 1, while the signature of the latter is an acceptance rate close to 0; both situations imply that a large number of moves are being "wasted." Hence, tuning the acceptance rate to 50% is an easy and simple way to improve the efficiency of an update method.

**Correlations** Any update method that uses a Markov chain algorithm necessarily results in configurations that are correlated with each other. This leads to several issues related to the choice of initial state and the computation of error bars.

The Metropolis algorithm must be initialized with some starting configuration; we chose

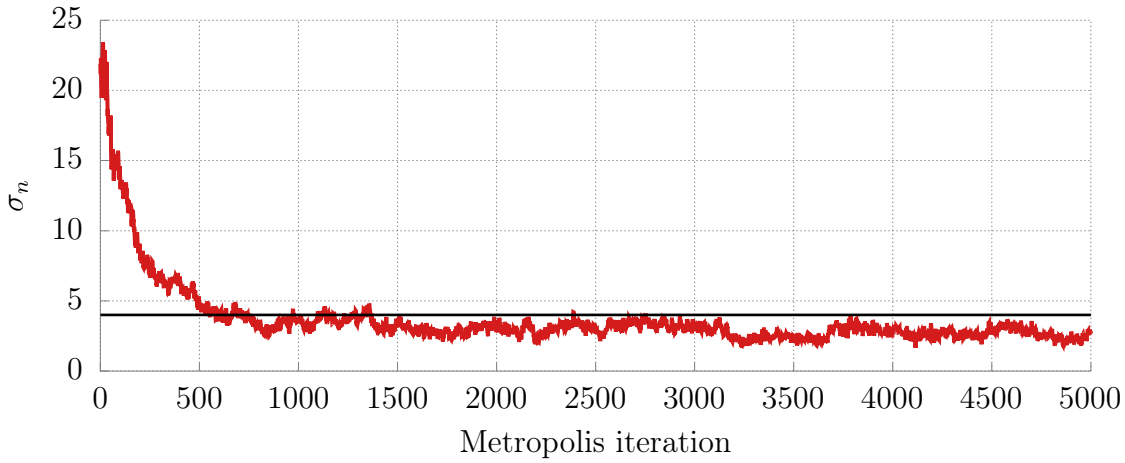


Figure 5.4: The standard deviation $\sigma_n$ of the number distribution of a double well BEC system with $N = 64$ atoms and scattering length $a = 0.05$ as a function of Metropolis algorithm iteration step for a Monte Carlo integration with $M = 100$ time slices. Notice that it takes about 1000 iterations before the value of $\sigma_n$ decorrelates from the initial randomly chosen configuration. The horizontal line is at $\sigma_n = 4$, which is the value of $\sigma_n$ in the noninteracting limit.

to generate a random starting configuration in a box of fixed size. Because states in a Markov chain are not independent of their neighbors, there is some number of iterations of the Metropolis algorithm necessary to decorrelate the set of accepted configurations from the choice of starting configuration. In general, it is not possible to know in advance how many iterations are necessary to achieve this decorrelation. In practice, we can plot the value of the observable(s) of interest as a function of Metropolis iteration step (see Figure 5.4 for an example) and throw out the data that is obviously still correlated.

Even after one has thrown out this initial data, there are still correlations present in the remaining data. The number of iterations of the Metropolis algorithm required to generate a configuration decorrelated from some initial configuration is known as the *correlation length*; there is generally no simple way to know the value of the correlation length in advance of computing a Monte Carlo integral. These correlations impact the computation of error bars by causing the standard error to underestimate the true statistical error in the data. One can solve this problem by estimating the error bars using the binning analysis described in [98]. For a given bin size $B$, one averages the first $B$ data points, the next $B$ data points, and so on, to produce $\lceil k/B \rceil$ new data points (where $k$ is the number of original data points, and the "remainder" data points are averaged into a point even if there are not $B$ of them). Then, one plots the standard error of the new data points as a function of $B$. Once the bin size becomes larger than the correlation length, the plot should asymptote to the true value of the error, although the larger $B$ gets, the fewer data points there are and therefore the larger the variance in the computed error. See Figure 5.5 for an example binning analysis

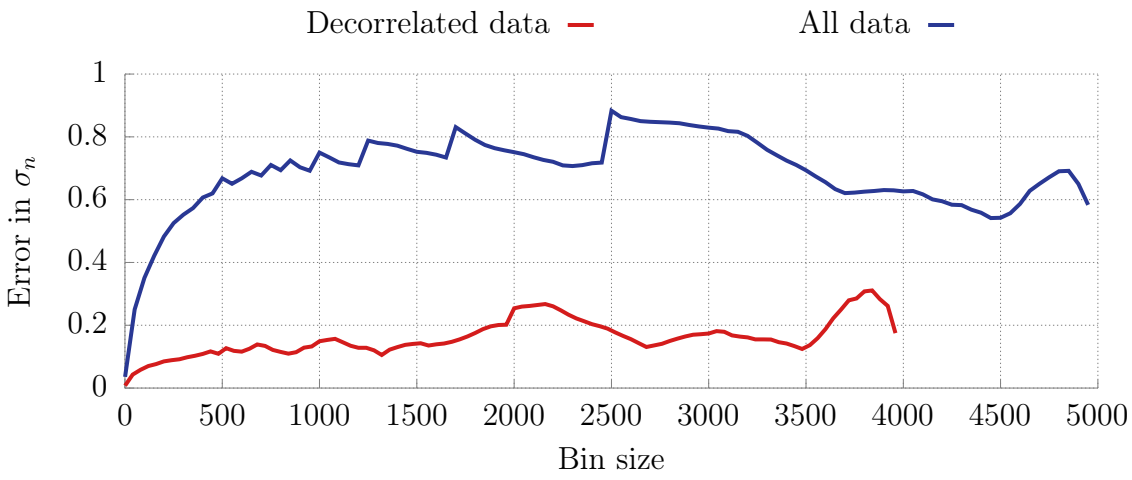


Figure 5.5: Error estimate for the data depicted in Figure 5.4 using the binning analysis of [98]. The value at which the error plateaus is the true error, and the bin size at which this happens is an estimate of the correlation length for the system. The "decorrelated data" ignores the first 1000 iterations worth of data in Figure 5.4. Unsurprisingly, the estimated error is larger when one includes the data that has not yet decorrelated from the initial state. Notice that for very large bin sizes, the variance in the error estimate grows; this happens because when the data is averaged into large bins, $\lceil k/B \rceil$ becomes small.

that corresponds to the data in Figure 5.4.

### Brownian Bridge Moves

The main "workhorse" update method we use is the *Brownian bridge move*, which is a specific realization of the more general Lévy construction [99, 100]. In the Brownian bridge move, a portion of the path of a single particle is updated. The particle is chosen randomly, as is the section of its path that is updated; the length of this section is a fixed parameter $K$, defined such that the section consists of $k+1$ time slices including the endpoints. As discussed above, we choose so as to achieve an acceptance rate of approximately 50% for efficiency purposes.

The move proceeds as follows. The endpoints of the section to be updated are chosen and held fixed; call these $\mathbf{r}_0$ and $\mathbf{r}_K$. Next, the coordinate of the particle at the first time slice, $\mathbf{r}_1$, is replaced with one drawn from a certain probability distribution that we will describe below. This coordinate becomes the new left endpoint for a section of length $K-1$ that runs from $\mathbf{r}_1$ to $\mathbf{r}_K$. The coordinate of the particle at the second time slice, $\mathbf{r}_2$, is replaced with one drawn using a probability distribution with the same form as the one used for determining $\mathbf{r}_1$, but with the updated left endpoint. This process continues until the entire section of path is reconstructed.

So what is the appropriate probability distribution to use? Suppose that we wanted to insert a new coordinate $\mathbf{r}_J$ at an arbitrary imaginary time between $\mathbf{r}_0$ and $\mathbf{r}_K$, such that $\tau_1$

is the amount of imaginary time separating $\mathbf{r}_0$ and $\mathbf{r}_J$ and $\tau_2$ is the amount of imaginary time separating $\mathbf{r}_J$ and $\mathbf{r}_K$. The new coordinate can be drawn from a probability distribution $P(\mathbf{r}_J)$ based on the free particle propagator:

$$\begin{aligned} P(\mathbf{r}_J) &\propto e^{-\frac{\hbar}{4\lambda}\left(\frac{(\mathbf{r}_0-\mathbf{r}_J)^2}{\tau_1}+\frac{(\mathbf{r}_J-\mathbf{r}_K)^2}{\tau_2}\right)} \\ &= e^{-\frac{\hbar}{4\lambda}\left(\frac{(\mathbf{r}_J-\mathbf{r}^*)^2}{\tau^*}+\frac{\mathbf{r}_0^2}{\tau_1}+\frac{\mathbf{r}_\tau^2}{\tau_2}\right)} \\ &\propto e^{-\frac{\hbar}{4\lambda}\left(\frac{(\mathbf{r}_J-\mathbf{r}^*)^2}{\tau^*}\right)}, \end{aligned} \tag{5.67}$$

where

$$\mathbf{r}^* = \frac{\tau_1\mathbf{r}_0 + \tau_2\mathbf{r}_K}{\tau_1+\tau_2} \tag{5.68a}$$

$$\tau^* = \frac{\tau_1\tau_2}{\tau_1+\tau_2}. \tag{5.68b}$$

This is a Gaussian probability distribution centered at $\mathbf{r}^*$ with a width set by $\tau^*$. By choosing $\mathbf{r}_0$, $\mathbf{r}_K$, $\tau_1$, and $\tau_2$ appropriately, one can use this distribution to implement Brownian bridge moves.

In general, the Brownian bridge move is an efficient way of sampling new paths, although it is susceptible to the ergodicity problem described above if the barrier is too strong and enough of the new path ends up in the barrier region. For the vast majority of our simulations, it was the only update method we used.

### Swap Moves

One potential way to address the ergodicity issue is to implement an additional type of move that explicitly transfers an atom from one side of the double well to the other [101]. In our implementation of this *swap move*, the $z$-coordinate is negated for the entire path of a random particle. If this leads to an overlap between the swapped path and a second path (i.e., it results in two atoms at the same time slice with a separation of less than $a$), then the second path is also swapped. This "cascade" continues until no overlaps remain.

Naively, one would think that this would be a good way to generate moves that change the difference in the number of atoms between the two sides of the double well. Unfortunately, swap moves did not work as well as intended. As the simulation progresses, Brownian bridge moves tend to nudge the atom paths into tight clusters near the well minima, as noted above. Once the system is in that sort of state, a swap move has a high probability of leading to a cascade that swaps every particle, which is the same as not swapping anything. This effect is worse for longer paths and larger $N$. Because of this, the swap move was mostly ineffective in practice for our double well simulations. We did not end up using it for our production runs.

### Potential Moves

Our *potential moves* were inspired by the parallel tempering technique [102]. In parallel tempering, one runs multiple copies of a simulation at different temperatures simultaneously, and exchanges configurations between two different simulations based on the Metropolis criterion. This allows a simulation at a given temperature to sample a wider variety of configurations, potentially avoiding an ergodicity problem.

In our potential moves, we run only one simulation, but we implement a move that changes the shape of the external potential, specifically by changing $L$ from among a set of pre-defined values. Given the current value of $L$, the potential move attempts to change $L$ to the next highest or lowest value in the pre-defined set and uses the Metropolis criterion to accept or reject the move. The motivation here is to allow for a way to more easily change $(n_l - n_r)^2$ for a high-barrier potential than would be possible with only Brownian bridge moves by lowering the potential and then raising it again.

One challenge with this method is that certain potentials are more probable (i.e., have higher average values of $\pi(X)$, with the average taken over all configurations) than others, so a simulation with potential moves as described would eventually end up only sampling the most probable potential. To avoid this problem, we introduce a set of weights, one per potential, and we multiply $\pi(x)$ by the appropriate one before applying the Metropolis algorithm. Because there is a unique weight per potential, all of the accepted configurations for a given potential will be correctly distributed according to the $\pi(X)$ for that potential, even though the configurations from different potentials will not appear in the "correct", unweighted ratios. Indeed, this is the point of the weights: we choose them so that the average probability of transitioning from one potential to another is the same as the probability of the reverse, which ensures that all of the potentials will be visited with equal probability in the long run, and that we will therefore get results for all of them.

One can choose these weights using a version of the Wang and Landau algorithm [103]. Let's imagine that we have only two potentials, $A$ and $B$. Each potential has a probability distribution for the possible configurations of the system, $\pi_A(X)$ and $\pi_B(X)$. The total probability of transitioning from potential $A$ to potential $B$ can be expressed as an integral of the Metropolis acceptance probability over all possible configurations of the system:

$$P_{AB} = \frac{\int \min\left(1, \frac{\pi_B(X)}{\pi_A(X)}\right)\, dX}{\int\, dX}. \tag{5.69}$$

Instead of an integral over configurations, one can rewrite this quantity in terms of a probability distribution $f_{AB}(\pi)$, which is defined as the probability of finding a value of $\pi = \pi_B/\pi_A$ over all possible configurations of the system. Then,

$$P_{AB} = \frac{\int_0^\infty f_{AB}(\pi) \min\left(1, \pi\right)\, d\pi}{\int_0^\infty f_{AB}(\pi)\, d\pi}. \tag{5.70}$$

Now suppose we introduce a weight $w$ and multiply all values of $\pi_B(X)$ by it. This changes the probability distribution $f_{AB}(\pi)$ to $g_{AB}(\pi) = f_{AB}(\pi/w)$, and therefore the total transition

probability becomes

$$\begin{aligned} P_{AB}(w) &= \frac{\int_0^\infty g_{AB}(\pi)\min(1,\pi)\ d\pi}{\int_0^\infty g_{AB}(\pi)\,d\pi} \\ &= \frac{\int_0^\infty f_{AB}(\pi/w)\min(1,\pi)\ d\pi}{\int_0^\infty f_{AB}(\pi/w)\,d\pi} \\ &= \frac{\int_0^\infty f_{AB}(\pi)\min(1,w\pi)\ d\pi}{\int_0^\infty f_{AB}(\pi)\,d\pi}. \end{aligned} \tag{5.71}$$

Notice that $P_{AB}(0) = 0$ and $P_{AB}(\infty) = 1$. A similar argument produces an expression for the total transition probability in the other direction:

$$P_{BA}(w) = \frac{\int_0^\infty f_{BA}(\pi)\min(1,\pi/w)\ d\pi}{\int_0^\infty f_{BA}(\pi)\,d\pi}, \tag{5.72}$$

for which $P_{BA}(0) = 1$ and $P_{BA}(\infty) = 0$. The weight that one wants is the one such that $P_{AB}(w) = P_{BA}(w)$.

To compute these weights in practice, we set up two simulations for each pair of adjacent potentials (i.e., potentials between which we allowed transitions). In one simulation, we used potential and Brownian bridge moves, and we set the weight of potential $B$ to zero, so that the simulation would fail to transition every time it tried to go from $A$ to $B$. We allowed it to attempt to transition 10,000 times and recorded the values of $\pi_B(X)/\pi_A(X)$ it generated; the Brownian bridge moves between transition attempts ensured that a variety of configurations $X$ were sampled. We used this list of values to construct a discrete version of $f_{AB}(\pi)$. In the other simulation, we did the same thing except for setting the weight of potential $A$ to zero; this allowed us to construct a discrete version of $f_{BA}(\pi)$. Using this data, we computed the weight that satisfied $P_{AB}(w) = P_{BA}(w)$, and we did this for each pair of potentials.

In practice, potential moves often work quite well once the correct weights are chosen. However, there is one significant caveat: while weights can be chosen to equalize the back-and-forth transition probabilities between two potentials, the actual *value* of that probability can be quite small. If that is the case, then even though in principle all potentials will be visited with equal frequency, that will only happen in practice in the limit of a very long simulation. This situation arises for high barrier potentials, and worsens for larger $N$ and longer paths; see Table 5.1 for an example. This means that these potential moves are only really useful for sampling the lower barrier potentials, but those potentials don't have the sampling problem that the potential moves were designed to solve. Hence, the potential moves also ended up not being particularly useful.

### Fixed Number Sampling

Another method that we developed to try to overcome the number configuration sampling problem was inspired by the thought that one way to avoid the problem is to run simulations where the number of particles on each side of the barrier is fixed.

| | Number of slices | | |
|---|---|---|---|
| $N$ | 100 | 200 | 800 |
| 8 | $4.8 \times 10^{-1}$ | $3.9 \times 10^{-1}$ | $6.1 \times 10^{-2}$ |
| 16 | $3.0 \times 10^{-1}$ | $1.5 \times 10^{-1}$ | $1.8 \times 10^{-2}$ |
| 32 | $1.2 \times 10^{-1}$ | $4.6 \times 10^{-2}$ | $1.0 \times 10^{-5}$ |
| 64 | $4.8 \times 10^{-2}$ | $1.1 \times 10^{-2}$ | $3.1 \times 10^{-12}$ |

Table 5.1: Probability of transitioning between $L = 2.875$ and 3 for $a = 0.1$ for various numbers of particles $N$ and path lengths in the potential move. Notice that the probability decreases mildly with increasing particle number and decreases significantly with increasing number of time slices. This makes the potential moves very impractical for potentials with strong double well barriers, because they require long paths to converge to the ground state.

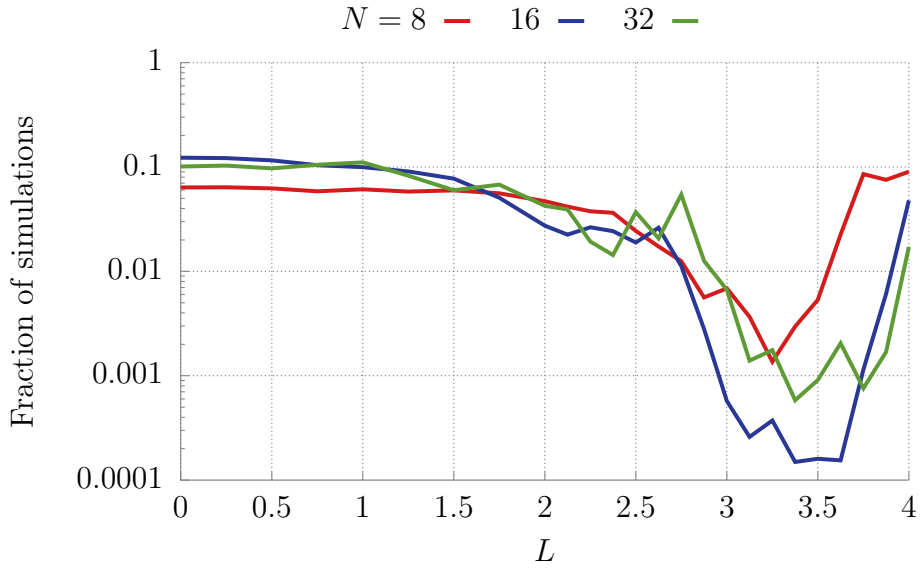


Figure 5.6: For simulations involving potential moves, the fraction of the total number of potentials (i.e., values of $L$) sampled during the simulation, as a function of $L$ for various particle number $N$. Each simulation attempted about $10^7$ potential moves. Notice that the fraction falls off significantly around the high barrier regime at $L = 3\,a_{ho}$.

Recall that, for a given operator $\hat{O}$, a PIGS simulation calculates

$$\langle \hat{O} \rangle = \frac{\int O(X)\pi(X)\,dX}{\int \pi(X)\,dX}, \tag{5.73}$$

where we have explicitly included the normalization in the denominator that we usually ignore; the reason for this will become apparent soon. Now, let's imagine that instead of running one simulation, we run $N+1$ simulations, each with a different, fixed number of particles on the left side of the double well (in fact, we need only run $(N+2)/2$ simulations because the symmetry of the double well means that a simulation with $n$ particles on the left is equivalent to one with $N-n$ particles on the left, so we can reuse the results of about half of the simulations). We fix the number of particles by rejecting any proposed update that changes the number of center slices on the left side of the barrier from the predetermined value for that simulation. This effectively changes $\pi(X)$; each fixed-number simulation has a new configuration probability distribution $\pi_i(X)$ given by

$$\pi_i(X) = \begin{cases} \pi(X) & \text{num}(z<0) = i \\ 0 & \text{otherwise} \end{cases}, \tag{5.74}$$

for $i = \{0, 1, 2, \ldots, N\}$, where $\text{num}(z<0)$ is the number of values $z_1, z_2, \ldots, z_N$ that are less than zero. With this definition,

$$\pi(X) = \sum_{i=0}^{N} \pi_i(X). \tag{5.75}$$

Additionally, we define $\langle \hat{O} \rangle_i$ such that

$$\langle \hat{O} \rangle_i = \frac{\int O(X)\pi_i(X)\,dX}{\int \pi_i(X)\,dX}. \tag{5.76}$$

This allows us to express $\langle \hat{O} \rangle$, the quantity we are interested in calculating, in terms of the quantities $\langle \hat{O} \rangle_i$ that we can calculate with the fixed-number simulations:

$$\begin{aligned} \langle \hat{O} \rangle &= \frac{\int O(X)\pi(X)\,dX}{\int \pi(X)\,dX} \\ &= \frac{\sum_i \int O(X)\pi_i(X)\,dX}{\sum_i \int \pi_i(X)\,dX} \\ &= \frac{\sum_i \langle O \rangle_i \int \pi_i(X)\,dX}{\sum_i \int \pi_i(X)\,dX} \\ &= \frac{\sum_i \langle O \rangle_i P_i}{\sum_i P_i}, \end{aligned} \tag{5.77}$$

where $P_i = \int \pi_i(X)\,dX$. So, in addition to calculating $\langle O \rangle_i$ for each fixed-number simulation, we also need to calculate $P_i$. We can do so by considering the following observable:

$$Q_i(X) = \begin{cases} \frac{1}{\pi_i(X)} & \pi_i(X) \neq 0 \\ 0 & \pi_i(X) = 0 \end{cases} \tag{5.78}$$

The expectation value of this observable, $\langle Q_i \rangle$, may be calculated by averaging over the reciprocal of the probabilities of the accepted configurations since no configurations with $\pi_i(X) = 0$ can ever be accepted. Formally, we can write $\langle Q_i \rangle$ as

$$\begin{aligned}
\langle Q_i \rangle &= \frac{\int Q_i(X)\pi_i(X)\,dX}{\int \pi_i(X)\,dX} \\
&= \frac{\int_{\pi_i(X)\neq 0} \frac{1}{\pi_i(X)}\pi_i(X)\,dX + \int_{\pi_i(X)=0} 0\,\pi_i(X)\,dX}{P_i} \\
&= \frac{\int_{\pi_i(X)\neq 0} dX}{P_i} \\
&= \frac{V_i}{P_i},
\end{aligned} \tag{5.79}$$

where $V_i = \int_{\pi_i(X)\neq 0} dX$ is the volume of the space for which $\pi_i(X) \neq 0$. In principle, this volume can be expressed as a fraction $f_i$ of the total (infinite) volume $\int dX$. All together, we have

$$\begin{aligned}
\langle \hat{O} \rangle &= \frac{\sum_i \langle O \rangle_i P_i}{\sum_i P_i} \\
&= \frac{\int dX \sum_i f_i \langle O \rangle_i / \langle Q \rangle_i}{\int dX \sum_i f_i / \langle Q \rangle_i} \\
&= \frac{\sum_i f_i \langle O \rangle_i / \langle Q \rangle_i}{\sum_i f_i / \langle Q \rangle_i}
\end{aligned} \tag{5.80}$$

Unfortunately, we found that it is not practical to use this method to compute $\langle \hat{O} \rangle$ for this system. The main problem is that $\langle Q \rangle_i$ is a numerically unstable quantity to calculate. Over the course of a simulation, $\pi_i(X)$ for accepted configurations ranges between 0 and 1; most values will be close to 1, but there will occasionally be improbable but accepted configurations with very small $\pi_i(X)$. These improbable configurations will disrupt the computation of $\langle Q \rangle_i$, because they will introduce occasional values into the average that are many orders of magnitude greater than the rest. The average will therefore be dominated by these infrequent outliers, making it impossible in practice to get a well-converged value for the average.

## 5.4 Summary

In this chapter, we described in detain our implementation of the path integral ground state Monte Carlo method. Much of this discussion was general background on PIGS. Our main novel contributions were

1. the factorization of the external potential from the propagator by grouping the kinetic and hard sphere parts of the Hamiltonian in the Chin decomposition,

2. the use of the difference between the free and exact hard sphere propagators, rather than the exact hard sphere propagator alone, increasing the rate of convergence of the propagator as higher $l$ terms are added, and

3. the development and implementation of update methods, like the swap and potential moves, which unfortunately were not of much help in overcoming the sampling problems we faced.

As suggested by the third item on this list, one significant source of difficulty in implementing these simulations is achieving ergodicity with respect to moving atoms across the double well barrier, which is increasingly difficult the stronger barrier. Ultimately, none of the solutions we attempted to mitigate this problem were more effective than simply running the simulations with Brownian bridge moves for long enough to achieve convergence. This restricted the barrier strength and number of particles that we could simulate to those reported in Chapter 6.

# Chapter 6

# Quantum Monte Carlo Results: Squeezing & Fragmentation

In this chapter, we present the squeezing and fragmentation results of our quantum Monte Carlo simulations, which use the path integral ground state method we described in the last chapter. We will use the predictions of the two- and eight-mode models, discussed in Chapters 3 and 4, to help us understand the new double well BEC physics revealed by our results.

## 6.1 Simulation Parameters

Before describing and interpreting our Monte Carlo results, we will review the physical and computational parameters associated with our simulations and describe the rationale for the choices we made in setting them.

First, we set the computer hardware context in which these choices were made. Our simulations were run on a variety of supercomputers maintained and operated by Lawrence Livermore National Laboratory. Each supercomputer consists of several thousand CPUs with speeds of between 2.4 and 2.8 GHz per processor. We implemented simple parallelization in our PIGS code so that we could run a simulation on multiple processors simultaneously; typically, we parallelized our simulations across 64 or 72 processors. In general, a run with particular values for $N$, $a$, and $L$ required between 100 and 1000 processor-days of continuous running to converge, with larger times corresponding to simulations with stronger barriers. Because there are many users requesting Livermore computing resources simultaneously, our runs were never continuous. "Dead time" due to other users' jobs running instead of ours could increase the effective time-to-convergence by anywhere between 25 and 50 percent, depending on the demand on the machine. Hence, these hardware constraints played a major role in determining what values of $N$ and $L$ were feasible for us to compute.

### 6.1.1 Physical Parameters

There are six physical parameters that can be altered in the double well Hamiltonian (2.33): the number of atoms $N$; the scattering length $a$; the atomic mass $m$; and the double well geometry parameters $\alpha$, $L$, and $\omega_{ho}$. Because we express all of our results in terms of the energy scale $E_{ho} = \hbar\omega_{ho}$ and the length scale $a_{ho} = \sqrt{\hbar/m\omega_{ho}}$, there is no need to explicitly consider varying $m$ or $\omega_{ho}$. However, we would like to understand how the ground state properties of the double well system vary as a function of the other four parameters, and in principle, we would like to study them in as large a range as possible.

**Atom number** For the number of atoms $N$, we choose to simulate systems with $N = 8$, 16, 32, and 64. The main constraint on these values is imposed by the PIGS simulations: more atoms in the simulation leads to larger dimensionality of the integral that needs to be computed and therefore longer simulation times. Due to hardware constraints, we could not reasonably go beyond $N = 64$, even though real physical systems typically have orders of magnitude more atoms than this. Additionally, we chose to simulate smaller values of $N$ for two reasons. First, by simulating several values of $N$, we can potentially extrapolate the results we have to predict behavior for larger $N$. Second, as we discussed in Section 4.1.3, it is not computationally feasible to use the eight-mode model to study ground state properties for $N$ greater than about 10; hence, we simulate a system with $N = 8$ in order to be able to use the predictions of the eight-mode model in our analysis.

**Double well shape** The strength of the double well barrier is extremely important in determining the ground state properties of the system, as we can already see based on multimode predictions of squeezing and fragmentation from Sections 3.4 and 4.2. Hence, we want to simulate systems under a wide variety of barrier strengths. We can characterize the barrier strength using parameters of the two-mode model, which are tabulated in Table 3.1. In particular, the two-mode Hamiltonian for a single atom is

$$\hat{H} = \Delta\hat{I} - \frac{\delta}{2}(\hat{a}_l^\dagger\hat{a}_r + \hat{a}_r^\dagger\hat{a}_l). \tag{6.1}$$

In the limit of a strong barrier, the off-diagonal (tunneling) terms become much smaller than the diagonal terms while for a weak barrier they are comparable. Hence, we can use the dimensionless ratio $\xi = \delta/2\Delta$ as a proxy for barrier strength.

The double well barrier strength is controlled by two parameters, $\alpha$ and $L$, so there are a wide variety of geometries we could choose to study. However, recall that the eight-mode model requires us to study geometries that are in the spherical potential regime as defined in Section 4.1.1. Additionally, the stronger the barrier becomes, the more difficult it is to overcome all of the sampling issues we discussed in Section 5.3.3 and generate reliable, converged results. Based on these considerations, we choose three geometries with $\alpha = 4/81\, a_{ho}^{-2}$ and $L = a_{ho}$, $2\,a_{ho}$, and $3\,a_{ho}$. These are all in the spherical potential regime

(see Figure 4.4), and correspond to barriers of increasing strength ($\xi = 1.8 \times 10^{-1}$, $7.1 \times 10^{-2}$, and $9.2 \times 10^{-4}$, respectively).

**Scattering length** One of the main motivations of conducting quantum Monte Carlo simulations of the double well BEC system in the first place is to study the system outside of the weakly-interacting regime in which mean-field theoretical work has thus far focused. Thus, we want to run simulations over as wide a range of scattering length $a$ as possible, in particular for large $a$.

This brings up the question of what "large $a$" means. There are at least three ways to think about what constitutes large $a$, two of which we have alluded two already in the context of the approximations that go into the construction of the double well Hamiltonian restricted to two-body interactions, Eqs. (2.33) and (2.34).

**1. Two-body interaction approximation** The double well Hamiltonian that we derived for use in our multimode models assumes that all interactions are two-body. Recall that in second quantized form, the two-body interaction term of the Hamiltonian is given by

$$\hat{H}_2 = \frac{2\pi\hbar^2 a}{m} \sum_{i,j,k,l=1}^{\infty} \hat{a}_i^\dagger \hat{a}_j^\dagger \hat{a}_k \hat{a}_l \int \phi_i^*(\mathbf{r}) \phi_j^*(\mathbf{r}) \phi_k(\mathbf{r}) \phi_l(\mathbf{r})\, d\mathbf{r}. \tag{6.2}$$

For a generic $N$-body double well state $|\psi\rangle$, we can write the expectation value of this Hamiltonian as

$$\begin{aligned}
\langle\psi|\hat{H}_2|\psi\rangle &= \frac{2\pi\hbar^2}{m} \sum_{i,j,k,l=1}^{\infty} \langle\psi|\hat{a}_i^\dagger \hat{a}_j^\dagger \hat{a}_k \hat{a}_l|\psi\rangle\, a \int \phi_i^*(\mathbf{r}) \phi_j^*(\mathbf{r}) \phi_k(\mathbf{r}) \phi_l(\mathbf{r})\, d\mathbf{r} \\
&= 2\pi\hbar\omega_{ho} a_{ho}^2 \sum_{i,j,k,l=1}^{\infty} \langle\psi|\hat{a}_i^\dagger \hat{a}_j^\dagger \hat{a}_k \hat{a}_l|\psi\rangle\, \frac{a}{a_{ho}^3} I_{ijkl} \\
&\propto (N\hbar\omega_{ho}) \frac{Na}{a_{ho}},
\end{aligned} \tag{6.3}$$

where in the second line we have nondimensionalized the integral and in the third line we have replaced the expectation value of the ladder operators with $N^2$, which is correct to leading order in the large $N$ limit. Using dimensional analysis, we can guess a form for the equivalent expectation value for a three-body interaction:

$$\begin{aligned}
\langle\psi|\hat{H}_3|\psi\rangle &\propto \hbar\omega_{ho} a_{ho}^2 \sum_{i,j,k,l,m,n=1}^{\infty} \langle\psi|\hat{a}_i^\dagger \hat{a}_j^\dagger \hat{a}_k^\dagger \hat{a}_l \hat{a}_m \hat{a}_n|\psi\rangle\, \frac{a^4}{a_{ho}^6} I_{ijklmn} \\
&\propto (N\hbar\omega_{ho}) \left(\frac{Na}{a_{ho}}\right)^2 \left(\frac{a}{a_{ho}}\right)^2.
\end{aligned} \tag{6.4}$$

Similarly, for an $m$-body interaction, we have

$$\langle\psi|\hat{H}_m|\psi\rangle \propto (N\hbar\omega_{ho})\left(\frac{Na}{a_{ho}}\right)^{m-1}\left(\frac{a}{a_{ho}}\right)^{2(m-2)}, \tag{6.5}$$

so that a Hamiltonian that included all orders of interaction would look like

$$\langle\psi|\hat{H}_2+\hat{H}_3+\cdots|\psi\rangle \propto (N\hbar\omega_{ho})\sum_{m=2}^{\infty}\left(\frac{Na}{a_{ho}}\right)^{m-1}\left(\frac{a}{a_{ho}}\right)^{2(m-2)}. \tag{6.6}$$

A necessary (although not sufficient) condition for one to ignore all but the two-body term in this series is for each subsequent term to be smaller than the previous one. Mathematically, we have

$$\frac{d}{dm}\left(N^{m-1}\left(\frac{a}{a_{ho}}\right)^{3m-5}\right)<0, \tag{6.7}$$

which leads to

$$a<\frac{a_{ho}}{N^{1/3}}. \tag{6.8}$$

Thus, we can use this limit to define "large $a$" as the regime in which we may need to take into account three- and higher-body collisions in our atom interactions.

**2. Two-mode approximation** The authors of [42] derive a condition under which the two-mode approximation is valid, which is when the interactions produce only small modifications to the ground state properties of the individual potential wells:

$$\hbar\omega_0 \gg N|U_0|V_{eff}^{-1}, \tag{6.9}$$

where $U_0 = 4\pi\hbar^2 a/m = 4\pi\hbar\omega_{ho}aa_{ho}^2$ and $V_{eff}^{-1} = \int |u_0(\mathbf{r})|^4\, d\mathbf{r}$, where $u_0(\mathbf{r})$ is the effective single particle ground state for a single well. For our situation, we can approximate $u_0(\mathbf{r})$ as the ground state of a 3D harmonic oscillator potential, with the $x$ and $y$ frequencies given by $\omega_{ho}$ and the $z$ frequency given by $\sqrt{4\alpha}L\omega_{ho}$. Then,

$$V_{eff}^{-1} = \frac{1}{2\pi a_{ho}^3}\sqrt{\frac{\sqrt{\alpha}L}{\pi}}, \tag{6.10}$$

and we estimate that the two-mode model should be valid as long as

$$a \ll \frac{a_{ho}}{N}\sqrt{\frac{\pi}{4L\sqrt{\alpha}}}. \tag{6.11}$$

**3. Negligible depletion approximation** When we introduced depletion in Section 2.4.1, we discussed the idea due to Bogoliubov that one can expand the double well Hamiltonian in terms of fluctuations around a single condensate wavefunction in order to determine the occupation of the condensed state as a function of scattering length for a homogeneous system. We repeat the result, Eq. (2.4.1), here:

$$n_0 = 1 - \frac{8}{3}\sqrt{\frac{na^3}{\pi}} + \cdots , \tag{6.12}$$

We see that the depletion is negligible (i.e. $n_0 \approx 1$) when

$$a \ll n^{-1/3}, \tag{6.13}$$

where $n$ is the atom density. In the context of an inhomogeneous system, it is reasonable to assume that there will be appreciable depletion if this inequality is violated locally anywhere in the condensate (i.e., there is a density somewhere that violates the inequality). Thus, "large $a$" is defined in this context as the limit in which the system exhibits significant depletion as a result of interactions.

**Summary** The three approximation-based constraints on $a$ are

$$a < \frac{a_{ho}}{N^{1/3}} \qquad \text{(two-body interaction approximation valid)} \tag{6.14a}$$

$$a \ll \frac{a_{ho}}{N}\sqrt{\frac{\pi}{4L\sqrt{\alpha}}} \qquad \text{(two-mode approximation valid)} \tag{6.14b}$$

$$a \ll n^{-1/3} \qquad \text{(negligible depletion approximation valid)} \tag{6.14c}$$

We chose to run our simulations with, equivalently, values of $a/a_{ho}$ ranging from $10^{-5}$ to 0.5, values of $N^{1/3}a/a_{ho}$ ranging from $2 \times 10^{-5}$ to 4, and values of $Na/a_{ho}$ ranging from $8 \times 10^{-5}$ to 32. This clearly extends past the range of validity of constraints (6.14a) and (6.14b). We argued in Section 2.4.1 that $n^{-1/3} \approx 0.25a_{ho}$, so these values of $a$ should also extend past the range of validity of constraint (6.14c). Thus, our Monte Carlo simulations, which one can think of as infinite-mode calculations with arbitrary $N$-body hard sphere collisions, should exhibit new physics for the larger simulated values of $a$ compared to the multimode models.

To relate these values to what is achievable in the laboratory, we again make use of the experiment described in [26] (as we did in Section 2.2.1 when describing the external potential). In this experiment, $N \approx 10^5$ $^{23}$Na atoms were trapped in a double well with $a_{ho} = 845\,\text{nm}$. Additionally, in the experiment described in [68], magnetic Feshbach resonances were used to tune the scattering length of $^{23}$Na atoms between about 1.2 and 18 nm. Together, these results imply that one can generate a $^{23}$Na BEC trapped in a double well with, equivalently, $a/a_{ho}$ ranging from $10^{-3}$ to $2 \times 10^{-2}$, values of $N^{1/3}a/a_{ho}$ ranging from $7 \times 10^{-2}$ to 1, and values of $Na/a_{ho}$ ranging from 100 to 2000. These values of $a/a_{ho}$ and $N^{1/3}a/a_{ho}$ lie well within the range of our simulations, while the experimentally achievable values of $Na/a_{ho}$ actually go beyond what our simulation achieve.

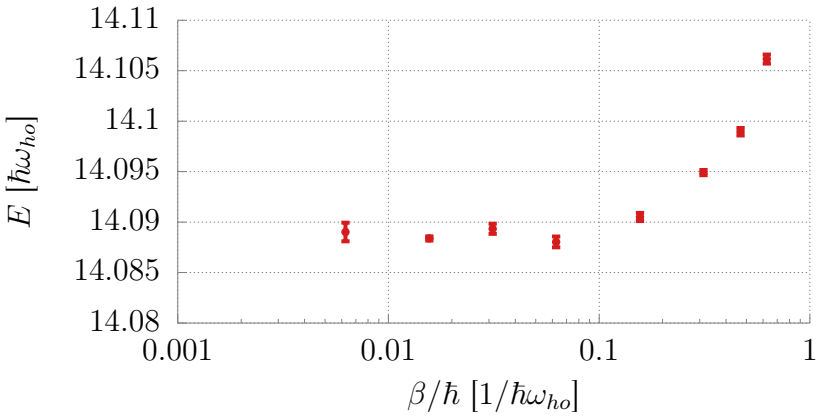


Figure 6.1: The energy of the double well system as a function of time step $\beta$ for a system of $N = 8$ particles with a scattering length of $a = 0.1\,a_{ho}$ and an imaginary time path length $\tau = 37.5\,\omega_{ho}^{-1}$. A $\beta$ almost as large as $0.1\,\omega_{ho}^{-1}$ is acceptable while still converging on the small-$\beta$ value of the energy.

### 6.1.2 Computational Parameters

In addition to physical parameters, we must also concern ourselves with parameters relating to the PIGS algorithm. The most important of these are the time step $\beta$ and the total imaginary time $\tau$ (or, equivalently, the time step $\beta$ and number of slices $M$). For a given set of physical parameters, one can empirically determine the largest $\beta$ and shortest $\tau$ required to reach the ground state by observing the behavior of the energy of the system as a function of $\beta$ and $\tau$.

To determine appropriate time step $\beta$ to use for our simulations, we ran simulations with a variety of physical parameters over a variety of $\beta$ for constant $\tau$. We expect that for a given total imaginary time, the system's energy should converge for low $\beta$. In practice, we find that the maximum $\beta$ for which the energy maintains the converged value is fairly insensitive to physical parameters like $N$ and $a$. Figure 6.1 shows an example of the energy convergence as a function of $\beta$ for $N = 8$, $a = 0.1\,a_{ho}$, and $\tau = 37.5\,\omega_{ho}^{-1}$. Based on these results, we chose $\beta = 0.0625$ for our simulations.

The path length $\tau$, on the other hand, is quite sensitive to the physical parameters, in particular those that control the barrier strength. For weak barriers ($L = a_{ho}$ and $2\,a_{ho}$) $\tau = 25\,\omega_{ho}^{-1}$ ($M = 400$) is often enough to get good convergence to the ground state. However, for strong barriers ($L = 3\,a_{ho}$), we need up to $\tau = 200\,\omega_{ho}^{-1}$ ($M = 3200$), which can lead to very long simulation times, especially if one takes into account the large number of iterations required (around $10^7$, for some of the worst situations) for the algorithm to overcome correlations and produce good error bars. Moreover, observables like the energy tend to converge for shorter $\tau$ than the main observables of interest, like the squeezing parameter $S$. In practice, we decided which $\tau$ was sufficient for a given set of physical parameters by doing a series of simulations with increasing $\tau$ until we achieved convergence for the observable of

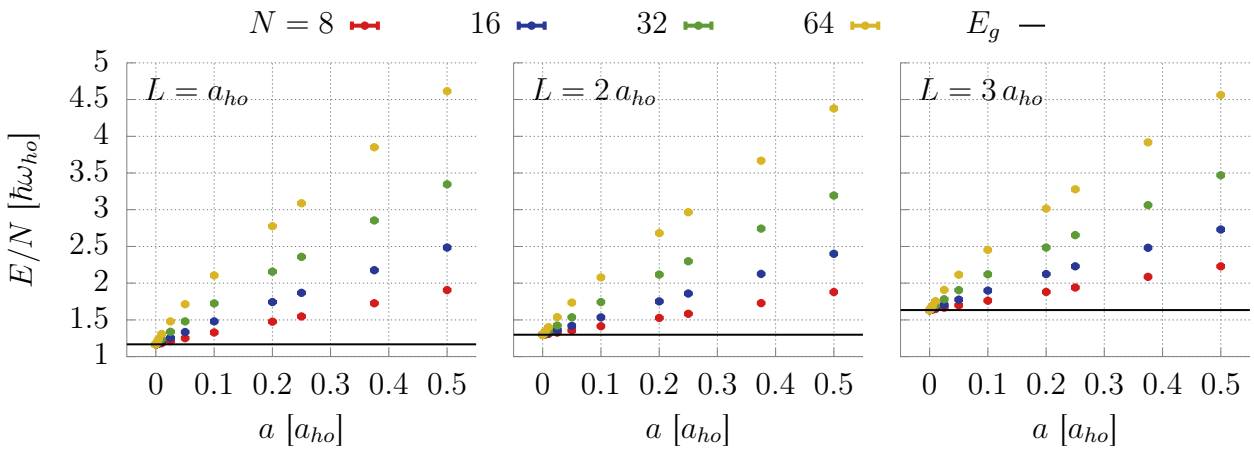


Figure 6.2: Monte Carlo results for the energy per particle $E/N$ as a function of scattering length $a$ for three different potentials ($L = a_{ho}$, $2\,a_{ho}$, and $3\,a_{ho}$, from left to right). The horizontal line indicates the energy of the single-body ground state in each geometry. The error bars on all of these data are smaller than the size of the points.

interest.

## 6.2 Results

In this section, we will summarise and discuss our quantum Monte Carlo results.

To begin, we plot in Figure 6.2 the energy per particle $E/N$ as a function of scattering length $a$ for the values of $N$, $L$, and $\alpha$ from Section 6.1.1. We see that in the limit of no interactions, the energy per particle for all values of $N$ become equal, as one would expect to be the case. We also see that for large interaction strength, the energy per particle grows with $N$. This is reasonable because a system with more particles has more pairwise interactions per particle and therefore more overall energy per particle. The growth of $E/N$ is roughly linear in $a$ and does not seem to depend much on the trap geometry.

In Figure 6.3, we plot the condensate density along the axis of the double well, $\rho_z(z)$, as a function of $z$ for our usual set of physical parameters. Unsurprisingly, the density tends to be higher where the potential is lower and vice versa, because it is energetically favorable for the condensate to sit at the potential minima. Increases in both $a$ and $N$ tend to cause the condensate to spread out, occupying higher potential regions than it would with small $a$ and $N$.

### 6.2.1 Squeezing Results

We now proceed to discuss our main squeezing results. In Figure 6.4 we plot the squeezing parameter $S$ as a function of $a$ for PIGS simulations with the values of $N$, $L$, and $\alpha$ from

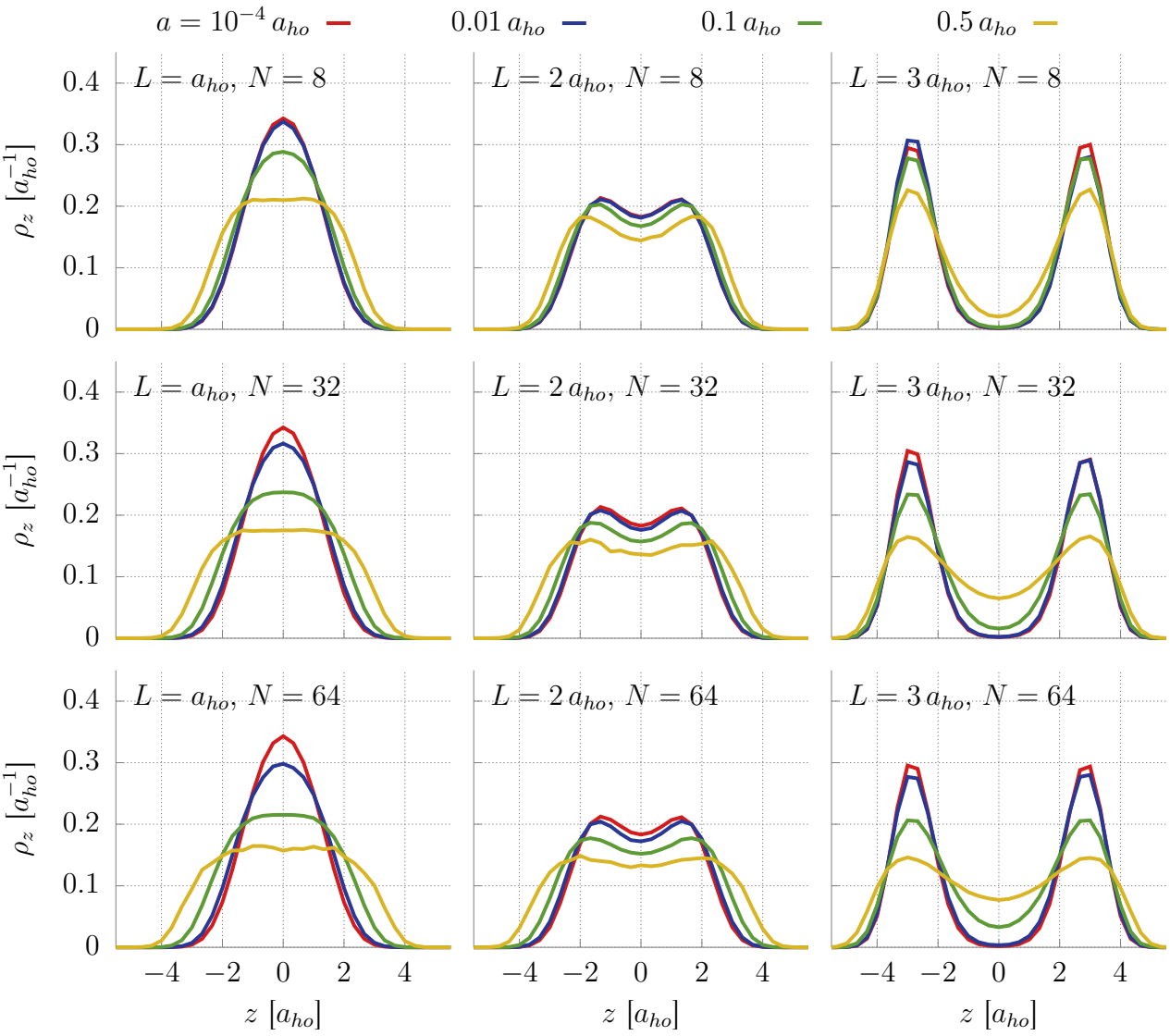


Figure 6.3: Monte Carlo results for the condensate density in the $z$ direction $\rho_z(z)$ as a function of coordinate $z$ for three different particle numbers ($N = 8$, 32, and 64, from top to bottom) and three different potentials ($L = a_{ho}$, $2\, a_{ho}$, and $3\, a_{ho}$, from left to right). Each plot include data for four representative values of the scattering length $a$ ($10^{-4}\, a_{ho}$, $0.01\, a_{ho}$, $0.1\, a_{ho}$, and $0.5\, a_{ho}$) that spanned the range of interaction strengths that we simulated.

Section 6.1.1, along with comparisons to the equivalent nearly degenerate two-mode, exact two-mode, and eight-mode models. We see that for the two weaker barriers ($L = a_{ho}$ and $2\,a_{ho}$), the squeezing increases monotonically with $a$. However, for the strongest barrier ($L = 3\,a_{ho}$), this is not the case. For all values of $N$ we simulated with this barrier strength, $S$ has a maximum for some value of $a$; this value decreases as $N$ increases. Furthermore, for larger values of $N$, the squeezing eventually reaches a minimum and increases again.

In Figure 6.4, we also indicate by vertical lines the values of $a$ for which condition (6.14b) should be satisfied. In general, we see that the models and the PIGS results agree well when this condition is met but deviate as $a$ increases. As one would expect, the nearly-degenerate two-mode model deviates from PIGS first, followed by the exact two-mode model, and then (for the cases where data is available) the eight-mode model. As we shall see, these discrepancies help to shed light on the physics at play in the full many-body treatment of the system provided by PIGS.

### Discrepancy Between PIGS and Multimode Models

Whether the models tend to over- or underestimate the PIGS results for large $a$ depends on the strength of the double well barrier (i.e., the value of $L$): for strong barriers ($L = 3\,a_{ho}$), we find less squeezing the more accurate the model (i.e., when going from nearly-degenerate two-mode to exact two-mode to exact eight-mode to PIGS), whereas for weak barriers ($L = a_{ho}$), we find the opposite (ignoring the nearly-degenerate two-mode curve since that model assumes a strong barrier to cause the ground and first excited states to be nearly degenerate with each other). The intermediate-strength case ($L = 2\,a_{ho}$) is a "crossover" between the other two cases, where the models and PIGS more closely agree. We propose two mechanisms to account for the discrepancies between the exact two-mode model and the PIGS data.

**1. Occupation of higher modes** The first mechanism has to do with avenues for reducing the interaction energy of the ground state. As the strength of repulsive interactions increases, the ground state has to change to minimize its energy given the value of $a$, and this of course causes $S$ to change with $a$. Recall the argument from Section 2.3 that strong repulsive interactions should suppress number fluctuations (and hence increase squeezing) because configurations with many particles on one side of the double well are disfavored due to their large interaction energy. This argument assumes that equalizing the difference in atoms between the two wells is the dominant mechanism that the system uses to reduce its interaction energy.

However, the behavior of the eight-mode ground state suggests another way. By comparing the top row of Figure 3.3 with Figure 4.7, we see that number fluctuations, which correlate with the spread of the ground state across values of $n$, are less suppressed for the eight-mode model. At the same time, Figure 4.8 illustrates that the eight-mode ground state involves increasingly large occupation of modes in the $n = 2$ energy level as $a$ increases. This suggests that, given more than the two $n = 1$ modes, the ground state favors the occupation of higher

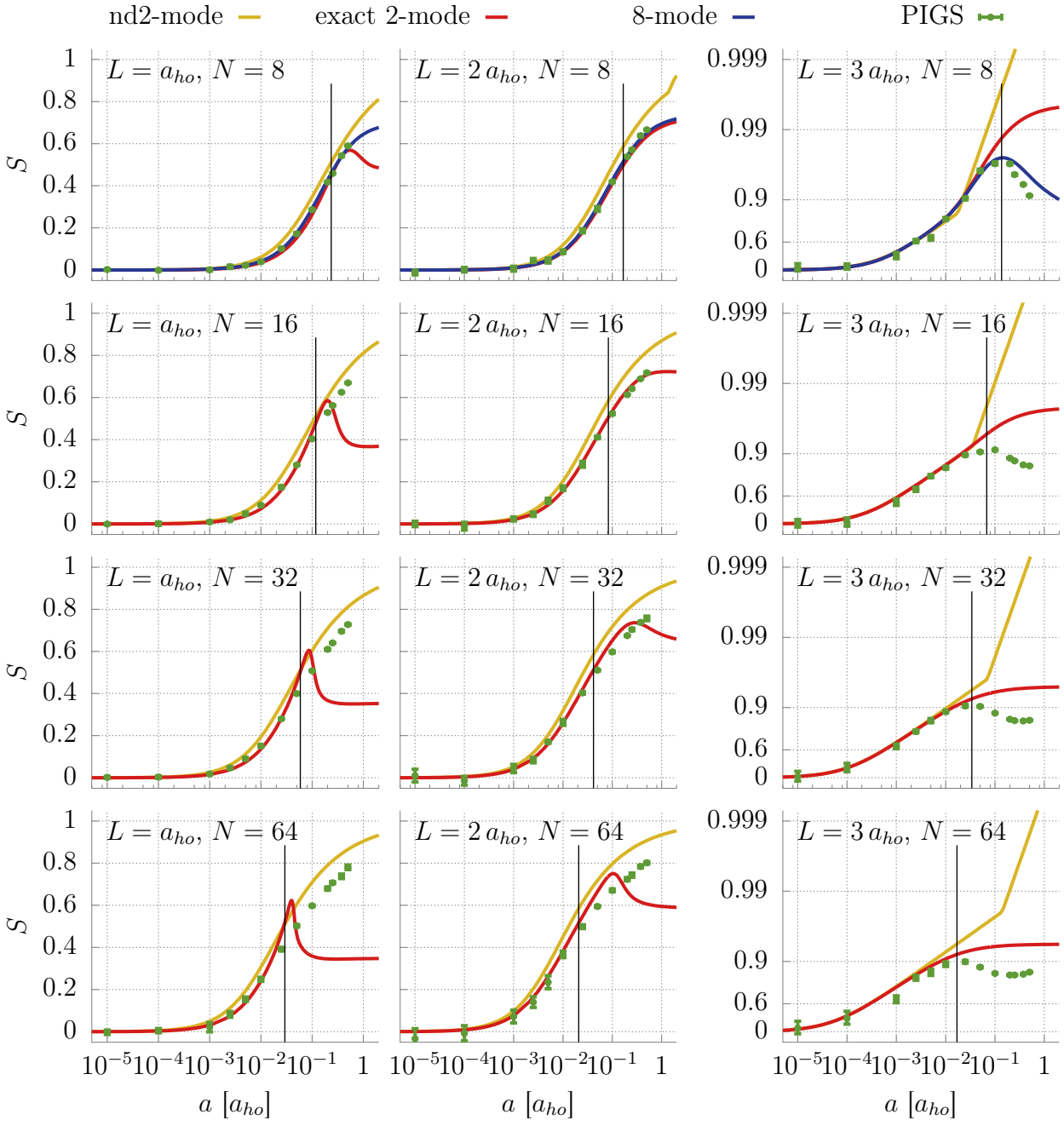


Figure 6.4: Squeezing parameter $S$ vs. scattering length $a$ for four different particle numbers ($N = 8$, 16, 32, and 64, from top to bottom) and three different potentials ($L = a_{ho}$, $2\,a_{ho}$, and $3\,a_{ho}$, from left to right). The plots include results from the nearly degenerate two-mode model, the exact two-mode model, the eight-mode model, and the PIGS simulations. Vertical lines indicate the values of $a$ below which we expect the two-mode model to be valid. The $L = 3\,a_{ho}$ plots have a logarithmic $S$-axis, while the other plots have a linear $S$-axis.

modes and less explicit suppression of number fluctuations as $a$ increases. If we think of PIGS conceptually as an "infinite-mode" model, then we would expect similar behavior in our simulations.

How does this impact squeezing? If there is less explicit suppression of number fluctuations, then by definition there is less squeezing. Additionally, there is another way in which this mechanism reduces squeezing. In Section 3.3.1, we defined the quantity $S_{max}$, which sets the maximum amount of squeezing possible given a particular double well geometry; the more that the modes encroach into the "wrong" side of the double well, the smaller $S_{max}$. Recall that certain modes with higher $n$ (for example, the mode with $nlm = 210$) tend to have more such encroachment than the $n = 1$ modes, which implies that they can support less squeezing (see Table 4.2 for comparisons of $S_{max}$). Hence, when strong repulsion drives particles into modes of higher $n$, it is driving some of them into modes with smaller $S_{max}$. Therefore, this will reduce squeezing compared with the two-mode model, in which all particles have $n = 1$.

**2. More two-body tunneling terms** The second mechanism has to do with the types of two-body tunneling terms present in the Hamiltonian due to the presence of higher modes. Recall from Section 3.4.2 that for large $a$ and small $L$, two-particle tunneling terms dominate the dynamics of the system. In the two-mode model, these tunneling terms couple even-numbered Fock states to other even-numbered Fock states (and likewise for odd-numbered states). This forces the ground state to occupy the even Fock states only (which we referred to as the striped configuration because of the pattern exhibited in the bottom left panel of Figure 3.3), which causes large number fluctuations and hence little squeezing. The availability of higher modes changes this situation by dramatically increasing the variety of two-particle tunneling terms in the Hamiltonian; in principle, two particles can tunnel from any two modes to any other two modes as long as the total value of $L_z$ is conserved. Hence, the "alternating $n$" restriction is lifted, and the ground state can have contributions from (multi-mode) Fock states with any value of the difference in the number of particles occupying left and right modes. This will lead to a reduction in the occupation of modes with large values of that difference, and hence squeezing will be greater than predicted by the two-mode model.

Note that this second mechanism varies in importance depending on the value of $L$. For small $L$, it operates as described above. However, for large $L$, tunneling between the wells is highly suppressed for all modes. In the two-mode case, this drives the ground state towards $|N/2\rangle$, an equal splitting of particles. The presence of higher modes has little effect on this distribution, again because all tunneling between the wells is suppressed. Therefore, the amount of squeezing will not be affected for large $L$. Contrast this with the first mechanism, where from Figure 4.8 we see that modes with smaller $S_{max}$ are occupied in about the same amount regardless of the value of $L$.

**Summary** To summarize, the first mechanism tends to reduce the true amount of squeezing compared with the two-mode model and is always relevant, while the second tends

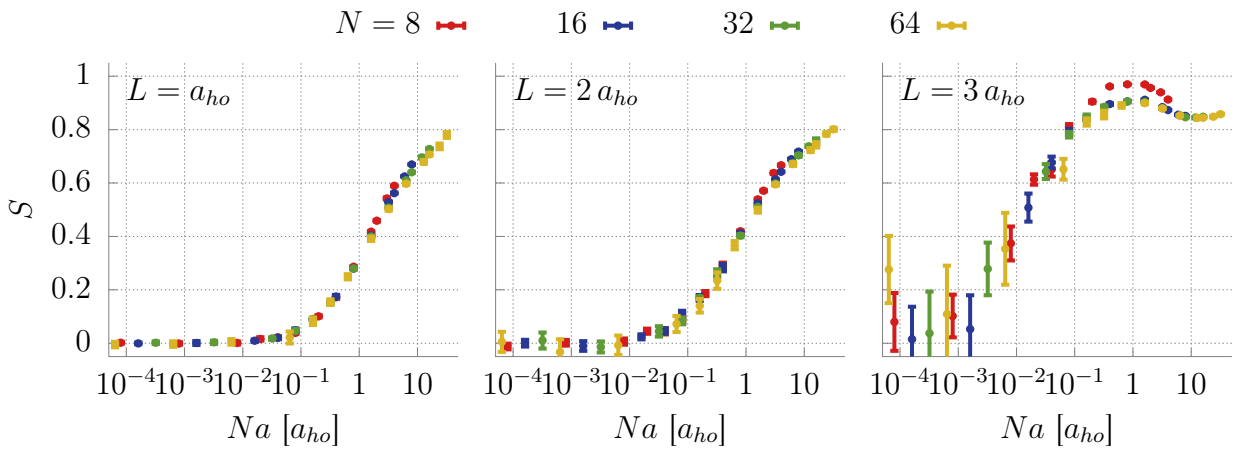


Figure 6.5: Monte Carlo results for the squeezing parameter $S$ vs. $Na$ (the product of the number of atoms and the scattering length) for three different potentials ($L = a_{ho}$, $2\,a_{ho}$, and $3\,a_{ho}$, from left to right). The plots include all of the PIGS results from Figure 6.4.

to increase squeezing and is only important for small $L$. This is sufficient to explain the pattern we see in the data in Figure 6.4: for small $L$, mechanism two dominates and the actual amount of squeezing is greater than predicted by the two-mode model while the opposite is true for large $L$.

Also note the lack of monotonicity in the $L = 3\,a_{ho}$ PIGS data. Since the second mechanism is not relevant for such a high barrier strength, this effect is likely due to an interplay between the reduction in number fluctuations (which increases squeezing) and the occupation of higher $n$ modes (which reduces squeezing) as the strength of the repulsive interactions increases.

### Validity of the Two-Body Interaction Approximation

In Figure 6.5 we plot the same PIGS squeezing data as in Figure 6.4, except that we plot it as a function of $Na$ for each value of $L$. The most striking feature of this plot is that the data for the various values of $N$ overlap each other (except that the $N = 8$ data for the strongest barrier ($L = 3\,a_{ho}$) shows slightly more squeezing than the data for the other values of $N$ for large $Na$). In other words, we have found that $S$ is a function of the product $Na$ to good approximation for the potentials and ranges of $N$ and $a$ presented here.

In the discussion that led to condition (6.14a), we determined that the only situation in which the interaction Hamiltonian depends on the product $Na$ is the one in which only two-body interactions are relevant to the physics. If higher-body interactions play a significant role, then the interaction Hamiltonian depends in a more complicated way on $N$ and $a$. Combined with the data in Figure 6.5, this observation implies that only two-body interactions are relevant for the squeezing of the double well system in the parameter regime presented here.

Given the lack of evidence for higher-body interactions in our data, one would expect that the values of $N$ and $a$ sampled would obey condition (6.14a), which says that three- and higher-body interactions should be suppressed as long as

$$N^{1/3}a < a_{ho}. \tag{6.15}$$

The data largely obey this condition, with the exception of one data point for $N = 8$, one for $N = 16$, two for $N = 32$, and three for $N = 64$. Even the few points for which this condition is violated could potentially be saved via the following observation. When we derived the $N$ dependance for the expectation value of the $m$-body interaction Hamiltonian (Eq. (6.5)), we assumed that the part of the expectation value that involved the ladder operators would become $N^m$. However, a detailed calculation would actually result in a value smaller than that (for example, in the Gross-Pitaevskii equation (2.40), the two-body interaction term has a coefficient proportional to $N(N-1)$, not $N^2$). This reduction in the "effective $N$" that should go into condition (6.14a) may make enough of a difference that all of our data ends up in the two-body interaction regime.

The observation that only two-body interactions are relevant in our Monte Carlo results is non-trivial because the form of the hard sphere propagator used in the PIGS simulations, Eq. 5.66, takes into account the interactions of all of the particles with each other simultaneously. Thus, this allows for any number of particles to interact strongly with each other if the simulation's update methods generate and accept a configuration where that number of particles are in close proximity to each other. Contrast this with the multimode models, in which the form of the Hamiltonian itself precludes interactions between more than two bodies.

### 6.2.2 Fragmentation Results

We now move on to our fragmentation and depletion results. In Figure 6.6 we plot the fragmentation parameter $F$ as a function of $a$ for PIGS simulations with the values of $N$, $L$, and $\alpha$ from Section 6.1.1 (except that we do not have $N = 64$ data), along with comparisons to the equivalent exact two-mode and eight-mode models. For weak barriers ($L = 2\,a_{ho}$ and $3\,a_{ho}$), there is a relatively modest amount of fragmentation at large $a$. For $L = 3\,a_{ho}$ and small $N$, there is a relatively large amount of fragmentation for large $a$. The amount of fragmentation decreases with increasing $N$. Additionally, as in the squeezing plots, the amount of fragmentation present does not vary monotonically with $a$.

In Figure 6.7 we plot the depletion parameter $D$ as a function of $a$ in the same way as we plotted $F$ vs. $a$ in Figure 6.6. We see a modest increase in depletion of comparable size across all plots for large values of $a$.

In both the fragmentation and depletion plots, we indicate by vertical lines the values of $a$ for which condition (6.14b) should be satisfied (recall that this is the condition under which the two-mode model should be sufficient to describe the physics of the system). As with the squeezing data, the models and the PIGS results agree well when condition (6.14b) is

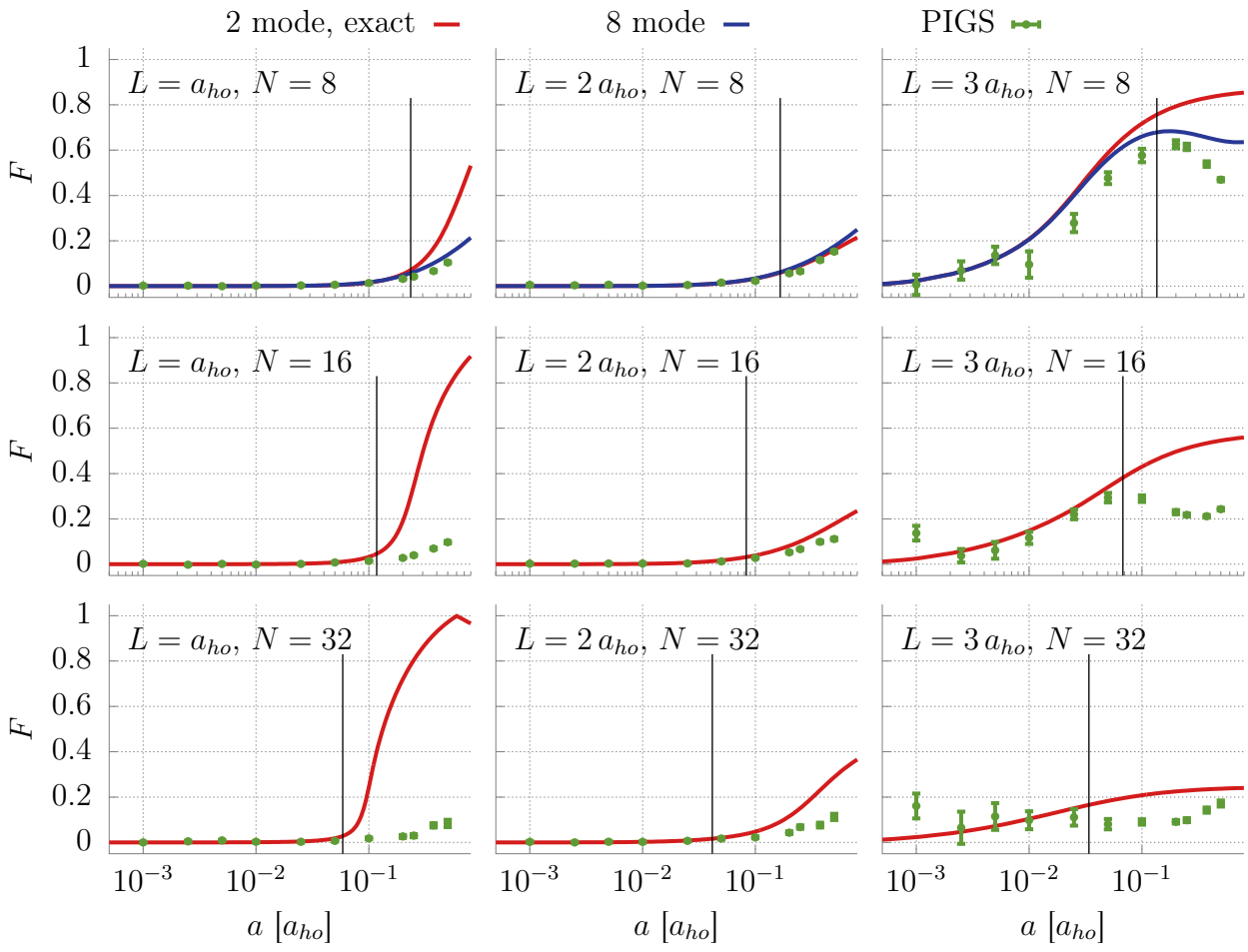


Figure 6.6: Monte Carlo results for the fragmentation parameter $F$ vs. scattering length $a$ for four different particle numbers ($N = 8$, 16, 32, and 64, from top to bottom) and three different potentials ($L = a_{ho}$, $2\,a_{ho}$, and $3\,a_{ho}$, from left to right). The plots include results from the exact two-mode model, the eight-mode model, and the PIGS simulations. Vertical lines indicate the values of $a$ below which we expect the two-mode model to be valid.

satisfied but deviate as $a$ increases. This deviation takes the form of less fragmentation than predicted in the multimode models. In terms of depletion, we see less than in the eight-mode model but more than zero, which is all that is possible for the two-mode model.

Finally, we plot the first and second natural orbitals, $\phi_0(z)$ and $\phi_1(z)$, in Figures 6.8 and 6.9, respectively. These orbitals look similar to the single-body ground and first excited states of the double well (see Figure 3.1), especially for small $N$ and $a$. As is the case for the overall density in Figure 6.3, increases in both $a$ and $N$ tend to cause the natural orbitals to broaden, occupying regions where the potential is larger.

For $L = 2\,a_{ho}$ and $3\,a_{ho}$, the natural orbitals $\phi_1(z)$ plotted in Figure 6.9 are rather noisy;

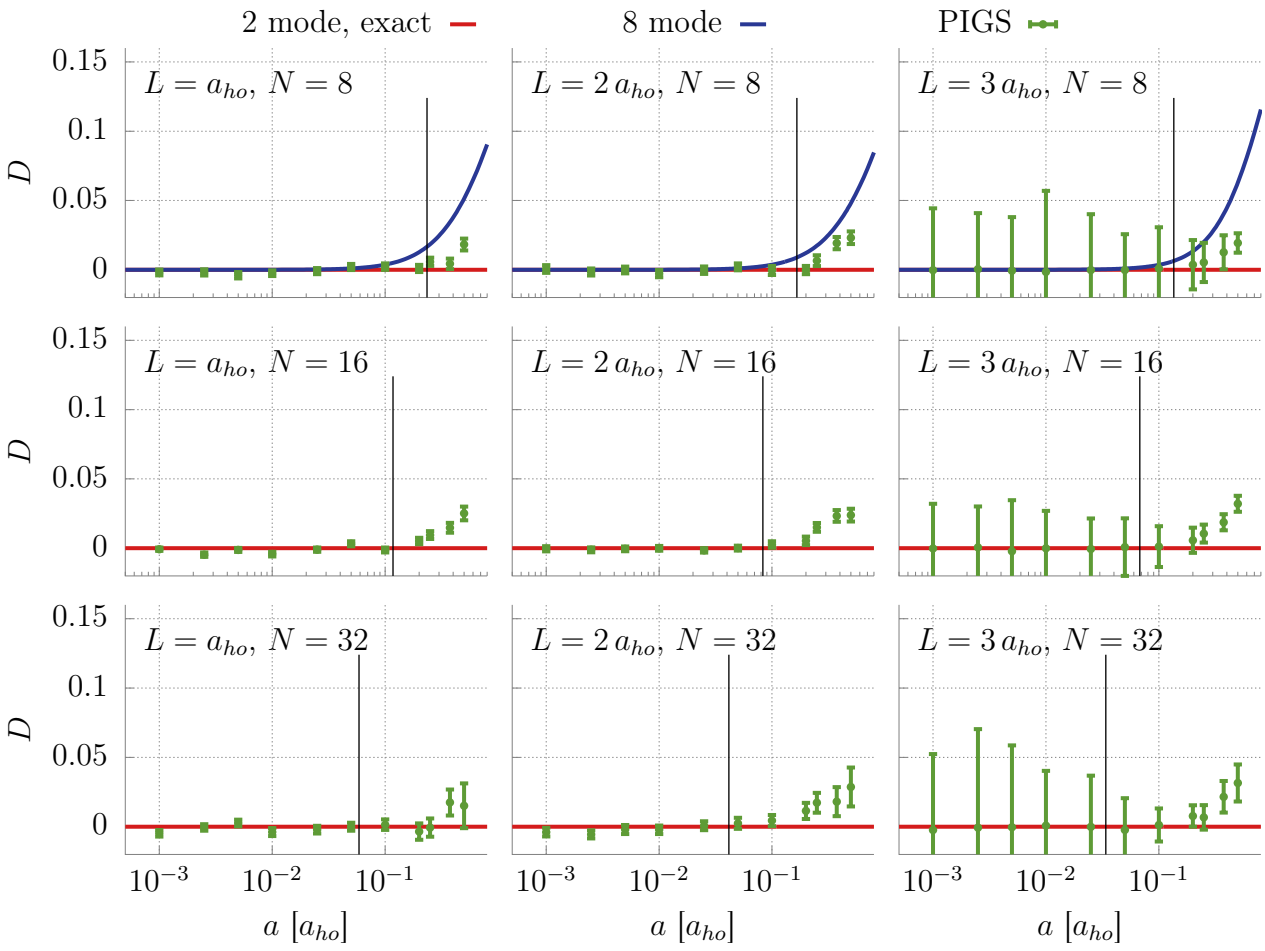


Figure 6.7: Monte Carlo results for the depletion parameter $D$ vs. scattering length $a$ for four different particle numbers ($N = 8$, 16, 32, and 64, from top to bottom) and three different potentials ($L = a_{ho}$, $2\,a_{ho}$, and $3\,a_{ho}$, from left to right). The plots include results from the exact two-mode model, the eight-mode model, and the PIGS simulations. Vertical lines indicate the values of $a$ below which we expect the two-mode model to be valid.

indeed, we did not plot the $a = 10^{-4}\, a_{ho}$ and $0.01\, a_{ho}$ natural orbitals for those potentials because they were so noisy as to be unrecognizable. For these potentials, the low amount of fragmentation means that the OBDM contains very little information about natural orbitals beyond $\phi_0(z)$. Hence, when one numerically diagonalizes the OBDM matrix, one generates noisy functions for the $\phi_1(z)$ natural orbital and beyond. For $L = 3\, a_{ho}$, however, there is enough fragmentation in the system to recover smooth plots for $\phi_1(z)$.

**Discrepancy Between PIGS and Multimode Models**

The deviation of the PIGS data from the multimode models is apparent in both the fragmentation and depletion data. In general, we see much less fragmentation than predicted by the two-mode model, and we also see roughly the same amount of depletion in the system regardless of $N$ and $L$.

The reduction in fragmentation can be accounted for via both of the mechanisms described in Section 6.2.1. As we discussed in Section 2.4.2, fragmentation in the double well system increases the more "isolated" the wells are, that is, the less likely it is for a particle to tunnel from one well to the other. This is the reason why potentials with larger $L$ experience more fragmentation. The first mechanism entails the occupation of modes with higher values of $n$, some of which have more spillover into the "wrong" side of the double well than the $n = 1$ modes. Hence, the occupation of these modes will lessen the isolation of the wells by putting atoms in states that span both sides of the double well barrier. This will reduce fragmentation.

Additionally, the structure of the two-mode fragmentation parameter Eq. (3.45a) is such that $F^{(2)}$ is large when the ground state is striped, that is, when every other Fock state is occupied. This is only possible for small $L$. The second mechanism involves the presence of many two-body tunneling terms in the double well Hamiltonian due to the addition of modes beyond $n = 1$, and these terms prevent the system from forming a striped state as we discussed above. Hence, this effect causes a dramatic reduction in fragmentation compared with the two-mode model for small $L$.

Finally, we comment on the degree of depletion seen in the PIGS data. From Bogoliubov's analysis, we know that depletion begins to become significant in a homogeneous BEC when the quantity $an^{1/3}$ approaches 1 (see condition (6.14c)). In Figure 6.10, we plot this quantity for our PIGS data as a function of the scattering length. We approximate $n$ as the maximum value of the quantity $N\rho_x(x)\rho_y(y)\rho_z(z)$, where $\rho_i$ is the single-body density in the $i$ direction, and we choose the maximum value because depletion will be dominated by the parts of the BEC where the density is greatest. The figure illustrates that $an^{1/3}$ is very close to 1 for large values of $a$ and that $n(a)$ is essentially independent of $N$ and $L$. This is all completely consistent with the depletion results we see in Figure 6.7.

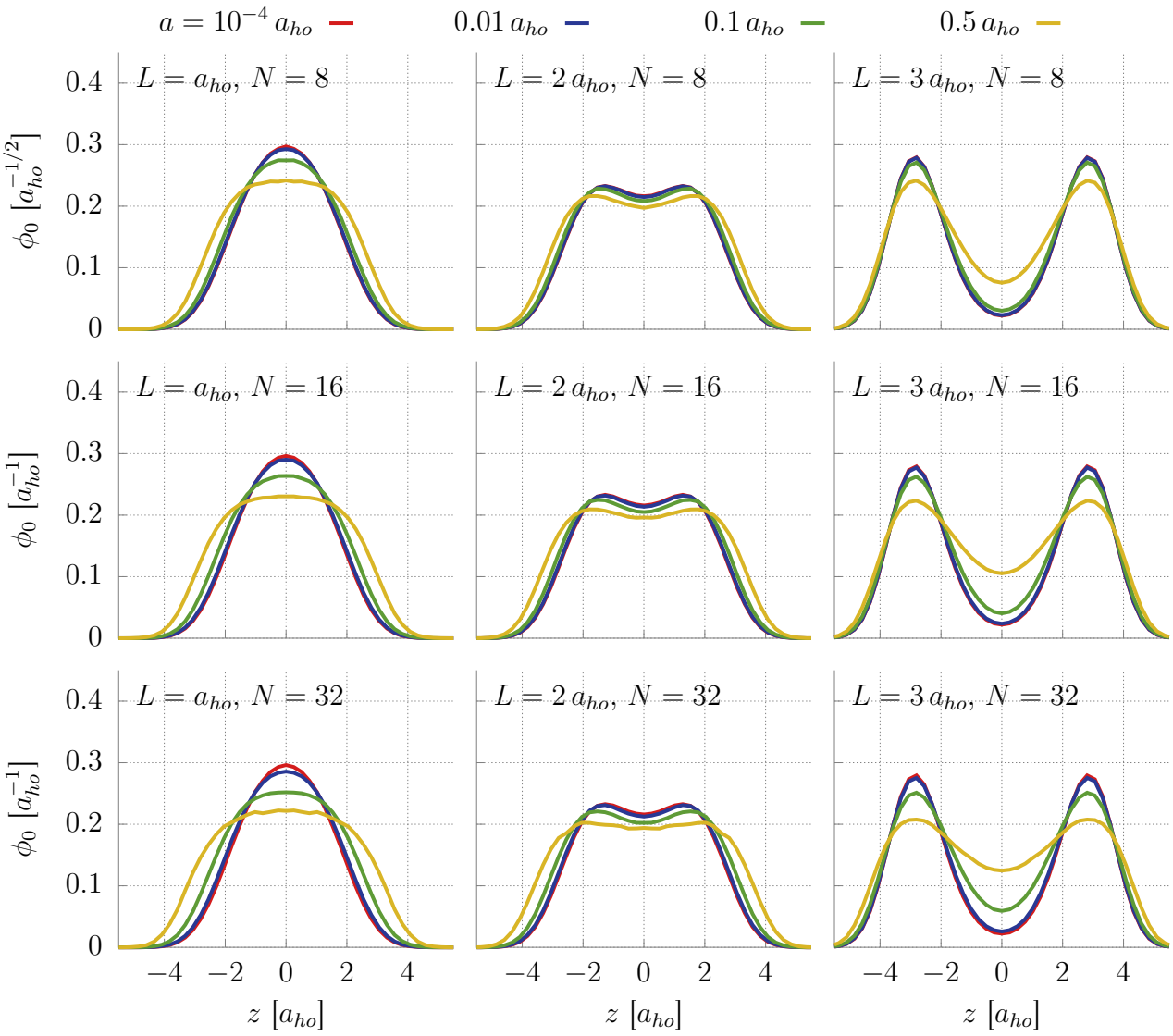


Figure 6.8: Monte Carlo results for the first natural orbital in the $z$ direction $\phi_0(z)$ as a function of coordinate $z$ for three different particle numbers ($N = 8$, 16, and 32, from top to bottom) and three different potentials ($L = a_{ho}$, $2\, a_{ho}$, and $3\, a_{ho}$, from left to right). Each plot include data for four representative values of the scattering length $a$ ($10^{-4}\, a_{ho}$, $0.01\, a_{ho}$, $0.1\, a_{ho}$, and $0.5\, a_{ho}$) that span the range of interaction strengths that we simulated.

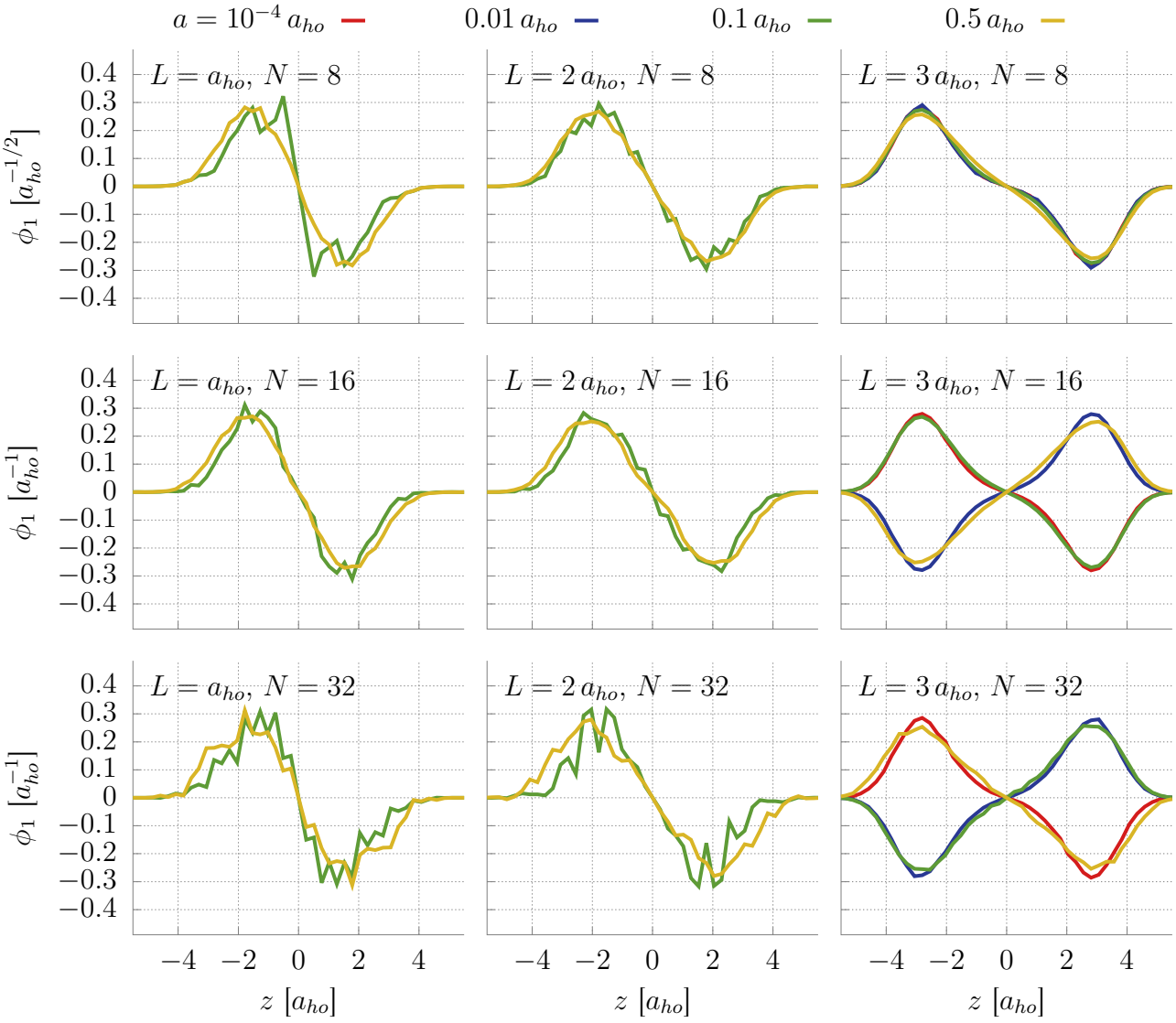


Figure 6.9: Monte Carlo results for the second natural orbital in the $z$ direction $\phi_1(z)$ as a function of coordinate $z$ for three different particle numbers ($N = 8$, 16, and 32, from top to bottom) and three different potentials ($L = a_{ho}$, $2\,a_{ho}$, and $3\,a_{ho}$, from left to right). Each plot include data for two values of the scattering length $a$ ($0.1\,a_{ho}$ and $0.5\,a_{ho}$). The $L = 3\,a_{ho}$ plots additionally include data for two other values of $a$ ($10^{-4}\,a_{ho}$ and $0.01\,a_{ho}$) although the resulting plots are so similar that they overlap almost completely. All together, there four values of $a$ span the range of interaction strengths that we simulated.

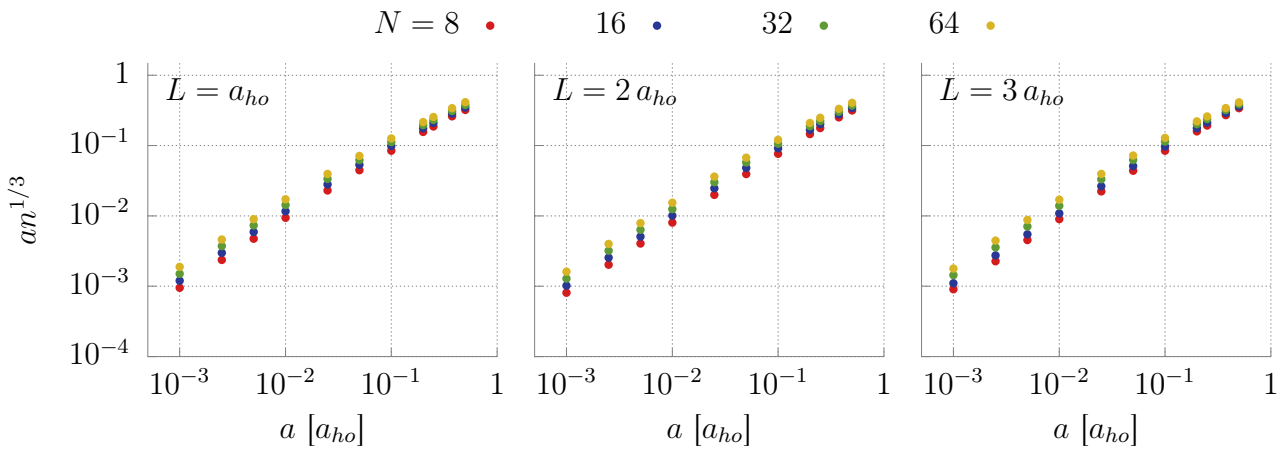


Figure 6.10: Monte Carlo results for the dimensionless quantity $an^{1/3}$ vs. scattering length $a$ for four different particle numbers ($N = 8$, 16, 32, and 64) and three different potentials ($L = a_{ho}$, $2\,a_{ho}$, and $3\,a_{ho}$, from left to right). The condition $an^{1/3} \ll 1$ specifies the condition under which depletion should be negligible in a homogeneous BEC. Notice that the relationship between $an^{1/3}$ and $a$ is essentially unaffected by changes in $N$ or $L$.

## 6.3 Conclusions and Outlook

In this work, we made a detailed study of the squeezing and fragmentation exhibited by the ground state of an ultracold, bosonic atomic gas in a double well trap. While these properties have been studied previously in the context of mean-field and two-mode models, we have greatly extended this analysis here by more deeply studying the two-mode model, by investigating squeezing and fragmentation phenomena in a recently-proposed eight-mode model, and by using quantum Monte Carlo methods to simulate the system for a variety of particle number, interaction strengths, and double well trap geometries. We discovered a number of interesting and surprising facts about these systems, including the fact that squeezing and fragmentation do not monotonically increase with interaction strength.

The observations and intuition about the double well system that we have derived from this study can be summarized as an updating of the intuitive picture of how squeezing and fragmentation in these systems come about. Recall that the suppression of number fluctuations corresponds to increased squeezing and the suppression of tunneling corresponds to increased fragmentation. Both the old and the new picture start the same way:

> The ground state of the noninteracting double well is a product of the single-body ground state of each particle, and these single-body states each occupy both wells equally. Hence, if one were to measure the number of atoms in the left well minus the number in the right well, one could get any value from $N$ to $-N$. Therefore, number fluctuations are large and squeezing is small. An equivalent way to think of this situation is that the structure of the noninteracting ground state is such

> that tunneling is strong, and therefore fragmentation is small. In fact, both $S$ and $F$ are defined to be 0 in the noninteracting case.

In the old picture, the introduction of repulsive interacting proceeds like this:

> The introduction of repulsive interactions causes the system to minimize its interacting energy by suppressing configurations in which many particles are in one well and few are on the other. This reduces number fluctuations and increases squeezing. Additionally, moving towards a configuration in which $N/2$ particles are locked into each side of the double well suppresses tunneling and increases fragmentation. These effects increase with increasing interacting strength.

whereas in the new picture, it proceeds like this:

> The introduction of repulsive interactions causes the system to minimize its interacting energy, but it can do this in several ways. One way is to suppress configurations in which many particles are in one well and few are on the other. This increases squeezing and fragmentation as in the old picture. Additionally, the system can also reduce its interaction energy by promoting atoms to modes in higher energy levels ($n > 1$). One can approximate these modes as each being localized in one of the two wells, although they will extend into the "wrong" well based on the strength of the double well barrier. There are some modes in each energy band $n > 1$ that extend into the wrong well much further than the $n = 1$ modes. Hence, a ground state dominated by modes with larger values of $n$ naturally have larger number fluctuations and tunneling than ground states dominated by $n = 1$ modes, and therefore they exhibit less squeezing and fragmentation. These two effects compete with each other to determine the overall amount of squeezing and fragmentation, which is not monotonic in many cases.

Thus, for sufficiently large enough values of $a$, one cannot appeal to either mean-field or multi-mode modes to correctly predict the amount of squeezing and fragmentation exhibited by the system. Instead, the full machinery of quantum Monte Carlo must be deployed.

Finally, we would like to connect back with one of the main motivations of this project as discussed in Section 1.1: the application of squeezed states to reduce the measurement uncertainty of atom interferometers. In general, the more squeezed the states used in the interferometers, the smaller the uncertainty. One way to generate a highly squeezed state is to use a Feshbach resonance to tune the interaction strength of the atoms in a BEC, thereby changing the amount of squeezing exhibited by the system. But, what interaction strength is the one that maximizes squeezing? In the context of the old picture described above, the answer is simple: stronger repulsive interactions mean more squeezing, so one should tune $a$ to as large a value as one can. However, we have shown that the real picture is more complicated: squeezing does not increase monotonically with interaction strength in many situations, and so there is some optimal value of $a$ that maximizes squeezing that one cannot

predict through the use of multimode models but must instead calculate using an exact method like PIGS. With the increasingly rapid advances of experimental methods for the study Bose-Einstein condensates, we look forward to laboratory confirmation of the results of this study in the near future.

# Appendix A

# Entanglement Entropy

In this Appendix, we discuss a proposed extension of the work discussed in this dissertation: the computation of the entanglement entropy between the two halves of the ground state of the double well system using a new PIGS method that we propose below.

## A.1 Introduction

This dissertation focuses on the study of two particular ground state quantum properties, squeezing and fragmentation, but there are of course many other properties of a quantum system that one might be interested in understanding. One such property that has garnered significant attention is entanglement. At a fundamental level, entanglement is the main phenomenon that distinguishes quantum from classical systems, so one can potentially gain significant insights into the nature of quantum mechanics and quantum information by studying it. However, it is not entirely clear how one can directly measure the entanglement in a quantum system experimentally, since it is a fundamentally nonlocal quantity.

One recent proposal for estimating the entanglement between two subregions of a quantum system involves measuring the fluctuations of observables that are relatively easily accessible to experiment [104, 105]. In particular, one can relate the particle number fluctuations across the boundary between two entangled subregions of a free fermion system in any number of dimensions to the system's Rényi entropy $S_n$, which is a family of related quantities indexed by an integer $n$ that can be used as a measure of the entanglement between the subregions [106, 107]. One problem with this method, however, is that the exact relationship between the number fluctuations and the Rényi entropy is not known for interacting systems, so one does not know how strong the interactions can become before laboratory estimates of the entanglement based on the fluctuations become unreliable.

This suggests that one should attempt to simulate a system of interest using quantum Monte Carlo methods to measure the Rényi entropy directly. However, until very recently, it was not at all clear how one could do this. The first successful proposal was implemented in a lattice system, specifically a Heisenberg chain, and involved the introduction of a new

operator, called the SWAP operator, whose expectation value is related to the $S_2$ Rényi entropy [108]. This method was very recently generalized for use in continuous-space QMC simulations of fermions [109–111]. A different method which does not rely on the SWAP operator has also been developed, but only for finite-temperature systems [112]. We now propose a generalization of the SWAP operator method suitable for studying the entanglement exhibited by the bosonic double well system using the PIGS QMC method. Using this method, the entanglement entropy for a system like the double well can be computed exactly, and the result can be compared to the entanglement entropy estimated via number fluctuations to reveal the limit beyond which this estimate fails.

## A.2 Estimation of Entanglement from Number Fluctuations

We will first discuss a method for estimating entanglement, via the Rényi entropy, from the number fluctuations. Reference [106] provides an excellent and thorough overview of the computation of Rényi entropy from the fluctuations of several different quantities for a variety of fermionic systems.

The starting point for these estimates is a system in a pure quantum state $|\psi\rangle$ that has been bi-partitioned into two subsystems, $A$ and $B$. One can compute the reduced density matrix of subsystem $A$ by tracing over the degrees of freedom in subsystem $B$:

$$\hat{\rho}_A = \mathrm{Tr}_B \, |\psi\rangle \langle\psi| \, . \tag{A.1}$$

Then the Rényi entanglement entropy is defined as

$$S_n(\hat{\rho}_A) = \frac{1}{1-n} \ln(\mathrm{Tr}(\hat{\rho}_A^n)), \tag{A.2}$$

which reduces to the von Neumann entropy in the $n \to 1$ limit:

$$S_1(\hat{\rho}_A) = -\,\mathrm{Tr}(\hat{\rho}_A \ln \hat{\rho}_A). \tag{A.3}$$

For a system in which particles can pass through the boundary between the $A$ and $B$ subregions, the fluctuations in the number of particles in the $A$ subregion is related to the Rényi entropy. In particular, one can define the *cumulant*

$$\begin{aligned} C_n &= \left(-i\frac{\partial}{\partial\lambda}\right)^n \ln \langle e^{i\lambda\hat{N}_A}\rangle \Big|_{\lambda=0} \\ &= \sum_{\sum_{1\le i\le n} n m_n = n} \frac{(-1)^{m_1+\cdots+m_n-1}(m_1+\cdots+m_n-1)!\,n!}{m_1!\cdots m_n!} \prod_{1\le j\le n} \left(\frac{1}{j!}\langle \hat{N}_A^j\rangle\right)^{m_j} \end{aligned} \tag{A.4}$$

where $\hat{N}_A$ is the operator that measures the number of particles in the $A$ subregion and where we derive the second line by using Faà di Bruno's formula [113]. The sum in this formula

is taken over all sets of non-negative integers $\{m_1, \ldots, m_n\}$ that satisfy the given condition, $\sum_{1 \leq i \leq n} n m_n = n$. The Rényi entropy is then given by [114]

$$S_n = \frac{2}{n-1} \sum_{k=1}^{\infty} \frac{1}{k!} \left( \frac{2\pi i}{n} \right)^k \zeta \left( -k, \frac{n+1}{2} \right) C_k, \tag{A.5}$$

where $\zeta(p, q)$ is the Hurwitz zeta function [115]. So, if one knows all of the cumulants of the system, and therefore everything about the number fluctuations, one can compute the value of the Rényi entropy for any $n$.

### A.2.1 Application to Double Well System

In the case of the double well system, the natural $A$ and $B$ subsystems are the left and right sides of the double well. In that case, we can identify $\hat{N}_A$ with $\hat{L}$ (defined in Eq. (2.52)), and a straightforward calculation shows that

$$C_2 = \sigma_n^2 = \frac{N}{4}(1 - S). \tag{A.6}$$

This is, of course, a quantity that our Monte Carlo simulation can already compute. Moreover, higher cumulants can be computed in terms of higher powers of $\langle \hat{L}^i \rangle$, which are all trivial to compute in the simulation as well. However, remember that Eq. (A.5) relates the Rényi entropy to the cumulants for a noninteracting system of fermions. In order to make this computation applicable to a BEC in a double well, one would have to derive the equivalent expression for a noninteracting system of bosons. This will be a topic for future work.

## A.3 Computation of Entanglement with Quantum Monte Carlo

We now describe a method for computing the Rényi entropy directly using quantum Monte Carlo. Reference [108] describes the initial implementation of this method, which involves the introduction of a new SWAP operator, which we will denote as $\hat{\mathcal{S}}$. After a general discussion of the technique, we will specialize to the case of the bosonic double well system.

The SWAP operator is defined on a space that includes the system of interest and a copy of that system that does not interact with the original. The Hamiltonian for the doubled system is given by $\hat{\mathcal{H}} = \hat{H} \oplus \hat{H}$, where $\hat{H}$ is the Hamiltonian for the system or its copy, which are identical. The states in this space are tensor products of the states in each copy: $|\Psi\rangle = |\psi\rangle \otimes |\tilde{\psi}\rangle$, where the tilde indicates the state of the copy. Each system is divided into two subregions: $A$ and $B$. If we assume that the state of each system can be decomposed into a product of a state in the $A$ region and a state in the $B$ region, then the SWAP operator acting on a generic state in the total space interchanges the states associated with the $A$ regions:

$$\hat{\mathcal{S}} |\psi_A\rangle |\psi_B\rangle \otimes |\tilde{\psi}_A\rangle |\tilde{\psi}_B\rangle = |\tilde{\psi}_A\rangle |\psi_B\rangle \otimes |\psi_A\rangle |\tilde{\psi}_B\rangle . \tag{A.7}$$

Suppose that both the system and its copy are in the same state $|\psi\rangle$. Then the overall state of the doubled system is given by $|\Psi\rangle = |\psi\rangle \otimes |\psi\rangle$, and one can show that [108]

$$S_2(\hat{\rho}_A) = -\ln(\mathrm{Tr}(\hat{\rho}_A^2)) = -\ln \langle \Psi | \hat{\mathcal{S}} | \Psi \rangle \,. \tag{A.8}$$

So computing the expectation value of $\hat{\mathcal{S}}$ in the doubled system is equivalent to computing the $S_2$ Rényi entropy.

### A.3.1 Application to PIGS

Recall that in PIGS, we compute expectation values of operators in (an approximation to) the system's ground state. To generalize the PIGS method we describe in Chapter 5 for use with the SWAP operator, we run a simulation that keeps track of $2N$ particles, where the first $N$ are the particles in the original system and the last $N$ are the particles in the copy. We denote a position eigenstate of the system by the $6N$-dimensional state vector $|\mathcal{R}\rangle$, so that

$$|\mathcal{R}\rangle = |\mathbf{r}_1, \ldots, \mathbf{r}_N\rangle \otimes |\tilde{\mathbf{r}}_1, \ldots, \tilde{\mathbf{r}}_N\rangle \,. \tag{A.9}$$

We impose the same real, $N$-body, symmetrized trial function on each copy, so that the overall trial function can be written as $|\Psi_T(\mathcal{R})\rangle = |\psi_T(R)\rangle \otimes |\psi_T(\tilde{R})\rangle$. Because of the structure of the Hamiltonian $\hat{\mathcal{H}}$, the imaginary time propagator for the doubled system is given by

$$\begin{aligned} \mathcal{G}(\mathcal{R}, \mathcal{R}', \beta) &= \langle \mathcal{R} | e^{-\beta \hat{\mathcal{H}}/\hbar} | \mathcal{R}' \rangle \\ &= \langle \mathcal{R} | e^{-\beta \hat{H}/\hbar} \otimes e^{-\beta \hat{H}/\hbar} | \mathcal{R}' \rangle \\ &= \langle R | e^{-\beta \hat{H}/\hbar} | R' \rangle \, \langle \tilde{R} | e^{-\beta \hat{H}/\hbar} | \tilde{R}' \rangle \\ &= G(R, R', \beta) G(\tilde{R}, \tilde{R}', \beta). \end{aligned} \tag{A.10}$$

It is a product of the imaginary time propagators for each system individually. With these components in hand, we can construct the analogous expression to Eq. (5.7) for the SWAP operator in the doubled system:

$$\begin{aligned} \langle \chi | \hat{\mathcal{S}} | \chi \rangle = \int \Psi_T(\mathcal{R}_0) \prod_{i=0}^{M-1} \mathcal{G}(\mathcal{R}_i, \mathcal{R}_{i+1}, \beta) \, \langle \mathcal{R}_M | \hat{\mathcal{S}} | \mathcal{R}_{M+1} \rangle \\ \times \prod_{j=M+1}^{2M} \mathcal{G}(\mathcal{R}_j, \mathcal{R}_{j+1}, \beta) \Psi_T(\mathcal{R}_{2M+1}) \, d\mathcal{R}_0 \ldots d\mathcal{R}_{2M+1}, \end{aligned} \tag{A.11}$$

To understand how to simplify the expression for $\langle \chi | \hat{\mathcal{S}} | \chi \rangle$, we first need to understand how the SWAP operator acts on $|\mathcal{R}\rangle$. Suppose that the system is in a state such that particles 1 through $\alpha$ are in the $A$ region of the system and particles 1 through $\tilde{\alpha}$ are in the $A$ region of the copy. Then we can write $|\mathcal{R}\rangle$ as

$$|\mathcal{R}\rangle = |\mathbf{r}_1, \ldots, \mathbf{r}_\alpha\rangle \, |\mathbf{r}_{\alpha+1}, \ldots, \mathbf{r}_N\rangle \otimes |\tilde{\mathbf{r}}_1, \ldots, \tilde{\mathbf{r}}_{\tilde{\alpha}}\rangle \, |\tilde{\mathbf{r}}_{\tilde{\alpha}+1}, \ldots, \tilde{\mathbf{r}}_N\rangle \,, \tag{A.12}$$

where we allow $\alpha$ and $\tilde{\alpha}$ to range from 0 to $N$ and we use $|\Omega\rangle$ to denote the "empty" state that results from all of the particles being in either the $A$ region ($\alpha$ or $\tilde{\alpha} = N$) or the $B$ region ($\alpha$ or $\tilde{\alpha} = 0$). With this form of $|\mathcal{R}\rangle$, the SWAP operator simply interchanges the states that correspond to the $A$ regions:

$$\begin{aligned}\hat{\mathcal{S}}\,|\mathcal{R}\rangle &= \hat{\mathcal{S}}\,|\mathbf{r}_1,\ldots,\mathbf{r}_\alpha\rangle\,|\mathbf{r}_{\alpha+1},\ldots,\mathbf{r}_N\rangle \otimes |\tilde{\mathbf{r}}_1,\ldots,\tilde{\mathbf{r}}_{\tilde{\alpha}}\rangle\,|\tilde{\alpha}_{\tilde{n}+1},\ldots,\tilde{\mathbf{r}}_N\rangle \\ &= |\tilde{\mathbf{r}}_1,\ldots,\tilde{\mathbf{r}}_{\tilde{\alpha}}\rangle\,|\mathbf{r}_{\alpha+1},\ldots,\mathbf{r}_N\rangle \otimes |\mathbf{r}_1,\ldots,\mathbf{r}_\alpha\rangle\,|\tilde{\mathbf{r}}_{\tilde{\alpha}+1},\ldots,\tilde{\mathbf{r}}_N\rangle\,. \end{aligned} \tag{A.13}$$

We can use this result to compute $\langle\mathcal{R}|\hat{\mathcal{S}}|\mathcal{R}'\rangle$:

$$\begin{aligned}\langle\mathcal{R}|\hat{\mathcal{S}}|\mathcal{R}'\rangle &= (\langle\mathbf{r}_1,\ldots,\mathbf{r}_\alpha|\,\langle\mathbf{r}_{\alpha+1},\ldots,\mathbf{r}_N| \otimes \langle\tilde{\mathbf{r}}_1,\ldots,\tilde{\mathbf{r}}_{\tilde{\alpha}}|\,\langle\tilde{\mathbf{r}}_{\tilde{\alpha}+1},\ldots,\tilde{\mathbf{r}}_N|) \\ &\quad\times \left(|\tilde{\mathbf{r}}'_1,\ldots,\tilde{\mathbf{r}}'_{\tilde{\alpha}'}\rangle\,|\mathbf{r}'_{\alpha'+1},\ldots,\mathbf{r}'_N\rangle \otimes |\mathbf{r}'_1,\ldots,\mathbf{r}'_{\alpha'}\rangle\,|\tilde{\mathbf{r}}'_{\tilde{\alpha}'+1},\ldots,\tilde{\mathbf{r}}'_N\rangle\right) \\ &= \langle\mathbf{r}_1,\ldots,\mathbf{r}_\alpha|\tilde{\mathbf{r}}'_1,\ldots,\tilde{\mathbf{r}}'_{\tilde{\alpha}'}\rangle\,\langle\mathbf{r}_{\alpha+1},\ldots,\mathbf{r}_N|\mathbf{r}'_{\alpha'+1},\ldots,\mathbf{r}'_N\rangle \\ &\quad\times \langle\tilde{\mathbf{r}}_1,\ldots,\tilde{\mathbf{r}}_{\tilde{\alpha}}|\mathbf{r}'_1,\ldots,\mathbf{r}'_{\alpha'}\rangle\,\langle\tilde{\mathbf{r}}_{\tilde{\alpha}+1},\ldots,\tilde{\mathbf{r}}_N|\tilde{\mathbf{r}}'_{\tilde{\alpha}'+1},\ldots,\tilde{\mathbf{r}}'_N\rangle\,. \end{aligned} \tag{A.14}$$

This expression is nonzero only when $\alpha = \tilde{\alpha} = \alpha' = \tilde{\alpha}'$. In that situation, it simplifies to

$$\begin{aligned}\langle\mathcal{R}|\hat{\mathcal{S}}|\mathcal{R}'\rangle &= \prod_{i=1}^{\alpha} \delta(\mathbf{r}_i - \tilde{\mathbf{r}}'_i)\,\delta(\tilde{\mathbf{r}}_i - \mathbf{r}'_i) \prod_{j=\alpha+1}^{N} \delta(\mathbf{r}_j - \mathbf{r}'_j)\,\delta(\tilde{\mathbf{r}}_j - \tilde{\mathbf{r}}'_j) \\ &= \delta(R_A - \tilde{R}'_A)\,\delta(\tilde{R}_A - R'_A)\,\delta(R_B - R'_B)\,\delta(\tilde{R}_B - \tilde{R}'_B), \end{aligned} \tag{A.15}$$

where $R_A = \{\mathbf{r}_1,\ldots,\mathbf{r}_\alpha\}$, $R_B = \{\mathbf{r}_{\alpha+1},\ldots,\mathbf{r}_N\}$, and so on.

We can use this result to simplify integrals of the form

$$I = \int f(\mathcal{R})g(\mathcal{R}')\,\langle\mathcal{R}|\hat{\mathcal{S}}|\mathcal{R}'\rangle\; d\mathcal{R}\,d\mathcal{R}', \tag{A.16}$$

of which $\langle\chi|\hat{\mathcal{S}}|\chi\rangle$, Eq. (A.11), is an example. Notice that this quantity involves integration over four sets of particle coordinates: $R$, $\tilde{R}$, $R'$, and $\tilde{R}'$. The integral for each individual coordinate can be expressed as the sum of an integral over the $A$ region plus an integral over the $B$ region. Hence, the integration region for the entire integral can be broken up into $2^{4N}$ subregions, where for each subregion each of the $4N$ particle position vectors is integrated over either region $A$ or region $B$. The total integral is the sum of these subintegrals.

For any given subintegral, a certain number of coordinates in each of $R$, $\tilde{R}$, $R'$, and $\tilde{R}'$ are integrated over the $A$ region, and in general these numbers are different. However, because of the form of $\langle\mathcal{R}|\hat{\mathcal{S}}|\mathcal{R}'\rangle$, the only nonzero subintegrals are the ones in which these four numbers are the same; let's call that number $\alpha$. Because of Bose symmetry, all subintegrals with the same $\alpha$ are equal to each other. For a given $\alpha$ and $N$, the number of such equivalent integrals is $\binom{N}{\alpha}^4$. Since they are all equivalent, we can choose one to be the single integral that we compute; we choose the integral in which the first $\alpha$ particles in each set of coordinates

are integrated over region $A$. Then, for convenience, we define a compact notation for this integration:

$$\int_{N,\alpha} f(\mathcal{R})\, dR\, d\tilde{R} = \overbrace{\underbrace{\int_A \cdots \int_A}_{\alpha \text{ integrals}} \int_B \cdots \int_B}^{N \text{ integrals}} \overbrace{\underbrace{\int_A \cdots \int_A}_{\alpha \text{ integrals}} \int_B \cdots \int_B}^{N \text{ integrals}} f(\mathcal{R})\, dR\, d\tilde{R}. \tag{A.17}$$

With this definition, we can simplify Eq. (A.16):

$$\begin{aligned} I &= \int f(\mathcal{R}) g(\mathcal{R}') \langle \mathcal{R}|\hat{\mathcal{S}}|\mathcal{R}'\rangle \; d\mathcal{R}\, d\mathcal{R}' \\ &= \sum_{\alpha=0}^{N} \binom{N}{\alpha}^4 \int_{N,\alpha} \int_{N,\alpha} f(\mathcal{R}) g(\mathcal{R}') \langle \mathcal{R}|\hat{\mathcal{S}}|\mathcal{R}'\rangle \; d\mathcal{R}\, d\mathcal{R}' \\ &= \sum_{\alpha=0}^{N} \binom{N}{\alpha}^4 \int_{N,\alpha} \int_{N,\alpha} f(\mathcal{R}) g(\mathcal{R}') \delta(R_A - \tilde{R}'_A)\, \delta(\tilde{R}_A - R'_A) \delta(R_B - R'_B)\, \delta(\tilde{R}_B - \tilde{R}'_B)\, d\mathcal{R}\, d\mathcal{R}' \\ &= \sum_{\alpha=0}^{N} \binom{N}{\alpha}^4 \int_{N,\alpha} f(\mathcal{R}) g(\overline{\mathcal{R}}_\alpha)\, d\mathcal{R}, \end{aligned} \tag{A.18}$$

where

$$\overline{\mathcal{R}}_\alpha = \{\tilde{R}_A, R_B, R_A, \tilde{R}_B\}, \tag{A.19}$$

is the swapped version of $\mathcal{R} = \{R_A, R_B, \tilde{R}_A, \tilde{R}_B\}$, and the $\alpha$ subscript reminds us that the exact set of coordinates that are swapped (i.e., the set of coordinates that constitute $R_A$) depends on $\alpha$. As written, it is not possible to compute Eq. (A.18) using PIGS because of the restricted integration region. However, this is easy to fix. By defining functions $A(\mathbf{r})$ and $B(\mathbf{r})$ such that

$$A(\mathbf{r}_i) = \begin{cases} 1 & \mathbf{r}_i \text{ in region } A \\ 0 & \text{otherwise} \end{cases} \tag{A.20a}$$

$$B(\mathbf{r}_i) = \begin{cases} 1 & \mathbf{r}_i \text{ in region } B \\ 0 & \text{otherwise} \end{cases}, \tag{A.20b}$$

we can replace the restricted integration with a function $\mathcal{O}_N(\mathcal{R})$:

$$I = \int f(\mathcal{R})\, \mathcal{O}_N(\mathcal{R})\, d\mathcal{R}, \tag{A.21}$$

where

$$\mathcal{O}_N(\mathcal{R}) = \sum_{\alpha=0}^{N} \binom{N}{\alpha}^4 g(\overline{\mathcal{R}}_\alpha) \left( \prod_{i=1}^{\alpha} A(\mathbf{r}_i) A(\tilde{\mathbf{r}}_i) \prod_{j=\alpha+1}^{N} B(\mathbf{r}_j) B(\tilde{\mathbf{r}}_j) \right). \tag{A.22}$$

Finally, we can use this to reexpress $\langle\chi|\hat{\mathcal{S}}|\chi\rangle$ as

$$\langle\chi|\hat{\mathcal{S}}|\chi\rangle = \int \Psi_T(\mathcal{R}_0) \prod_{i=0}^{M-1} \mathcal{G}(\mathcal{R}_i, \mathcal{R}_{i+1}, \beta)\, \mathcal{O}_N(\mathcal{R}_M, \mathcal{R}_{M+1}) \times \prod_{j=M+1}^{2M-1} \mathcal{G}(\mathcal{R}_j, \mathcal{R}_{j+1}, \beta)\Psi_T(\mathcal{R}_{2M})\, d\mathcal{R}_0 \ldots d\mathcal{R}_{2M}. \tag{A.23}$$

where

$$\mathcal{O}_N(\mathcal{R}_M, \mathcal{R}_{M+1}) = \sum_{\alpha=0}^{N} \binom{N}{\alpha}^4 \mathcal{G}(\overline{\mathcal{R}}_{\alpha,M}, \mathcal{R}_{M+1}, \beta) \left( \prod_{i=1}^{\alpha} A(\mathbf{r}_i)A(\tilde{\mathbf{r}}_i) \prod_{j=\alpha+1}^{N} B(\mathbf{r}_j)B(\tilde{\mathbf{r}}_j) \right). \tag{A.24}$$

Therefore, we can compute the expectation value of the SWAP operator with PIGS by sampling the observable $\mathcal{O}_N(\mathcal{R}_M, \mathcal{R}_{M+1})$ over a probability distribution

$$\pi(\mathcal{X}) = \Psi_T(\mathcal{R}_0)\Psi_T(\mathcal{R}_{2M}) \prod_{i=0}^{M-1} \mathcal{G}(\mathcal{R}_i, \mathcal{R}_{i+1}, \beta) \prod_{j=M+1}^{2M-1} \mathcal{G}(\mathcal{R}_j, \mathcal{R}_{j+1}, \beta), \tag{A.25}$$

and averaging the accepted values. In terms of update methods, one can use whatever methods are appropriate to sample the single system (see the discussion of these methods in Section 5.3.3) and apply them to the doubled system by randomly choosing whether to update the system or its copy with each iteration of the Monte Carlo algorithm.

### A.3.2 Application to Double Well System

To apply this to the double well system, we define the $A$ subregion as the left half of the double well and the $B$ subregion as the right half. Then the functions $A(\mathbf{r}_i)$ and $B(\mathbf{r}_i)$ in Eq. (A.24) are given by

$$A(\mathbf{r}_i) = \begin{cases} 1 & z_i < 0 \\ 0 & z_i > 0 \end{cases} \tag{A.26a}$$

$$B(\mathbf{r}_i) = \begin{cases} 0 & z_i < 0 \\ 1 & z_i > 0 \end{cases}. \tag{A.26b}$$

The challenges inherent in ergodically sampling the double well system, especially one with a strong barrier, persist in this computation.

## A.4 Summary

In this appendix, we discussed a possible extension to our double well project to study the degree of entanglement exhibited by the system as a function of interaction strength. The

main thrust of the extension would be to compare two different calculation of the $S_2$ Rényi entanglement entropy: one estimated calculation based on cumulants related to number fluctuations and one exact calculation using quantum Monte Carlo. The main tasks that still need to be done are:

- Derive the equivalent expression to Eq. (A.5) relating the cumulants and Rényi entropies of a noninteracting bosonic system.
- Implement the PIGS method for calculating the expectation value of the SWAP operator to directly compute the entanglement entropy of the double well system as a function of interaction strength.

# Bibliography


[1] M. Planck. "Ueber das Gesetz der Energieverteilung im Normalspectrum (On the Law of Distribution of Energy in the Normal Spectrum)". In: *Annalen der Physik* 309.3 (1901), pp. 553–563.

[2] S. N. Bose. "Plancks Gesetz und Lichtquantenhypothese (Planck's law and the hypothesis of light quanta)". German. In: *Zeitschrift für Physik* 26.1 (1924), pp. 178–181.

[3] A. Einstein. "Quantentheorie des einatomigen idealen Gases (Quantum theory of the monatomic ideal gas)". German. In: *Sitzungsberichte der Preussischen Akademie der Wissenschaften, Physikalisch-mathematische Klasse* (1924), pp. 261–267.

[4] A. Einstein. "Quantentheorie des einatomigen idealen Gases, 2 Abhandlung (Quantum theory of the monatomic ideal gas, part 2)". German. In: *Sitzungsberichte der Preussischen Akademie der Wissenschaften, Physikalisch-mathematische Klasse* (1925), pp. 3–14.

[5] F. London. "The $\lambda$-phenomenon of liquid helium and the Bose-Einstein degeneracy". In: *Nature* 141 (Apr. 1938), pp. 643–644.

[6] F. London. "On the Bose-Einstein condensation". In: *Phys. Rev.* 54 (11 Dec. 1938), pp. 947–954.

[7] C. E. Hecht. "The possible superfluid behaviour of hydrogen atom gases and liquids". In: *Physica* 25.7–12 (1959), pp. 1159–1161.

[8] M. H. Anderson, J. R. Ensher, M. R. Matthews, C. E. Wieman, and E. A. Cornell. "Observation of Bose-Einstein condensation in a dilute atomic vapor". In: *Science* 269.5221 (1995), pp. 198–201.

[9] K. B. Davis, M.-O. Mewes, M. R. Andrews, N. J. van Druten, D. S. Durfee, D. M. Kurn, and W. Ketterle. "Bose-Einstein condensation in a gas of sodium atoms". In: *Phys. Rev. Lett.* 75 (22 Nov. 1995), pp. 3969–3973.

[10] C. C. Bradley, C. A. Sackett, J. J. Tollett, and R. G. Hulet. "Evidence of Bose-Einstein condensation in an atomic gas with attractive interactions". In: *Phys. Rev. Lett.* 75 (9 Aug. 1995), pp. 1687–1690.

[11] C. C. Bradley, C. A. Sackett, and R. G. Hulet. "Bose-Einstein condensation of lithium: Observation of limited condensate number". In: *Phys. Rev. Lett.* 78 (6 Feb. 1997), pp. 985–989.

[12] C. Orzel, A. K. Tuchman, M. L. Fenselau, M. Yasuda, and M. A. Kasevich. "Squeezed states in a Bose-Einstein condensate". In: *Science* 291.5512 (2001), pp. 2386–2389.

[13] M. Greiner, O. Mandel, T. Esslinger, T. W. Hansch, and I. Bloch. "Quantum phase transition from a superfluid to a Mott insulator in a gas of ultracold atoms". In: *Nature* 415.6867 (Jan. 2002), pp. 39–44.

[14] R. Gati, B. Hemmerling, J. Fölling, M. Albiez, and M. K. Oberthaler. "Noise thermometry with two weakly coupled Bose-Einstein condensates". In: *Phys. Rev. Lett.* 96 (13 Apr. 2006), p. 130404.

[15] M. Albiez, R. Gati, J. Fölling, S. Hunsmann, M. Cristiani, and M. K. Oberthaler. "Direct observation of tunneling and nonlinear self-trapping in a single bosonic Josephson junction". In: *Phys. Rev. Lett.* 95 (1 June 2005), p. 010402.

[16] J. E. Simsarian, J. Denschlag, M. Edwards, C. W. Clark, L. Deng, E. W. Hagley, K. Helmerson, S. L. Rolston, and W. D. Phillips. "Imaging the phase of an evolving Bose-Einstein condensate wave function". In: *Phys. Rev. Lett.* 85 (10 Sept. 2000), pp. 2040–2043.

[17] M. R. Andrews, C. G. Townsend, H.-J. Miesner, D. S. Durfee, D. M. Kurn, and W. Ketterle. "Observation of interference between two Bose condensates". In: *Science* 275.5300 (1997), pp. 637–641.

[18] H. R. Glyde, O. Plantevin, B. Fåk, G. Coddens, P. S. Danielson, and H. Schober. "Dynamics of liquid $^4He$ in Vycor". In: *Phys. Rev. Lett.* 84 (12 Mar. 2000), pp. 2646–2649.

[19] G. E. Astrakharchik, J. Boronat, J. Casulleras, and S. Giorgini. "Superfluidity versus Bose-Einstein condensation in a Bose gas with disorder". In: *Phys. Rev. A* 66 (2 Aug. 2002), p. 023603.

[20] L. Tian and P. Zoller. "Quantum computing with atomic Josephson junction arrays". In: *Phys. Rev. A* 68 (4 Oct. 2003), p. 042321.

[21] Z.-B. Chen and Y.-D. Zhang. "Possible realization of Josephson charge qubits in two coupled Bose-Einstein condensates". In: *Phys. Rev. A* 65 (2 Jan. 2002), p. 022318.

[22] T. L. Gustavson, P. Bouyer, and M. A. Kasevich. "Precision rotation measurements with an atom interferometer gyroscope". In: *Phys. Rev. Lett.* 78 (11 Mar. 1997), pp. 2046–2049.

[23] M. J. Snadden, J. M. McGuirk, P. Bouyer, K. G. Haritos, and M. A. Kasevich. "Measurement of the Earth's gravity gradient with an atom interferometer-based gravity gradiometer". In: *Phys. Rev. Lett.* 81 (5 Aug. 1998), pp. 971–974.

[24] J. M. McGuirk, M. J. Snadden, and M. A. Kasevich. "Large area light-pulse atom interferometry". In: *Phys. Rev. Lett.* 85 (21 Nov. 2000), pp. 4498–4501.

[25] J. A. Stickney. "A theoretical analysis of Bose-Einstein condensate based beamsplitters, interferometers, and transistors". PhD thesis. Worcester Polytechnic Institute, Sept. 2007.

[26] Y. Shin, M. Saba, T. A. Pasquini, W. Ketterle, D. E. Pritchard, and A. E. Leanhardt. "Atom interferometry with Bose-Einstein condensates in a double-well potential". In: *Phys. Rev. Lett.* 92 (5 Feb. 2004), p. 050405.

[27] T. Schumm, S. Hofferberth, L. M. Andersson, S. Wildermuth, S. Groth, I. Bar-Joseph, J. Schmiedmayer, and P. Kruger. "Matter-wave interferometry in a double well on an atom chip". In: *Nat. Phys.* 1 (Oct. 2005), pp. 57–64.

[28] D. J. Wineland, J. J. Bollinger, W. M. Itano, F. L. Moore, and D. J. Heinzen. "Spin squeezing and reduced quantum noise in spectroscopy". In: *Phys. Rev. A* 46 (11 Dec. 1992), R6797–R6800.

[29] D. J. Wineland, J. J. Bollinger, W. M. Itano, and D. J. Heinzen. "Squeezed atomic states and projection noise in spectroscopy". In: *Phys. Rev. A* 50 (1 July 1994), pp. 67–88.

[30] J. J. . Bollinger, W. M. Itano, D. J. Wineland, and D. J. Heinzen. "Optimal frequency measurements with maximally correlated states". In: *Phys. Rev. A* 54 (6 Dec. 1996), R4649–R4652.

[31] S. F. Huelga, C. Macchiavello, T. Pellizzari, A. K. Ekert, M. B. Plenio, and J. I. Cirac. "Improvement of frequency standards with quantum entanglement". In: *Phys. Rev. Lett.* 79 (20 Nov. 1997), pp. 3865–3868.

[32] J. A. Dunningham, K. Burnett, and S. M. Barnett. "Interferometry below the standard quantum limit with Bose-Einstein condensates". In: *Phys. Rev. Lett.* 89 (15 Sept. 2002), p. 150401.

[33] J. A. Dunningham and K. Burnett. "Sub-shot-noise-limited measurements with Bose-Einstein condensates". In: *Phys. Rev. A* 70 (3 Sept. 2004), p. 033601.

[34] H. Feshbach. "Unified theory of nuclear reactions". In: *Ann. Phys.* 5.4 (1958), pp. 357–390.

[35] U. Fano. "Effects of configuration interaction on intensities and phase shifts". In: *Phys. Rev.* 124 (6 Dec. 1961), pp. 1866–1878.

[36] S. E. Pollack, D. Dries, M. Junker, Y. P. Chen, T. A. Corcovilos, and R. G. Hulet. "Extreme tunability of interactions in a Li-7 Bose-Einstein condensate". In: *Phys. Rev. Lett.* 102 (9 Mar. 2009), p. 090402.

[37] C.-S. Chuu, F. Schreck, T. P. Meyrath, J. L. Hanssen, G. N. Price, and M. G. Raizen. "Direct observation of sub-poissonian number statistics in a degenerate Bose gas". In: *Phys. Rev. Lett.* 95 (26 Dec. 2005), p. 260403.

[38] G.-B. Jo, Y. Shin, S. Will, T. A. Pasquini, M. Saba, W. Ketterle, D. E. Pritchard, M. Vengalattore, and M. Prentiss. "Long phase coherence time and number squeezing of two Bose-Einstein condensates on an atom chip". In: *Phys. Rev. Lett.* 98 (3 Jan. 2007), p. 030407.

[39] J. Esteve, C. Gross, A. Weller, S. Giovanazzi, and M. K. Oberthaler. "Squeezing and entanglement in a Bose-Einstein condensate". In: *Nature* 455.7217 (Oct. 2008), pp. 1216–1219.

[40] J. Appel, P. J. Windpassinger, D. Oblak, U. B. Hoff, N. Kjærgaard, and E. S. Polzik. "Mesoscopic atomic entanglement for precision measurements beyond the standard quantum limit". In: *Proc. Natl. Acad. Sci. USA* 106.27 (2009), pp. 10960–10965. eprint: `http://www.pnas.org/content/106/27/10960.full.pdf+html`.

[41] K. W. Mahmud, J. N. Kutz, and W. P. Reinhardt. "Bose-Einstein condensates in a one-dimensional double square well: Analytical solutions of the nonlinear Schrödinger equation". In: *Phys. Rev. A* 66 (6 Dec. 2002), p. 063607.

[42] G. J. Milburn, J. Corney, E. M. Wright, and D. F. Walls. "Quantum dynamics of an atomic Bose-Einstein condensate in a double-well potential". In: *Phys. Rev. A* 55 (6 June 1997), pp. 4318–4324.

[43] J. Javanainen and M. Y. Ivanov. "Splitting a trap containing a Bose-Einstein condensate: Atom number fluctuations". In: *Phys. Rev. A* 60 (3 Sept. 1999), pp. 2351–2359.

[44] C. Bodet, J. Estève, M. K. Oberthaler, and T. Gasenzer. "Two-mode Bose gas: Beyond classical squeezing". In: *Phys. Rev. A* 81 (6 June 2010), p. 063605.

[45] R. W. Spekkens and J. E. Sipe. "Spatial fragmentation of a Bose-Einstein condensate in a double-well potential". In: *Phys. Rev. A* 59 (5 May 1999), pp. 3868–3877.

[46] E. J. Mueller, T.-L. Ho, M. Ueda, and G. Baym. "Fragmentation of Bose-Einstein condensates". In: *Phys. Rev. A* 74 (3 Sept. 2006), p. 033612.

[47] K. Sakmann, A. I. Streltsov, O. E. Alon, and L. S. Cederbaum. "Number fluctuations of cold, spatially split bosonic objects". In: *Phys. Rev. A* 84 (5 Nov. 2011), p. 053622.

[48] D. Ananikian and T. Bergeman. "Gross-Pitaevskii equation for Bose particles in a double-well potential: Two-mode models and beyond". In: *Phys. Rev. A* 73 (1 Jan. 2006), p. 013604.

[49] X. Jia, W. Li, and J. Q. Liang. "Nonlinear correction to the boson Josephson-junction model". In: *Phys. Rev. A* 78 (2 Aug. 2008), p. 023613.

[50] M. A. García-March, D. R. Dounas-Frazer, and L. D. Carr. "Macroscopic superposition of ultracold atoms with orbital degrees of freedom". In: *Phys. Rev. A* 83 (4 Apr. 2011), p. 043612.

[51] K. Sakmann, A. I. Streltsov, O. E. Alon, and L. S. Cederbaum. "Exact quantum dynamics of a bosonic Josephson junction". In: *Phys. Rev. Lett.* 103 (22 Nov. 2009), p. 220601.

[52] K. Sakmann, A. I. Streltsov, O. E. Alon, and L. S. Cederbaum. "Quantum dynamics of attractive versus repulsive bosonic Josephson junctions: Bose-Hubbard and full-Hamiltonian results". In: *Phys. Rev. A* 82 (1 July 2010), p. 013620.

[53] P. Nozières and D. Saint James. "Particle vs. pair condensation in attractive Bose liquids". In: *J. Phys. France* 43.7 (1982), pp. 1133–1148.

[54] K. Xu, Y. Liu, D. E. Miller, J. K. Chin, W. Setiawan, and W. Ketterle. "Observation of strong quantum depletion in a gaseous Bose-Einstein condensate". In: *Phys. Rev. Lett.* 96 (18 May 2006), p. 180405.

[55] A. E. Leanhardt, A. P. Chikkatur, D. Kielpinski, Y. Shin, T. L. Gustavson, W. Ketterle, and D. E. Pritchard. "Propagation of Bose-Einstein condensates in a magnetic waveguide". In: *Phys. Rev. Lett.* 89 (4 July 2002), p. 040401.

[56] A. I. Streltsov, L. S. Cederbaum, and N. Moiseyev. "Ground-state fragmentation of repulsive Bose-Einstein condensates in double-trap potentials". In: *Phys. Rev. A* 70 (5 Nov. 2004), p. 053607.

[57] A. D. Jackson, G. M. Kavoulakis, and M. Magiropoulos. "Fragility of fragmentation in Bose-Einstein condensates". In: *Phys. Rev. A* 78 (6 Dec. 2008), p. 063623.

[58] A. Sarsa, K. E. Schmidt, and W. R. Magro. "A path integral ground state method". In: *J. Chem. Phys.* 113.4 (2000), pp. 1366–1371.

[59] S. Moroni and M. Boninsegni. "Condensate Fraction in Liquid 4He". In: *J. Low Temp. Phys.* 136 (3-4 2004), pp. 129–137.

[60] J. E. Cuervo, P.-N. Roy, and M. Boninsegni. "Path integral ground state with a fourth-order propagator: Application to condensed helium". In: *J. Chem. Phys.* 122.11, 114504 (2005), p. 114504.

[61] E. W. Weisstein. *Polylogarithm*. From MathWorld—A Wolfram Web Resource. URL: `http://mathworld.wolfram.com/Polylogarithm.html` (visited on 10/30/2013).

[62] C. Pethick and H. Smith. *Bose-Einstein Condensation in Dilute Gases*. 2nd ed. Cambridge University Press, 2008.

[63] G. F. Gribakin and V. V. Flambaum. "Calculation of the scattering length in atomic collisions using the semiclassical approximation". In: *Phys. Rev. A* 48 (1 July 1993), pp. 546–553.

[64] K. Huang and C. N. Yang. "Quantum-mechanical many-body problem with hard-sphere interaction". In: *Phys. Rev.* 105 (3 Feb. 1957), pp. 767–775.

[65] E. Fermi. "Sul moto dei neutroni nelle sostanze idrogenate (On the motion of neutrons in hydrogenous substances)". Italian. In: *Ricerca Sci.* 7 (2 1936), pp. 13–52.

[66] G. Breit. "The scattering of slow neutrons by bound protons. I. Methods of calculation". In: *Phys. Rev.* 71 (4 Feb. 1947), pp. 215–231.

[67] A. J. Moerdijk, B. J. Verhaar, and A. Axelsson. "Resonances in ultracold collisions of $^6$Li, $^7$Li, and $^{23}$Na". In: *Phys. Rev. A* 51 (6 June 1995), pp. 4852–4861.

[68] S. Inouye, M. R. Andrews, J. Stenger, H.-J. Miesner, D. M. Stamper-Kurn, and W. Ketterle. "Observation of Feshbach resonances in a Bose-Einstein condensate". In: *Nature* 392 (6672 Mar. 1998), pp. 151–154.

[69] P. Courteille, R. S. Freeland, D. J. Heinzen, F. A. van Abeelen, and B. J. Verhaar. "Observation of a Feshbach Resonance in cold atom scattering". In: *Phys. Rev. Lett.* 81 (1 July 1998), pp. 69–72.

[70] J. L. Roberts, N. R. Claussen, S. L. Cornish, and C. E. Wieman. "Magnetic field dependence of ultracold inelastic collisions near a Feshbach resonance". In: *Phys. Rev. Lett.* 85 (4 July 2000), pp. 728–731.

[71] L. P. Pitaevskii. "Вихревые нити в неидеальном бозе-газе (Vortex lines in a nonideal Bose gas)". Russian. In: *ЖЭТФ (J. Exp. Theo. Phys.)* 40 (2 1961), pp. 195–207.

[72] E. Gross. "Structure of a quantized vortex in boson systems". In: *Il Nuovo Cimento* 20.3 (1961), pp. 454–477.

[73] H. A. Gersch and G. C. Knollman. "Quantum cell model for Bosons". In: *Phys. Rev.* 129 (2 Jan. 1963), pp. 959–967.

[74] M. Holzmann, P. Grüter, and F. Laloë. "Bose-Einstein condensation in interacting gases". In: *Eur. Phys. J. B* 10.4 (1999), pp. 739–760.

[75] O. Penrose. "On the quantum mechanics of helium II". In: *Phil. Mag.* 42.335 (1951), pp. 1373–1377.

[76] L. D. Landau and E. M. Lifshitz. *Статистическая физика (Statistical Physics)*. 1st ed. Moscow: Физматгиз (State Physics and Mathematics Publishing House), 1951.

[77] P.-O. Löwdin. "Quantum theory of many-particle systems. I. Physical interpretations by means of density matrices, natural spin-orbitals, and convergence problems in the method of configurational interaction". In: *Phys. Rev.* 97 (6 Mar. 1955), pp. 1474–1489.

[78] O. Penrose and L. Onsager. "Bose-Einstein condensation and liquid helium". In: *Phys. Rev.* 104 (3 Nov. 1956), pp. 576–584.

[79] T. D. Lee, K. Huang, and C. N. Yang. "Eigenvalues and eigenfunctions of a Bose system of hard spheres and its low-temperature properties". In: *Phys. Rev.* 106 (6 June 1957), pp. 1135–1145.

[80] C. N. Yang. "Concept of off-diagonal long-range order and the quantum phases of liquid He and of superconductors". In: *Rev. Mod. Phys.* 34 (4 Oct. 1962), pp. 694–704.

[81] S. Goedecker and C. J. Umrigar. "Natural orbital functional for the many-electron problem". In: *Phys. Rev. Lett.* 81 (4 July 1998), pp. 866–869.

[82] S. Goedecker and C. Umrigar. "Natural orbital functional theory". English. In: *Many-Electron Densities and Reduced Density Matrices*. Ed. by J. Cioslowski. Mathematical and Computational Chemistry. Springer US, 2000, pp. 165–181.

[83] N. Bogoliubov. "К теории сверхтекучести (On the theory of superfluidity)". Russian. In: *Изв. АН СССР, Сер. физ. (Bull. Acad. Sci. USSR, Phys.)* 11 (1 1947), pp. 77–90.

[84] A. J. Leggett. "Bose-Einstein condensation in the alkali gases: Some fundamental concepts". In: *Rev. Mod. Phys.* 73 (2 Apr. 2001), pp. 307–356.

[85] D. R. Dounas-Frazer. "Ultracold bosons in a multi-dimensional, tilted, couble-well trap: Potential decoherence, tunneling resonances, and two-level phenomina". MA thesis. Colorado School of Mines, 2007.

[86] C. P. Friedman and E. F. Taylor. "Quantizing angular momentum via the simple harmonic oscillator". In: *Am. J. Phys.* 39.9 (1971), pp. 1073–1078.

[87] R. P. Feynman. "Space-Time Approach to Non-Relativistic Quantum Mechanics". In: *Rev. Mod. Phys.* 20 (2 Apr. 1948), pp. 367–387.

[88] S. A. Chin. "Symplectic integrators from composite operator factorizations". In: *Phys. Lett. A* 226.6 (1997), pp. 344–348.

[89] S. A. Chin and C. R. Chen. "Gradient symplectic algorithms for solving the Schrödinger equation with time-dependent potentials". In: *J. Chem. Phys.* 117.4 (2002), pp. 1409–1415.

[90] J. Cao and B. J. Berne. "A new quantum propagator for hard sphere and cavity systems". In: *J. Chem. Phys.* 97.4 (1992), pp. 2382–2385.

[91] N. Metropolis, A. W. Rosenbluth, M. N. Rosenbluth, A. H. Teller, and E. Teller. "Equation of state calculations by fast computing machines". In: *J. Chem. Phys.* 21.6 (1953), pp. 1087–1092.

[92] W. H. Press, S. A. Teukolsky, W. T. Vetterling, and B. P. Flannery. *Numerical Recipes: The Art of Scientific Computing*. 3rd ed. New York: Cambridge University Press, 2007.

[93] H. F. Trotter. "On the product of semi-groups of operators". In: *Proc. Amer. Math. Soc.* 10 (4 Aug. 1959), pp. 545–551.

[94] J. A. Barker. "A quantum-statistical Monte Carlo method; Path integrals with boundary conditions". In: *J. Chem. Phys.* 70.6 (1979), pp. 2914–2918.

[95] G. Jacucci and E. Omerti. "Monte Carlo calculation of the radial distribution function of quantum hard spheres at finite temperatures using path integrals with boundary conditions". In: *J. Chem. Phys.* 79.6 (1983), pp. 3051–3054.

[96] S. Y. Larsen. "Quantum-mechanical pair-correlation function of hard spheres". In: *J. Chem. Phys.* 48.4 (1968), pp. 1701–1708.

[97] C. P. Robert and G. Casella. *Monte Carlo Statistical Methods*. 2nd ed. Springer, 2004.

[98] V. Ambegaokar and M. Troyer. "Estimating errors reliably in Monte Carlo simulations of the Ehrenfest model". In: *Am. J. Phys.* 78.2 (2010), pp. 150–157.

[99] P. Lévy. "Sur certains processus stochastiques homogènes (On certain homogeneous stochastic processes)". French. In: *Compositio Math.* 7 (1940), pp. 283–339.

[100] D. M. Ceperley. "Path integrals in the theory of condensed helium". In: *Rev. Mod. Phys.* 67 (2 Apr. 1995), pp. 279–355.

[101] W. Krauth. *Statistical Mechanics: Algorithms and Computations*. Oxford University Press, 2006.

[102] R. H. Swendsen and J.-S. Wang. "Replica Monte Carlo simulation of spin-glasses". In: *Phys. Rev. Lett.* 57 (21 Nov. 1986), pp. 2607–2609.

[103] F. Wang and D. P. Landau. "Efficient, multiple-range random walk algorithm to calculate the density of states". In: *Phys. Rev. Lett.* 86 (10 Mar. 2001), pp. 2050–2053.

[104] I. Klich, G. Refael, and A. Silva. "Measuring entanglement entropies in many-body systems". In: *Phys. Rev. A* 74 (3 Sept. 2006), p. 032306.

[105] I. Klich and L. Levitov. "Quantum Noise as an Entanglement Meter". In: *Phys. Rev. Lett.* 102 (10 Mar. 2009), p. 100502.

[106] H. F. Song, S. Rachel, C. Flindt, I. Klich, N. Laflorencie, and K. Le Hur. "Bipartite fluctuations as a probe of many-body entanglement". In: *Phys. Rev. B* 85 (3 Jan. 2012), p. 035409.

[107] P. Calabrese, M. Mintchev, and E. Vicari. "Exact relations between particle fluctuations and entanglement in Fermi gases". In: *EPL* 98.2 (2012), p. 20003.

[108] M. B. Hastings, I. González, A. B. Kallin, and R. G. Melko. "Measuring Renyi entanglement entropy in quantum Monte Carlo simulations". In: *Phys. Rev. Lett.* 104 (15 Apr. 2010), p. 157201.

[109] N. M. Tubman and J. McMinis. "Renyi entanglement entropy of molecules: Interaction effects and signatures of bonding". In: *ArXiv e-prints* (Apr. 2012). arXiv: `1204.4731 [cond-mat.str-el]`.

[110] J. McMinis and N. M. Tubman. "Renyi entropy of the interacting Fermi liquid". In: *Phys. Rev. B* 87 (8 Feb. 2013), p. 081108.

[111] B. Swingle, J. McMinis, and N. M. Tubman. "Oscillating terms in the Renyi entropy of Fermi gases and liquids". In: *Phys. Rev. B* 87 (23 June 2013), p. 235112.

[112] S. Humeniuk and T. Roscilde. "Quantum Monte Carlo calculation of entanglement Rényi entropies for generic quantum systems". In: *Phys. Rev. B* 86 (23 Dec. 2012), p. 235116.

[113] E. W. Weisstein. *Faà di Bruno's formula*. From MathWorld—A Wolfram Web Resource. URL: `http://mathworld.wolfram.com/FaadiBrunosFormula.html` (visited on 10/30/2013).

[114] H. F. Song, S. Rachel, C. Flindt, I. Klich, N. Laflorencie, and K. Le Hur. *Supplemental material for "Bipartite fluctuations as a probe of many-body entanglement"*. Nov. 28, 2011. URL: `http://prb.aps.org/epaps/PRB/v85/i3/e035409/main.pdf`.

[115] J. Sondow and E. W. Weisstein. *Hurwitz zeta function*. From MathWorld—A Wolfram Web Resource. URL: `http://mathworld.wolfram.com/HurwitzZetaFunction.html` (visited on 10/30/2013).